Phase-Change Materials for Photonic Memories and Optoelectronic Applications

Carlos Andrés Ríos Ocampo
Linacre College

Supervisor: Prof. Harish Bhaskaran

A thesis submitted for the degree of
Doctor of Philosophy

Trinity Term 2016

Dedicado a mis padres, Luz Mary Ocampo y Elkin Ríos

Acknowledgements

I am eternally thankful and indebted to the people that allowed the successful completion of this Thesis; the culmination of my rather long stage as student. I am also grateful to all the great human beings that inspired and influenced my life throughout these years in academia, which, fortunately, counts many more ups than downs. Special thanks to:

Prof. Harish Bhaskaran for welcoming me in his lab, for the supervision during these almost three years, his confidence, support, and right advice.

Prof. Wolfram Pernice (University of Münster) for opening the doors of this fascinating project and the world of integrated photonics during my time as Master student in Karlsurhe.

Prof. David Wright (University of Exeter) for his valuable inputs and discussion. To his group members Santiago García-Cuevas Carrillo and Arseny Alexeev for their support with nanofabrication.

Matthias Stegmaier (University of Münster), for the hard work towards improving the field of phase-change photonics and for all the help with the experimental setup during his visiting time in Oxford.

Ben, Daniel, Frederica, Gerardo, Ghazi, Jasmin, Jeremy, Kylee, Nathan, Madhav, Merce, Nhlakanipho, Peiman, Sarolta, Zengguang, past, and present members of the Advanced Nanoscale Engineering group for the support, friendship, and good moments. Special mention to Peinman Hosseini and Gerardo Rodríguez, the phase-change materials guys, for sharing their secrets with me; to Ben Porter for proof-reading this thesis and for sweetening these years with his incredible baking skills; and to Nathan Youngblood for proof-reading this thesis.

The people behind the scene who make our life easier in the labs: Paul Pattinson at the Physics Department cleanroom and Radka Chakalova at Begbroke science park cleanroom, and in the office: the IT team and the officials of the Materials department.

The University of Oxford, through the Clarendon Fund, and JEOL Uk, through Linacre

College, for the co-sponsored Clarendon Scholarship that made my DPhil a reality. There are no words or actions to express my gratitude for this unique opportunity.

All my Oxford friends—I am very humbled to realise that you are so many, and so good. My dear friends from Linacre college, the coffee/hiking club, Colombian Society, Latin American society, Karate Club, 8BR and 64WR housemates, Clarendon friends, and the many of you made in pubs, bops, formals, balls, and all those Oxonian attractions. Thanks for filling these years with uncountable and unforgettable memories, laughs, and love. Many thanks, in particular, to Christoph Riedel for proofreading this thesis.

To my dearest Anna for proof-reading this thesis and providing me with the happiness required to stay sane during the time of its preparation.

My academic mentors throughout these years. To Bernardo Obando for introducing me to the wonderful world of physics back at school at the IEJMG. To John Fredy Barrera and Edgar Rueda for supervising my long work as undergraduate student at the Optics and Photonics Group at Universidad de Antioquia, Medellin, Colombia.

All my old and good friends in Colombia and around the world for their support and caring no matter the distance.

A la mayor y más importante motivación e inspiración: mi familia. A mi Madre Luz Mary, a mi Padre Elkin, mis hermanos Jhon Jader, Juan Pablo y José Daniel, a mi sobrino Juan Manuel, mis abuelas, mis tías, tíos y primos. Su incondicional amor y apoyo han sido mi soporte a pesar de la distancia; la fuerza necesaria para cumplir con éxito, éste, mi último objetivo en este largo camino como estudiante. A ellos quiero dedicar esta tesis, los logros y las alegrías que han dejado tantos años de esfuerzo.

To all of you—and those whom I might have involuntarily forgotten—I want to express my deepest thank you.

Carlos A. Rios Ocampo
Oxford, 30 September 2016

Abstract

The content of this thesis encompasses the fundamentals, modelling, chip design, nanofabrication process, measurement setup, and experimental results of devices exploiting the optical properties of phase-change chalcogenide materials. Special attention is paid to integrated Si_3N_4 nanophotonic circuits for optical switching and memory applications, as well as to multilayer stacks for colour modulation.

Herein, the implementation of the first robust, non-volatile, phase-change photonic memory is presented. By utilising optical near-field effects for *Read*, *Write* and *Erase* operations, bit storage of up to eight transmission levels is demonstrated in a single device employing $Ge_2Sb_2Te_5$ as the active material. These on-chip memory cells feature single-shot read-out of the transmission state and switching energies as low as 13.4 pJ at speeds approaching 1 GHz. The capability to readily switch between intermediate states is also demonstrated, a feature that requires complex iteration-based algorithms in electronic phase-change memories. This photonic memory is not only the first truly non-volatile memory—a long-term elusive goal in integrated photonics—but could also potentially represent the first multi-level memory, including electronic counterparts, that requires no computational post-processing or drift correction. These findings provide a pathway towards solving the throughput limitations of current computer architectures by eliminating the so-called von-Neumann bottleneck and portend a new paradigm in all-photonic memory, non-conventional computing, and tunable photonic devices.

Finally, novel capabilities in electro-optic colour modulation using phase-change materials are demonstrated. In particular, this thesis offers the first implementation of $Ag_3In_4Sb_{76}Te_{17}$-based optical cavities for colour modulation on low-dimensional multilayer stacks. Moreover, "gray-scale" image writing is demonstrated by establishing intermediate levels of crystallisation via voltage modulation. This finding, in turn, corresponds to the first demonstration of nonvolatile colour-depth modulation in the emerging phase-change materials nanodisplay technology, featuring resolutions down to 50 nm. Furthermore, a comprehensive comparison is carried out for two types of materials: growth- ($Ag_3In_4Sb_{76}Te_{17}$) and nucleation-dominated ($Ge_2Sb_2Te_5$) alloys in terms of colour, energy efficiency, and resolution. These results provide new tools for the new generation of bistable and ultra-high-resolution displays and smart glasses while allowing for other potential applications in photonics and optoelectronics.

Contents

List of Figures

List of Acronyms and Symbols

AIST	$Ag_3In_4Sb_{76}Te_{17}$ phase-change alloy
CAD	Computer-Aided Design
CIE	Commission Internationale de l'Éclairage / International commission on illumination
CW	Continuous wave
EDFA	Erbium-doped fibre amplifier
EIM	Effective index method
EOM	Electro-optical modulator
FEM	Finite Element Method
FIB	Focused ion beam
GST	$Ge_2Sb_2Te_5$ phase-change alloy
PCM	Phase-change materials
PMMA	Poly(methyl methacrylate) : positive photoresist
RIE	Reactive ion etching
RMS	Root mean square
SMF	Single mode fibre
SNR	Signal to noise ratio
TE	Transverse Electric polarised light
TM	Transverse Magnetic polarised light

Chapter 1

Introduction

1.1 Motivation

The discovery of chalcogenide materials capable of switching between two stable crystallographic phases by Ovshinsky in 1968 [1], along with the development of such materials in subsequent decades [2, 3, 4, 5, 6, 7, 8], gave birth to revolutionary non-volatile optical data storage devices including rewritable compact disks (CD's) and Blue-ray disks [9, 10]. Such phase-change materials (PCMs) offer a striking combination of properties including: nano- and pico-second switching, high optical and electrical contrast between the crystalline and the amorphous phases, and high stability, i.e. non-volatility, thus retaining the phase state for a period of time spanning into decades. All these qualities together in a compact disk allowed for tremendous improvement compared to any other external memory device existing at that time in terms of speed, cyclability, and storage density [11, 12]. However, recent years have seen a technological shift: the amount of data has increased rapidly while devices miniaturised to improve storage density. Following this tendency, the

conventional CD architecture has reached its limit and become rendered obsolete, as its form factor cannot be further reduced due to the external diffraction-limited laser required to switch the material. Instead, the development of new electronic solid-state alternatives has relegated optical PCM-based devices to a second plane [13].

The possibility of controlling phase-change materials such as $Ge_2Sb_2Te_5$ in a full electronic fashion in sub-100nm configurations [10, 12] and nanowires [14]—displaying permanent data storage and high speeds [8]—has caught the attention of researchers. Such a development could return phase-change memories to the commercialisation landscape, this time eliminating the optical component. PCM electronic devices could add functionalities, such as multilevel storage and memrisistive performance, that in turn allow for cognitive computing architectures [15, 16, 17, 18]. Thus, the phase-change materials community has been researching the development of new alloys that can represent an improvement in any of the above-mentioned properties and focused on realising better electronic memories [19, 20, 21]. Yet, apart from such memresistive applications on neuromorphic computing [15, 22, 23, 24, 25], no other novel application was reported until 2012. During that year, W. Pernice and H. Bhaskaran [26] proposed a new approach using integrated photonic circuits based on PCMs for on-chip light modulation and all-optical data storage. Soon, researchers realised that, behind the outstanding refractive-index switching, lay a huge potential for applications in nanophotonics, plasmonics, and optoelectronics [27, 28, 29, 30, 31, 32]. Furthermore, in 2014, P. Hosseini, C.D. Wright, and H. Bhaskaran [33] demonstrated a completely new application based on phase-change materials, this time in bistable colour modulation samples with a promising future for nanodisplays, smart glasses, and security tags. These new ideas opened the doors to several fresh, interesting, and novel applications and, in turn, brought a renovated phase-change materials field back within the radar of science. Hence, with the increasing interest in these topics, a new *Phase-change photonics and optoelectronics* field has begun

to develop and has gained strength based, in part, on the results presented in this thesis.

1.1.1 All-photonic data storage and PCMs

The advent of photonic technologies, particularly in the area of optical signalling, coupled with advances made in nanofabrication capabilities, has created a growing need for practical all-photonic memories [34, 35, 36, 37, 38]. Such memories are essential to boost the computational performance in serial computers by speeding up the von-Neumann bottleneck—i.e. the information traffic jam between the processor and the memory, the main units of the von-Neumann arquictecture used in conventional computers. This bottleneck limits the speed of almost all processors today, a limitation that has been partially circunvented by using multicore processor architectures and fibre optics to bridge the units. However, shuttling information optically from the processor to electronic memories is presently not efficient, as electrical signals must be converted to optical signals and vice-versa. Instead, information transfer and storage exclusively by optical means is highly desirable because of the inherently large bandwidth [34, 39], low residual cross-talk, and high speed of optical information transfer. On a chip, this objective has been challenging to achieve because practical photonic memories would need to retain information for long periods of time, and would require full integration with the ancillary electronic circuitry, thus requiring compatibility with semiconductor processing [40]. Such compatibility is challenging even in the context of emerging electronic memories—one reason why (CMOS compatible) phase-change memories have been the subject of intense research and development over the last decade [12, 41, 42, 43]. Furthermore, the same operational principle used in optical memories (i.e. transmission/reflection measurements) could potentially be applied to create on-chip light switches and modulators to have better control and larger flexibility of device architectures and applications [44].

Phase-change materials combine a variety of advantageous properties which make them

ideal candidates for all-optical memories and modulators. A striking and functional feature of these materials is the high contrast between the crystalline and amorphous phase of both their electrical and optical properties [12, 25]. In particular, chalcogenide-based PCMs have the ability to switch between these two states in response to appropriate heat stimuli (crystallisation) or melt-quenching processes (amorphisation) [1]. These materials, mainly tellurides and antimonides, can be switched on a sub-nanosecond timescale [12, 45] with high reproducibility, which enables ultra-fast operation over switching cycles up to 10^{12} times [46, 47] using current-generation materials (with new and improved materials, such as phase-change super-lattice materials [19], it is expected to deliver even better performance in the future). In addition, at normal operating temperatures the states are highly stable for years [12, 14], a key requirement for a truly nonvolatile memory. These beneficial properties have already led to prominent commercial applications in optical data storage such as rewritable optical discs (in DVD and Blu-ray formats) [9] and, more recently, in phase-change random access and multi-level memories [10, 21, 48] as well as stochastic phase-change neurons [15].

In this thesis, by using nanoscale PCMs embedded in nanophotonic circuits, fast and repeatable all-optical, multi-level, multi-bit, nonvolatile memory operations are demonstrated at telecommunications wavelengths compatible with on-chip optical interconnects. In this wavelength range, several phase-change materials show significant contrast in the refractive index of their amorphous and crystalline states [26, 49]. Moreover, a wide range of high-efficiency and ultra-fast optical components operate in this wavelength range thanks to the transparency window of silicon, especially in the C- and L-bands—wavelengths within 1530-1625nm [40]. In contrast to free-space optical implementations, where PCM cells are switched with a focused laser, these new on-chip devices are operated in the optical near-field in analogy to plasmonic devices. Waveguide-integrated memory cells are thus not restricted in size by the diffraction limit of the input light and can hence be miniaturised to nanoscale dimensions. The well-studied alloy $Ge_2Sb_2Te_5$ is employed

because of its data-retention capabilities [1, 12] and high state discrimination [27] down to nanoscale cell sizes, which enable dense packaging and low-power memory switching. In the approach presented in this work, data are stored in a nanoscale GST device placed directly on top of a nanophotonic waveguide. Both writing into the memory cell and read-out of the stored information is carried out using nanosecond optical pulses within the waveguide with the phase-change material. This approach provides a promising route towards fast all-optical data storage in photonic circuits.

1.1.2 Colour modulation and PCMs

Colour modulation has been a topic of longstanding interest in science and engineering given its multiple applications in display technology, smart glass, security marks, and active optical components [50, 51]. Passive elements such as optical coatings, multilayer stacks, or structured films, have been extensively used in reflective and transmissive optical systems to attain a specific colour [50, 51, 52, 53, 54, 55]. Moreover, active materials with tunable physical or chemical properties, such as electrochromism [56, 57, 58], piezochromism[59], plasmonic effects [60], photoluminescence [61, 62], and volatile phase-change materials [63], have been exploited for colour modulation purposes. The dynamic modulation of optical properties by such materials has given rise to new remarkable improvements in terms of resolution, low dimensionality, and low energy operation of a display [64]. However, a combination of both active control and colour retention—for instance, a device with high resolution featuring offline colour retention that still allows full-gamut modulation—has proved challenging; some proposals either lack resolution [65] or required external chemical agents [66]. These issues, however, changed recently when an optoelectronic framework using nonvolatile nucleation-dominated phase-change materials was proposed to fill this gap. Employing $Ge_2Sb_2Te_5$ as an active yet bistable component, researchers were able to switch between two stable colours using multilayer optical cavities [33].

Phase-change materials promise great potential, given that state-of-the-art alloys are capable of switching between two optically and electrically differentiable states. In response to appropriate heat stimuli for crystallisation or melt-quenching for amorphisation, PCMs are capable of undergoing such switching in picosecond timescales [46, 67, 68]. More interestingly, they present room-temperature non-volatile behaviour by stably retaining either state for years [1, 14, 69]. All these properties together enable two highly differentiable optical states, allowed by the modulation in both the real and the imaginary refractive index upon phase switching. This active yet stable optical properties modulation can be achieved on a thin film, which in turn can be harnessed to switch colours [16, 33, 70]. The approach presented by Hosseini et al. [33] relies on strong Fabry-Perot type interferences undergone within a stack of layers featuring a highly absorptive medium [54], GST in this case. By using such a material, colours were obtained with just a few layers, thus presenting low-dimensionality (70 to 300 nm for the whole stack), that allows for flexible substrates to be employed. Furthermore, GST can be locally and reversibly switched at nanometric scales, enabling resolution beyond any other display previously reported. Here, it is demonstrated that $Ag_3In_4Sb_{76}Te_{17}$ (AIST), a growth-dominated phase-change alloy [71], can be employed for similar colour modulation, but with better depth-modulation capability (i.e. grey-scale). The resolution and switching energy limits of this technique are also studied, together with a comparison between the performance of AIST and GST in terms of colour modulation, resolution, and energy efficiency in multilayer samples.

1.2 Outline and Objectives

1.2.1 Objective

This thesis reports research that aims to exploit the merging of phase-change materials with nanophotonic and optoelectronic structures for the development of novel devices towards innovative applications. In taking advantage of the unique optical properties and tunable refractive index of such materials, experiments were carried out using two different kinds of devices:

- Integrated photonic circuits evanescently coupled to phase-change materials for on-chip all-photonic multi-level non-volatile memories.
- Low-dimensional multilayer optical cavities with phase-change material thin films for colour switching and nanodisplay applications.

This manuscript advances the science of phase-change materials and portends new paradigms in which all the optical properties of PCMs are harnessed in, and beyond, data storage.

1.2.2 Layout

The content of this thesis is structured in the following way:

- **Chapter 2** reviews the state-of-the-art developments that have led to a better understanding and applications of chalcogenide phase-change materials in the memory industry and scientific research. Furthermore, this chapter encompasses and criticises the multiple applications of merging PCMs with photonics and optoelectronics.

- **Chapter 3** contains the theory, design, and nanofabrication of integrated photonic circuits based on phase-change materials. Specifically, this chapter contains the theory used to calculate the parameters of the waveguides and the finite-element method (FEM) modelling of electromagnetic modes within photonic circuits. Moreover, this chapter describes the process to create a chip CAD layout using a script-based software whose library was developed on Cadence Virtuoso®. Lastly, chapter 3 includes the methods employed during the nanofabrication of the photonic chips used in the measurements realised in Ch. 5, including e-beam lithography, etching, sputtering, evaporation, and characterisation.

- **Chapter 4** describes the actual integrated pump/probe photonic experimental setup built from scratch for the measurements carried out in Ch. 5. It introduces the transmission measurements completed in order to characterise the nanophotonic circuits, the pump/probe measurements for on-chip active control of GST phase-state, and describes the different instruments employed: telecom laser, piezo-stage, low-noise and fast photo-receivers, EDFA amplifier, optical fibre array, electro-optical modulators, and electronic equipment.

- **Chapter 5** presents the demonstration and dynamics of the first truly non-volatile phase-change photonic memory using GST as an active material in a telecommunication-wavelength pump/probe experimental setup. In addition, up to 3-bit multi-level storage was proven in a single memory cell with accessible intra-level transitions. Finally, this chapter considers the limits and performance of this type of memory.

  All the results shown in Chapter Five were obtained in experiments carried out by the author. The only exception is Sec. 5.2.3 which contains TEM data obtained by collaborators at the Institute of Nanotechnology at the Karlsruhe Institute of Technology on samples fabricated as part of this work. This TEM information, which is original, is added to this thesis with the intention of complementing and

probing whether the results presented in this chapter are indeed due to phase-change switching.

The results in this chapter have led to the patent in ref. [72] and the publication found in ref. [67], which is why similarities between both texts are to be expected. Note that, although the aforementioned publication has two first authors who contributed equally, chapter five includes only the results obtained by the author of this thesis: the design and fabrication of the devices, the development of the photonic switching protocol, and the demonstration of binary and multilevel memory operation. These findings are the basis of this photonic device, which were taken to further wavelength-division experiments by Matthias Stegmaier at the Karlsruhe Institute of Technology.

- **Chapter 6** describes the implementation of $Ag_3In_4Sb_{76}Te_{17}$ (AIST), a growth-dominated phase-change alloy, in multilayer stack optical cavities for colour modulation in reflection mode and display capabilities with nanoscale resolution. In particular, depth modulation capability (i.e. grey-scale) is for the first time demonstrated for phase-change based displays. The limits of this technique in terms of resolution and switching energy are also studied, together with a comparison between the performance of AIST and GST as bistable nanodisplay materials.

  The results of this chapter led to the patent in ref. [73] for which the author of this thesis and two more researchers hold the intellectual property. However, other group of scientists have independently reported similar multi-colour approaches and confirmed experimentally in [74] the computational-only results presented herein. The aforementioned paper came later than the original patent-filing date.

1.2.3 Statement of originality

This manuscript is an original contribution written in its totality by the author. It contains an original literature review and novel findings and procedures all carried out during a period of eight academic terms, as part of the DPhil studies at the University of Oxford. The only exception is the inclusion of the brief TEM results presented in Sec. 5.2.3, which are original and carried out on samples fabricated by the author, yet obtained by collaborators. This exception is, however, as mentioned explicitly, not a central point of the results presented and aims only to support the analysis of the experimental results.

1.2.4 Key results and new science

The main findings of this thesis—merging phase-change materials with nanophotonic circuits and optoelectronics— are described in Chapters 5 and 6, supported with fundamentals and procedures presented in the other chapters. The key results and new science presented throughout this manuscript include:

- First protocol for all-photonic reversible switching of phase-change materials in on-chip nanophotonic circuits using near-field coupling.
- First truly non-volatile all-photonic memory (phase-change photonic memory).
- Demonstration of multi-level operation of phase-change photonic memories with intra-level transitions.
- Analysis of speed, modulation depth, and energy consumption of phase-change photonic memories.
- Computational analysis of the near-field phase-change switching dynamics.

- Demonstration of depth-colour modulation enabling grey-scale image rendition in multilayer optical cavities containing phase-change materials.
- First application of growth-dominated phase-change materials in colour modulation.
- Analysis of the resolution and switching-voltage limits in scanning and pixel-by-pixel modes in phase-change material nanodisplays.
- Comparison between GST and AIST in display applications.

Moreover, this project has left new tools developed by the author which will be useful for current and future members of the Advanced Nanoscale Engineering group at the University of Oxford, where this thesis was conceived. Some of these new tools include:

- A complete integrated photonic and optoelectronic setup for transmission characterisation, all-optical pump-probe, and integrated optoelectronic experiments in the C and L-band range. The setup includes also the LabView codes for automatic and remote control of all the components. For more details, see Ch. 4.
- A characterised fabrication process to obtain nanophotonic circuits based on phase-change materials. More details in Ch. 3.
- A Cadence Virtuoso® programming language library for the design of photonic chips CAD layouts, featuring the most important components such as gratings, ring resonators, Mach-Zehnder interferometers, electrodes, beam splitters, etc. For more details, see Ch. 3.
- A Matlab program to calculate the reflectance, transmittance, and absorptance of any multilayer stack using a transfer-matrix formalism. This code allows any arbitrary number of layers with arbitrary complex refractive indices and with variable input parameters, such as angle, polarisation, etc. as described in Ch. 6.

Chapter 2

Photonics and phase-change materials: a literature review

This chapter reviews the state-of-the-art developments and fundamentals that have led to a better understanding and applicability of chalcogenide phase-change materials, especially in the context of memory industry and research. Furthermore, it encompasses and criticises all the multiple applications of merging phase-change materials with photonics and optoelectronics.

2.1 Chalcogenide phase-change materials

Phase-change materials (PCMs), in the broadest of the definitions, refer to materials whose phase can be switched between at least two different and stable states by means of heat-exchange processes [75, 76]. Phase change, and therefore heat storage, can be found in solid to solid, solid to liquid, solid to gas, and liquid to gas transitions depending on the material composition.

Ranging from thermal energy to data storage, PCMs have been extensively utilised in everyday technological devices [75, 77]. Compounds such as salt hydrates, fatty acids and esters, and various paraffins present a solid to liquid transition which is currently employed in thermal control of engines, houses, the human body, etc. by absorbing or releasing heat [78]. However, chalcogenide PCMs are materials which have drawn more attention within the scientific community because of their unique scalability, optical, and electronics properties. These have revolutionised non-volatile data storage and still hold huge promise in nanoscale opto-electronic technologies [12, 76].

Glasses containing at least one of the chalcogen elements, sulfur (S), selenium (Se), tellurium (Te), or Polonium (Po), known as chalcogenide glasses, have given rise to the so-called phase-change recording materials (PCRM) and represent nowadays a very active research topic, especially for data storage in non-volatile memories [11, 12, 43, 76]. The majority of PCRMs are tellurium- or selenium-based alloys, examples being Ge-Te, Ge-Sb-Te, Ge-Te-Sn-O, Sn-Te-Se, In-Sb-Te, In-Se and Ag-In-Sb-Te [79] but also oxides such as V-O compounds [63]. They can be stabilised in at least two different physical states that present considerable contrast in the optical and electrical properties. These states are the amorphous and the crystalline phase (or one of the possible crystalline phases). Doped Sb-Te compositions are the most common as they achieve higher crystallisation rates. However, dopants like Ge, In or Ag promote the amorphisation and therefore the phase-change condition of the materials [80]. The stability of the amorphous state decreases with the dopants in the order Ge>Ag>Ga,In>Sn. Therefore, a trade-off between stability and phase-change rates must be considered when choosing a material.

$Ge_2Sb_2Te_5$ (GST) and Ag:In:Sb:Te (AIST)—with different compositions— represent two common and promising alloys. They have allowed the development of commercial

non-volatile memories for rewritable optical data storage, such as the blu-ray disk, and more recently enabled phase'change random access memories (PC-RAM) [2, 9, 10, 12]. Although their optical and electrical properties present astonishing similarities, their crystallisation dynamics differ radically. The first is a so-called nucleation-dominated material, while the latter is growth-dominated [81], as detailed in Sec. 2.2. This review will pay particular attention to GST given its interesting combination of properties: it is fast, scalable, stable, and offer high optical and electrical contrast between the amorphous and the crystalline states. These are the reasons why GST is the most common PCM used in research and industry. Moreover, when citing phase-change materials, it will implicitly refer to chalcogenide PCMs.

2.2 Nucleation- and growth-dominated PCMs

Phase-change materials are grouped in two categories depending on their crystallisation dynamics [12, 82, 83]:

Nucleation-dominated: This group contains materials in which, under optical or electrical excitation, crystallisation takes place in randomly located small nuclei as shown in Fig. 2.1. The optical and electrical properties adopt intermediate states—as result of the superposition of amorphous and crystalline material—until a growth process, where many small crystals expand and merge, gives rise to the complete phase-state switching. The most common nucleation-dominated materials are the GeSb alloys, including the vast family of GeSbTe compounds. The formation of nuclei occurs in pico- to nanosecond time scales.

Growth-dominated: In this kind of material, there are very few nuclei or only one nucleus formed during the nucleation stage. However, the growth process is predominant

during the phase-change, which is a slower process compared to nucelation-dominated materials happening on the order of nanoseconds [82]. Each, or the only, nucleus grows considerably bigger until they eventually form one crystal. In-Sb-Te alloys, such as AgInSbTe, are the most common alloys of this group [80, 84].

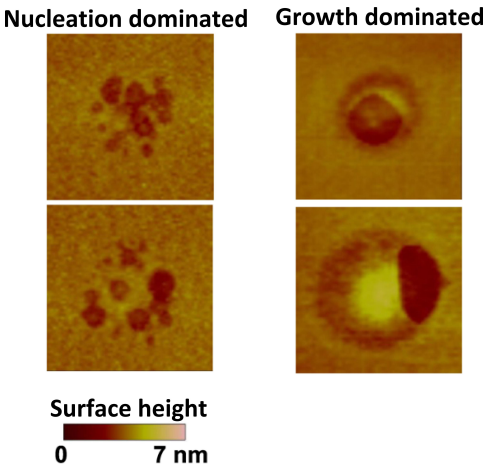

Figure 2.1: Crystallisation of nucleation (GST) and growth (AIST) dominated materials under laser pulse irradation. Adapted with permission from [84].

The difference in the crystallisation dynamics does not imply differences in optical or electrical properties. In fact, GST and AIST show remarkable similarities in their refractive-indices and conductivities. Moreover, reamorphisation is realised in the same manner in both, by melt-quenching the material. Although the nanostructural origin of the dynamics difference has not been clearly demonstrated, experimental approaches have observed this different nuclei formation [83].

2.3 $Ge_2Sb_2Te_5$ phase-change material

The alloy $Ge_2Sb_2Te_5$ is, to date, the material with the best combination of properties for data storage systems [85]. Not only does it exhibit one of the fastest crystallisation dynamics but it also switches at low energies and has one of the most pronounced electrical resistivity and dielectric function contrast amongst known PCMs [9, 12, 86]. The refractive-index contrast is maintained over a spectral bandwidth that ranges from

visible to infrared wavelengths [6]. Fast switching times and the ability to retain the desired state at room temperature for periods of time spanning into decades are also some of the main characteristics of this compound [12, 14]. Because of these properties, GST has been the most common alloy in the development of PCM-based devices [11].

X-Ray Diffraction (XRD), Differential Scanning Calorimetry (DSC), and other techniques have shown that GST has three stable crystallographic solid states, namely amorphous, metastable rock salt (face centred cubic, fcc) when heated above $150°C$, and the thermodynamically favourable hexagonal structure when the temperature is higher than $300°C$ [27, 76, 85, 87]. These three structures can be observed in the XRD data in Fig. 2.2 . Each phase possesses different optical and electrical properties. However, although there is a large contrast between amorphous and both crystalline states, there is no significant difference between the properties of the two crystalline structures [88, 89]. Nonetheless, only the switching between the amorphous phase and the fcc crystalline state is considered in technological applications due to the speed of this transition. For this reason, the ambiguous term "crystalline state" is used herein to refer to the fcc structure, given the switching timescales in the photonic memory applications.

There is not an universally accepted explanation for the structural change between the amorphous and the crystalline states in materials like GST. One recently proposed model, widely accepted but not definitely proven, promotes that the transition mechanism between the crystalline and the amorphous state is based on a change in the coordination of Ge ions through an umbrella-flip transition, which in turn modifies the material properties [90]. The changes in optical absorption and reflectivity have been explained in terms of such structural transition, especially as a change in the atomic bonding of each state, as described in Sec. 2.3.1.

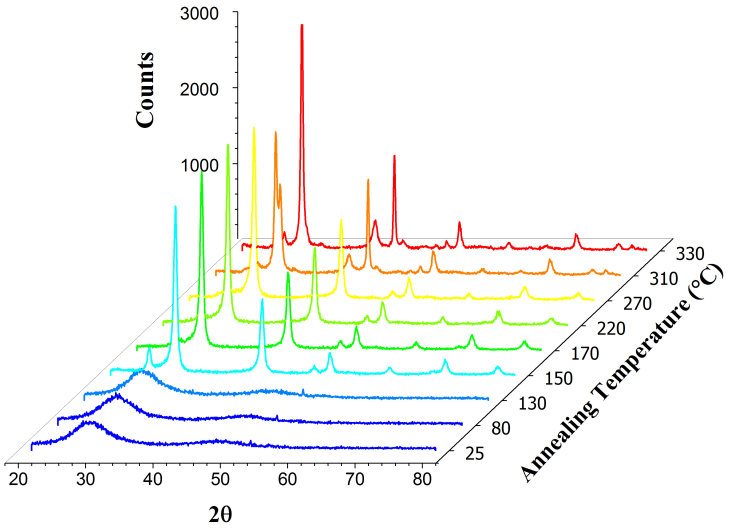

Figure 2.2: X-Ray diffraction pattern of GST as a function of the annealing temperature. Below 150 ^oC: amorphous sctructure. Between 150^oC and 300^oC, a characteristic face-centred cubic (fcc) crystalline diffraction pattern. Above 300 ^oC the spectra shows characteristic hexagonal crystalline diffraction. Reprinted with permission from [27].

Back and forth transitions can be induced by properly controlling the duration of fast thermal excitation pulses, whether electrical or optical, following the mechanism depicted in Fig. 2.3 [12, 91]. Given the remarkably rapid crystallisation kinetics of GST [92], heating amorphous material over 150°C—but below the melting temperature—by annealing or sending a long excitation pulse would be enough to reach the fcc or hexagonal phase state (SET). To switch back from the crystalline state to the amorphous ($RESET$), a high intensity short pulse must be applied in order to melt-quench the GST. Rapidly cooling at rates higher than $10^9\,Ks^{-1}$ quenches the liquid-like state (molten GST) into a disordered, amorphous phase. The latter state shows different optical/electrical properties from the crystalline state, so detecting amorphous regions is straightforward with a low-intensity laser beam or low currents [12]. One important parameter for the cooling process is the pulse trailing edge; this should fall in times shorter than the characteristic crystallisation times, usually less than $10\,ns$, otherwise the GST will crystallise once again after melting. Usual switching times for back and forth optical switching of GST

comprise $1\,ns$ amorphisation and $13\,ns$ crystallisation [68].

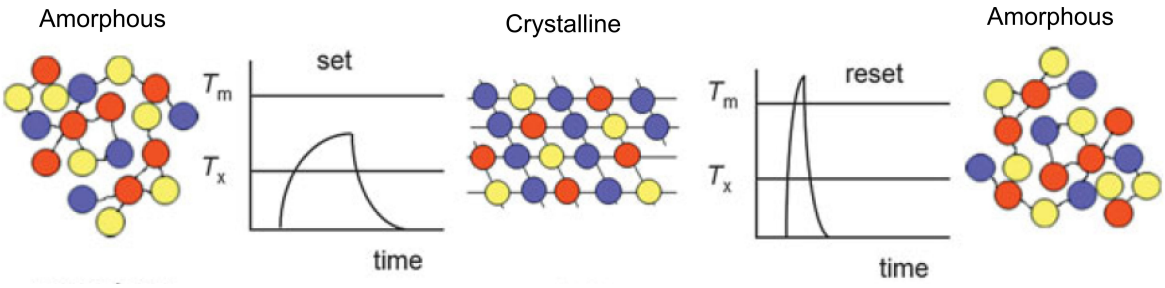

Figure 2.3: Rewritable optical data storage using phase-change materials. To *SET*, optical/electrical pulse with intermediate power is used. The laser locally heats the phase-change film above the crystallization temperature T_X. To *RESET*, a short pulse locally heats the phase-change material above its melting temperature. The colours are intended for good visualisation and have no physical meaning. Reprinted with permission from [46].

2.3.1 Optical properties

$Ge_2Sb_2Te_5$ offers one of the most pronounced contrasts in the dielectric function when comparing the amorphous and the crystalline states [10, 11]. This implies a significant difference for the real (n) and the imaginary part (k) refractive indices over a broad spectral range from visible to infrared wavelengths, as shown in Fig. 2.4. The absorption amplitude decreases during the phase transition from the crystalline to the amorphous state, which in turn implies a decrease in the peak maximum for the imaginary part of the dielectric constant (ϵ_2) and therefore, for k. Furthermore, the width of the ϵ_2 peak in the amorphous state is broader due to smearing of electronic states and the formation of tail states characteristic of amorphous materials [93].

The contrast between the two states—assuming a unique crystalline phase given the similarity between fcc and hexagonal phases—increases with Ge concentration [94]. For $Ge_2Sb_2Te_5$ the contrast in the refractive index is given by $\Delta n + i\Delta k = n(cry) - n(am) + i[k(cry) - k(am)] = -1.20 + i1.05$, while for $Ge_8Sb_2Te_{11}$ the contrast is $\Delta n + i\Delta k = -1.48 + i1.35$. Although theoretical approaches have considered the source

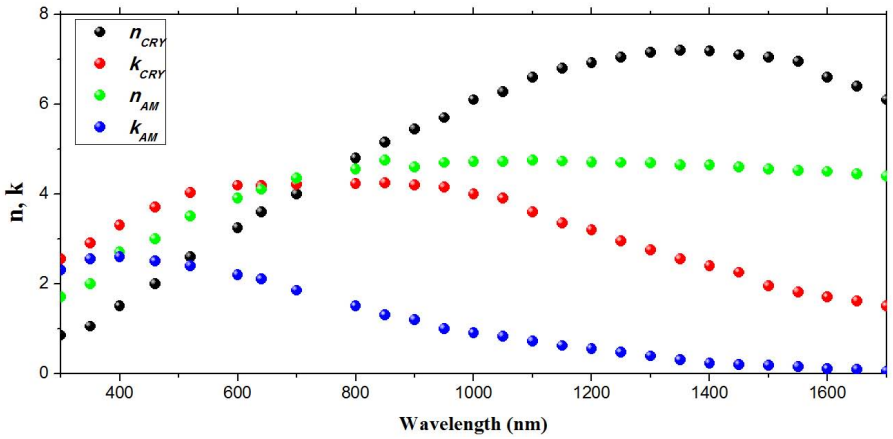

Figure 2.4: Complex refractive index $\tilde{n} = n - ik$ for the crystalline and the amorphous states of GST obtained experimentally by [6].

of the large contrast between the two states, there is not yet an universally accepted explanation [12]. Since the density between the amorphous and the crystalline states exhibits a change of 5–10%, it has been suggested that this difference is responsible for the large optical contrast [86]. However, the most accepted explanation suggests that the optical dielectric constant changes as a result of different atomic bondings for the amorphous and the crystalline states. While for the amorphous phase, the dielectric constant is similar to that of a covalent semiconductor, for the crystalline phases, it has been suggested that there is a strong enhancement by resonant-bonding effects, thus behaving similar to a metallic material under this structure [95, 96, 97, 98]. The lack of accurate amorphous phase models, and the difficulties in calculating optical properties from first principles, makes the design of PCMs for optical applications difficult using theoretical concepts and instead rely on empirical findings.

Since amorphous $\longleftrightarrow$ crystalline transitions are temperature driven, the switching can be carried out by absorbing energy from optical means. This is done with nanosecond laser pulses to heat up the material and rearrange the molecular structure by means of photon absorption [2, 68]). This absorption is mostly dictated by the extinction coefficient, k, and, to a lesser extent, by electronic excitation [99]. This is the reason why, in order

to improve the energy efficiency by absorbing more light, large values in the imaginary part of the refractive index are highly desirable. As the GST heats up due to photon absorption, its complex refractive index varies varies, in the linear regime, as:

$$n(T_{0+\Delta T}) = n_0 + \beta\Delta T \qquad k(T_{0+\Delta T}) = k_0 + \gamma\Delta T, \tag{2.1}$$

where the constants β and γ are known as the thermo-optical coefficients and have beem measured experimentally for GST deposited onto on-chip photonic circuits in Ref. [99]. More details about optical switching and new findings in the optical properties of GST are described in Sec. 2.4.1.

2.3.2 Electronic properties

Besides the clear differentiation in optical properties, $Ge_2Sb_2Te_5$ exhibits three orders of magnitude contrast in resistance between the amorphous and crystalline states ($k\Omega$ and $M\Omega$, respectively, for $\approx 50\,nm$ thick material), which makes it good candidate for electrical memory [12]. GST also exhibits high electrical endurance demonstrated up to 10^{12} cycles [46, 47, 100] and keeps the state for over 10 years at room temperature [14, 101]. Analogous to the optically induced phase change, electrical pulses can also be applied to induce phase transitions. This is possible given that Joule heating takes place and thus the different thermal effects that can lead either to the amorphous (from a short and intense pulse) or crystalline (from a long pulse) states [1]. A typical I/V curve characteristic of the back and forth switching between states is shown in Fig. 2.5. Starting in the amorphous state, a linear high resistance is observed if a small voltage is applied. When the bias voltage is increased over a certain threshold a resistance switch takes place. Subsequently, the resistance drops several orders of magnitude and gives rise to a more conductive state (denominated amorphous ON) before crystallisation takes place. When the Joule heating has reached the transition temperature ($\approx 150°$), the

material is quickly crystallised (*SET* in data-storage applications). When sweeping the voltage back to $0\,V$, a hysteresis curve evidences the new stable lower resistance state, a consequence of the phase transition. To *RESET*, i.e. amorphise, a short and high-power electrical pulse is used.

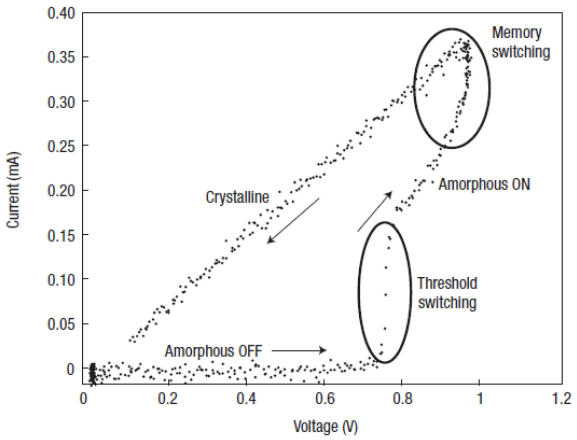

Figure 2.5: Characteristic current vs voltage curve of GST initially in the amorphous state. Adapted with permission from [12].

As electrical properties are in principle out of the goals of this project, they are not further explored. However, for more information about electronic properties of PCMs, particularly GST, refer to [10, 11, 101, 102, 103].

2.3.3 Non-volatile data storage

The inherent contrasting electric and optical properties of GST have enabled multiple data storage technologies. The most successful and commercially important development was the creation of non-volatile data storage compact disks (CD) that could be written, erased, and re-written many times [9, 10]. These disks employed different GeSbTe- or AgInSbTe-based alloys and were switched back and forth by means of diode laser pulses. Eventual advances in optical systems and the development of new high-intensity diode lasers at shorter wavelengths led to a reduction in the spot size of the beam focused

on top of the recording material [12]. Consequently, the memory storage density increased considerably, going from $0.9\,Gbit/in^2$ at $\lambda = 780\,nm$ in a CD to $2.2\,Gbit/in^2$ at $\lambda = 650\,nm$ in a DVD, or between $7.5 - 12.5\,Gbit/in^2$ at $\lambda = 405\,nm$ in a single layered Blu-ray disk (BD) or high-density optical disk. From CD to DVD and DVD to BD , the effective laser beam cross-section has been reduced by a factor of 2 and 5, respectively. The recording density increased by a factor of 7 going from CD to DVD. Going from DVD to the dual-layer BD, another increase by a factor of 11 has been accomplished (see Fig. 2.6). Beyond this relevant application, there have been not many contributions towards more all-optical applications in data storage as will be detailed in Sec. 2.4.

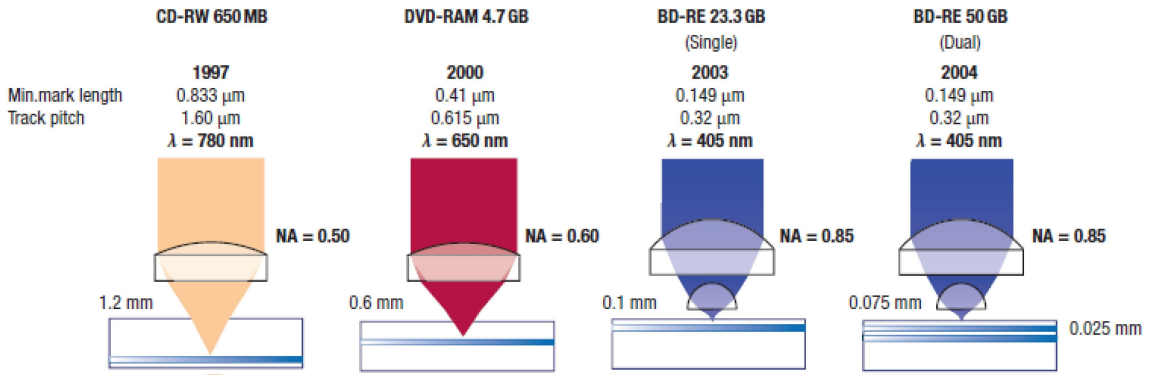

Figure 2.6: Comparison of optics, recording densities, recording capacities, and disk structures used for CD, DVD and BD. Changes in the lens system are shown in the upper portion; the disk structure is depicted beneath. Adapted with permission from [12]

Switching energies as low as $100\,fJ$, demonstrated using carbon nanotubes electrodes [104], and sub-nanosecond switching times [8] have given rise to a long development in terms of low-cost, nanometric, non-volatile memories compatible with silicon-chip technologies [10, 14, 41]. Using cross bars, planar devices and mushroom-like structures, different approaches have been proposed for devices compatible with silicon-based integrated circuits in the electronic domain [43, 46]. Such approaches have allowed for the realisation of phase-change random access and multi-level memories [10, 21, 48], and, more recently, stochastic phase-change neurons [15]. These devices, however, are expensive

due to intrinsic nanofabrication and slower than traditional silicon-based data-storage devices. Therefore, they do not represent an improvement in terms of bit-storage (0 or 1) if considering only traditional Von-Neumann architectures. The real advantages of using such integrated devices under electrical control are not only the non-volatile nature of the memory cell but also the memristor-like properties together with the accumulation and multilevel capabilities of PCMs, which enable unconventional computing architectures like neuro-synaptic [21, 23, 25].

Multilevel data storage is highly desirable to increase memory storage density and overcome the evident miniaturization limit. Because of this, storing data in intermediate values between the amorphous and crystalline states of the GST is a subject undergoing intense study within the PCM research community [17, 105]. Previous studies presented by IBM Research proposed a multilevel logic operation using GST [18, 105]. Starting with the device in the low-resistance state (crystalline), successive increasing current pulses are used to write by partially melting, in different proportions, the crystalline GST such that some areas are amorphised. Low-voltage pulses are used to read out the information by measuring the changes in resistance. However, this initial approach struggled with the variations among levels and devices, which avoids the scalability of the multilevel PCM. One level could not be exactly retrieved given that the resistance drifts and varies within *SET-RESET* cycle [105]. Moreover, small fabrication variations can cause a significant impact in the multilevel reliability. To mitigate this, the study proposed an algorithm that compares different control procedures in several switching cycles such that the resistive level converges to a common value. This post-processing is, however, impractical in terms of speed. Further studies towards understanding the resistance drift of electrically controlled phase-change memory cells were done by the same IBM team [106]. In their paper, the authors present a comprehensive description of the time-temperature dependence of the resistance variation in a PCM memory cell by applying

structural relaxation and electrical transport models. All this previous knowledge offered a good insight, in theory and practice, of the drift phenomena and allowed a more convincing development, published in summer 2016, that finally demonstrates reliable triple-level-cell phase-change memory [48]. This is the best result so far in the electrical domain. In the all-optical domain, as studied in this thesis, a memory cell featuring 3-bit storage capability with intra-level transitions is the device with the largest number of reliable and stable levels—without having to compensate drift—reported in literature [67].

2.3.4 GST, memristors, and neuromorphic processing

The memory resistor or memristor is a non-linear passive electrical component whose resistance depends on the direction and magnitude of the current that flowed through it in the past. This element was theoretically proposed by Leon Chua in 1971 [107]. However, only until recently, memristivity has been discovered as an effect that arises naturally in nanoscale systems, in which solid-state electronic and ionic transport are coupled under an external bias voltage [108]. The characteristics of the memristors have been related to biological synapses. This, in turn, has brought interest in their applications in neuromorphic processing [109] and stateful logic operations[110].

Memristors are difficult to fabricate, they present low yield and short life-times. As an alternative to overcome these problems, phase-change materials are being considered given that the characteristic I/V curve, when switching between the amorphous and the crystalline states, resembles that for memristors and, therefore, the spike timing characteristic curve in a synapse. Spike Time Dependent Plasticity (STDP), the learning rule found in biological neural systems, has been demonstrated using GST as synapse [22]. According to this work, the potentiation and depression of a synapse (see [111]) can be imitated by inducing intermediate resistance levels between the crystalline and

the amorphous state. An alternative approach was proposed using two PCM cells to create a synapse capable of supporting STDP in such a way that one PCM is used to store the current status of potentiation and the other one the depression [24]. In this technique, both GST sections start in the amorphous state and are crystallised after each electrical pulse sent to each electrode. While this method can be more efficient in terms of energy consumption and present a simpler pulse scheme, the control logic requires a higher complexity. In spite of this disadvantage, this approach has led to the demonstration of 165,000 synapses [25] and has been successfully used in complex visual pattern extraction [112, 113]. More recent developments are the first accumulation-based computing protocol using phase-change memories with field-effect transistor (FET) access devices [16]; the first demonstration of a phase-change device that imitates the integrate-and-fire functionality and the stochastic dynamics of a biological neuron [15, 23]; and access devices for 3D crosspoint memory [114]. In general, the high interest raised by this research field has implied important improvements in switching powers, switching speeds, state retention, reliability, and data density (either by means of multiple levels or 3D integration), all comprehensively summarised in [21].

2.4 Photonics meets phase-change materials

Phase-change materials and nanophotonics possess attributes that can be merged to understand the intrinsic molecular dynamics behind such materials, and also to create new technological applications in, and beyond, data storage. In general, the ability of PCMs to switch between two highly differentiable refractive indices offers active components that can be harnessed in many optoelectronic devices. Tuning capabilities in colour, resonances, band gaps, transmission/reflection, etc. could revolutionise photonics by opening up new research lines and technology. Despite all the potential, the field is yet in its early stages and with slow progress due to the technical difficulty in realising

fully reversible optical switching. The recent and most relevant contributions in the field "phase-change photonics" and the challenges to face in the near future are presented in the following sections.

2.4.1 Optical switching

After reporting the discovery of phase-change materials in 1968[1], Ovshinsky continued his research focusing on the synthesis of newer and better PCMs. Moreover, he investigated if the same phenomenon originally observed in electrical experiments could be taken to the optical domain. He succeeded. By 1971 the first demonstration of optical switching from amorphous to crystalline was presented using 100 nm thin films of $Te_{81}Ge_{15}Sb_2S_2$ and $10 - 100\,mW$ optical pulses of 1 to $16\,\mu s$ [2]. The decades after these historical discoveries brought plenty of contributions towards the synthesis of new alloys, better control of phase transitions by exploring different ways to achieve reversible switching, and developments in data storage. It was precisely this latter application that motivated the scientific community to focus their attention on optical switching of PCMs. The eventual application of this material in non-volatile data storage boosted the research in this field in the $1980\,s$. In 1986, working with GeTe, reversible optical switching was achieved by using pulses in 50 to $100\,nm$ layers [3]. In 1987, the field started moving towards GeTe-SbTe based alloys such as $GeSb_2Te_4$ as they presented higher optical contrast [4]. In the same article, the authors demonstrated high speed overwriting, achieving for the first time speeds up to 7 MHz by using $50\,ns$ and $8\,mW$ pulses. This increased in 1988 when InSbTe alloys showed crystallisation times shorter than $15\,ns$ [5]. By the end of the 1990s $Ge_2Sb_2Te_5$ had already been recognised as an optimum material given that, out of all PCM alloys, it offers the fastest crystallisation and amorphisation rates together with a large contrast between the extinction coefficient in the amorphous and the crystalline states [6, 7, 8]. This is shared with AgInSbTe compounds given the similarity between the properties of both [115]. These developments

led to the later implementation of dense all-optical (switching and read-out using laser sources) non-volatile data storage such as the compact disk (CD) and the digital versatile disk (DVD) including their rewritable capabilities (See also Sec. 2.3.3) [11, 12].

Subsequent interest was in understanding the intrinsic material properties of PCMs. The advent of faster light sources allowed for pump-probe measurements to study real-time phase-transformation dynamics. In 2004, a detailed picosecond laser characterisation of GST was realised for the first time [68]. In this work, reversible switching using $30\,ps$ pulses enabled the measurement of real-time reflectivity changes in a thin film of GST. From the thermo-optical effect—the real time change in reflection induced by and during the pulse excitation—it was concluded that thermal diffusivity plays a crucial role in determining phase switching time scales. It was also found that the amorphisation process requires times less than $1\,ns$, whereas crystallisation needs around $13\,ns$ to be completed. A first theoretical approach was proposed the same year; by realising similar experiments and comparing with computational models, the microscopic phase transformation between both states was described as a change in the coordination of the Ge ion through an umbrella-flip transition, which in turn modifies the optical properties [90]. Further studies complemented these experiments in other material domains or advanced technologies. Some of them include ultrafast femtosecond characterisation of their crystallisation properties [45] and a study of the local structure and nanosecond recrystallisation dynamics in other PCMs such as AgInSbTe [20]. A recent report in this direction showed how the optical functionality of GST can be modified without changing the lattice because the optical response is decoupled from the structural order [116]. This important result shows how electronic relocation within the atomic lattice takes place slowly—picoseconds to nanoseconds—while the optical properties, i.e. dielectric constant, change in a femtosecond scale as the ultrafast pulse breaks the resonant bonding even before any atomic structure change. Moreover, it explores the possibility of realising data

storage using different optical properties in the same lattice structure by demonstrating several different stable amorphous states.

In parallel to these attempts to understand the intrinsic nature of PCMs, the advent of nanotechnology meant an imminent miniaturisation of PCM-based devices into electronic, photonic and electro-optic CMOS compatible devices [10, 12]. Smaller GST junctions are now investigated under many kinds of conditions [8, 14]. Faster lasers, better electronics, and faster detection have led to a better understanding of materials in general. Focusing only on all-optical applications, the most important applications proposed so far are introduced below.

2.4.2 All-optical computing using PCMs

Notwithstanding the extensive and well characterised use of PCMs in neuromorphic computation by means of electrical switching (see Sec. 2.3.4), only one all-optical approach has tackled the Von-Neumann paradigm by exploiting the accumulation properties of GST [117]. The experiment consisted of a pump-probe setup in which femtosecond pulses perpendicularly incident on a GST thin film induce phase switching while reflectance is constantly recorded as shown in Fig. 2.7a. Using a similar approach in the electrical domain [42], the phase state of the material interacting with the light pulse is transformed from the amorphous to the crystalline state in small (SET) steps, depending on pulse fluence. This occur until a fixed number of pulses—under exactly the same conditions—have induced full crystallisation and the maximum in reflectance is reached. A shorter and more energetic pulse is subsequently applied to RESET, i.e. to reamorphise the material. The number of steps used in the SET transition establish a basis for calculations once a reflectivity threshold is fixed (see Fig. 2.7b). Hexadecimal arithmetic was proposed in this work, where the four fundamental mathematical operations are demonstrated by means of counting the number of incident pulses and the number remaining to reach the

maximum reflectance.

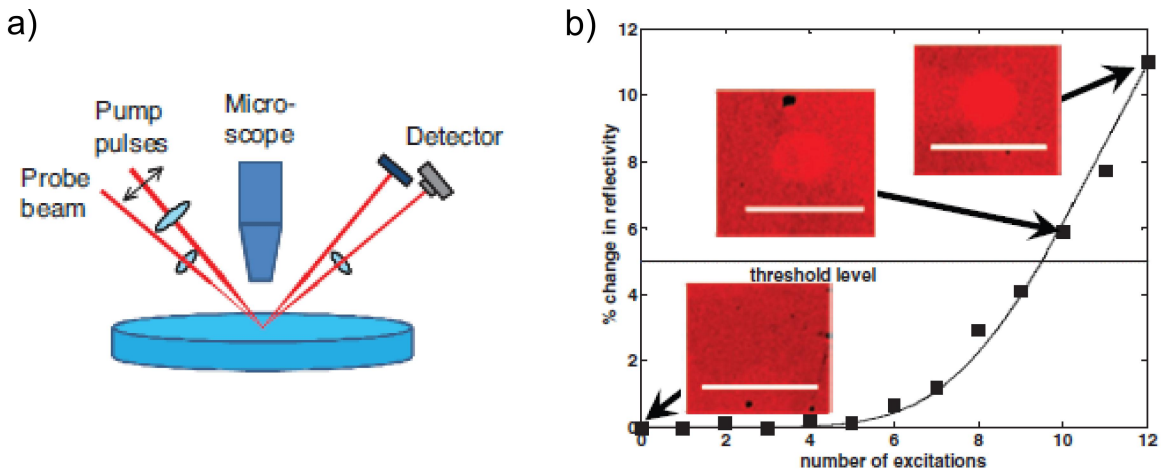

Figure 2.7: Optical computing using a uniform GST layer. a) Experimental setup scheme. b) Change in reflectance as a function of the number of pulses with a threshold defined to realise sum and multiplication in base 10. Adapted with permission from [117]

This optical computing approach is very impractical from the point of view of a technological application. To carry out multiple bit processing, the sample or the pump laser has to be moved from one spot to another, or many lasers and detectors are required for each independent computing cell. However, it showed key capabilities of these materials in non-von Neumann arithmetic.

2.4.3 Nanophotonic circuits based on PCMs

The advent of photonic technologies in the last decade, coupled with advances made in nanofabrication capabilities, has created a growing need for, and a drive to discover, practicable all-photonic memories. The search for new architectures to exploit the memristor-like properties of materials such GST have resulted in the implementation of on-chip photonic circuits evanescently coupled to PCMs to provide a platform for data storage and possible optical computing. From the coupling between the optical mode propagating along the waveguide and the PCM, dynamic changes in the optical

transmission are expected as result of Joule heating (See Fig. 2.8) [26].

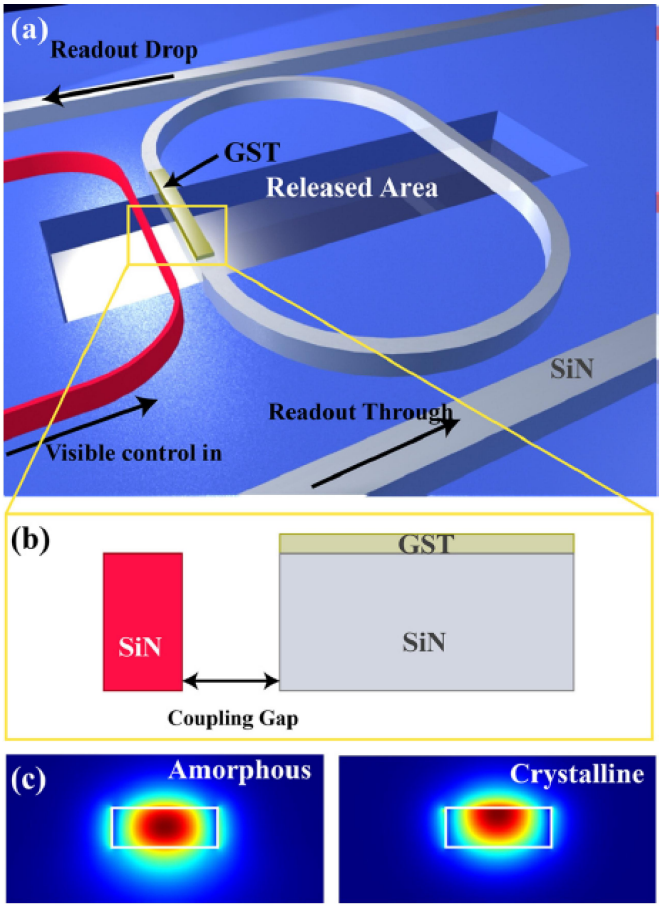

Figure 2.8: 3D scheme of a hybrid nanophotonic-chalcogenide circuit. (a)Schematic overview of the optical memory element. (b) Cross section view of the coupling region showing the GST covered section of the SiN waveguide. (c) The calculated modal profiles of the $700 \times 330\,nm^2$ waveguide cross-section (white rectangle) with $10\,nm$ thick GST on top (not visible due to the dimensions of the waveguide), when the GST is in the amorphous state (left) and the crystalline state (right). Adapted with permission from [26].

Using the same evanescent-coupling principle, first experiments in this direction led to the development of optical gate switches using GST junctions integrated with Si nanophotonic waveguides [49, 118]. The same group, at Keio University, has also, and more recently, demonstrated experimentally a Mach-Zehnder interferometer switch based on GST [119]. In these contributions, the transmission of the infrared mode confined within the waveguide was significantly altered as the attenuation increased when taking

GST from the amorphous to the crystalline state. The phase switching was obtained by means of external laser pulses but its reversible switching was not demonstrated, i.e. only the amorphous to crystalline transition was obtained. This is a slow and low-energetic transition achieved by just heating up the material over 150°, contrary to the reamorphisation that requires short and high-power pulses to quickly melt-quench GST. Further work showed transmission modulation using the volatile PCM VO_2 [120, 121]. By sending external diode-laser pulses on top of the VO_2 junction, the temperature resulting from Joule heating led to the modulation of the refractive index of the material. The modulation in this case was dynamically demonstrated as a function of fluence. However, the volatile nature of this material did not allow for long-term state retention.

In 2012, the first theoretical proposal of a fully photonic non-volatile memory reintroduced PCMs to data storage, this time using nanophotonic circuits [26]. By placing a section of GST on top of a micrometric ring-resonator, optical switching was computationally predicted. From the changes in the quality-factor (Q-factor) and the resonance frequencies upon switching between the two crystallographic states of the GST, a binary memory was proposed. One year later, the experimental verification of these numerical simulations was carried out. Using annealing to switch between states, the attenuation coefficient was calculated for GST as a function of the section size, and the optical switching was demonstrated by measuring $Q-$factor, resonance and extinction ratio in race-track resonators, along with other architectures including Mach-Zehnder interferometers [27, 122]. Optical switching in race-track resonators was also independently demonstrated by switching between states—in a reversible way—with external (i.e. out of the chip) laser-pulse irradiation [28]. Moreover, a proper understanding of the temperature-induced refractive index fluctuations, the thermo-optical effect, was essential for controlled and optimised device operation, especially in the optical domain. In this direction, the first comprehensive light-matter interaction study carried out within integrated circuits was recently

presented in [99]. This study provides new and important tools to understand the physics behind this kind of device.

In spite of the novelty of the advances described above in merging photonic circuits and PCMs, the lack of an integrated method to switch the GST back-and-forth has limited their applicability. The use of external pulses or static annealing to induce phase switching are not efficient when thinking about future computational architectures where large amount of data must be stored and processed at high frequencies. However, in 2015, the first all-optical memory using PCM with complete on-chip operation was achieved. These achievements are presented within this thesis, described in detail in Ch. 5, and are summarised in [67].

2.4.4 Colour modulation

Regardless of all the attention that PCMs have drawn and the increasing interest of the scientific community in the optical properties of PCMs, it was only in 2014 when an optoelectronic framework enabled by GST thin films was demonstrated to exploit the colour variations induced by the GST refractive-index modulations [33], as shown in Fig. 2.9. This work represents the first applications of phase-change materials in colour-related technologies. Follow-up papers have been published in 2015 and 2016 showing a similar structure with optimised physical parameters [123]. Other recent contributions feature: switching using femtosecond laser pulses to locally modulate colour instead of using electrical currents [70]; a double layer of GST to generate three colours in one sample [74]; colour modulation via electrothermal switching [124]; and colour-depth modulation [125], which is part of this thesis and is described in detail in Ch. 6.

Created out of thin multilayers in either continuous films or nanopillars, an optical cavity ITO - GST - ITO on top of a mirror enables dynamic reflected colour selection as a

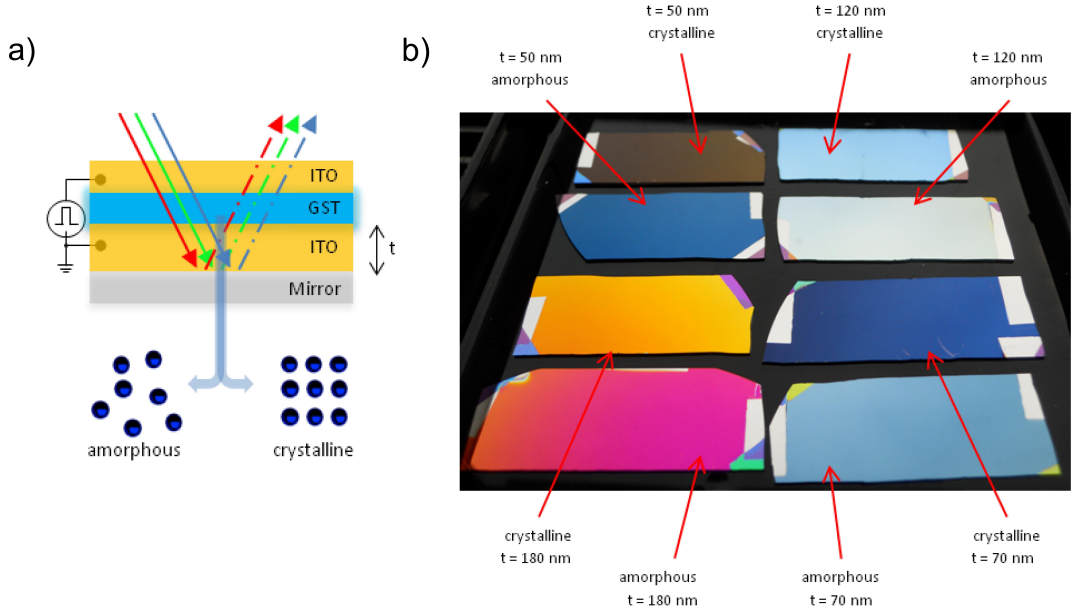

Figure 2.9: Colour modulation using GST. a) ITO-GST-ITO optical cavity on top of a metallic mirror. b) Examples of different colour variation as a function of the GST crystallographic states and bottom ITO thickness. Adapted with permission from [33].

function of the bottom ITO thickness and the crystallographic state of GST, as shown in Fig. 2.9a. Moreover, by using the conductivity properties of ITO, a current can be induced by inserting a high voltage between an Atomic Force Microscope (AFM) tip and the bottom ITO. This way, local phase-change switching takes place and micrometric size images with nanopixel resolution were written pixel by pixel on top of the continuous layers or nanopillars, as depicted in Fig. 2.10. Furthermore, as the devices comprised only thin multilayers [54], flexible devices were also fabricated. Finally, by using cross bars of ITO and GST at the intersection, nanopixel sizes down to 300 *nm* were obtained, as shown in Fig. 2.10d.

Resonators made out of transparent and thin absorber layers had been used before but with a passive metal, such as silver; in this way, nanopixels are obtained but with fixed colour [55]. Other approaches, such as plasmonic absorbers [126] and aluminium nanorod structures [60], exhibit colours with an ultra-high resolution lying on the nanometric

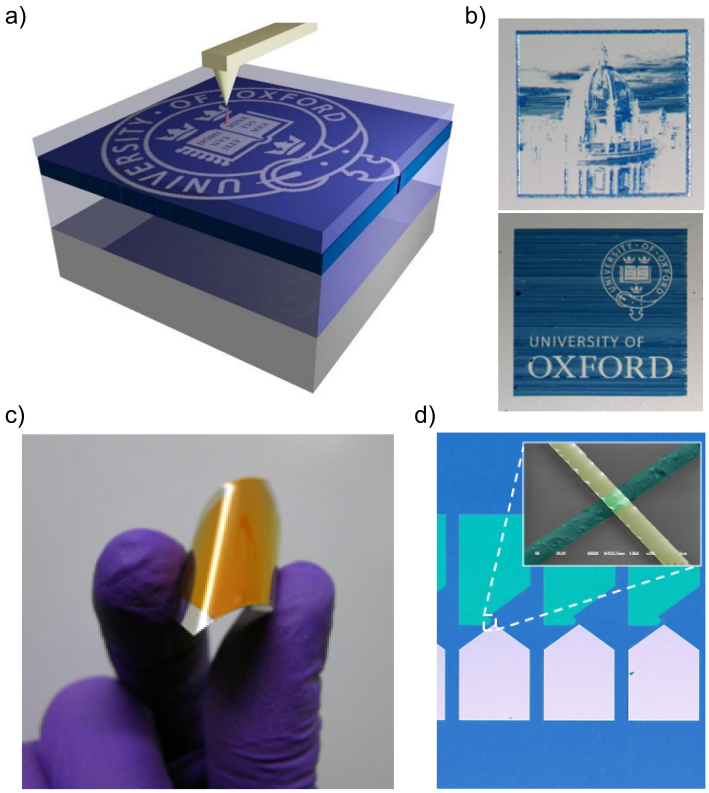

Figure 2.10: Display technology demonstration. a) Scheme of an electrical switching locally induced on GST by means of an AFM. b) Example $70 \times 70\,\mu m$ images written on top of continuous layers of GST. c) Demonstration of reflective colour using a GST-based sample on flexible substrates. d) $300\,nm$ nanopixel using ITO-GST-ITO cavities in a cross bar structure. Adapted partially with permission from [33].

scale but also with the disadvantage of presenting a unique colour pattern that cannot be switched.

The ability to switch between colours on such a scale and on flexible substrates holds promise for large advances in display technology with ultra-high definition. However, further studies need to be done, especially towards transmission-mode operation and better wavelength selectivity.

2.4.5 Optical metadevices and plasmonics

Metadevices using PCMs and featuring plasmonic-enhanced phenomena in waveguides, nanoantennas, and absorbers; as well as reconfigurable surfaces and photonic crystals, have been explored in recent research papers. Most of them describe new concepts that make use of PCMs for active tunability; however, very few have been experimentally realised and even fewer have achieved reversible back-and-forth switching. Fully reversible optical switching between the amorphous and the crystalline states has proved difficult, yet possible.

Metamaterials

In 2008, GaAs-based chalcogenide materials were used to tune a photonic crystal bandgap by employing a laser [127, 128]. Although the material did not present a non-volatile phase change, it was photosensitive, i.e. its refractive index changed dynamically depending on incident laser intensity. This meant that as the refractive index was locally modulated the bandgap of the crystal was tuned to different frequencies while the light source was kept on. This experiment was one of the first approaches towards wavelength tuning and unique optical responses using chalcogenide-based nanostructures. The use of non-volatile phase-change materials, on the other hand, is still challenging due to complicated reversible switching. Nonetheless, multiple theoretical approaches have been realised towards tuning reflectance and absorptance spectra with multiple geometries [129, 130, 131, 132, 133], and also in other applications, such as tuning the emission spectra of quantum dots [134]. The experimental control in an all-optical fashion has been relegated to fewer contributions. One example is the demonstration of stacked metallic nanorods using two enantiomer configurations, with a layer of PCM ($Ge_3Sb_2Te_6$) in between, which allowed for the first switching of a chiral metamaterial [135]. Also, the first experimental demonstration of a switchable perfect-absorber with potential

application in thermal imaging was presented in [136].

Plasmonic nanoantennas

Metallic nanostructures with simple geometrical shapes such as rods or squares, or more complicated such as bow-tie or yagi-uda configurations, have been widely used as nanoantennas to enhance optical modes by means of plasmonic resonances [137]. The field enhancement at the tip/gap/edge is strongly dependent on the refractive index of the materials used for the resonators and substrates. Because of this, switching between the amorphous and the crystalline phase permits a modulation that can be applied to change the typical resonance frequency, and thus the extinction cross section, of a particular nanoantenna when placing PCMs underneath, on top, or in the centre of the structures. In this direction, a first contribution demonstrated that GST and InSb layers can be used to tune the resonance in the infrared spectrum [138]. By depositing layers under the metallic resonant structures, the authors were able to find a blue-shift in the resonance peak when switching from amorphous to crystalline GST and a red-shift when realising the same switching with InSb. Nevertheless, the phase switching was done statically by annealing the sample, which is a strong limitation in terms of applicability. A similar configuration use nanoantennas on top of thin-films of non-volatile phase-change materials to modulate the extinction cross section [139, 140]. However, with the growing understanding of the optical properties of GST (as the most representative of all PCMs), new demonstrations of all-optical reversible switching of nanoantenas employing GST have emerged. Devices modulating the infrared spectrum [141, 142], as shown in Fig. 2.11, have been proposed. In particular, in [141], the switching is carried out with femtosecond laser pulses following a fixed protocol including many pulses during recrystallisation, which opens the way to real dynamic modulation with a reversible and controllable method. Dynamic modulation of plasmonic nanoantennas has been achieved also, and in a fully functional fashion, by using volatile phase-change materials such as VO_2 [143, 144, 145]. The technological

applications of these nanoantennas in photovoltaics, light emission, nanoscale imaging, and spectroscopy [137], plus the potential of quantum dots and photonic crystals, makes desirable having further active resonance-frequency tuning. This, in turn, would enable nano-optical devices with novel active functionalities; which is why exploiting PCMs in such structures has witnessed fast growth within the last few years.

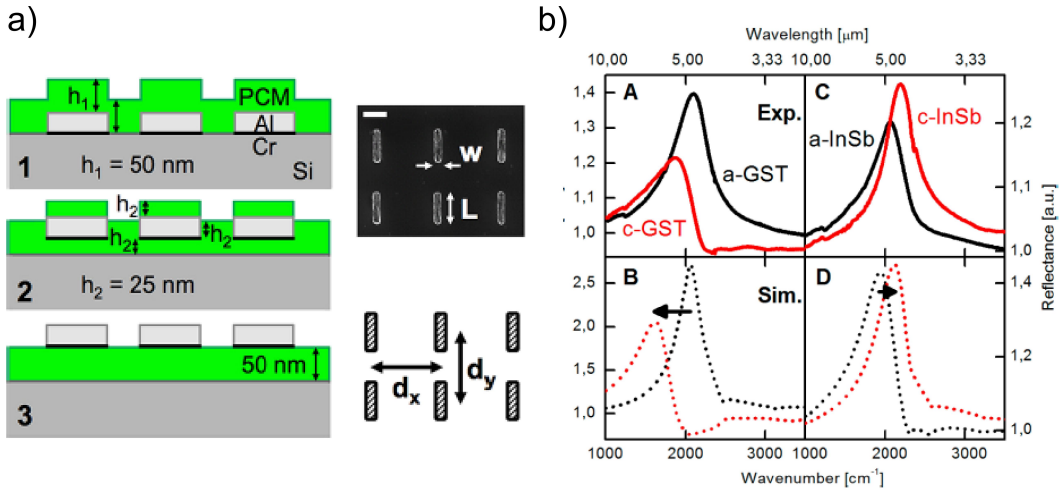

Figure 2.11: Reflectance variations as a consequence of resonance frequency modulation in nanoantennas using PCMs. a) Scheme of the different configurations where the nanoantennas are on top, inside and below the PCM. b) Experimental vs. simulation results for GST and InSb. Adapted with perission from [138]. Copyright 2013 American Chemical Society.

Plasmon- and phonon-polaritons

Plasmonic waveguides are structures that guide the electromagnetic waves that propagate at a metal-dielectric interface, known as a surface plasmon-polariton (SPP). Such waveguides can be made with a smaller footprint compared to dielectric waveguides for photonics. In analogy to photonic waveguides, as described in Sec. 2.4.3, "active plasmonics"—where the wavelength of the plasmon on the waveguide is tuned—can be achieved by introducing optically activated chalcogenides [146], including phase-change materials. By placing nanoscale junctions of PCM next to the plasmonic waveguide, it was possible to optically switch GST and thus control the transmission[147].

By replacing the metal in the plasmonic waveguides by a polar crystal, surface phonon-polaritons(SPhP)—the infrared counterpart of surface plasmon-polaritons—can be optically excited at the interface with a dielectric. In particular, using an ultra-thin layer of $Ge_3Sb_2Te_6$ deposited on top of quartz, it was demonstrated that the SPhP can be strongly confined on the quartz surface, while sub-wavelength resonators can be created by locally switching the active PCM. This approach allows for changing the functionality of the nanostructure in a non-transient manner and represents a novel rewritable platform for nanoscale optical components [148].

Reconfigurable photonics

Optically reconfigurable photonic devices using phase-change materials were demonstrated using $Ge_2Sb_2Te_5$ [29, 149]. Patterns that can be written-erased-rewritten are transferred to a multilayer stack—including the PCM— by using fs-laser pulses to locally switch the GST between the amorphous and the crystalline state. By doing so, the refractive index of the "metasurface" can be modulated and this, in turn, can be exploited to create functional patterns such as holograms, bichromatic and multi-focus Fresnel zones, and super-oscillatory lenses. In a similar approach, another novel hybrid planar lens was proposed to engineer the phase front of light with phase-change material based planar lenses. It consists of an array of slits which are filled with phase-change material (GST in this case). By varying the crystallisation level of GST, the Fabry-Pérot resonance supported inside each slit can be spectrally shifted across telecom wavelengths, which results in a transmitted electromagnetic phase modulation [150].

2.5 All-optical memories and computation

The exploitation of photonic technologies, coupled with advances made in nanofabrication techniques, have offered new tools in the search for practicable all-photonic memories [40], although the implemention of such memories on-chip and their non-volatile operation has been an elusive goal. So far, on-chip memories based on coupled micro-ring lasers [35] and tunable photonic crystal cavities [34, 37, 151] have been volatile (or transitional), i.e. data is retained only for a short period. Other approaches allow read-only memories, thus losing any processing capability [152]. This is the same situation for semiconductor-based memories converting photons into electron-hole pairs that are locally stored in a quantum well laterally modulated by a tunable electrostatic superlattice [36] and for flip-flop memories based on modulation of resonances within microdisks [38] and Mach-Zehnder interferometers [153]. In 2016, an optoelectronic approach claimed to have built a non-volatile multi-level photonic memory based also in semiconductor-based micro-ring structures [154]. However, this memory operates by electrically controlling the refractive index of n-doped poly-Si waveguides by applying voltages up to $20\,V$. In this memory, the information stored can be affected by another external electric field that can alter the static electric field generated by the induced charges. Moreover, the long-term (days) non-volatility thereof is in doubt and not further discussed in the paper. The only remaining approach proposed for a fully optical non-volatile memory, but not on a silicon-on-insulator chip, compromised complicated light-driven nanocrystals up-conversion by inducing atomic transitions within well-established electronic levels [155]. More recent publications have approached this problem by using phase-change materials in such a way that both on-chip and non-volatile memories can be fabricated, as described in Sec. 2.4.3.

In combination with optical interconnects, photonic data storage would drastically im-

prove performance in existing computing architectures [156] by greatly reducing latencies associated with electrical memories [101] and potentially eliminating power-consuming optical-electrical and electrical-to-optical conversions [34]. Including multi-level access would allow for leveraging even greater computational capability [155], in particular for all-optical parallel and non-von Neumann arithmetic processors [157, 158]. Consequently, future supercomputing needs optics [39, 159] and recent progress has shown that it is feasible not only with classical photonics in "conventional architectures"[160]—binary computation—but also in neuromorphic computing schemes [161], and in quantum architectures [162]. The single-chip microprocessor that communicates directly using light, demonstrated in [160], represents a milestone towards all-photonic processing and the beginning of an era of chip-scale electronic-photonic systems with the potential to transform computing.

If phenomena that are unique to optics are harnessed, it would create new exciting fields of research. In this respect, intrinsic classical and quantum properties such as orbital angular momentum [163], polarisation, and light-matter interactions [117, 164], should be exploited. All-photonic applications are desirable but so are architectures where processing is done with photons and storage with atomic media. Despite the lack of a robust and reliable architecture that can deal with computation at the level that is done electronically, plenty of options are at hand and future research will therefore bring a fierce competition aiming for the best device in terms of efficiency, speed, and reliability. In this regard, phase-change materials are potential candidates to overcome the current problems, as will be described in Sec. 2.4.2.

Chapter 3

Integrated photonic circuits: Theory, design, and nanofabrication

This chapter contains the theory, design, and fabrication of integrated circuits for nanophotonic applications, including the basic formulation of light-matter interaction between an electromagnetic mode and absorptive materials placed onto the waveguide. Moreover, the finite-element method (FEM) modelling of electromagnetic modes within photonic circuits is presented as a tool to optimise the circuit geometrical parameters. Finally, this chapter describes the chip CAD layout design and the process followed for the nanofabrication of the photonic chips used in the measurements realised in Ch. 5.

3.1 Fundamentals

In analogy to electronic circuits, silicon-based integrated circuits for photonic processing, or simply (nano)photonic circuits, are devices that confine, guide, and manipulate light

within transparent waveguides that are patterned on a chip [165]. Such circuits have witnessed a growing demand, development, and both intellectual and financial investment given their projected—and to some extent, current—potential on telecommunications industry and fundamental science [40]. Micro and nanometric architectures using integrated silicon photonics allows for all-optical functionalities [166], but also enables the application of the interaction of light with mechanical [167], electrical [168], and magnetic components [169]. This technology promises not only to increase functionality, density, and to significantly reduce cost when comparing to free-space optical systems, but also to overtake the speed, crosstalk, heat issues, and bandwidth limitation of electronic circuits while adding parallel processing and extra degrees of freedom such as polarisation, orbital angular momentum, and non-classical light sources/phenomena. Furthermore, silicon photonics promises to be the platform for the desired all-optical computing, as discussed in Sec. 2.5. However, the progress towards new developments and commercialisation is limited to the accessibility of manufacturing foundries and techniques, which are challenging as the device complexity increases while price and robustness are yet not comparable to that in the electronics industry [170]. Moreover, 2D photonic architectures cannot yet offer circuit densities similar to those in Silicon electronics. Hence, the promise of silicon photonics relies on those extra functionalities, as described above, that can be harnessed in completely new technology beyond electronics.

3.1.1 Silicon-nitride for optical applications

Silicon-on-insulator (SOI) technology is extensively used as platform for photonic circuits [40, 171, 172]. However, due to the shortcomings of Si in very specific applications in terms of bandwidth—it is not transparent in the visible spectrum; electrical properties—it is an insulator; and mechanical properties—it is rigid, other materials are also employed as alternatives. This is the case of silicon nitride (Si_3N_4), whose bandwidth is broader expanding to the visible, and aluminium nitride (AlN), whose mechanical properties

allows for on-chip opto-mechanics [172].

In this thesis, particular attention is paid to silicon-nitride (Si_3N_4) on insulator (SiO_2) wafers as this is the substrate used in the fabrication process described in Sec. 3.3. Si_3N_4 is chosen given its optical transparency spanning from ultra-violet to far-infrared wavelengths [173, 174]. The refractive index for the visible spectrum can be calculated from the dispersion relation given by the Sellmeier equation ($n \approx 2$ for the whole visible) [175]:

$$n(\lambda) = \sqrt{1 + \frac{2.8939\lambda_{\mu m}^2}{\lambda_{\mu m}^2 - 0.019508}}, \tag{3.1}$$

where $\lambda_{\mu m}$ is the wavelength given in microns. Furthermore, this material has a refractive index of $n = 1.977$ for $\lambda = 1550nm$ in the infrared telecommunication band [176]. This value for the refractive index allows for good optical confinement and waveguiding, given the large contrast with respect to the refractive indices of the interface materials: air ($n = 1$) and SiO_2 ($n = 1.54$) [177, 178, 179]. This wafer, created by means of low-pressure chemical vapor deposition, offers also a smooth surface which minimises scattering losses at the interfaces[180].

3.1.2 Channel waveguides

Waveguides are for photonics what wires are for electronics. On-chip silicon-based channel waveguides allow the light propagation, manipulation, and connectivity within photonic devices, the reason why they are also known as photonic circuits. There are two main geometries: rib (partially etched) and ridge/slab (fully etched) waveguides, as shown in Fig. 3.1. They confine electromagnetic waves in a two-dimensional core whose refractive index is larger than that of the surrounding materials (cladding and/or substrate), whilst the wave propagates in the third dimension (z-direction by convention) [181].

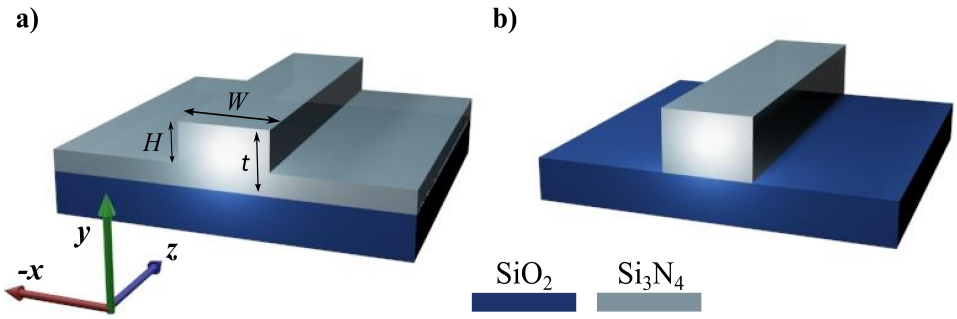

Figure 3.1: Geometries of Silicon-nitride nanophotonic waveguides: (a) rib and (b) ridge/slab waveguides.

Considering the geometries shown in Fig. 3.1 with xy confinement, defining ε_0 as the dielectric constant in vacuum, and having non-magnetic (i.e $\mu = 0$) materials with electric permittivity $\varepsilon_m = \varepsilon_0 \varepsilon$, then, the electric $\vec{E}(x, y, z, t)$ and magnetic $\vec{H}(x, y, z, t)$ fields inside the waveguide, assuming time-harmonic fields and propagation in the z-direction, are given by:

$$\vec{E}(x, y, z, t) = \vec{\mathcal{E}}_{mn}(x, y)\, e^{i(\beta_{m,n}\, z - \omega\, t)} \quad \vec{H}(x, y, z, t) = \vec{\mathcal{H}}_{mn}(x, y)\, e^{i(\beta_{m,n}\, z - \omega\, t)}, \tag{3.2}$$

where $\beta_{m,n} = \frac{2\pi}{\lambda} \cdot n_{eff,mn}$ is the propagation constant of the mode $m, n \in \mathbb{N}$ in the z-direction and satisfies $\vec{k} = \vec{k}_T + \beta_{m,n}\, \hat{z}$ with the transversal propagation constant defined as $\vec{k}_T = k_x\, \hat{x} + k_y\, \hat{y}$. $\hat{x}$, $\hat{y}$, and $\hat{z}$ are the unit vectors in the three orthogonal Cartesian coordinates. λ is the wavelength in vacuum. $\vec{\mathcal{E}}_{mn}(x, y)$ and $\vec{\mathcal{H}}_{mn}(x, y)$ are the spatial vectorial amplitudes given by $\vec{\mathcal{E}}_{mn}(x, y) = \mathcal{E}_{x,mn}(x, y)\, \hat{x} + \mathcal{E}_{y,mn}(x, y)\, \hat{y} + \mathcal{E}_{z,mn}(x, y)\, \hat{z}$ and $\vec{\mathcal{H}}_{mn}(x, y) = \mathcal{H}_{x,mn}(x, y)\, \hat{x} + \mathcal{H}_{y,mn}(x, y)\, \hat{y} + \mathcal{H}_{z,mn}(x, y)\, \hat{z}$. The indices m, n in $\vec{\mathcal{E}}_{mn}$ and $\vec{\mathcal{H}}_{mn}$ characterise all the possible electromagnetic modes allowed in the waveguide. In particular, if rectangular waveguides (rib waveguides, for instance) with dimensions W and H in the x and y directions, respectively, are considered, then the modes m, n satisfy $m \cdot \lambda = 2 \cdot W$ and $n \cdot \lambda = 2 \cdot H$.

From Maxwell's equations, it can be demonstrated that the electrical field $\vec{E}(x, y, z, t)$ follows the wave equation

$$\nabla^2 \vec{E}(x, y, z, t) = \mu_0 \varepsilon_0 \varepsilon \frac{\partial^2 \vec{E}(x, y, z, t)}{\partial t^2}. \tag{3.3}$$

The magnetic amplitude, on the other hand, can be found using the result for $\vec{E}(x, y, z, t)$ and using Maxwell's equations from

$$\nabla \times \vec{E}(x, y, z, t) = -\mu_0 \frac{\partial^2 \vec{H}(x, y, z, t)}{\partial t^2}. \tag{3.4}$$

The problem can be reduced to finding the amplitude $\vec{\mathcal{E}}_{mn}(x, y)$ and the propagation constant $\beta_{m,n}$. By replacing the ansatz in Eq. 3.2 into Eq. 3.3, the Helmholtz equation is obtained [182, 183]:

$$\nabla_T^2 \vec{\mathcal{E}}_{mn}(x, y) - (\beta_{mn}^2 - k_o^2 n_i^2) \vec{\mathcal{E}}_{mn}(x, y) = 0, \tag{3.5}$$

where $\nabla_T^2 = \frac{\partial^2}{\partial x} + \frac{\partial^2}{\partial y}$, $k_o^2 = \omega^2 \mu_0 \varepsilon_0 = \omega^2/c^2 = (2\pi/\lambda_0)^2$, and $n_i = \sqrt{\varepsilon_i}$, where $i = 1, 2, 3$ represents the three different materials for core, cladding, and substrate. Two important situations are of particular interest. When $\mathcal{E}_{z,mn} = \mathcal{E}_{y,mn} = 0$ and $\mathcal{H}_{z,mn} = \mathcal{H}_{x,mn} = 0$ the so-called transverse electric mode (TE_{mn}) is obtained (i.e. there is an electric field parallel to the substrate, and a magnetic field perpendicular to the same). On the other hand, the transverse magnetic mode (TM_{mn}) is found when the inverse situation takes place.

The coupling between the amplitudes in x and y coordinates due to the two-dimensional confinement and the non-symmetric geometries of both rib and ridge waveguides means that the Eq. 3.5 has no analytical solution. For an exact calculation of $n_{eff,mn}$, numerical calculations need to be done. However, a good approximate solution can be obtained

from the effective-index method (EIM) presented in the following section.

3.1.3 Effective-index method

The formulae for the effective refractive index of channel waveguides have no exact analytical solution. Instead, modelling, such as the finite-element method, has to be employed to obtain an exact numerical value, as done in Sec. 3.2.3. However, an analytical approximation can be obtained by using the exact solutions for optical modes in step-index planar waveguides (one-dimensional waveguides), which can have the two following configurations [40]:

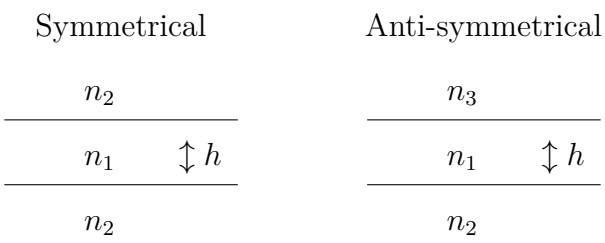

Eq. 3.5 for a symmetrical planar waveguide, which is infinite in x and confined only in y, takes the form [40]:

$$\nabla_T^2 \vec{\mathcal{E}}_m(y) - (\beta^2 - k_o^2 n_i^2)\vec{\mathcal{E}}_m(y) = 0, \tag{3.6}$$

In particular, considering only the TE fundamental mode where $\vec{\mathcal{E}}_m(y) = \mathcal{E}(y)\hat{x}$, Eq. 3.6 can be rewritten as the scalar unidimensional differential equation

$$\frac{\partial^2 \mathcal{E}(y)}{\partial y^2} - (\beta^2 - k_o^2 n_i^2)\mathcal{E}_m(y) = 0, \tag{3.7}$$

whose analytical solution is given by

$$\mathcal{E}(y) = Ae^{\pm\sqrt{\beta^2 - (k_o^2 n_i^2)}\, y}. \tag{3.8}$$

Eq. 3.8 corresponds to an oscillatory (wave) solution with amplitude A only if $\beta^2 - k_o^2 n_i^2 \leq 0$, which implies that $\beta^2 \leq k_o^2 n_i^2$. Thus, by replacing $\beta = k_0 n_{eff} = k_0 n_1 \sin\theta_1$ with θ_1 being the angle of propagation between $\vec{k}$ with respect to the y axis, the inequality becomes $n_1 |\sin\theta_1| \leq n_i$. In the core with n_1, this relation always holds. Therefore, a wave propagating in z is obtained in this region. However, to obtain a guided mode, a repeatedly reflected wave inside the core has to have constructive interference with itself. For this to happen, the field in the cladding and substrate should be an evanescent wave, i.e. propagation must be forbidden by total internal reflection. This is $n_1 |\sin\theta_1| \geq n_i$ for $i = 2, 3$ so that Eq. 3.8 becomes a decaying exponential (+ sign is physically forbidden). Thus, the coupling angle should be larger than the critical angle $\theta_1 \geq \theta_c = \sin^{-1}(n_i/n_1)$. This is the reason why the contrast between the refractive indices of the core and the surrounding has to be as large as possible. In the case of Si_3N_4 with air ($n_3 = 1$) as a cladding, $\theta_{c,cladding} = 9.75°$. For SiO_2 ($n_2 = 1.44$) as substrate, $\theta_{c,subs} = 35.8°$. It is thus easier to overcome modes leaking towards air than to the substrate. Considering a guided mode with propagation angles over the critical angle and the centre of coordinates for y at the centre of the core of width h, the Eq. 3.2 for the three regions can be written as

$$\vec{E}(x,y,z,t) = \begin{cases} A_{clad}\, e^{i(\beta_{m,n}\, z - \omega\, t)} e^{-k_{clad}\,(y+h)} \hat{x}, & y \geq h/2, & clladding \\ A_{core}\, e^{i(-k_{core}\, y + \beta_{m,n}\, z - \omega\, t)} \hat{x}, & -h/2 \leq y \leq h/2, & core \\ A_{subs}\, e^{i(\beta_{m,n}\, z - \omega\, t)} e^{k_{subs}\,(y+h/2)} \hat{x}, & y \leq -h/2, & substrate \end{cases} \quad (3.9)$$

where, A is the amplitude given for the three materials, k_{core}, k_{clad} and k_{subs} are real numbers (in the case of dielectrics) given by $k_{clad} = \sqrt{\beta^2 - k_0^2 n_3^2}$, $k_{core} = \sqrt{k_0^2 n_1^2 - \beta^2}$, and $k_{subs} = \sqrt{\beta^2 - k_0^2 n_2^2}$. The three fundamental TE modes are plotted in Fig. 3.2.

The boundary conditions imply that both the electric field and its derivative $\frac{\partial E}{\partial y}$ are continuous at the boundaries in $y = \pm h/2$. From studying the fields at the boundaries, the amplitudes A_i can be calculated as well as the eigenvalue equations for these TE

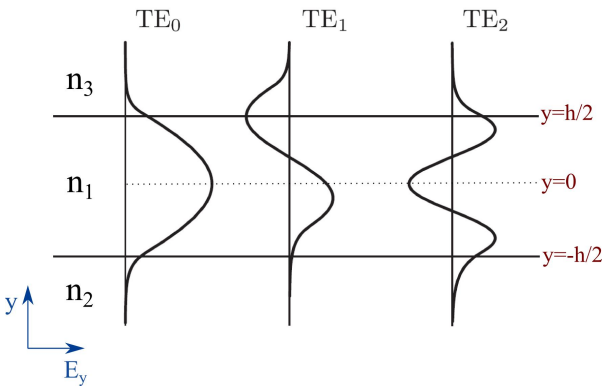

Figure 3.2: TE modes in an anti-symmetrical planar waveguide with $n_3 \geq n_2$.

guided modes, which are given by [40]:

$$\tan\left(\frac{k_0 n_1 h\cos\theta_1 - m\pi}{2}\right) = \frac{\sqrt{\sin^2\theta_1 - (n_2/n_1)^2}}{\cos\theta_1} \quad \text{for symmetrical waveguides}$$

$$(k_0 n_1 h\cos\theta_1 - m\pi) = \quad \text{for anti-symmetrical waveguides}$$
$$\tan^{-1}\left[\frac{\sqrt{\sin^2\theta_1 - (n_2/n_1)^2}}{\cos\theta_1}\right] + \tan^{-1}\left[\frac{\sqrt{\sin^2\theta_1 - (n_3/n_1)^2}}{\cos\theta_1}\right], \tag{3.10}$$

where $m = 1, 2, 3..., m_{max}$ are the number of modes. Moreover, the symmetrical TM mode is also (which is relevant in the following analysis) given by

$$\tan\left(\frac{k_0 n_1 h\cos\theta_1 - m\pi}{2}\right) = \frac{\sqrt{(n_1/n_2)^2\sin^2\theta_1 - 1)}}{(n_2/n_1)\cos\theta_1} \tag{3.11}$$

From Eqs. 3.10 and 3.11, the propagation angle θ_1 is calculated, which allows to calculate the effective refractive index for ridge waveguides with propagation in the z-direction, and therefore the propagation constant by using:

$$\beta = k_0 n_{eff} = \frac{2\pi}{\lambda} n_1 \sin\theta_1 \tag{3.12}$$

This is done by decoupling the two-dimensional geometry into one vertical (symmetrical

with infinite extension in y and z) and one horizontal (anti-symmetrical with infinite extension in x and z) planar waveguide. The eigenvalue equations can be solved first in one direction and then in the other, taking the effective index of the first as the value for the core in the second. For rib waveguides, the decomposition includes three

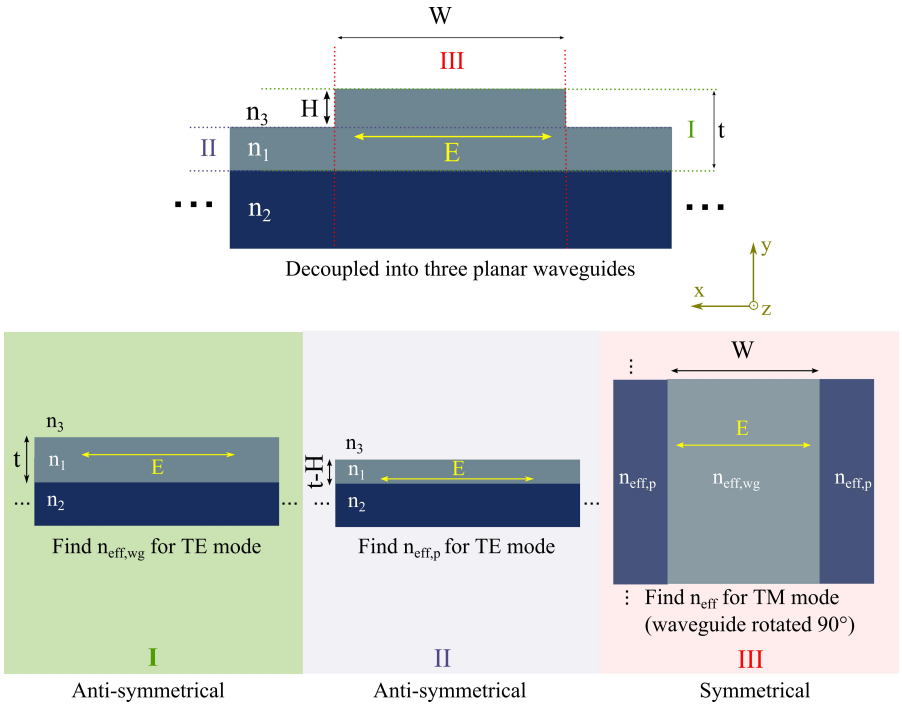

Figure 3.3: Decomposition of a two-dimensional rib waveguide into three planar waveguides for the effective-index method of analysis.

planar waveguides, two in a similar way as for ridge waveguides and one more that gives account of the planar region that consists of the same material as the core, as depicted in Fig. 3.3. In this case, which is the case study in this thesis, the eigenvalue equation for the horizontal anti-symmetrical planar waveguide (I) provides the $n_{eff,wg}$ used as effective index for the core in the symmetrical vertical planar waveguide (III). Moreover, the solution to the horizontal anti-symmetrical waveguide for the planar region in the core (II), $n_{eff,p}$, is used as the refractive index of cladding in III. Thus, the solution of the symmetrical planar waveguide in III—for a TM mode, as the waveguide is rotated by 90°—, using the corrected indices found in I and II, provide an approximate value for the total effective index of the rib waveguide. This method, however, may become

inaccurate when there are poorly confined modes (i.e. low contrast between the cladding and core refractive indices), or for large index steps [40].

3.1.4 Single-mode rib waveguides

For channel waveguides, the geometry of the problem is not as trivial as for planar waveguides. In the previous section it was shown how EIM needs to be used to bypass the lack of an analytical solution by using the eigenvalues for one-dimensional waveguides, given in Eq. 3.10 and Eq. 3.11. For such planar waveguides, an estimation of the maximum number of modes (m_{max})that can propagate within a core of thickness t is analytically given by[40]

$$\frac{k_0 n_1 t \cos\theta_1 - m_{max}\pi}{2} = 0. \tag{3.13}$$

A relation of this kind is not achievable for rib waveguides. In fact, although these waveguides are in practice commonly claimed to be single-mode, what really happens—by correctly designing the waveguide—is that higher-order modes leak out of the waveguide over short distances leaving only the fundamental mode propagating. An estimation based on the geometrical parameters of the rib waveguide has been proposed using EIM and the eigenvalue equations for planar waveguides [40, 184]. Considering waveguides with a width W, thickness t, and etch-depth H, as shown in Fig. 3.1 and 3.3, single-mode propagation can be obtained if the following conditions are fulfilled [40]

$$\lambda \leq \frac{(t+H)}{2}\sqrt{\frac{t^2}{W^2}+1} \quad or \quad W \leq \frac{t(t+H)}{\sqrt{(2\lambda)^2+(t+H)^2}}. \tag{3.14}$$

This equation is valid for shallow etched ribs (down to half of the total thickness) in order to cut off modes other than the fundamental vertical mode, and make the rib a single-mode waveguide. Nevertheless, the parameters used in this thesis $W = 1300\,nm$,

$t = 330\,nm$, and $H = 165\,nm$ do not satisfy this inequality as $\lambda < 255.35\,nm$ should be used, or considering $\lambda = 1550nm$, a width $W < 53.4nm$. However, this geometry is chosen given that it offers low attenuation by the Si_3N_4, which is preferred over single-mode guiding in the application presented herein. Moreover, the measurements are carried out for a single, or maximum two counter-propagating waves, thus not having no problems with dispersion effects. Multi-mode allowable structure with larger width (thus, easier to fabricate) and small thickness ($330\,nm$) were considered.

3.1.5 Bragg-grating couplers

In-plane techniques, such as putting together optical fibres to ends of the channel waveguide (aka. butt-coupling), using fibre taper coupling, and focusing micro-lenses, allow for coupling efficiencies as high 70% [185, 186, 187] and no much more coupling bandwidth restriction beyond that of the waveguides themselves. However, due to the sophisticated alignment requirements, these solutions may imply that fibres and/or lenses have to be glued to the integrated channel waveguides, thus hindering the access to large number of devices on the same chip. Out-of-plane coupling techniques, on the other hand, offer the advantage to readily access every device at the cost of lower efficiency, given to reflection and scattering effects. However, in order to couple to the guided mode in the channel waveguide, a phase-match condition has to be fulfilled. This means that the phase velocities in the direction of propagation (z direction in cartesian coordinates, by convention) has to be the same between the incident beam and the guided mode [40, 187]. This is, however, not possible by shining light directly onto the waveguide because the propagation constant of any radiation mode is always smaller than the propagation constant of the guided mode (due to the higher refractive index of the core compared to the surrounding). Nonetheless, this can be overcome by using a prism or a grating to guarantee the optical phase-matching between these two modes. The bandwidth for out-of-plane coupling will be limited to those wavelengths that fulfill the

phase-matching condition, which is a very limiting condition of this method. Prisms on top of the waveguides [188] have been used, reaching theoretical efficiencies of up to 94%. In spite of that, the most common approach is to align the input and output optical fibres to Bragg gratings on both extremes of the on-chip photonic devices. Bragg gratings are chosen given that they can be patterned in the same process, together with the waveguides. Simple fabrication means that it is possible to write several Bragg gratings within a chip, which is much easier than placing a prism on top of each of them. Using this approach, efficiencies up to 30% and 50 nm bandwidth have been reported [177, 189, 190].

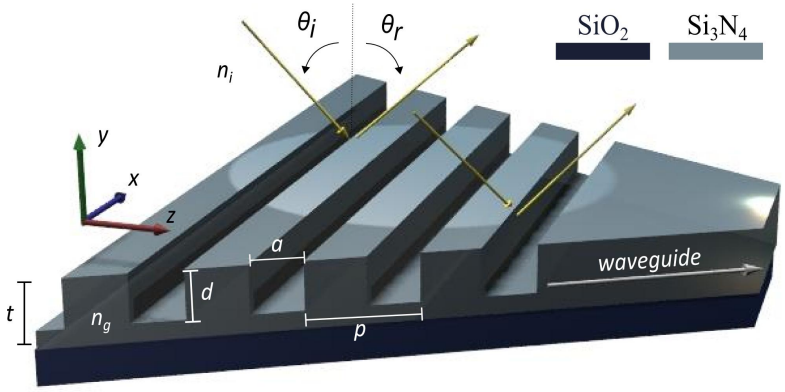

Figure 3.4: Grating coupler sketch. n_i and n_g are the refractive indices of the incident medium and the material of the grating, respectively, p is the period of the grating, θ_i and θ_r are the incident and reflected angles.

For a uniaxial periodic grating with period p along the z-direction, as sketched in Fig.3.4, optical phase-matching takes place if [183]

$$k_i \sin\theta_i + \frac{2\pi m}{p} = \beta, \tag{3.15}$$

where n_i is the refractive index of the incident medium (i.e. the medium on top of the grating, in which the incident beam propagates), θ_i is the incident angle, $m \in \mathbb{N}$ is the diffraction order, and λ_0 is the incident wavelength. $\beta = \frac{2\pi}{\lambda_c} n_{eff}$ and $k_i = \frac{2\pi}{\lambda_c} n_i$ are the propagation constants inside the waveguide and for the incoming light, respectively. n_{eff}

is the effective refractive index, as explained in the previous section. By replacing β and k_i into Eq. 3.15, taking $m = 1$ (first diffraction order), and considering air as the incident medium ($n_i = 1$), the period p to couple a wavelength λ_c is given by

$$p = \frac{\lambda_c}{n_{eff} - \sin\theta_i}. \tag{3.16}$$

Therefore, by choosing λ_c (the central wavelength), n_{eff}, and the angle of incidence, the period of the grating to be used in the fabrication and experiments can be determined. In particular, λ_c is chosen within the range $1535 - 1610\,nm$. Also, the commercial 8^0 angle-polished connectors (FC/APC), at the output of fibre, are used to direct the light onto the waveguide; therefore, $\theta_i = 8°$ (See Sec. 4.3.1) as the fibre is tilted to match the surface of the grating and minimise the separation between them. This angle is large enough to avoid back reflections into the fibre, whereas high coupling is still achieved. The problem of finding the grating period is then reduced to finding the n_{eff} of the channel waveguide, which can be obtained from finite-element methods, as explained in Sec. 3.2.3. Having the values for all the parameters, the period of a specific grating can be calculated from Eq. 3.16. In order to find the electromagnetic modes and polarisations that are coupled, a more exhaustive electromagnetic theory is required [191, 192, 193]. Lastly, other factors such as the fill factor ($FF = (a - p)/p$ from Fig. 3.4), the taper length and angle, the thickness of the gratings (t), and the etched depth (d) impact the overall efficiency of the coupling, yet conserving bandwidth [191]. In particular, the fabrication details and parameters used in this thesis are found in Sec. 3.3.3.

3.2 Guided-mode coupling to absorptive media

Thus far, only dielectric materials have been considered, that is, materials whose electric permittivity $\varepsilon \in \mathbb{R}_{>0}$. A more general analysis should include the case $\varepsilon(\omega) = \varepsilon'(\omega) + i\varepsilon''(\omega)$, where ε'' is related to the dissipation (or loss) of energy by photon absorption

in the medium. Semiconductors are good examples of such materials with large ε'', in which the photons are absorbed, exciting electrons from the valence band directly into the conduction band. A complex permittivity, in non-magnetic materials ($\mu = 1$), means that the refractive index given by $\overline{n} = \sqrt{\varepsilon}$ also becomes complex in the form $\overline{n}(\omega) = n(\omega) + i\kappa(\omega) \rightarrow \overline{n}(\lambda) = n(\lambda) + i\kappa(\lambda)$. Phase-change materials are good examples of materials having a complex refractive index, which in turn changes in both the real and the imaginary part when switching between the amorphous and the crystalline state, as shown previously in Fig. 2.4. κ takes account of absorption and is known as the extinction coefficient. Moreover, by knowing the $\kappa(\lambda)$ of a particular material, the attenuation coefficient $\alpha(\lambda)$ (given in dB per micron) for a particular wavelength λ and per material length unit can be calculated from

$$\alpha_{dB}(\lambda) = \frac{10}{ln\,10}\frac{4\pi}{\lambda}\kappa(\lambda) = 4.34\frac{4\pi}{\lambda}\kappa(\lambda). \tag{3.17}$$

3.2.1 Evanescent-field variation in channel waveguides

In Sec. 3.1.2, the general electric-field formulation for channel waveguides was studied. There, it was shown that, in order to calculate the effective refractive index, the problem had to be reduced to a set of planar waveguides, whose electric field is given by Eq. 3.9. Pursuing a conceptual-only analysis of the problem, a similar solution for the TE electric field in the core and the cladding of a channel waveguide can be approximated to

$$\vec{E}(x,y,z,t) \propto \begin{cases} A_{clad}\, e^{i\left(k_{x,clad}\, x + \beta_{m,n}\, z - \omega\, t\right)} e^{-k_{y,clad}\,(y+h)}\hat{x}, & y \geq h/2, \qquad cladding \\ A_{core}\, e^{i(k_{x,core}\, x + k_{y,core}\, y + \beta_{m,n}\, z - \omega\, t)}\hat{x}, & -h/2 \leq y \leq h/2 \qquad core \end{cases} \tag{3.18}$$

The core confines an electric mode in x and y directions while propagating in the z-direction. In the cladding, an evanescent wave is found to decay with $k_{y,clad}$. If an

absorptive material with $\overline{n} = n + i\kappa$ is considered as the cladding, then

$$k_{y,clad} = \sqrt{\beta^2 - k_{y,0}^2(n + i\kappa)^2} = k'_{y,clad} + ik''_{y,clad}. \tag{3.19}$$

By introducing Eq. 3.19 in Eq. 3.18, a new propagative term $e^{-ik''_{y,clad}\,(y+h)}$ in the cladding implies that the wave can couple to the absorptive material that is placed on top and propagate inside. Moreover, the critical angle $\theta_c = \sin^{-1}(n_i/n_1)$ will have a complex component, which in turn implies that the effective refractive index becomes complex: $n_{eff} = n_1 sin\theta_1 \Rightarrow n_{eff} + i\kappa_{eff}$ and so does the propagation constant $\beta = \beta' + i\beta''$. Therefore, by introducing the complex β into Eq. 3.18, the electric field in the core is given by

$$\vec{E}_{core}(x, y, z, t) \propto A_{core}\, e^{-\beta''_{m,n} z} e^{i(k_{x,core}\, x + k_{y,core}\, y + \beta_{m,n}\, z - \omega\, t)} \hat{x}, \tag{3.20}$$

which is decaying with $\beta'' = k_0 \kappa_{eff}$. The effective extinction coefficient κ_{eff} will then determine the total attenuation inside the channel waveguide due to the presence of an absorptive medium placed on top. When calculating the total effective refractive index via numerical simulation, the net attenuation per micrometre length of the absorptive material, similarly to Eq. 3.17, will be given by

$$\alpha_{dB}(\lambda) = 4.34 \cdot \frac{4\pi}{\lambda} \kappa_{eff}(\lambda). \tag{3.21}$$

The coupling with an absorptive material is not just evanescent in the sense of having only a decaying field into the material. It is in fact a coupling between the propagating mode and the material, within which the wave travels while experiencing attenuation. Whereas near-field interaction should be a more accurate name, this technique is broadly known in fibre optics and integrated optics as evanescent-wave coupling [194], including an entire field on evanescent-wave spectroscopy[195, 196]. When placing GST on top of

Si_3N_4, the coupling is strong. The real part of the refractive index in the cladding is larger than the refractive index of the core (in most of the visible and infrared spectrum, as shown in Fig. 2.4); therefore $\theta_c = \sin^{-1}(n_i/n_1)$ implies that the effective refractive index has a large imaginary component (taking into account also that n_i has already a large imaginary part), thus presenting strong attenuation, particularly in the crystalline state.

3.2.2 Electromagnetic heat transfer

As light is attenuated due to the coupling with a complex refractive index material, energy is dissipated as heat. In a lossy isotropic non-magnetic medium, ε'' is a measure of the ability of a dielectric material to convert electromagnetic field energy into heat via displacement currents. Due to the complex dielectric constant (or permittivity), the induced dipoles in the material present a polarisation that is not parallel, or even randomly oriented compared to the electric field. Therefore, power dissipation takes place which, averaging over time, represents the heat rate ($Q_{Edipole} = \langle P_D \rangle$). Assuming time-harmonic fields, this rate takes the form [197]

$$Q_{Edipole} = \langle P_D \rangle = \langle E \cdot J_{dipole} \rangle = \langle E \cdot \frac{\partial D}{\partial t} \rangle. \tag{3.22}$$

where J is the total current, E is the electric field, and D is the electric displacement, which are vectorial functions of space and temporal coordinates, but whose notation is simplified for clarity. Using the time-average theorem $\langle \Re\{Ae^{-i\omega t}\} \cdot \Re\{Be^{-i\omega t}\} \rangle = \frac{1}{2}\Re(A \cdot B^*)$, where $\Re$ stands for the real part, the Eq. 3.22 becomes [198]

$$Q_{Edipole} = \frac{1}{2}\Re\{-i\omega D \cdot E^*\} = \frac{1}{2}\Re\{-i\omega(\varepsilon' + i\varepsilon'')E \cdot E^*\} = \frac{1}{2}\omega\varepsilon'' E \cdot E^*. \tag{3.23}$$

This last equation is the most general approach. In conductive materials characterised by the conductivity σ, the complex permittivity takes the form $\varepsilon'' = \sigma/\omega$. Then, by

replacing this into Eq. 3.23, the heat rate takes account of Joule heating:

$$Q_{cond} = \frac{1}{2}\Re\{E \cdot J_c^*\} = \frac{1}{2}\sigma E \cdot E^* \tag{3.24}$$

Ohmic conduction is the primary source of heat generation in materials. In this case, ohmic currents are induced inside the medium by capacitive coupling with an electric field, thus dissipating energy from the latter. Whether the heat source is given by an electrical current or by an electromagnetic wave, the heat will spread over the whole volume of the material, thus inducing different temperature gradients. This effect is mediated by the specific heat capacity at constant pressure C_P, the thermal conductivity κ_T, and density ρ of the material. The pure conductive heat transfer in solids for a temperature T is given by the equation displayed in 3.25 [199].

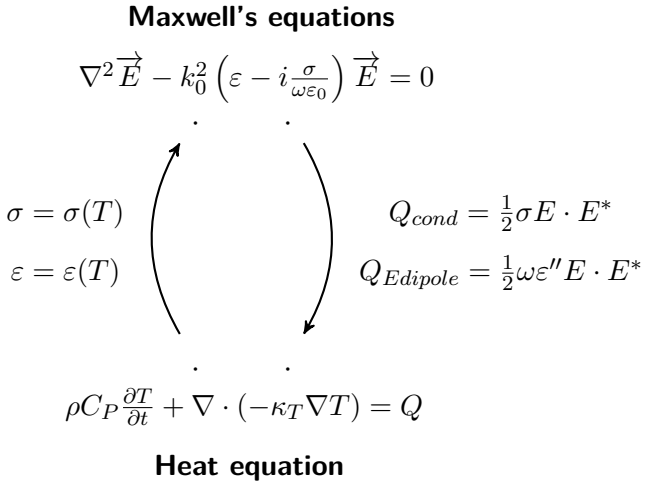

(3.25)

This equation includes the heat source(s) Q, which, in the case of electromagnetic waves, is given by Eq. 3.23, or by Eq. 3.24 if the absorptive material of study is also conductive—crystalline GST, for instance. The coupling of these two equations through the heating rates is a numerical problem of high complexity, which is even more challenging when considering full coupling: as the material heats up, the material parameters change, as

they are temperature dependent too, i.e. $\sigma \rightarrow \sigma(T)$ and $\varepsilon \rightarrow \varepsilon(T)$. A diagram of the equations coupling is presented in Eq. 3.25.

The numerical solution of these equations requires significant computational resources and a powerful method to solve them. In the case of heat transfer to GST embedded in a rib waveguide, which is the interest of this thesis, calculations are done using finite-element method modelling in COMSOL multiphysics.

3.2.3 FEM Modelling

Realistic problems associated with electrodynamics involve complicated geometries, material properties, and intricate calculations beyond those with analytical solutions—which are few and for simplified ideal cases. Such problems require sophisticated numerical methods and computational resources, given the level of complexity and heavy calculations. One of those is the Finite Element Method (FEM), which solves partial differential equations (PDE) without inherent geometric limitation [200] by projecting the equations onto the nodes and edges of a three-dimensional mesh. This projection is done by converting differential operators into sparse matrices that operate on the fields (also matrices) that are discretised on the mesh, thus converting the problem into a linear algebra calculation. COMSOL Multiphysics® is one commercial software that specialises on FEM solving for problems with any arbitrary geometry and under different physical interactions. In particular, COMSOL offers great computational tools for electromagnetic problems with its *RF module* and, more directly linked to optics, with the *Wave Optics* module. Electromagnetic heat transfer can also be studied by coupling Maxwell's equations and the heat-transfer equation as shown in Eq. 3.25.

FEM on COMSOL Multiphysics® was used to understand the interaction between a propagating mode, confined to a integrated waveguide, and a GST section placed on

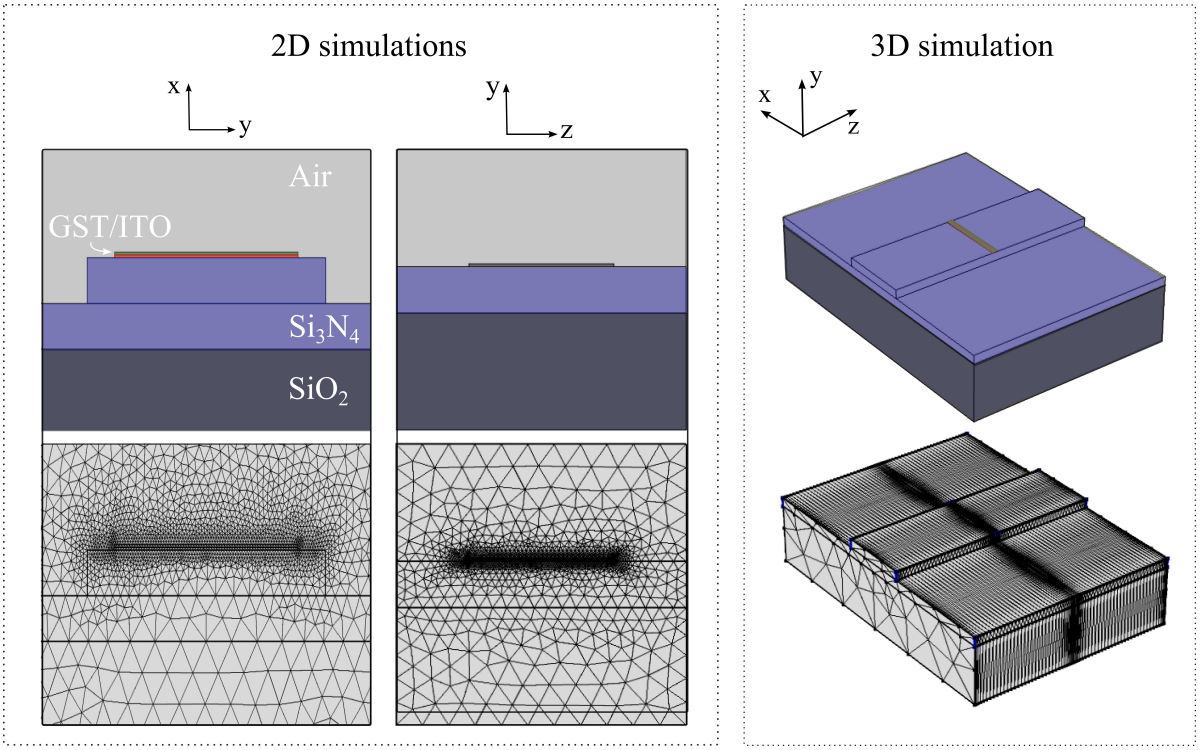

Figure 3.5: Guided-mode coupling to absorptive material: 2D and 3D simulation geometries and mesh using COMSOL.

top. The simulations presented in this section and later in Sec.5 provided qualitative and quantitative information that enabled the optimisation of parameters for the design and fabrication; the calculation of physical variables such as the attenuation coefficient; and a better understanding of the heat transfer to the GST. In particular, three different types of simulations, 3D and 2D with two different transversal cuts, can be done to approach the geometry of interest in this thesis, as shown in Fig. 3.5. Assuming always propagation in the z-direction (as done for the theory in the previous chapter) and perfect electric-conductor boundaries, two-dimensional simulations of the cross section—xy plane— allows to find n_{eff}, therefore the attenuation coefficient of a particular waveguide and whether TE, TM, or both, modes can propagate. However, the calculation will be done assuming an infinite waveguide in the z-direction, including the absorptive material capping. This implies that information about reflection and scattering when adding a finite-sized element on top are lost. By taking the yz-plane, the actual propagation mode

can be studied, together with the way it couples to the absorptive material. From this study, a more realistic power transmission simulation can be done. However, it loses geometrical information in the x-direction, i.e. it considers a slab waveguide rather than a rib waveguide which has been etched down partially. A more complete study is possible when considering a 3D simulation which gives account of the whole geometry and the propagation depth. This simulation, however, demands more computational resources and is not as straightforward. Whether 2D or 3D simulations are run, in any case, COMSOL allows to study the electromagnetic mode, and also the thermodynamic coupling to the absorptive material, thus enabling the study of heat exchange, temperature evolution, and even, the phase change of the material.

Silicon nitride waveguides with GST junctions

Taking into account half-etched Si_3N_4 waveguides on top of SiO_2, FEM analysis is useful to find the modes propagating inside the bare waveguide and also, when placing the $10\,nm$ GST and a protective $10\,nm$ of indium-tin oxide (ITO) on top. This has been done previously in [201, 202] to study the influence of geometrical parameters on the total attenuation. In those theses, the optimum geometric parameters for a TE-like propagation were found to be: half-etched rib waveguides of $1.3\,\mu m$ in width for $330\,nm$ thick Si_3N_4 onto $3300\,nm$ SiO_2 wafers. Such a set of parameters offers the modes shown in Fig. 3.6, considering the GST refractive index shown in Fig. 2.4 and the ITO refractive index in Ref. [203].

The horizontally extended geometry favours the TE mode, i.e. the TM does not propagate for wavelengths around $1550\,nm$ with the bare waveguide ($n_{eff,TM} = 1.42 < n_{SiO_2}$). However, when introducing GST, its strong refractive index allows the TM mode to propagate, although very weakly ($\mathbb{R}(n_{eff,TM}) \approx n_{SiO_2}$). Experimentally, TM modes are not obtained because the gratings themselves are optimised only for TE polarisa-

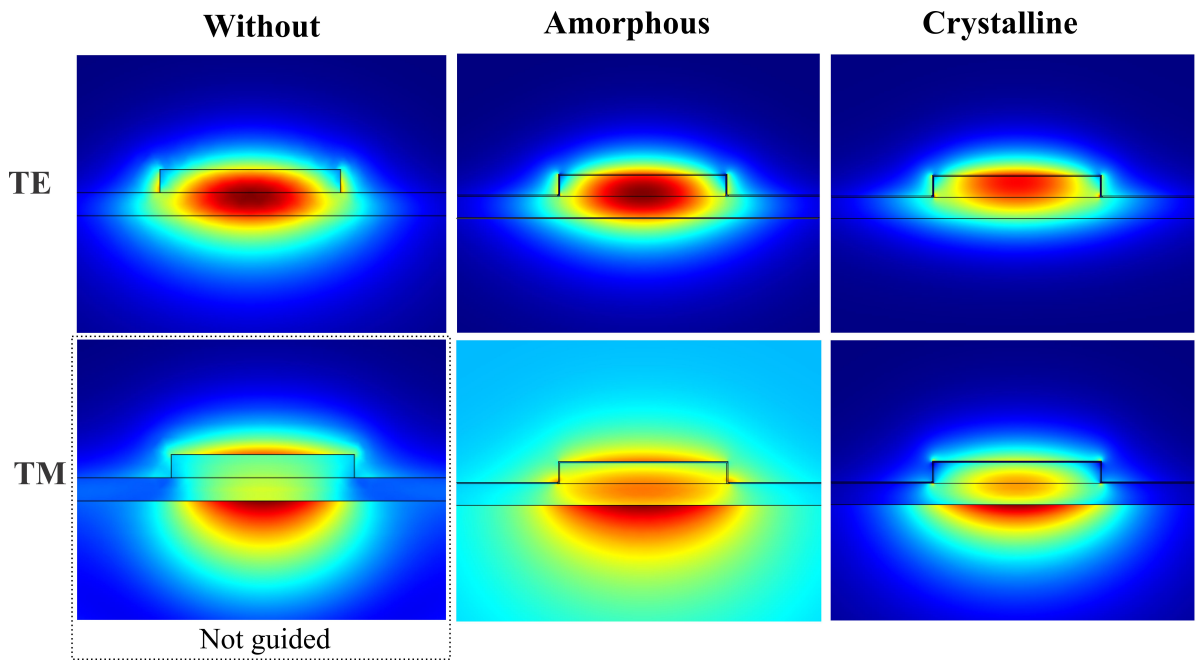

Figure 3.6: TE and TM modes for waveguides with GST in the amorphous and the crystalline phase, and without GST. This simulation uses the geometry shown in Fig. 3.5a, both black rectangles represent Si_3N_4 (there is a continuous boundary condition between the two of them despite the way COMSOL draws the geometry with a line in between). The waveguide is half-etched from a $330\,nm$ Si_3N_4 wafer, the substrate is $3300\,nm$ SiO_2, and the cladding is air.

tion; therefore only this polarisation will be considered for the simulations carried out in Ch. 5, where FEM modelling is done to study the coupling between the mode and GST.

The same parameters are going to be used throughout this thesis. Besides, and to complete the computational characterisation of $\overline{n}_{eff} = n_{eff} + i\kappa_{eff}$, when GST is placed on top, as a function of factors that can influence the fabrication and design, simulations where done to study the influence of different wavelengths in the $1520 - 1620\,nm$ range. Results are shown in Fig. 3.7, where α is obtained from κ_{eff} using Eq. 3.21. The results show that there are no important changes in this wavelength range, which is due to the flatness of the GST refractive index in this part of the spectrum. This results were validated experimentally in [27].

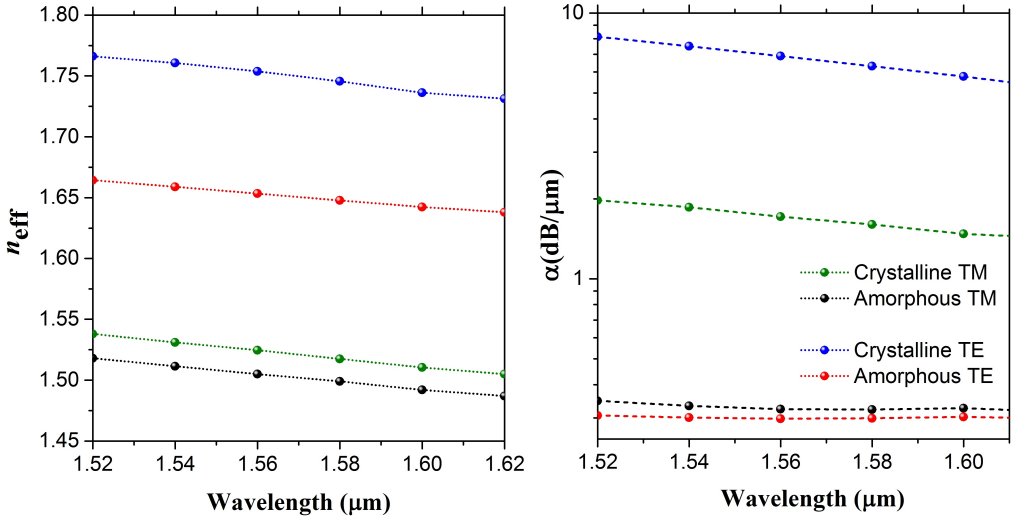

Figure 3.7: Effective refractive index ($\overline{n}_{eff} = n_{eff} + i\kappa$)and attenuation coefficient α calculations for TE and TM modes in the C and L transmission bands. α is the attenuation coefficient calculated from the imaginary effective refractive index κ_{eff}.

Moreover, in Fig. 3.8, the attenuation coefficient is studied as a function of the GST cover width for $\lambda = 1550\,nm$. This is important to consider, given that the aim is to use as low energies as possible and also, to have devices with small form factors. Nonetheless, when such a dimension is smaller than the waveguide width, precise alignment is required during the fabrication using e-beam lithography (See Sec. 3.3). In the same figure, the attenuation of a fully covered waveguide, including the side walls as sketched in Fig. 3.8c, is taken into account as reference. This sort of geometry is frequently used herein because of its simplified nanofabrication (long stripes do not need local marker alignment), although it adds more coupling losses due to the side walls.

Given the shape of the TE mode (See Fig. 3.6), the coupling to GST becomes stronger as the width increases. However, for GST thicknesses larger than $\approx 0.9\,\mu m$, the difference in attenuation gets smaller, showing that this is the area where most of the energy is delivered to the phase-change material. This effect is studied in Ch. 5, where further FEM modelling is done, focusing on the interaction between the light and GST.

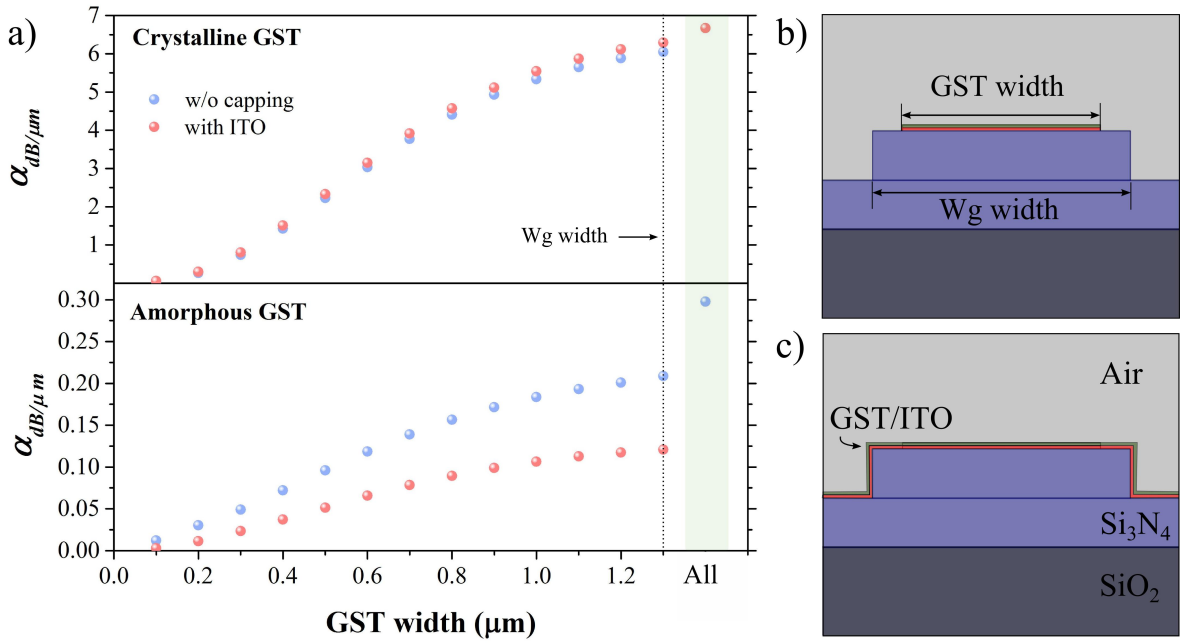

Figure 3.8: GST width effect on mode attenuation. a) attenuation coefficient as a function of GST width for the amorphous and the crystalline states at $\lambda = 1550\,nm$. *All* stands for α when the waveguide is fully covered with GST/ITO as shown in c). b) Cross-section used in the FEM calculations when varying the GST width. c) Same as b) when the GST covers the whole waveguide including side walls.

3.3 Fabrication overview

Silicon-nitride-on-insulator substrate wafers were chosen as the platform for the photonic devices within this thesis. The low losses of this material—resulting from its transparency in a wavelength-range covering from the visible to the far infrared—allow for devices with large bandwidth operation [27, 178, 202]. Specifically, in this work, 330 nm stoichiometric Si_3N_4 on 3300 nm buffered SiO_2 wafers were used. The whole fabrication process, including the chip CAD layout design for the simplest memory element, is briefly described in this section. Although more complex fabrication was carried out while exploring ideas for devices, such as suspended waveguides, they turn out not to be the optimum solution and were discarded. For more details, refer to [201], the Master's dissertation written by the same author of this thesis.

3.3.1 Chip design

A Computer-Aided Design (CAD) was required for each layer of every chip that was fabricated by e-beam lithography. For that reason, the software *CADENCE Virtuoso*®, widely used for micro-electronics layouts and simulations, was used for multi-layer chip design by means of scripts using SKILL programming language. This tool is necessary due to the intricate geometries of the photonic circuit elements such as the Bragg-grating couplers, beam-splitters, and bending waveguides. Moreover, a script-based CAD design allows for better management of multiple layers and controllable sweeps of parameters, such as the GST window size, which can be easily manipulated within loops. In the practical implementation, a library containing most of the basic geometrical shapes, elements, and photonic devices, was created and has been in constant development. The library was based on the library built by Prof. Wolfram Pernice's group at the University of Münster, Germany, although it was rebuilt to a 70% extent. From this library, every element can be imported in a script which compiles the whole chip. *CADENCE Virtuoso*® was run on the Linux server of the Engineering Department at the University of Oxford.

A sample chip CAD layout featuring balanced-splitter devices for photonic memories using phase-change materials is shown in Fig. 3.9. This layout is exported in *.gds* files, which are imported directly to the e-beam lithography system. The layout of this chip—as of all the chips fabricated within this thesis—consists mainly of three layers, which requires the same number of lithography steps: reference markers (usually put together with labels and frames), photonic circuits, and rectangular windows for the subsequent GST deposition, which are explained in detail in the following sections.

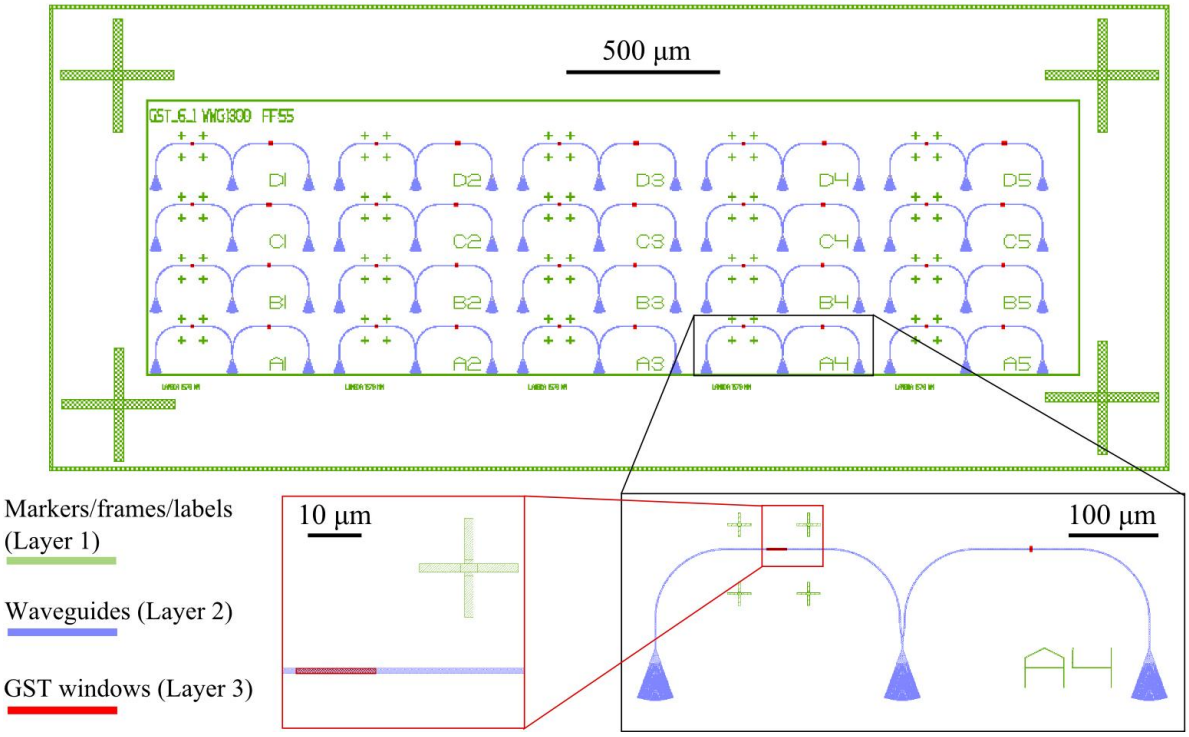

Figure 3.9: Design of balanced-splitter devices using *CADENCE Virtuoso*.

3.3.2 Reference markers, labels, and frames (Layer 1):

This layer contains elements for alignment reference during the e-beam lithography writing, such as crosses (for *JEOL* system) or squares (for *Nanobeam* system). Frames and labels are also written in this step; they are useful in the localisation and differentiation of devices during the optical measurements. This layer is usually written on positive resists and undergoes a lift-off process to transfer a good electron scatterer—such as gold—to the pattern.

In particular, this layer, shown in Fig. 3.10a, is transferred onto Si_3N_4 chips following the nanofabrication steps in the scheme depicted in Fig. 3.10b. The positive resist poly(methyl-methacrylate) (PMMA) 495k is spin-coated onto the chips. E-beam writing using a $50\,kV$ JEOL JBX-5500ZD system is carried out to transfer the CAD file onto the PMMA. This layer, which does not require high resolution or alignment precision,

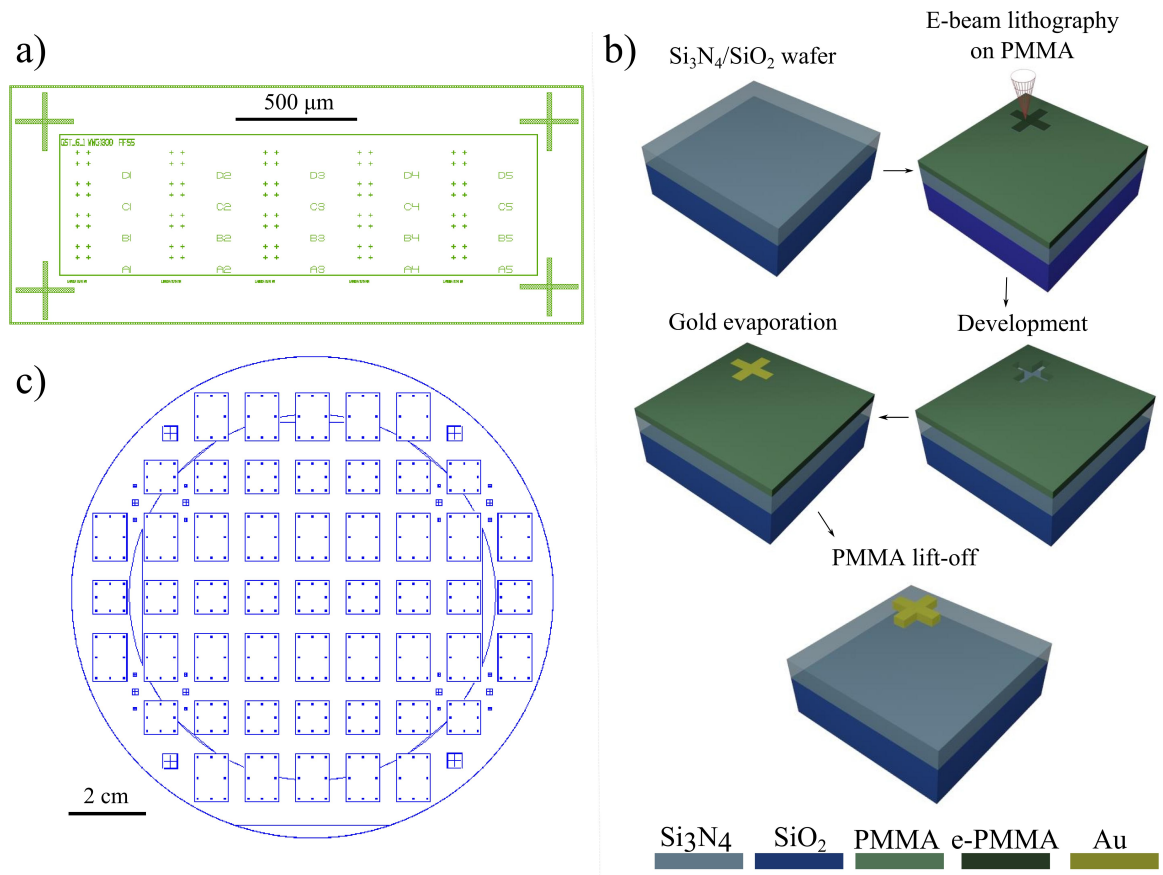

Figure 3.10: Nanofabrication layer 1: Reference markers, labels, and frames. a) CAD for the first layer. b) Sketch of fabrication steps. e-PMMA stands for exposed PMMA resist. c) CAD of the 4″ wafer optical lithography mask to write, in mass, up to 46 chips in one exposure.

is written using the higher currents available at the system: 1 to 10 nA. Doses around 600 $\mu C/cm^2$ are delivered for this particular resist. Exposed PMMA is developed using isopropyl alcohol (IPA) and methyl isobutyl ketone (MIBK) in a 3:1 proportion, respectively. Subsequently, 5 nm of chromium followed by 100 nm of gold are thermally evaporated onto the developed sample. A final lift-off process using acetone removes the unexposed PMMA leaving only the pattern, originally given by the CAD design, all made of gold.

A more time-efficient approach, given the low requirements in terms of resolution and alignment precision, is to write several chip frames and markers onto a whole 4″ wafer by

means of optical lithography using a *Quintel*® Q4000-6 Mask Aligner and MICROPOSIT® S1813 positive resists. To do so, the layout shown in Fig. 3.10c was designed such that 46 chips with two different sizes could be processed simultaneously. This layout was converted into a high-resolution optical mask by the company JD-Photodata® who fabricated it using chrome-oxide on quartz (used silica). Thus, the whole process of writing frames and markers was reduced to an 8 *s* exposure using the optical lithography system, a single gold/chromium evaporation, and wafer dicing. Lift-off was done in the same way presented above.

3.3.3 Nanophotonic circuits (Layer 2):

The second layer, in blue in Fig. 3.9, contains the actual nanophotonic circuits that are transferred to the Si_3N_4 substrate via e-beam lithography and dry etching. This layer is the most delicate given the geometrical complexity and low dimensional features, which is why script-based chip design was preferred. Nanophotonic circuits were optimised for operation in a particular wavelength, as detailed in the above in Sec. 3.2.3, using different optical architectures, such as the balanced splitter shown in Fig. 3.9b. These balanced splitters offers two identical optical paths coupled to the same grating placed in the centre, which allows for optimum comparison between two balanced waveguides, one with and the other without a passive or active component of interest, such as PCMs. Because of this, such an architecture was preferred for the demonstration of the phase-change photonic memories and is the only one considered within this thesis. Mach-Zehnder interferometers, ring and race-track resonators [27] and directional couplers are common architectures that represent other examples of typical photonic circuitry.

The actual steps followed during the second layer fabrication are sketched in Fig. 3.11. The photonic circuits are written on ma-N 2403 negative resist (by MicroChem®) which is spin-coated on top of the chips after having coated a Ti-Prime (by MicroChem®) adhesion

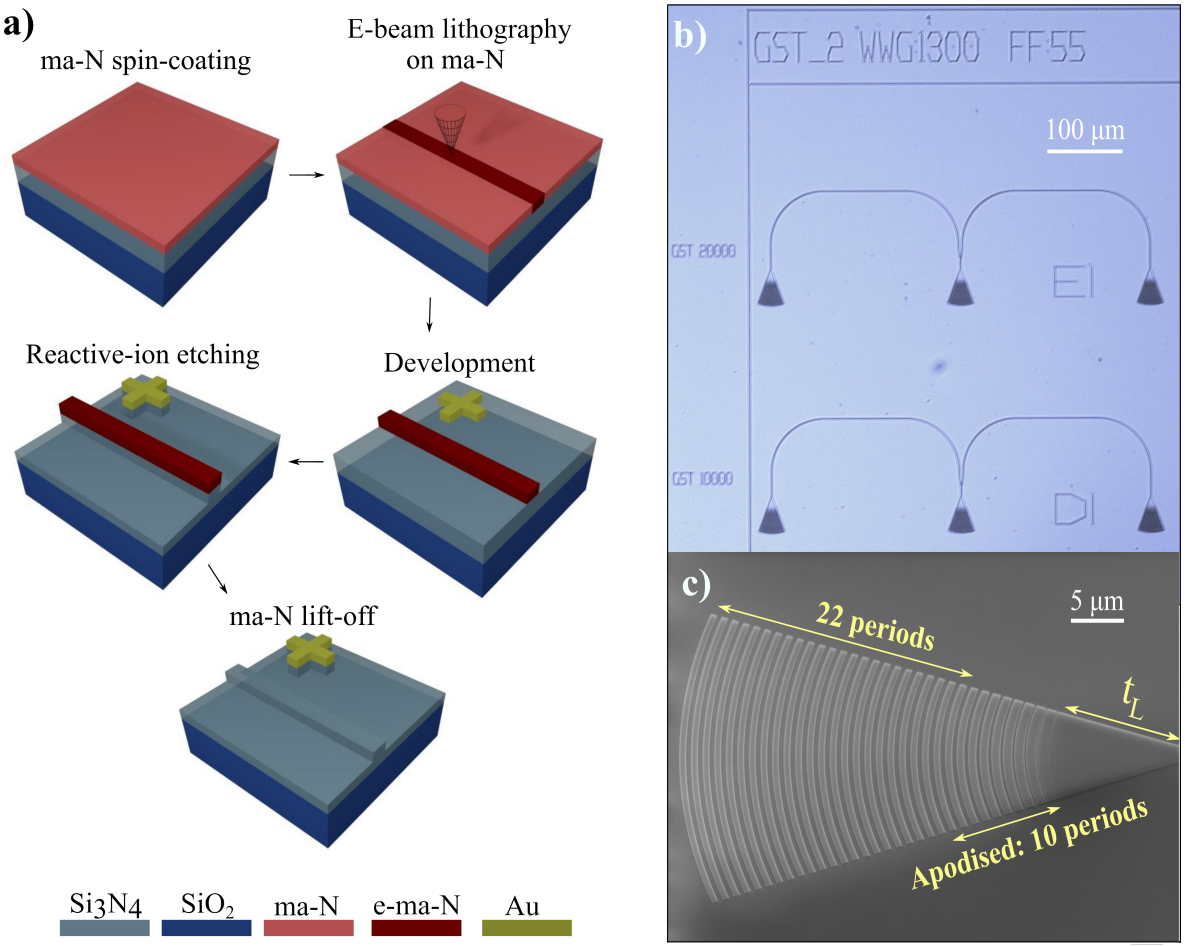

Figure 3.11: Fabrication layer 2: nanophotonic circuits. a) Sketch of fabrication steps. e-ma-N stands for exposed ma-N 2403 resist. b) Optical microscope image of bare photonic circuits transferred to Si_3N_4, featuring frames written in the previous step. c) SEM micrograph of a Bragg-grating coupler. $t_L = 16\,\mu m$ is the taper length.

promoter layer. The resolution of this resist allows features as small as $80\,nm$—optimum for the Bragg gratings which have features down to $90\,nm$. The reference markers written in the previous step are used as reference for proper alignment. The $50\,kV$ JEOL JBX-5500ZD electron-beam system is used to write, this time with a lower current: $\approx 100\,pA$, and a dose of $200\,\mu C/cm^2$. Development is carried out using MF-319 and, afterwards, a reflow annealing process of $90\,s$ at $100°C$ is applied to reduce the intrinsic roughness and round the corners of the exposed resist, thus allowing for sharper edges when etching down in the next step [178, 202]. Subsequently, reactive-ion etching (RIE) is used to etch down Si_3N_4 by $165\,nm$, half of the total layer thickness, everywhere but in those areas

protected by ma-N. A recipe consisting of 50 $sccm$ of CHF_3, 10 $sccm$ of Ar , and 2 $sccm$ of O_2 are used for this process with 120 W RF power, 25 $mTorr$ of pressure. The rate was constantly checked given the system fluctuations, in average, the etching rate was found to be 26.6 nm/min. Finally, the ma-N resist is removed using mr-Rem 660, the custom remover for this resist also provided by MicroChem®. Additionally, an acetone bath and O_2 plasma ashing can be used in case there is ma-N remaining on top of the waveguides. An optical image of what a chip looks like after this step, featuring the bare photonic circuits and the frames/labels, is shown in Fig. 3.11.

Grating coupler

In Fig. 3.11c, an SEM micrograph is shown for one of the Bragg gratings that couple light in and out of the waveguide. The set of parameters of the grating (see Sec. 3.1.5) for the fabrication of such couplers are based on the results of [201, 202]. For all the devices, gratings composed of 32 Si_3N_4 slabs are used, compromising and area of $\approx 40 \times 30\,\mu m^2$, more than enough for a beam of around 8 μm in diametre (beam size out of single-mode optical fibre). However, the last 10—the slabs closer to the waveguide—are apodised. This is, the fill-factor (i.e. the width of the grating slab compared to the period) defined as $(a - p)/p$, using the parameters shown in Fig. 3.4, is varied in equal steps from 0.5 to 0.985 (55% to 98.5%). The reason behind this fabrication feature is that the apodised couplers decrease significantly the back-reflection into the waveguide, thus avoiding Fabry-Perot-type interferences that distort the transmission spectrum [204, 205]. The result is a grating where the slabs closest to the waveguide have smaller air gaps, reaching down to 90 nm for the smallest one. The fill factor for the remaining 22 slabs is set at 55%, i.e. 55% Si_3N_4 and 45% air. The taper length (t_L) and the angle of the coupler are set to 16 μm and 40°, respectively [202]. This angle, and the curvature of the grating, is implemented to improve the light focusing into the rib waveguide, thus improving the coupling efficiency.

The central wavelength of the coupling bandwidth, λ_c, as a function of the grating period has been characterised in [201, 202]. For the experiments carried out in Ch. 5, the grating periods are calculated from $p(\lambda_c)_{\mu m} = \frac{\lambda_c[nm]-559.11}{898.73}$ for 1.3 μm wide and half-etched (165 nm) waveguides [201]. A parameter optimisation realised in [201], showed that the light transmission in a grating with these parameters is larger for $\lambda_c > 1580\,nm$, this being the reason why the experiments carried out in this thesis are around this wavelength.

3.3.4 GST windows (Layer 3) and sputtering:

The third and last layer to be written, in red in Fig. 3.9, includes the rectangular windows where GST will be sputtered. These windows may vary in size over the waveguide plane depending on the application; however, the thickness was set to 10 nm. The fabrication process is sketched in Fig. 3.12 and corresponds to another lithography process using the same 50 kV JEOL JBX-5500ZD electron-beam system on PMMA 950k positive resist—a higher molecular weight is chosen, given the high resolution required for some of the GST windows. The exposure parameter and development are carried out in the same way as for markers and frames in Sec. 3.3.2. Once the rectangular windows are developed, 10 nm of $Ge_2Sb_2Te_5$ are sputtered followed by either 10 nm of indium-tin oxide (ITO) or SiO_2 to avoid its oxidation, without adding extra absorption given their known transparency in the visible and infrared spectrum [40, 206]. A final lift-off process reveals the completed chip, which may contain within 1 cm^2 hundreds of devices similar to those in Fig. 3.12b. SEM micrographs of GST sections on top of two different photonic waveguide geometries—results of this fabrication process—are presented in Fig. 3.12c-d. The micrograph in Fig. 3.12d represents a device with a suspended waveguide on air. To achieve this, the same three fabrication steps are carried out. However, another electron-beam lithography on PMMA is done to pattern a window in which hydrofluoric (HF) acid is subsequently used to etch the silica layer.

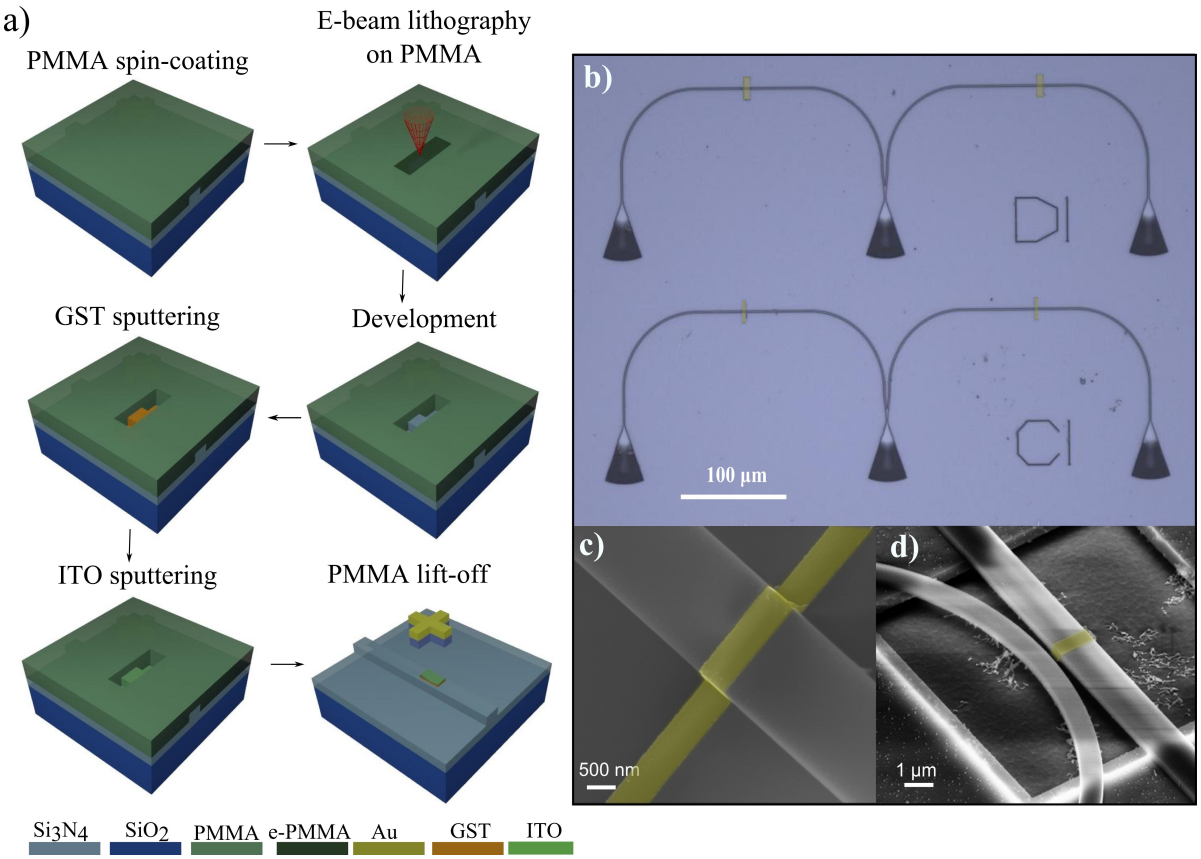

Figure 3.12: Fabrication layer 3: GST windows and sputtering. a) Sketch of fabrication steps. e-PMMA stands for exposed PMMA resist. b) Optical microscope image of the completed photonic circuits with GST memory cell in both arms of balanced-splitter devices. c) SEM micrograph of one memory cell of b). d) SEM micrograph of a memory cell on an air-suspended waveguide.

GST and ITO deposition parameters

GST and ITO are sputtered in an argon atmosphere using a Nordiko® sputering system with the parameters presented in Table 3.1. The average RMS surface roughness of the 10 nm GST plus 10 nm ITO section is, in normal conditions, around 2.4 nm, which is small enough to avoid light scattering [201].

Table 3.1: GST sputtering parameters

	GST	**ITO**
Base pressure (mbar)	2×10^{-7}	2×10^{-7}
Working pressure (mbar)	6.5×10^{-4}	6.5×10^{-4}
Power (W)	30	30
Atmosphere (sccm Ar)	100	100
Voltage (V)	420	400
Target (inches)	2.5	3
Temperature (^{o}C)	21	21
Time (min)	2.67	6.63
Thickness (nm)	10	10

Chapter 4

Experimental setup

This chapter introduces the experimental setup that was built to perform static transmission measurements and dynamic pump-probe experiments on integrated photonic circuits. The main components, their characterisation, and their function within the setup are detailed here. In particular, the system is optimised for all-optical switching and read-out of phase-change photonic memories to carry out the measurements presented in Chapter 5. Lastly, an additional electrical extension that allows for integrated optoelectronic measurement is described as a feature for future experiments outside the scope of this Thesis.

4.1 Integrated all-optical setup outline

The construction of the integrated all-photonic setup, as part of this DPhil project, consisted of two different stages, which, at the same time, allowed for two types of measurements. The transmission setup described in Sec. 4.1.1, was afterwards embedded in the upgraded system depicted in Sec. 4.1.2. This setup has been in constant development

towards having more functionalities and degrees of freedom. The aim has been to obtain a system in which intricate studies of advanced optical materials integrated to photonic circuits can be carried out.

4.1.1 Static transmission characterisation

The first step towards putting together a complete system for fully optical control, consisted of building the setup sketched in Fig. 4.1. This setup allowed for the first continuous-wave (CW) laser transmission measurements in integrated photonic circuits, which were enough to characterise the attenuation by phase-change materials if switched using external means (e.g. by annealing) [27].

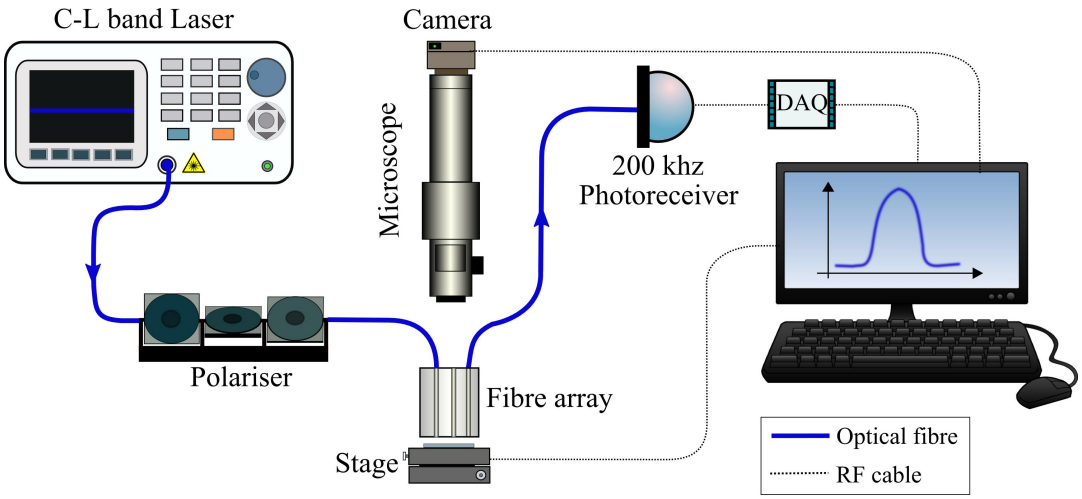

Figure 4.1: Diagram of the experimental setup for transmission characterisation. DAQ stands for data acquisition system

The setup, in short, consists of a CW laser-sourced light that is polarised and coupled into the photonic devices by aligning one optical fibre in a micro-spaced fibre-array with an on-chip Bragg grating (See stage in Sec. 4.5). The light at the output of the fibre is not collimated; however, the fibre is placed as close as possible to avoid losing light from beam divergence. The transmitted light is collected with another fibre (in the array) directly from a second grating, which is connected to the first one through photonic

circuitry where the active of passive components are contained. The collected light is sent to a photoreceiver using an optical fibre, which subsequently sends the information to the computer using a data acquisition (DAQ) unit. An external CCD camera coupled to a microscope is employed to monitor the position of the devices and align the fibre array to the gratings. The setup diagram is shown in Fig. 4.1.

4.1.2 Pump-probe: optical switching and real-time read-out

The acquisition of specialised equipment enabled the upgrade of the setup to that sketched in Fig. 4.2. The new system featured dynamic measurements and better data acquisition, thus allowing the study of time-resolved characteristics by means of a pump-probe technique. In particular, this setup is used to switch and read-out of on-chip phase-change photonic memories, as discussed in Ch. 5.

This setup involves two tunable CW infra-red lasers operating in the $1530 - 1565\,nm$ (C-band) and/or $1565 - 1625\,nm$ (L-band) wavelength bands, broadly used in fibre-optic telecommunications. One source is required for the pump signal (green trace in Fig. 4.2) to excite the material —here, to switch GST— and, another for the low-power probe light to measure device transmission (blue trace). In this setup, the transmission was continuously measured using the CW signal generated by the probe laser, which was linearly polarised before the device. The pump signal is pulsed by means of an electro-optical modulator (EOM) coupled to an electrical pulse generator. Such an EOM, as explained in Sec. 4.3.1, converts the CW optical input from the laser into a customised optical output, shaped by the electrical input signal. The pulse is subsequently power amplified by using a low-noise erbium-doped fibre amplifier (EDFA) coupled to a pass-band filter to reduce noise associated with parasitic wavelengths (see Sec. 4.3.1). With this implementation, the pulse wavelength, length, shape and power can be controlled, enabling pulses as short as $10\,ns$ (limited by the pulse generator) with peak powers up to $275\,mW$. Moreover,

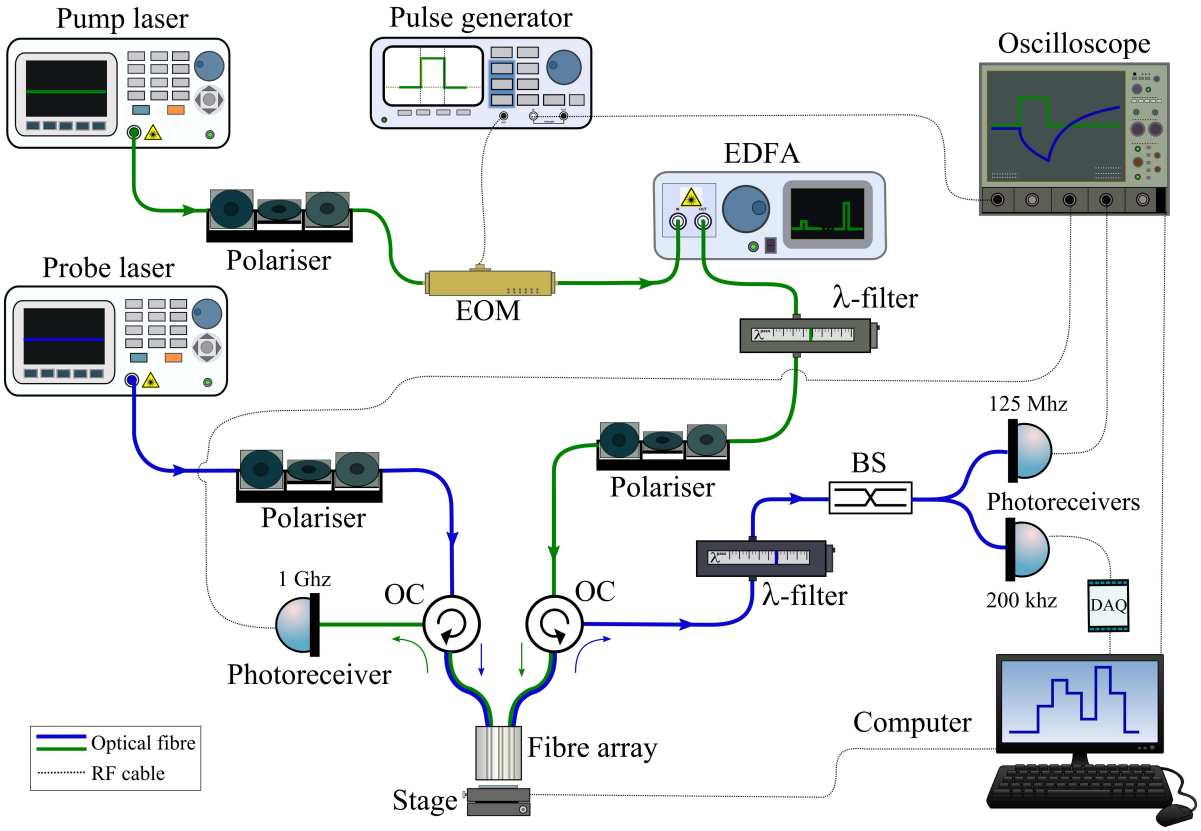

Figure 4.2: Diagram of the experimental pump-probe setup. Here, EOM stands for electro-optical modulator, BS for Beam splitter, OC for Optical circulator, EDFA for erbium-doped fibre amplifier and DAQ for data acquisition unit. λ-filter represents a wavelength-tunable filter.

when polarisation-sensitive elements are found in the setup, as in the case of the EOM and the on-chip Bragg-grating couplers, fibre polarisers are added to the light lines.

Both pump and probe signals are coupled into the integrated optical chip by focusing onto grating couplers via an optical fiber array (see 3D-rendered illustration in Fig. 4.5). The gratings are optimised for operation in the telecommunications C and L-bands. The chip, in turn, is mounted on a 3-axis piezoelectric-controlled stage for convenient automated alignment. Fast photodetectors are used to record real-time pump and probe traces, with high resolution, after propagation through the photonic circuit. The photodetector response is then measured with a fast sampling oscilloscope. A further low-noise sensitive photodetector is used to monitor the transmission of the probe signal through

the photonic circuit at all times.

The bidirectional scheme in Fig. 4.5 (blue and green traces in opposite directions) is used extract the changes in transmission from the probe signal without interfering with the pump-pulse signal, and vice-versa. In such a scheme, the pump and probe beams are coupled to different gratings and co-propagate inside the circuit following opposite directions. The input port for one signal is therefore the output port for the other. This is achieved experimentally with a set of two optical circulators which direct the light coming from the laser sources onto the chip and simultaneously, the collected light, at the same port, onto the detectors. In addition, two different wavelengths can be used to suppress the influence of back-reflections with an optical band-pass filter. However, this is not a limiting factor and only one laser source, by means of a beam splitter, can act as both the pump and the probe light source at the extra cost of overlapping measured signals (in real-time measurements only).

4.2 Integrated optoelectronic setup outline

Another system upgrade added real-time electrical measurements to the already all-photonic setup. This system was built to explore a mixed-mode operation of integrated optoelectronic devices based on phase-change materials. In this type of devices, the phase switching and the read out could be realised either fully photonically, fully electrically, or in a combination of both. This is, however, and ongoing project that started as part of this DPhil project but has not shown results so far, despite of the first samples being fabricated and measured. The main challenge is the complex nanofabrication, which requires further optimisation before obtaining functional devices. A reduced sketch of the complete setup used in these measurements—the optical pump-probe part is not shown for the sake of clarity—is sketched in Fig. 4.3.

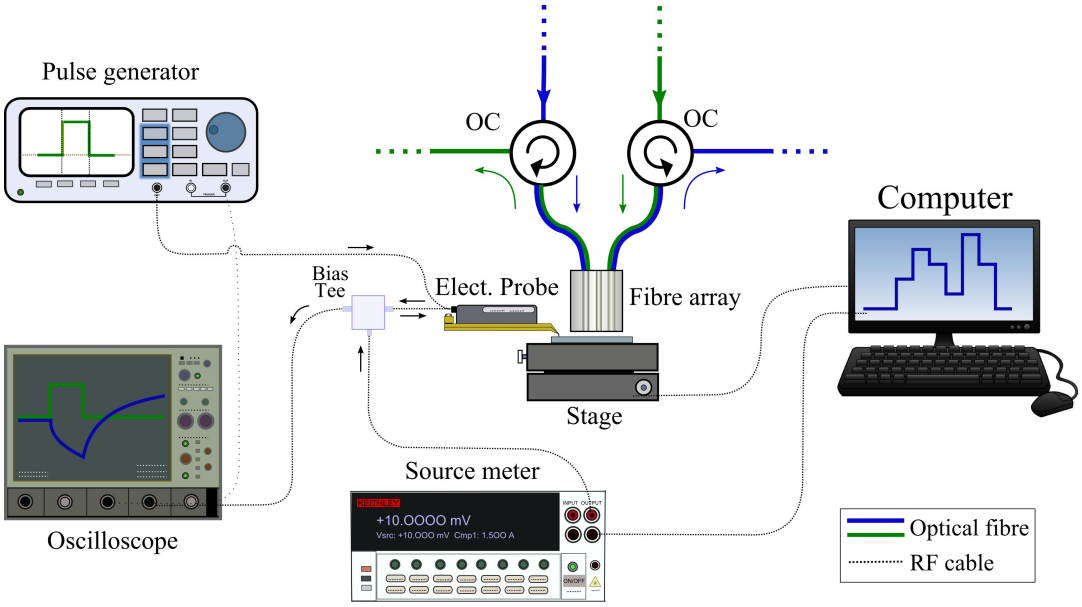

Figure 4.3: Diagram of the experimental optoelectronic setup. OC stands for optical circulator. The discontinued fibres in dotted lines indicate the coupling to the pump-probe setup in Fig. 4.2.

The new addition consisted of introducing micro-scaled probes to connect electrical test equipment, such as pulse generator and source meter, to integrated on-chip electrodes. This being so, electrical pulses can be coupled to the chip and, in the case of PCM-based devices where electrodes are connected to the photonic circuits, used to switch (here *Write/Erase*) while reading optically. Also, electrical read-out—that is, changes in resistance/conductance—is made possible by using the source meter when optical switching is induced. Moreover, by using a bias-tee, the direct-current (DC) component from the source meter is separated from the fast signal changes from either electrical or optical pulse excitations, thus allowing for real-time electrical-signal measurements. Therefore, the whole system allows for four kinds of measurement, referring in order to switching and read-out mechanisms, photonic-photonic, photonic-electrical, electrical-photonic, electrical-electrical, at the same time that real-time optical and electrical response are monitored.

4.3 Actual setup

A picture of the actual setup is shown in Fig. 4.4. This system integrates the on-chip all-optical and optoelectronic schemes outlined in the previous Sec. 4.2 and 4.1.2. The description of the components, such as the stage and the microscope, are will be described in the next section.

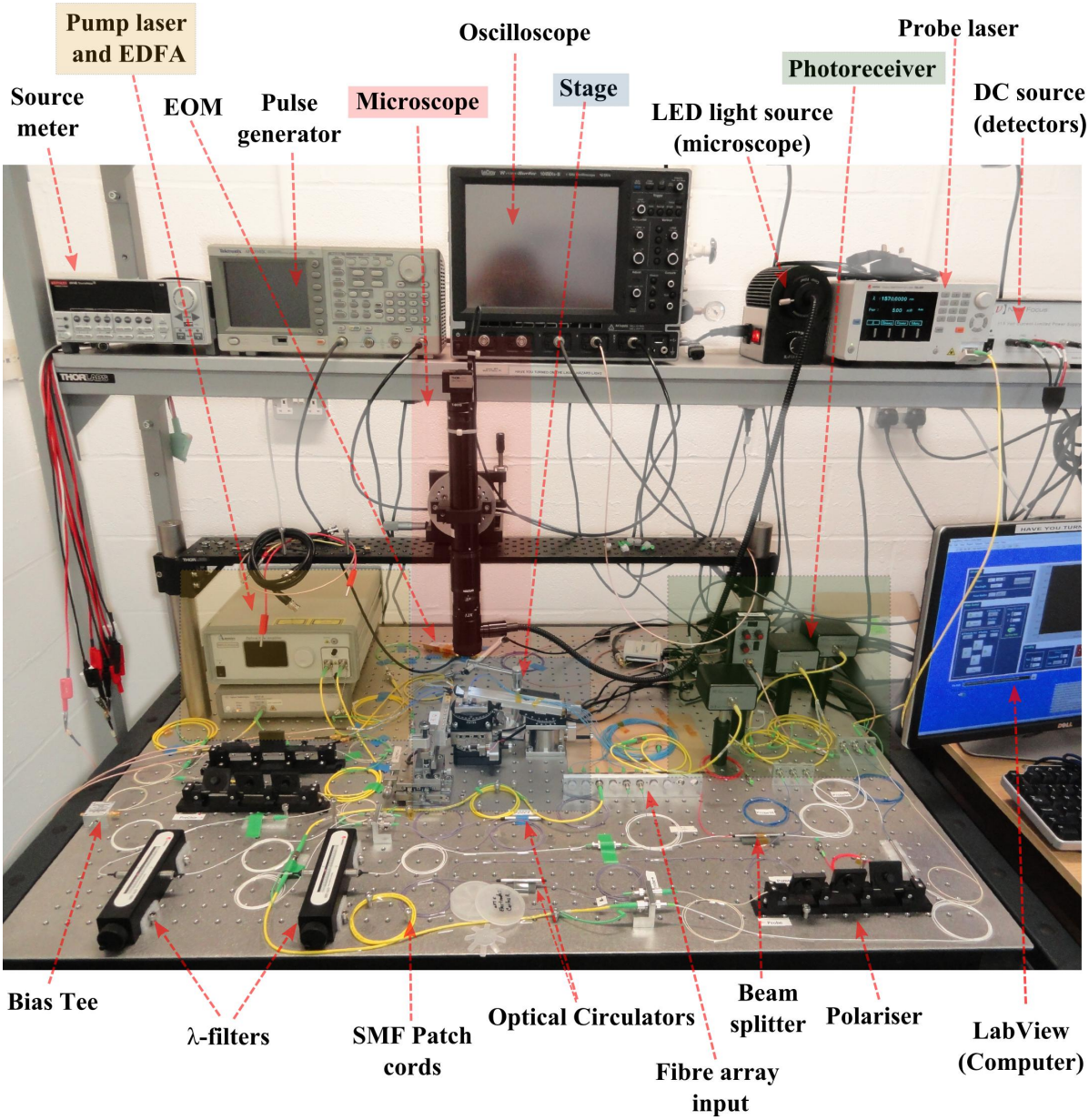

Figure 4.4: Photo of the experimental setup.

4.3.1 Mechanical and optical components

The setup in Fig. 4.4 includes all the optical and electronic instruments shown in the sketches Fig. 4.2 and 4.3. It includes also customised parts and devices to put together the stage and the microscope. These instruments, their description, reference, and most relevant specifications are listed below.

Optical fibre and patch cords

Standard single-mode optical fibres (SMF) operating in the wavelength range $1260 - 1625\,nm$, known by the reference SMF-28e, were used to optically integrate the different optical components. In particular, patch cords with a fibre-optic connector (FC) with a threaded body and with polished coupling (PC) and 8°-angled polished coupling (APC) were bought from Thorlabs with the references P1-SMF28E-FC-1 and P3-SMF28E-FC, respectively. APC connectors redirect the reflections outwards thanks to the tilted surface, thus avoiding parasitic back-reflections that could damage the equipment. For this reason, the setup employed FC/APC-terminated fibres and connectors, except in devices such as detectors and electro-optical modulators which use PC connectors. Matting sleeves for both kind of fibres were also bought from Thorlabs.

Fibres were constantly inspected in order to keep the couplers clean and thus avoid damage due to scattering, back reflections, and optical losses. To do so, a fibre microscope compatible with FC/APC (Thorlabs, FS200) was used to inspect and a fibre cleaner (Thorlabs, FCC7020) used to remove any dirt on the surface of the connector.

C-L band Lasers

Low-noise tunable laser sources in the telecommunication wavelengths are required to measure light transmission of the photonic devices. In particular, a TSL-550 tunable laser

by Santec was employed, which is controlled remotely via LabView. This laser features $1500 - 1630\,nm$ (C+L bands) wavelength range, non-polarised single-mode output with a FC/APC connector, up to $13\,dBm$ output power, $90\,dB/0.1\,nm$ signal-to-noise ratio, $\pm 20\,pm$ wavelength accuracy, and, very importantly, fast wavelength-sweep mode. The pump laser consists of another tunable laser, but only in the L-band. A laser model N7711A-201 from Agilent technologies was used for this source. This laser, much simpler than the TSL-550, features wavelength tunability without quick sweep (which is not required for pump pulses) in the range $1570 - 1608\,nm$ with $\pm 0.8\,pm$ wavelength accuracy, power output up to $15.5\,dBm$ and $60\,dB/0.1\,nm$ SNR. Both lasers are controlled remotely from a central computing unit running LabView.

Stage

The optical and electrical signals come together at the sample stage shown in Fig. 4.5 where the chip containing photonic circuits is finally tested. Here, an optical fibre couples light into the chip and collects the out-coupled light. To do so, the fibres in the array are aligned to the Bragg gratings on the photonic circuits with 2D precise positioning, on the stage holding the sample (here XY), providing two linear stages stacked perpendicularly. The fibre array, on the other hand, is held on top of the sample by a separate customised aliminium piece that is machined in such a way that the fibre can be brought as close as possible to the gratings, thus guaranteeing maximum coupling efficiency. This is achieved by employing a third linear and vertical (here Z) stage with a goniometer mounted on top to set the 8° required for the incident light. The stages are moved with sub-100nm precision by picomotor actuators controlled remotely from the computer via *LabView*.

The electrical probe is mounted on another separate X,Y and Z stage with picomotor control only in the Z direction, which controls the approach to the sample. Another aluminium customised piece was machined to hold this probe directly on top of the

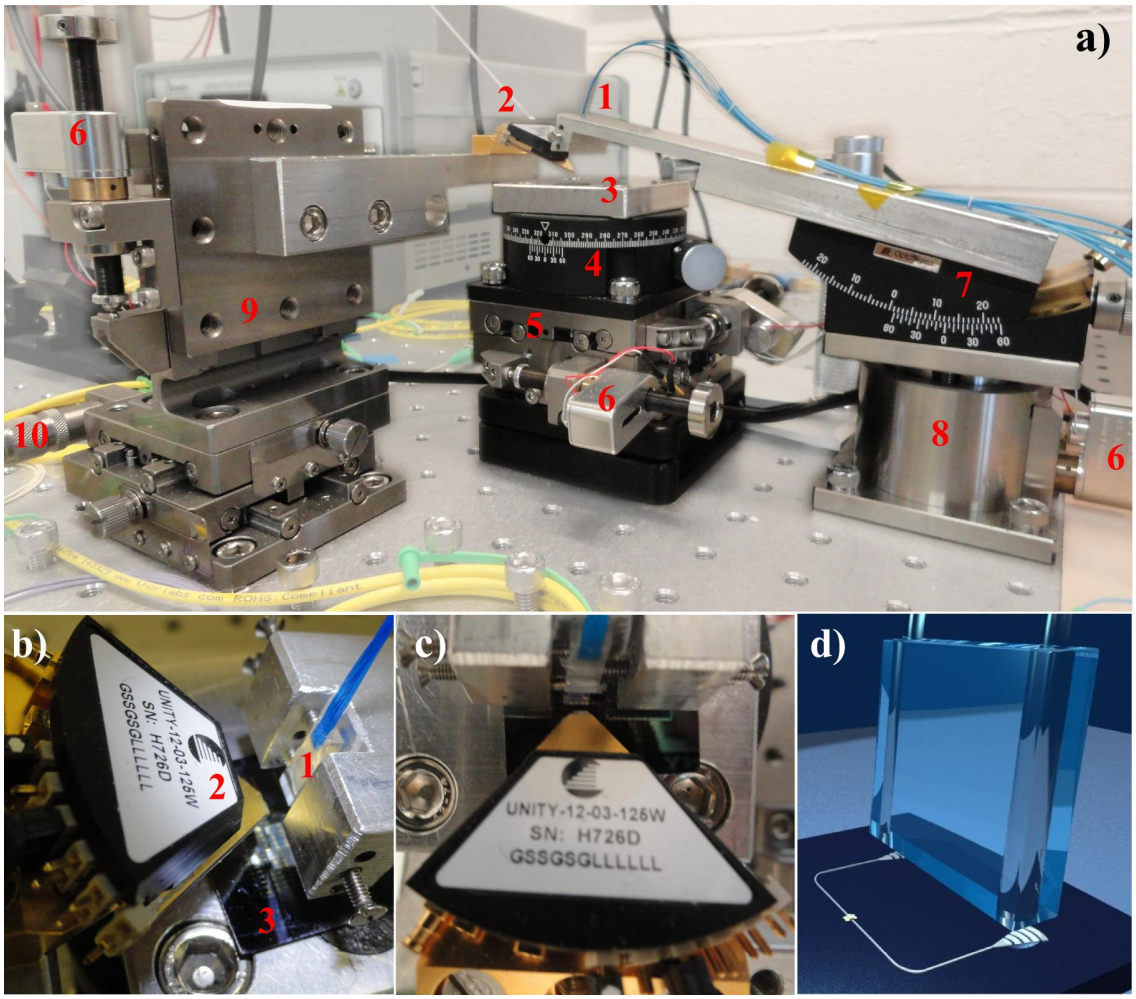

Figure 4.5: Main stage for integrated optoeletronic measurements. a) Components of the stage. 1: Fibre array and holder. 2: Electrical probe. 3: Sample holder. 4: Manual rotation stage. 5: Linear stages for X and Y in-plane positioning. 6: Picomotor actuators for the linear stages. 7: Goniometer. 8: Z-stage for the fibre array. 9: X,Y and Z stage system for the probe. 10: manual positioning screws. b) Lateral zoom-in to the sample area featuring the fibre array, electrical probe and sample holder (same numbers as for a). c) Top view of b). d) 3D rendered image illustrating the way in which the fibre array is aligned to the Bragg gratings in the photonic devices.

sample. The sample stage is monitored by using a CCD camera coupled to a microscope placed directly on top; this allows the correct positioning of the on-chip devices.

Fibre array

Customised fibre arrays with the 1×8 and 4×4 configurations shown in Fig. 4.6 were obtained from the company *PLC Connections*. They consist of arrays of SMF-28 fibres

with FC/APC connectors on one side and, on the other side, bare fibres featuring 2D micro-scaled configurations with a $250 \pm 2\,\mu m$ pitch. The fibre array is used to couple light into the photonic circuits and collect the out-coupling light by aligning properly to the Bragg gratings on the devices, as shown in Fig. 4.5d. Given that the light coupling using gratings is optimised for incidence under an angle of 8° (same as for FC/APC connectors), and that the array needs to be placed as close as possible to the chip, the array was polished to the same angle, thus facing parallel to the sample. Different fibre configurations within the array allow to fabricate devices where gratings are placed anywhere in two dimensional structures, as long as their separation is a multiple of the fibres pitch, keeping in mind the total size of the array.

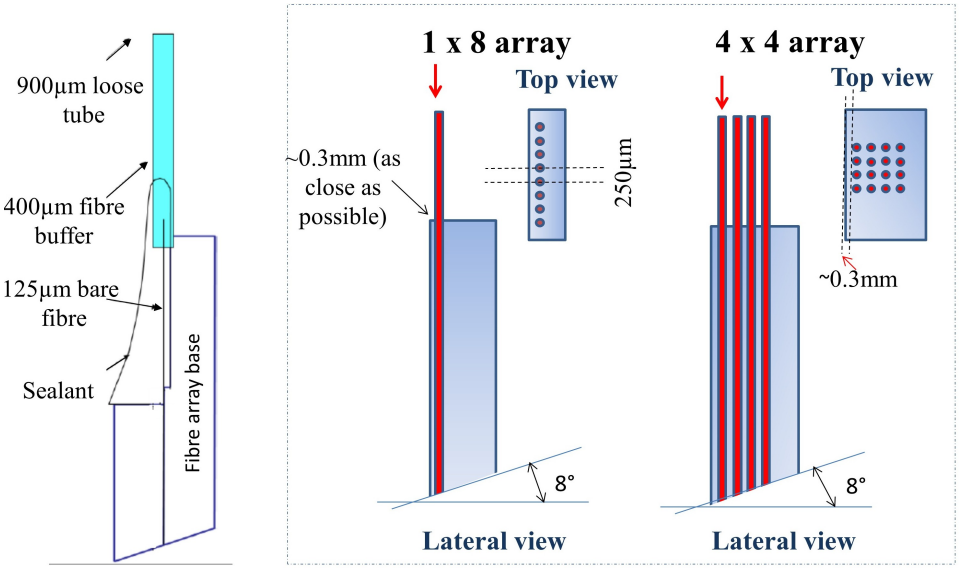

Figure 4.6: Sketches of (*left*) the final design of the head of the array featuring the different parts of it (from the manufacturer) and (*inside the box*) simplified 1×8 and 4×4 arrays

Picomotor actuators

Four vacuum-compatible picomotor actuators with 1 inch travel manufactured by *New Focus* and sold by *NewPort* (model 8301-V) were used to fine-position linear stages in the optical setup. These actuators possess better than $30\,nm$ resolution with minimal backlash, and can exert up to $22\,N$ force. Moreover, they offer long-term stability

and the ability to hold their position with no power applied, ideal for the set-and-hold measurements realised on integrated photonics. The four picomotors (three of which are labeled with number 6 in Fig. 4.5) were controlled via *LabView* by using a four-axis controller/driver (*Newport*, model 8742) to enable computer connection.

Polariser

The coupling efficiency into the photonic circuits through Bragg gratings, and to optical devices such electro-optical modulators, depends strongly on the polarisation of the incoming light. Moreover, the photonic circuits are optimised for single-mode TE or TM modes (See Sec. 3.2.3), thus requiring linearly polarised light. However, an optical fibre setup presents large polarisation fluctuations because of fibre bending and fibre-to-fibre connections. In addition, fibre-coupled light sources are predominantly not polarised. Therefore, fibre-polarisation controllers have to be added to the experimental setup. The most common device for this purpose is a 2 or 3-paddle polariser, shown in Fig. 4.7, which adjusts the polarisation by (manually) rotating three wave plates in the order: $\lambda/2$, $\lambda/4$ and $\lambda/2$. The rotation, in turn, applies stress on the fibre thus inducing birefringence and changing the fast-axis direction (which is in the plane of the spool) [207]. Consequently, by controlling the fast axis and having the three half/quarter wave plates, any conversion between linear, circular, and elliptical polarisation states is achievable.

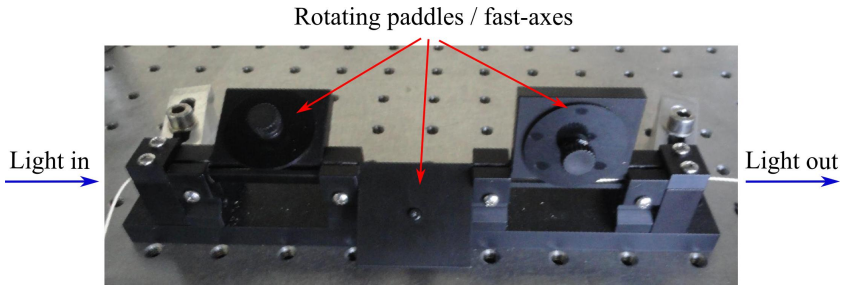

Figure 4.7: 3-paddle fibre polariser.

In the experimental setup, sketched in Fig. 4.1, Thorlabs FPC030 polarisers with FC/APC

connectors were used. For each device, the polarisation was adjusted manually by finding the plate combination that offers the maximum transmission value at the photoreceiver.

Photodetectors

Different photodetectors were employed to measure the different light signals. Their characteristics have to be chosen carefully as this will represent whether data is obtained or lost, especially when dealing with strong attenuation, as in GST sections on top of Si_3N_4 waveguides, and fast responses. Three different photoreceivers were employed for this setup, in particular. These were:

- Prolonged transmission measurements of the devices before and after switching require photodetectors featuring high sensitivity and low-noise, rather than fast detection. For this reason, *2011-FC-M* fibre-coupled photoreceivers from *Newport*, operating in the $900 - 1700\,nm$ range, were employed. These detectors offer an adjustable gain within a five orders of magnitude range, tunable cutoff frequency from DC up to 200 kHz, FC/PC optical input and a SMA electrical output. This detector is connected to a computer using a *National Instruments*® data acquisition unit (DAQ) USB device (NI USB-6008) and manipulated via LabView.

- Real-time measurements, on the other hand, require fast response InGaAs PIN-photodiodes as receivers. To measure the pump pulse transmitted after the device, a *NewFocus* detector (sold by *Newport* by the references *1811-FC-AC*) was integrated to the setup. This detector offers a 30 kHz-1 GHz bandwidth in the $900 - 1700\,nm$ wavelength range. Moreover, it includes an AC filter that allows for measuring the signal coming only from the pulse and, based on the scheme in Fig. 4.2, filters out the reflection from the probe. As for the thermo-optical response measurements from the probe signal, another InGaAs PIN-photodiode by *NewFocus* (reference *1611-FC* from *Newport*) was used, with a bandwidth from DC up to 125 MHz also in the $900 - 1700\,nm$ wavelength range. With a maximum conversion gain

of $40\,V/mW$, this detector is not as fast but it overtakes the total sensitivity of the 1 GHz detector ($0.7\,V/mW$), which is the reason why this was used to measure the real-time transmission changes as they are weaker signals. However, given that $10\,ns$ is the length of the shortest pulse used in this Thesis, two 125 MHz detectors could have also worked. These two detectors are powered by a $\pm 15\,V$ DC power supply provided by *NewFocus* (model 0901).

Microscope and CCD camera

A microscope with a long working distance was placed on top of the stage to monitor, in real time, the position of the sample with respect to the fibre array and the electrical probe, as shown in the red highlighted area in Fig. 4.5. For doing so, on an elevated breadboard, a *Navitar* 12× Ultazoom microscope with co-axial port, $3\,mm$ fine focus and a zoom range from 0.58× to 7× was employed. This microscope was furthermore extended using a 5× adapter and connected to a $24\,W$ white LED light source connected via a flexible light guide for illumination. The microscope image was collected with a 1280×1024 pixels CMOS camera (Thorlabs DCC1240C) and subsequently recorded on the computer.

The microscope and camera hang on a customised aluminium piece that allows different angular positions. This piece works also as a clamp to mount the system on a XYZ manually-controlled stage with $2''$ travel linear axes.

Optical circulator

An optical circulator is a device that allows light to travel in only one direction among three different ports. Signals entering to port 1 and port 2 will exit port 2 and port 3, respectively, with minimal loss. Light entering port 2 experiences a large amount of loss at port 1, and light entering port 3 experiences a large amount of loss at ports 2 and 1.

Optical circulators are non-reciprocal devices, i.e. any change in the properties of the light caused by passing through the device are not reversed by travelling in the opposite direction.

This device, from Thorlabs (model 60153APC), was introduced to the setup in Fig. 4.4 in order to separate light coupling into and out of the photonic circuits. In particular, when carrying out counter-propagating pump-probe measurements, optical circulators help to separate pump input and probe output from one channel in the fibre array, and probe input and probe output at the other end of the devices (see setup diagram in Fig. 4.2). This device operates in the whole C+L band, uses SMF-28e fibres with FC/APC connectors, and offers selectivity (i.e. high directionality) between ports of at least $40\,dB$ between the ports $2 \rightarrow 1$ and $3 \rightarrow 2$, and at least $50\,dB$ for $1 \rightarrow 3$.

Beam-splitter

Beam splitters are devices capable of splitting one beam into two with different weights such as $50:50$ or $90:10$ (i.e. one port takes 90% of the light and the other one 10%). These devices are used in the pump-probe setup to split the output of the probe signal into two beams: one for a fast real-time characterisation, and the second, for long-term but sensitive measurements. A beam splitter is also required in case both the pump and the probe are generated by only one laser. These passive components were bought from Thorlabs having the references TW1550R5A2 ($50:50$) and TW1550R2A2 ($90:10$) for $1550 \pm 100\,nm$ wavelengths, with SMF-28e+ fibres and FC/APC connectors. The insertion loss is as low as $\leq 0.7\,dB$.

Tunable optical bandpass filter

The optical bandpass filter (denoted by λ-filter in Fig. 4.4) is a narrow band-pass device that introduces high losses to those wavelengths outside the band and high transmission to

that being manually selected. This device is useful when doing pump-probe experiments with two different wavelengths and which need to be separated for the sake of a clear measurement on the photoreceivers (which are wavelength insensitive). In particular, an *OTF-320* tunable filter fabricated by *Santec Corp.* in the C+L band ($1530 - 1610\,nm$) was used in the setup featuring SMF-28e+ fibres with FC/APC connectors and $0.3\,nm$ bandwidth.

Electro-optical modulator

An electro-optical modulator (EOM) is an active device that modulates a CW optical signal to that given by an arbitrary electrical signal. This is done by modulating the optical path of one of the arms of a Mach-Zehnder interferometer (which is inside the EOM case) by using the piezo-electric property of crystalline lithium niobate [208]. Constructive and destructive interference is achieved as a function of the applied voltage that stretches or compresses the crystal, which in turn modulates the optical output.

In the setup shown in Fig. 4.4, a 2623CS EOM by *Lucent Technologies®* (now *Alcatel-Lucent®*) with insertion losses around $3.7\,dB$ was employed. This model, for C+L-band modulation, exhibits a minimum bandwidth of 8GHz, and operates for DC signal and both CW and pulsed lasers. The EOM was characterised using $10\,\mu s$ pulses and the 200 kHz detector (See Sec. 4.3.1). In Fig. 4.8, the maximum output power was measured for two different wavelengths, while monitoring on the oscilloscope that the optical pulse shape was the same as the electrical signal. The electrical pulse minimum (voltage that blocks most of the light) and maximum (voltage that allows maximum transmission) determines the optical modulation, which in turn depends on the input wavelength. In particular, it was found that for $\lambda = 1593\,nm$ the electrical pulse given by voltages $-1.1\,V$ and $0.58\,V$ gave a good modulation (i.e. keeps the pulse shape and optimises optical output power) with 28.1% transmission. Also, for $\lambda = 1580\,nm$, the voltages $-0.9\,V$ and

$0.61\,V$ were found to work better with 28.6% transmission. The lower voltages are crucial to avoid unwanted light coupling into the device, especially if amplified afterwards, when not pulsing the EOM; therefore, it has to be biased at all times at such lower voltages until a pulse is triggered.

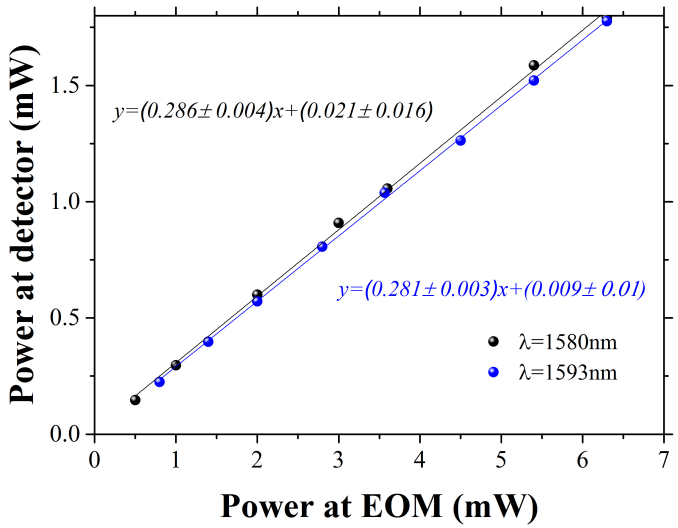

Figure 4.8: Electro-optical characterisation using $10\mu s$ pulses. Black curve for $\lambda = 1580nm$ with pulse parameters $V_{min} = -0.9\,V$ and $V_{max} = 0.61\,V$, and $V_{min} = -1.1\,V$ and $V_{max} = 0.58\,V$ for $\lambda = 1580\,nm$.

When using shorter pulses, i.e. $\leq 100\,ns$ around $\lambda = 1580\,nm$, it was found that the minimum voltage was the same to block the light, but there was no restriction in the maximum voltage to achieve a pulse. However, when using pulses with a maximum voltage $< 0.61\,V$, as for long pulses, a sub-$100\,ns$ pulse is deformed with a non-uniform energy plateau on top. This is caused by the difference in extinction ratio of the EOM when operated in DC ($\approx 27\,dB$) and frequencies approaching 1Ghz ($\approx 13\,dB$), which is the case for sub-$100\,ns$ pulses. To circumvent this issue, electrical pulses between $1\,V$ and $3\,V$ were found to preserve the shape, with $3\,V$ having the maximum energy transmission, as shown below for the EDFA. This broad range of $2\,V$ for the modulation to work properly was used to modulate the power of the pump pulse together with the EDFA.

Erbium-doped fibre amplifier

Erbium-doped fibre amplifiers (EDFA) are based on fibres, incorporated directly into an optical network, containing erbium ions. The fibre is pumped with a $\lambda = 980\,nm$ light source to excite the erbium ions and thus, add gain to the material. The amplification takes place when the optical input (around $1550\,nm$) undergoes stimulated emission when passing through the excited erbium-doped fibre, thus converting all the gain into emission of identical photons to those at the input. Erbium-doped fibre amplifiers are common and widely used in long-range optical fibre communications, given that they can amplify light in the C+L wavelength region, known as the telecommunications bands, where fibres have their loss minimum.

Regarding the phase-change photonic memory in Ch. 5, pulse power amplification is required in order to reach energies high enough to heat up GST over the crystallisation temperature and to melt-quench it to amorphise afterwards. Given that the light sources used in this setup emit up to $13\,dBm$ and $15.5\,dBm$, and that the coupling efficiency of one Bragg grating is not higher than 30%, it was mandatory to amplify the pulses by employing an EDFA, as shown in the diagram in Fig. 4.2. For this reason, an *Amonics* EDFA model *AEDFA-CL-PS-23-B-FA* was added to the setup, and was optimised to amplify pulses in the range $1 - 100\,ns$ for input powers lower than $3\,mW$. It features output powers (in CW) of $\sim 24\,dBm$ (i.e $250mW$) for $1\,dBm$ ($1\,mW$) inputs, as shown in Fig. 4.9a.

As in the case of the EOM, the EDFA had to be characterised before coupling to the experimental setup. Given that these units are designed to amplify CW signals, significant differences were found between the amplification curves provided by the manufacturer (for CW), in Fig. 4.9a, and the actual output when using $sub - 100\,ns$ pulses, shown in Fig. 4.9b-c. From amplifications up to $310\,mW$ ($\approx 25\,dB$) in CW, it was found that

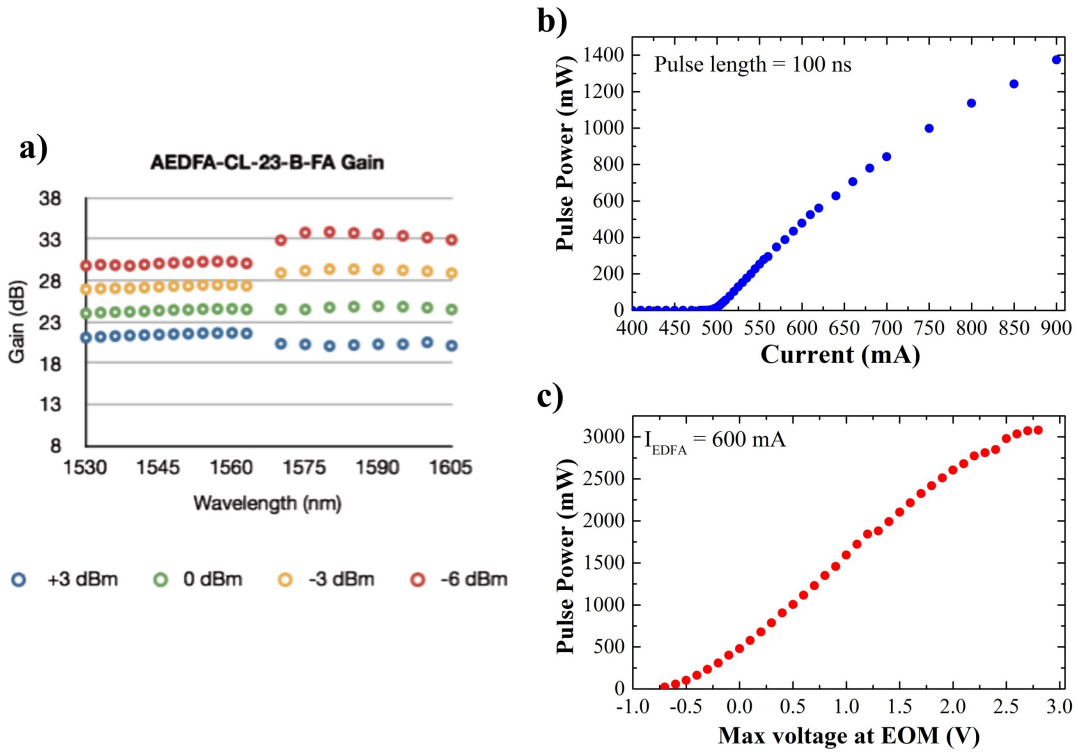

Figure 4.9: Erbium-doped fibre amplifier characterisation. a) Amplification curves provided by the manufacturer under CW operation. b) amplification as a function of EDFA current for $100ns$ pulses when biasing the EOM between $-1.1\,V$ and $0\,V$. c) Pulse power amplification as a function of the EOM voltage by using $100ns$ pulses and fixing the EDFA current to $600\,mA$.

pulses with powers even larger than $3\,W$ are achievable. When a pulse enters the fibre with excited ions, it takes all the gain available as there are no other competing signals and therefore, at the output, it is more powerful. The gain in the EDFA recovers quickly as it is not taken by further signals and remains at its maximum until the next pulse comes. In the case of a continuous wave, the gain is constantly taken by the signal and the output power is determined by the dynamics of the excitation and stimulated emission, which allows for a much lower output power. In particular, it was found that by increasing the current at the amplifier (which runs from 0 to $1200\,mA$) and tuning the EOM bias voltage, any pulse power between 0 and $3.1\,W$ can be obtained. This is shown in Fig. 4.9b for a fixed EOM voltage and variable EDFA current, and in Fig. 4.9 for variable EOM voltage and fixed EDFA current. These values are taken into account when

running experiments to estimate the energy of the pulse inside the photonic circuits.

The fact that electrons are excited inside the erbium-doped fibre means that besides stimulated emission, spontaneous emission can also take place adding white noise over the whole C+L band spectrum. This noise, which can also be amplified inside the same EDFA, is a source of high-energy noise (low power but over a broad spectrum which sum up enough energy altogether) that may induce phase-switching in the memories. To avoid this problem, an optical bandpass filter is added at the output of the EDFA, as shown in Fig. 4.2, thus letting through the exact wavelength of the amplified pulse and absorbing the noise spread over the rest of the C+L spectrum.

4.3.2 Electrical equipment

This subsection describes the purely electrical equipment devoted to capture optical signals that are converted into digital ones, or to source/monitor the micro-structured electrical probe for optoelectronic measurements. Small devices such as Bias-Tee (model *ZFBT-4R2GW+*), amplifiers (model *ZFL-1000LN+*) and connector (models *SF-SF50+,SM-BF50+, SM-BM50+, SF-BM50+*) were obtained from the company *Mini-Circuits*.

Electrical probe

The customised electrical probe shown from different angles in Fig. 4.5 was obtained from *CascadeMicrotech*. This probe features 12 tungsten tips with a 125 μm pitch and the following configuration (each letter corresponding to one tip in the given order): GSSGSGLLLLLL, where G stands for ground (all connected to a common ground), S for RF signal up to 20 GHz, and L for logical signal up to 500 MHz. This probe is used to bring electrical pulses and DC signals to the on-chip electrodes of optoelectronic devices.

Pulse generator

Electrical pulses were generated by means of a *Tektronics* AFG3102 arbitrary/function generator, which in turn modulates the optical signal through the EOM (See Sec. 4.3.1). This device, shown also in Fig. 4.4, features 100 MHz effective frequency out, 50 Ω load and output impedance, two output channels as well as input and output trigger and LabView interface via GPIB connectors. An *HP 8131A* pulse generator was also used for the experiments in Ch. 5; this device offers 500 MHz of repetition rate and pulse widths between 0.50 ns and 99.9 ms.

Oscilloscope

A *WaveSurfer MXs-B* oscilloscope by *Teledyne LeCroy* featuring a bandwidth of 1 GHz and easy data processing and storage was used for this setup, as shown in Fig. 4.5. This device is able to measure signals from four different channels at up to 10 GS/s. This oscilloscope, in particular, is used to capture the signal from the 1 GHz and 125 MHz detectors measuring respectively the transmitted pump pulse and the real-time fluctuations of the probe in the experiments shown in Sec. 5.

Source meter

Single-channel voltage/current sourcing and measurements through the electrical probe were done by using a 2614B source meter unit by *Keithley*® (now part of *Tektronix*®). This device allows for simultaneously sourcing and measuring both voltage and current with high-speed technology, which is over 190% faster than traditional computer-to-instrument communication techniques. It features 60 W power output (30 W per channel), four quadrant source/measure with 61/2 digit resolution, 1.5 A DC, 100 fA−10 A current range, 200 V maximum voltage, and 100 nV minimum.

Chapter 5

Phase-change photonic memory

Phase-change materials placed onto photonic circuits provide a novel way to realise integrated tunable optical components. Relying on the enormous refractive-index contrast between the amorphous and the crystalline states, such materials are promising candidates for on-chip memories which are switched and accessed optically, thus bridging a gap towards all-photonic chip-scale information processing. To this end, this chapter presents the experimental demonstration and switching-dynamics modelling of the first non-volatile phase-change photonic memory based on $Ge_2Sb_2Te_5$. The memory operation is demonstrated using telecommunication wavelengths in a pump-probe experimental setup. In addition, up to 3-bit multi-level storage is proven in a single memory cell with intra-level transitions possible. Finally, this chapter offers a study on the limits and performance of these types of photonic memories.

5.1 The device

Integrated photonic circuits were used as a platform to demonstrate all-photonic near-field switching of phase-change materials deposited directly on top. Given the large optical absorption of PCMs, such as $Ge_2Sb_2Te_5$, near-field coupling emerges as a promising solution for optical applications: light is attenuated without directly blocking the transmission. The alternative approach, having the PCM embedded inside the waveguide, would provide a much larger attenuation, but would drastically reduce the optically transmitted signals. Moreover, near-field attenuation, with PCMs deposited on top of the circuits, offers a much simplified nanofabrication process than embedding other materials in the circuit.

Balanced-splitter devices were chosen as the photonic circuit architecture to study the switching dynamics and subsequently demonstrate the phase-change photonic memory. These devices offer two identical optical paths coupled to the same grating placed in the centre, as shown in Fig. 5.1a, which, in turn, allows for optimum comparison between waveguides with and without a passive or active component, such as PCMs. In particular, half-etched rib waveguides in $330\,nm$ Si_3N_4/ $3300\,nm$ SiO_2 substrates with a width of $1.3\,\mu m$ were fabricated using the process described in Sec. 3.3. Such waveguides are designed to propagate TE modes with C- and L-band wavelengths. Bragg-gratings were employed to couple light in (through the central port) and out (on either side ports) centred at the wavelength $\lambda_c \approx 1580\,nm$. On top of a straight section of the waveguide, on one of the arms, $10\,nm$ thick GST strips with a $10\,nm$ thick protective ITO—to avoid oxidation of the GST—were sputtered. The other arm of the balanced splitter was used as reference channel for comparison purposes. The GST strips completely covered the waveguide, including the sidewalls, with lengths (along the waveguide axis) of $0.5\,\mu m$, $1\,\mu m$, $5\,\mu m$, $10\,\mu m$, and $20\,\mu m$ all fabricated. However, mainly devices with $1\,\mu m$ and

5 μm are considered in the following experiments given that they provided an optimum trade-off between transmission signal and switching contrast, as will be explained in Sec. 5.4.3.

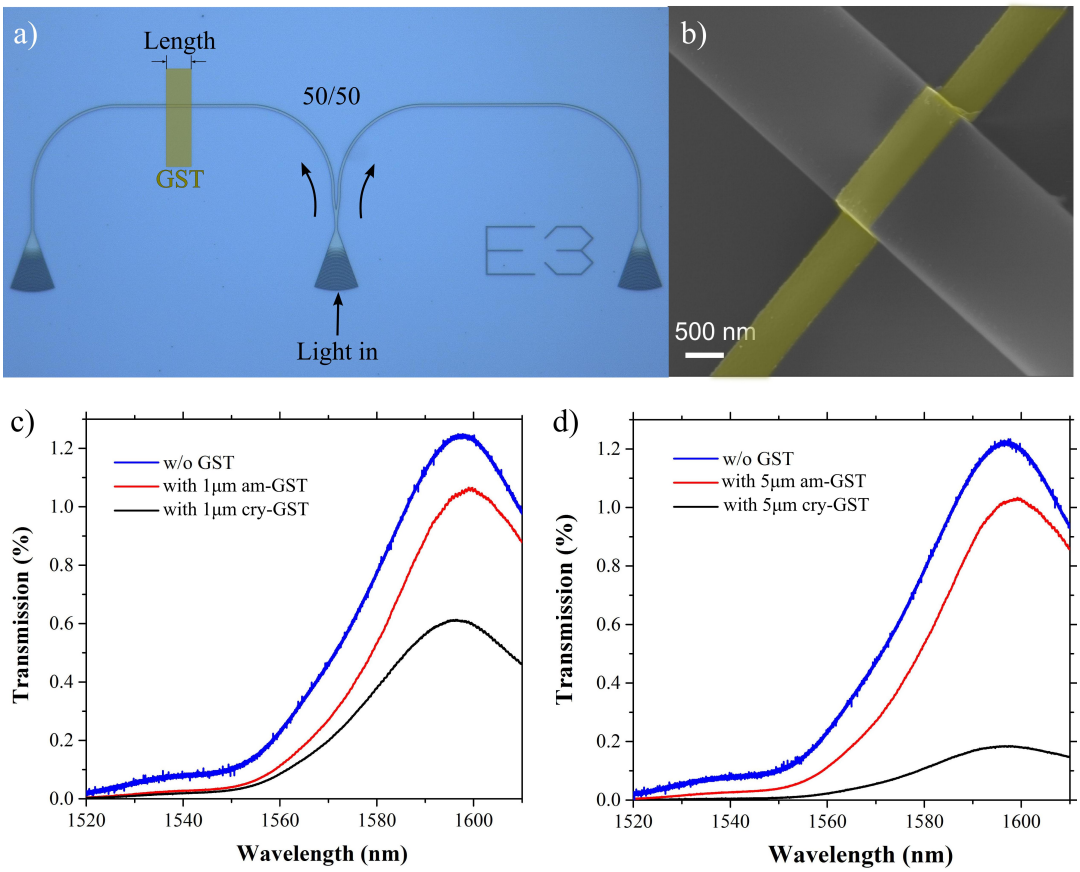

Figure 5.1: Experimental device and transmission characterisation. a) Optical microscope image of a balanced-splitter used as a phase-change photonic memory device. b) SEM micrograph of the GST section on top of the device in a). c) Transmission characterisation of a device without and with 1 μm long GST in amorphous and crystalline states. d) Same as in c) for 5 μm long GST. In c) and d), light is coupled in through the central Bragg-grating and measured in both gratings on the sides: one carrying the information of the GST, the other one as a reference.

5.1.1 Transmission characterisation

Transmission measurements were carried out for all devices before and after GST deposition, with GST initially prepared in the as-deposited amorphous (am-GST) state. Subsequently, the sample was annealed at 300°C for 2 min to obtain fully crystalline

GST (cry-GST); then, the transmission was recorded again. The transmission curves, plotted in Fig. 5.1 for two GST lengths, show the strong effect of GST, especially in the crystalline state, which absorbs a significant portion of the incoming light to convert it into heat. This, in turn, allows the attenuation coefficient to be calculated, by measuring how much light has been absorbed by GST in either state, as done in Ref. [27]. This coefficient provides further relevant information to calculate the absorbed energy per unit length of GST and to determine how much attenuation will distort the propagating mode in the waveguide.

In particular, by measuring the transmission spectra with and without GST, $P_{GST}(\lambda)$ and $P_0(\lambda)$, respectively, the attenuation coefficient (or insertion loss)—due only to the GST—can be calculated from:

$$\alpha_{dB}(\lambda) = 10\ log_{10}\left(\frac{P_0(\lambda)}{P_{GST}(\lambda)}\right). \tag{5.1}$$

Note that, by comparing with and without GST transmission spectra, intrinsic losses of the photonic devices are discarded, given that they are common to both measurements. Therefore, information about attenuation due only to the GST insertion is calculated in Eq. 5.1. Some of those intrinsic losses are back reflections, light scattering due to the roughness of the waveguide walls, and the insertion loss of the beam-splitter [40]. Eq. 5.1 was applied to find the experimental attenuation coefficients at $\lambda = 1595nm$, as a function of the GST length (L), and phase state. The results were:

$$\begin{aligned} \alpha_{dB,AM}(L) &= (0.095 \pm 0.005\, dB\mu m^{-1})L + (0.21 \pm 0.05\, dB), \\ \alpha_{dB,CRY}(L) &= (1.10 \pm 0.01\, dB\mu m^{-1})L + (1.465 \pm 0.03\, dB). \end{aligned} \tag{5.2}$$

Considering that the propagating mode is a TE by design, these experimentally measured attenuations are smaller than the attenuation calculated using FEM simulations, for the same device, in Sec. 3.2.3. Although these attenuation values were initially attributed to

the TM mode [27], this explanation is not completely satisfactory given the geometry and parameters used for the circuitry. Instead, variations in the $Ge_2Sb_2Te_5$ stoichiometry, resulting from the sputtering process, have gained strength as an explanation for this effect [99]. The reasoning for this is because the refractive index of GST, in both phases, varies significantly in the infra-red as a result of slight changes in the chemical composition [98]. Moreover, the refractive index used in the FEM modelling, which is plotted in Fig. 2.4, corresponds to measurements realised on 100 nm GST films [6], which may vary for 10 nm, as used herein. The experimental attenuation coefficients, however, will be the values considered in the experiments presented in this chapter.

5.2 Optical-switching dynamics

The device shown in the previous section displayed more absorption for the crystalline phase-change material. In this case, the light is pulled towards the cry-GST cell, which in turns induces strong attenuation of the passing optical signal. In the amorphous phase, on the other hand, the absorption is approximately five times smaller; therefore, the GST film does not attenuate the waveguide transmission to the same degree. Here, the near-field coupling and heat transfer that leads to these effects is studied numerically. Moreover, the experimental demonstration of on-chip amorphisation and crystallisation is presented, together with a brief description of the switching dynamics.

5.2.1 Near-field coupling to phase-change materials

The near-field coupling between the guided mode, inside the rib waveguide, and the GST, was studied using FEM modelling in COMSOL Multiphysics®. Although 3D modelling is preferred, 2D simulations offer good qualitative information on the interaction, with reduced computational time and complexity. The simulations were done similarly to the cross-sectional study of the TE mode in Sec. 3.2.3, considering only GST sections

completely covering the waveguide. The effect of the phase transition on the normalised electric field amplitude was analysed across a vertical line cutting the centre of the GST/ITO capping, as shown in Fig. 5.2. Upon switching, the maximum amplitude of the electric field moves from the centre of the Si_3N_4 waveguides (am-GST), to the vicinity of GST (cry-GST). Given the large real and imaginary part of the refractive index of cry-GST, the propagating mode couples and propagates inside the GST, where its magnitude is maximum, thus experiencing a strong attenuation. This effect is in good agreement with the theoretical analysis in Sec. 3.2. In Fig. 5.2b, on the same vertical line, the normalised electromagnetic heat transfer (Q_e) (see Sec. 3.2.2), on the GST and ITO layers, was calculated. It was found that for cry-GST, there is two orders of magnitude more heat transfer than for am-GST, which was expected due to their large difference in extinction coefficient. The influence of the thickness of the GST can also be observed as a logarithmically slow decay of the electric field. Also, considering that the GST capping is only $10\,nm$ thick, upon pulse excitation the whole of the GST will probably be at a similar temperature or fully switched along this axis.

More interestingly, the heat-transfer distribution inside the GST on the waveguide plane, plotted at the half point of its thickness, i.e. 5 nm into the GST, in Fig. 5.2c, shows how the heat transfer is maximum at the centre of the GST, being two orders of magnitude larger for cry-GST than for am-GST. The results in this figure also evidence the influence of the ITO in the heat transfer, given that at $\lambda = 1550\,nm$ ITO offers a complex refractive index $\overline{n}_{ITO} = 0.6 + 0.04i$, whose extinction coefficient is comparable to that of am-GST [99]. Therefore, ITO will also absorb energy, giving rise to larger attenuation coefficients than if there were no capping or absorptive material on top (See Fig. 3.8). The normalised heat transfer was subsequently projected over the propagation direction considering the $5\,\mu m$ long cry-GST, which is plotted in Fig. 5.2d. This plot was obtained by considering the experimental value for the attenuation of the mode as it propagates along the waveguide with a GST section of length L, given by the coefficient

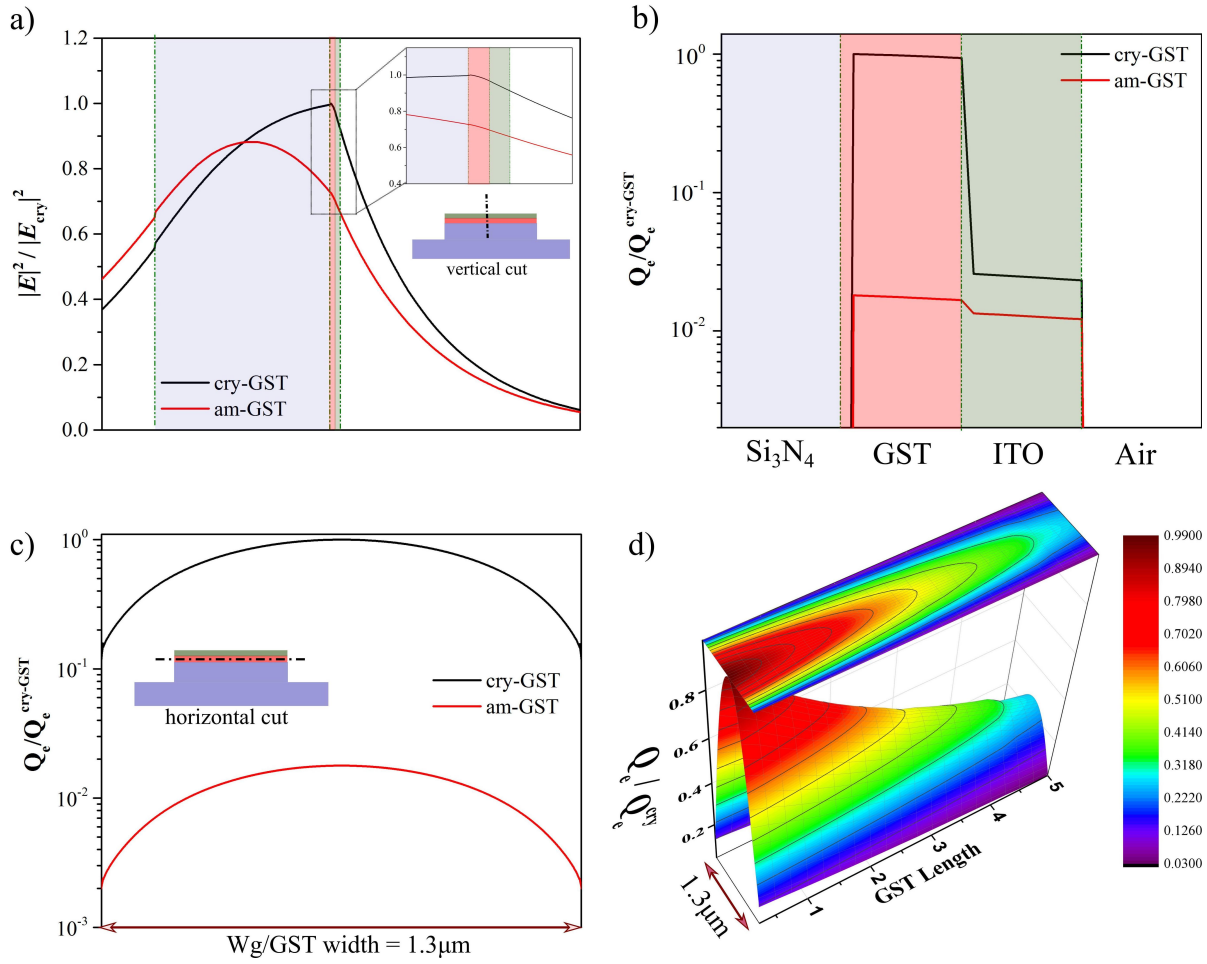

Figure 5.2: Electric field and heat transfer on the GST/ITO capping. a) Normalised electric field norm across the vertical line cutting shown in the inset. b) Normalised electromagnetic heat transfer (Q_e) with respect to the maximum heat that can be transferred to GST (i.e. $Q_e^{cry-GST}$ to the fully crystalline state) on the same vertical cut of a). c) Normalised Q_e on a horizontal line cut shown in the inset, which is traced at half the thickness of the GST. d) Projection of c) into cry-GST along the propagation direction.

$\alpha_{eff,cry}(L) = (1.10 \pm 0.01 dB\mu m^{-1})L + (1.465 \pm 0.03 dB)$ (See Sec. 5.1.1). The isosurfaces of the heat transferred to GST provide good insight on the pulse penetration along the GST and the areas that would be switched to the amorphous state, provided an energy higher than the threshold to melt-quench it. It is found, in particular, that most of the heat is accumulated within $\approx 0.9\mu m$ of the GST width, which is in good agreement with the simulations presented previously in Fig. 3.8.

5.2.2 Real-time switching dynamics

Optical pulses can initiate either amorphisation or crystallisation if the energy absorbed by the GST is high enough to heat it up to its transition temperature. For amorphisation, the crystalline GST is melted and quenched rapidly to favour a disordered state. On the other hand, heating the amorphous GST above the crystallisation temperature (but below the melting temperature), for a few nanoseconds, enables recovery of the atomic ordering [12].

To study such an optical-switching scheme, the balanced-splitter devices with crystalline GST on top were operated using the pump-probe setup described in Ch. 4. Experiments were performed using nanosecond light pump pulses with $\lambda_{pump} = 1560\,nm$. Such pulses were generated off-chip with an electro-optical modulator (EOM) and subsequently coupled into the on-chip waveguides. The probe, to read out the transmission, is performed with low-intensity continuous wave (CW) light using $\lambda_{probe} = 1570\,nm$. To separate the read-out from the pump pulses, a wavelength filter with a spectral extinction ratio of approximately 40 dB was used. Further suppression of the pump light was achieved by letting the pump and probe light-waves counter-propagate through the photonic circuitry. The output signal for the pump pulse was coupled to a 1 GHz detector. The probe, on the other hand, was split into two parts, one directed to a 125 MHz photodetector which was able to observe real time changes by filtering out the DC component, and the second, to a 200 kHz high-sensitivity IR detector to measure long-term transmission variations.

Amorphous GST exhibits nearly five times lower optical attenuation compared to crystalline GST, as shown in Sec. 5.1. This conveniently allows the use of pulses within the same energy range when switching back-and-forth between states: one pulse can induce amorphisation, while a subsequent, identical pulse will either keep the same state or

partially crystallise the PCM device. This is possible, because the resulting Joule heating of a pulse that heats up amorphous GST over the crystallisation temperature ($150°C$) can also induce amorphisation of crystalline GST, given that it reaches temperatures of nearly 750^oC, enough to melt-quench the material. However, the transitions are not in the same order, i.e. the same pulse can induce more material amorphisation than crystallisation—measured as changes in transmission. In particular, it was found that one single pulse is able to amorphise a large area of the GST cell or, if the pulse energy is too large, it can induce ablation; thus burning away part of the memory cell. To instead crystallise the cell, as the absorption is lower, one single pulse induces a small crystallisation step. Hence, in order to recrystallise completely, several pulses are required.

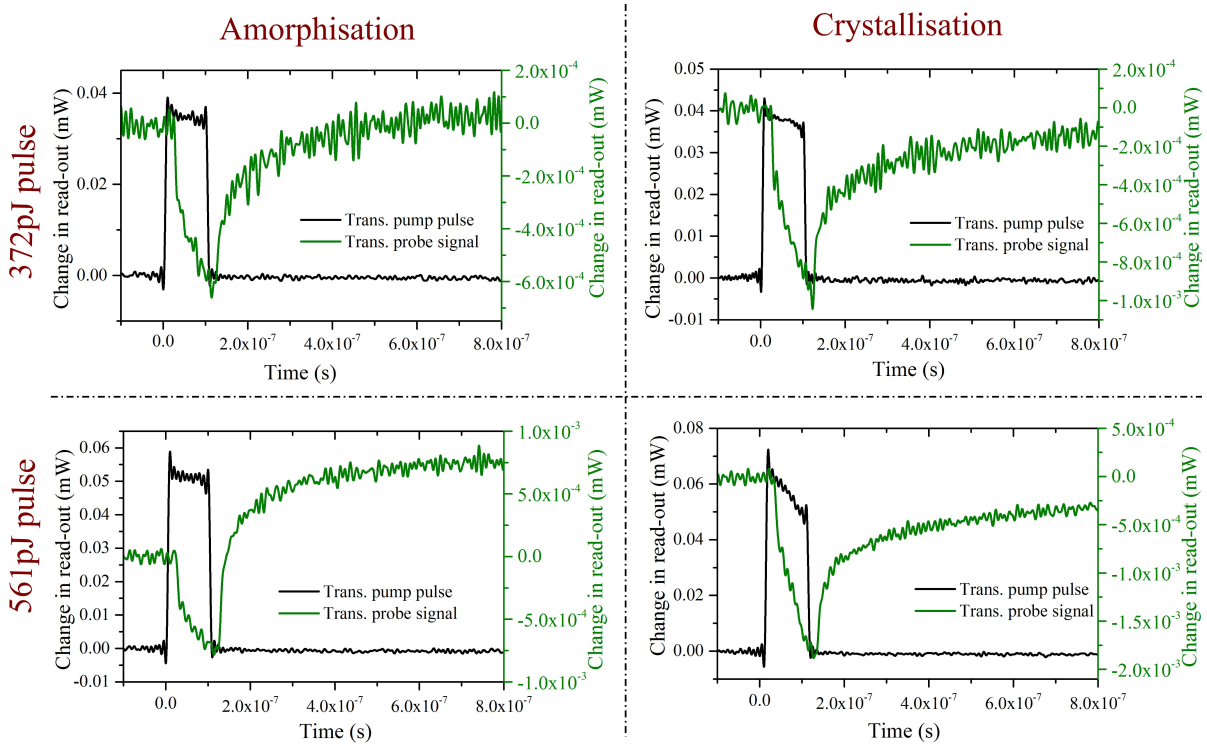

Figure 5.3: Real-time pump pulse and probe signal measurements on $5\,\mu m$-long GST, using $100\,ns$ pulses with energies of $373\,pJ$ and $561\,pJ$ (inside the waveguide).

Fig. 5.3 shows the real-time change in transmission (green lines), known as thermo-optical response, and the $100\,ns$ pump pulse (black lines) measured after the interaction with the

GST, which were captured simultaneously for the amorphisation and the crystallisation processes in a $5\,\mu m$-long GST cell. The time delay between signals is due to the difference in the optical path for the pump and the probe; the latter is delayed due to the insertion of a beam-splitter that adds approximately $1\,m$ extra propagation within an optical fibre, which, considering the speed of light inside the silica, implies a delay of $\approx 4.9\,ns$. It is observed that a pump pulse with the same initial energy (either $372\,pJ$ or $561\,pJ$ inside the waveguide) can induce amorphisation in a GST cell that was originally prepared in the crystalline state. In this case, there is an increase in the transmission measured from the probe signal, which becomes larger as the pulse gets more energetic, i.e. as more material is amorphised inside the GST section. After the amorphisation, the same pulses were sent to the GST cell where recrystallisation takes place on a smaller scale, even when using more energetic pulses (this effect will be described in Sec. 5.3.2). The thermo-optical effect relaxation towards a lower transmission level, after pulse excitation, shows that the recrystallisation needs to be done in several steps in order to compensate for the large change in transmission obtained previously in the amorphisation process.

In Fig. 5.4, four different SEM images for phase-change photonic memories are shown before and after pump pulses with different conditions. In particular, amorphisation and recrystallisation with the same pulse is shown in Fig. 5.4b. This micrograph shows the difference in scale between both amorphisation and crystallisation, displaying a similar pattern as the numerical results calculated in Sec. 5.2.1. Moreover, Fig. 5.4c shows the amorphisation and recrystallisation using counter-propagating pulses showing that the same GST cell can be switched independently from the two opposite sides, each one offering a different response. This, in turn, shows that this type of device could be used as the optical counterpart of an electrical memristor. In the same figure, one of the sides show a complicated pattern whose recrystallisation process led to crystalline stripes whose nature is not yet understood. Lastly, the micrograph in Fig. 5.4d shows a device

that has undergone ablation after a very energetic ($\approx 30\,nJ$) pulse.

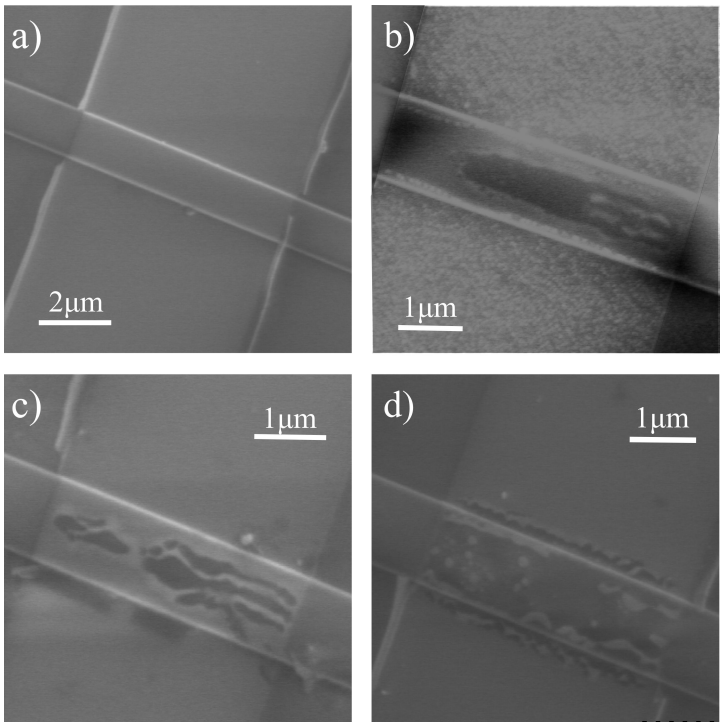

Figure 5.4: SEM images of $5\,\mu m$ long GST sections, on top of photonic circuits, after pump-probe measurements. a) In the fully crystalline state. (b) Amorphisation from fully crystalline with a $561\,pJ$ pump-pulse (after several back-and-forth switchings). c) Amorphisation from fully crystalline with $524\,pJ$ and $415\,pJ$ pump-pulses from the two opposite directions (after several back-and-forth switchings). d) Ablation after a $\approx 30\,nJ$ pulse.

The transmitted pulse measured in Fig. 5.3 shows how the GST absorbs energy during the pulse excitation. Such measurements correspond to the transmitted pulse after propagating inside the device containing the PCM cell. This pulse provides information about how much light is being absorbed. For instance, in Fig. 5.3, during amorphisation of cry-GST, the transmitted pump pulse displays less power than in the same measurement for the crystallisation process, which is due to a larger attenuation in that case. The shape of the pulse, in turn, offers information on the rate at which the GST is being heated up. Additionally, the energy absorption from the pulse can change its rate upon material switching in times shorter than the pulse itself, which is the reason why there

are changes on the pulse shape. This can offer valuable information in understanding the intrinsic phase-transition dynamics and the time-scales of the process.

The dynamics of the heat absorption and material switching can be studied from the thermo-optical response in real-time probe measurements, which has been done extensively by M. Stegmaier *et al.*, in collaboration with the author of this thesis, in Ref. [99]. This effect is the combination of the optical response to a change in the complex refractive index (which depends on the GST temperature) and the generation, by the pulse, of free carriers inside the material. The latter is thus an electronic contribution that implies light attenuation by contributing to the intraband absorption rate. The former is the optical response due to the changes in refractive index as a function of temperature, given by the equations:

$$\begin{aligned} n_{eff}(T_0 + \Delta T) &= n_{eff,0} + \beta_{eff}\,\Delta T, \\ k_{eff}(T_0 + \Delta T) &= k_{eff,0} + \gamma_{eff}\,\Delta T, \end{aligned} \tag{5.3}$$

where T_0 is the room temperature, ΔT stands for temperature variation, and n_{eff} and k_{eff} are the real and imaginary parts of the effective refractive index for the propagating mode, respectively. γ and β are the thermo-optical coefficients, which were measured experimentally in [99] for near-field coupling in Si_3N_4, which is the case-study of this thesis. They are given by:

$$\begin{aligned} \beta_{eff,am} &= -(2.2 \pm 2.0) \times 10^{-4}\,\mathrm{K}^{-1} \\ \beta_{eff,cry} &= (1.1 \pm 0.34) \times 10^{-3}\,\mathrm{K}^{-1} \\ \gamma_{eff,cry} &= (1.56 \pm 0.21) \times 10^{-3}\,\mathrm{K}^{-1} \\ \gamma_{eff,am} &= (4.1 \pm 1.2) \times 10^{-4}\,\mathrm{K}^{-1} \end{aligned} \tag{5.4}$$

The change in the imaginary part, given by the coefficients $\gamma_{eff,cry}$ and $\gamma_{eff,am}$, implies that the attenuation coefficient (α) changes as a function of the temperature as well,

i.e. $\alpha(T_0 + \Delta T) = \alpha(T_0) + \zeta\,\Delta T = \alpha_0 + \zeta\,\Delta T$. Thus, when the electromagnetic wave heats up the GST, this changes its optical properties, thus affecting the mode; this is the fully coupled interaction described in Sec. 3.2.2. In this case, the power measured at the detector as a function of the temperature T is given by [27, 67]

$$\begin{aligned} P(T) &= P_0 e^{-\alpha(T)L} = P_0\, e^{-\alpha_0 L}\; e^{-\zeta\,\Delta T\,L} \\ P(T) &= P_{GST} e^{-\zeta\,\Delta T\,L}, \end{aligned} \tag{5.5}$$

where L is the length of GST, P_0 and $P_{GST} = P_0\, e^{-\alpha_0 L}$ are the room-temperature transmitted power measured at the output of the device without and with GST, respectively. P_{GST} corresponds to the experimental curves measured for GST in both phase states presented in Sec. 5.1.1. From Eq. 5.5, as the material heats up, an exponential decay in the signal is predicted, which is indeed the case of the real-time measurements in Fig. 5.3 during the pulse excitation. After the pulse excitation, the material cools down, following the same effect but with a slower change in temperature since the cooling is achieved passively, in air at room temperature. From these two thermo-optical effects, it is deduced that the total time required for the switching depends on the pulse duration rather than the energy itself. Moreover, from the experimental data in Fig. 5.3, it can be observed that at after a time $t = 7\tau$, with τ being the pulse width, the transmission has approached an asymptote for the exponential decay that dictates the cooling process. At $t = 2\tau$, however, the transmission reaches up to 70% of the asymptote value. These times are important to consider, given that they will determine the speed limits of the memory applications, i.e. the time required before another phase-switching can be realised, as will be discussed in Sec. 5.6.

From these results, it is concluded that shorter pulse widths are better in order to get fast back-and-forth switching, which is mainly restricted by the "dead time" that the material takes to cool down. Although these fast-response measurements provide plenty

of interesting data to understand the phase-change transitions, this chapter will rather focus on the long-term results of such transitions and their applicability. More details of the real-time pump-probe measurements and thermo-optical effect can be found in [67, 99].

5.2.3 TEM Analysis

TEM specimens were prepared and imaged by collaborators in the Institute of Nanotechnology at the Karlsruhe Institute of Technology (KIT), Germany. Using focused ion beam (FIB) in a FEI strata Dualbeam system, cross-sectional lamellae were cut from a GST memory device along the waveguide and thinned to a thickness of less than $50\,nm$ for TEM imaging. The TEM specimens were examined in a FEI Titan 80-300 electron microscope equipped with CEOS image spherical aberration corrector, Fischione model 3000, high-angle annular dark-field (HAADF), a scanning transmission electron microscopy (STEM) detector, an EDAX SUTW energy-dispersive X-ray spectroscopy (EDX) detector, and a Gatan Tridiem image filter. The microscope was operated at an accelerating voltage of $300\,kV$.

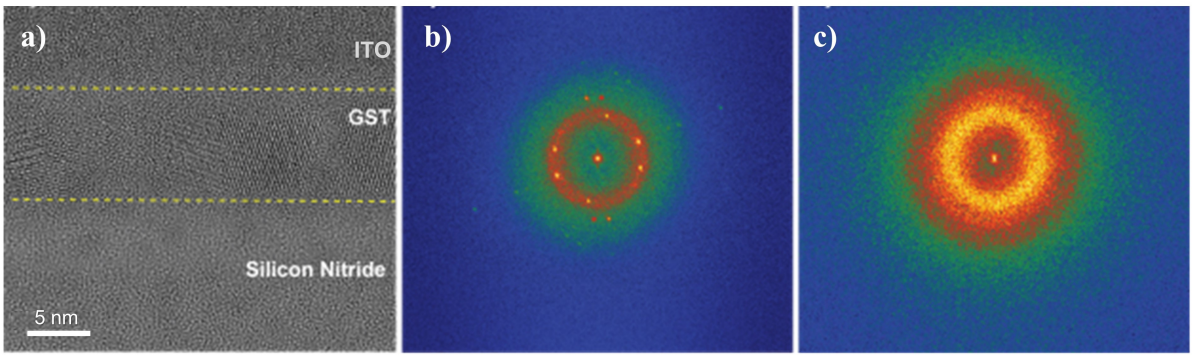

Figure 5.5: TEM imaging of GST photonic memory cross-section. a) TEM image of a cross-section through a memory cell in the crystalline state, showing also the SiO_2 substrate and the ITO capping. b) Fourier analysis of the TEM image for the memory device in the crystalline state from a), showing clear features of the ordered lattice structure. c) Fourier analysis of the TEM data from a device optically switched into the amorphous state with diffuse haloes expected for the amorphous phase.

The optical switching of the phase-change material element was confirmed by high-resolution transmission electron microscopy (HRTEM). Devices were prepared in both the amorphous and the crystalline phases using the optical-switching processes outlined above. A thin lamella along the direction of propagation in the waveguide was cut through the GST section for TEM imaging. From the images, the deposited GST layer and the ITO layer can be seen, as indicated in Fig. 5.5a; the measured thickness for each layer is about $10\,nm$ as expected from the deposition rates. The HRTEM image in Fig. 5.5a also clearly shows the crystalline phase written into (the GST element of) this device. To further illustrate the crystalline order, a Fourier transform of Fig. 5.5a is shown in Fig. 5.5b, where the diffractogram reveals the features of cubic GST. The diffractogram of a device written into the amorphous state is shown in Fig. 5.5c, where the presence of only diffuse haloes confirms amorphisation.

5.3 Binary memory and switching protocol

The geometry of the phase-change photonic memory cell and the operating principle is shown schematically in Fig. 5.6. Information is stored in the GST by employing near-field coupling between light travelling along the waveguide and the GST element, as explained in Sec. 5.2. This interaction results in the absorption of optical power due to the non-vanishing complex refractive index of GST [26, 67]. As illustrated in Fig. 5.6, the crystalline state (Level 0) exhibits higher attenuation and thus less optical transmission than the amorphous state (Level 1). Therefore, stored data can be encoded in the amount of light transmitted through the waveguide (i.e. exiting the end of the waveguide) and can be read out with a continuous wave (CW) laser or low-power optical pulses. The phase state of the memory element influences the optical properties of the propagating light field and therefore the waveguide mode profile, as illustrated in Sec. 3.2.

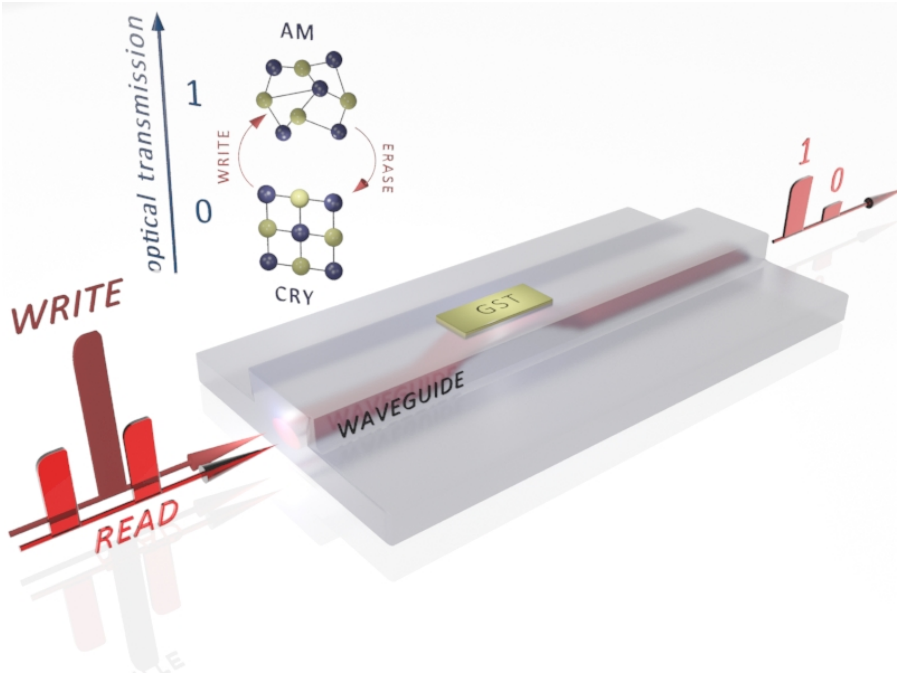

Figure 5.6: Operation principle of the phase-change photonic memory. The GST section is originally prepared in a fully crystalline state; thus, a first read-pulse will lead to a low transmission (level 0) measurement. Once the GST is amorphised with a subsequent *Write* pump-pulse, a second read-pulse will measure a higher transmission (level 1). The inset shows the two crystallographic states and their corresponding transmission level in a binary memory.

To demonstrate memory operation, the phase-switching was obtained optically by realising pump-probe measurements on the waveguides containing memory cells, in the same manner, with the same devices, and using the same pulse parameters and setup configuration as presented earlier during this chapter, in Sec. 5.2. The difference, however, is that in memory operation it is critical to obtain well-established transmission levels that can be retrieved after several cycles. To achieve this, evanescent switching was tested, as originally proposed in Ref. [26], using one input waveguide for the pulses and another waveguide with GST on an integrated ring-resonator cavity. This approach, however, proved challenging because the power required to switch was too high and the coupling efficiency to the ring-resonator changed dynamically upon and during phase-switching. The optimum design for memory operation was later found by placing GST cells directly on top of the same waveguide where pulses were sent. Different pulse schemes were

also tried unsuccessfully before finding the *Write* and *Erase* processes explained in the following sections. One of the key aspects for the correct operation of phase-change photonic memories is to initiate the *Write/Erase* cycle from the crystalline state, and set its low transmission as the ground level or Level 0. In this way, reliable levels and good cyclability were guaranteed, as will be discussed in detail when describing the conditioning process in Sec. 5.5. For this reason, after sputtering, GST was always annealed at $300°C$ for $2\,min$ to crystallise the as-deposited amorphous material. Secondly, the *Write*, *Erase* and *Conditioning* processes needed to be performed following the steps described below. This method represents the first demonstration of complete cycle switching in this type of architecture. As the first prototype, there is plenty of room for improvement, which could also include different switching schemes or methods.

5.3.1 *Write* (amorphisation)

Information is written in the phase-change photonic memories by means of energy absorption from pump-pulses, which create distinctive amounts of amorphous GST embedded in the initial crystalline state. The more energetic the pulse, the deeper—along the waveguide—and broader the area that is melt-quenched (amorphised) in the memory cell, as indicated using FEM simulations in Fig. 5.2. Therefore, by controlling the pump-pulse power, different levels of transmission can be written by reaching different partial amorphous states, as shown in Fig. 5.7.

In detail, if P_{min} is the minimum pulse power able to amorphise GST, then, when a *Write* pulse with fixed length and with power $P_n^{write} \geq P_{min}$ is sent to the GST cell (prepared in the crystalline state with transmission T_0), amorphisation is induced. Therefore, the transmission of the probe signal increases from T_0 to a characteristic value T_n, the transmission of Level n. This T_n is unique to the pulse power P_n^{write}. Level n can be accessed every time the same *Write* pulse is sent to the memory cell, provided that a

proper conditioning process is carried out beforehand [67].

In Fig. 5.7a, the real-time thermo-optical effect on the probe transmission is plotted when amorphisation takes place in a $5\,\mu m$ long memory cell, for different P_n^{write}. Therefore, for a fixed pulse width of $100\,ns$ with $500\,ps$ rise/fall times, it is shown that the higher the energy absorbed, due to an increase in pulse power, the higher is the final transmission level. As GST absorbs more energy—seen in the thermo-optical curve shown in Fig. 5.7 as the transmission reaches lower values during the pulse excitation—the pulse amorphises a larger area of the memory cell. Furthermore, tuning the power is not the only way to reach an energy that is enough to amorphise GST; this can also be done by using pulses with different widths and fixed power. In particular, by using a pulse power of $6.1\,mW$ and varying the pulse width from $10\,ns$ to $200\,ns$, different transmission levels were reached, as plotted in Fig. 5.7b.

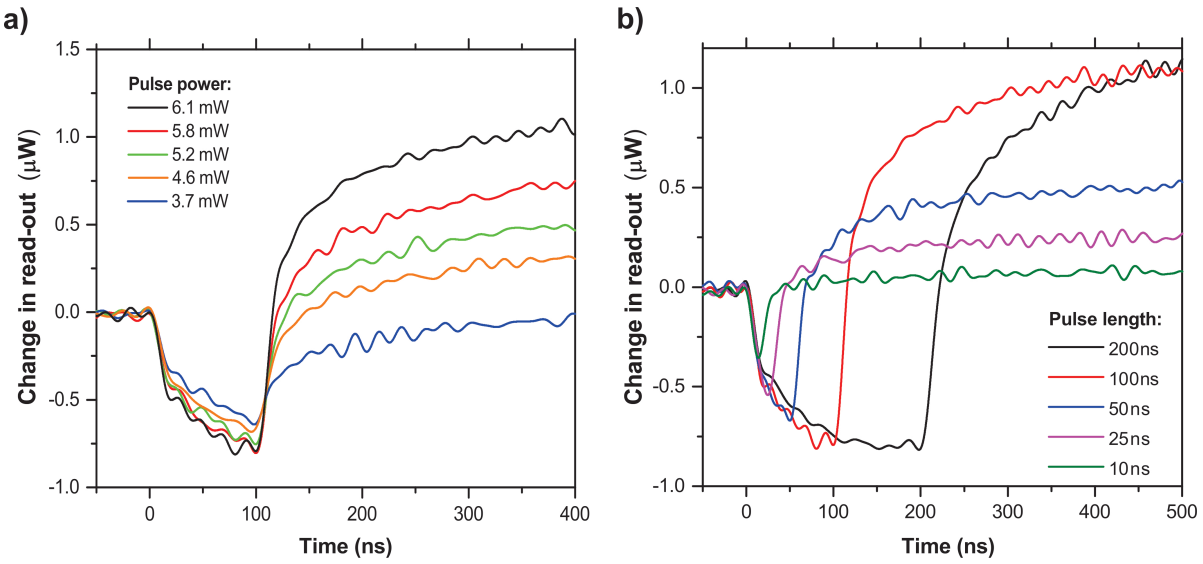

Figure 5.7: *Write*: Amorphisation in a $5\,\mu m$ long phase-change photonic memory. Thermo-optic effect and amorphisation by a) varying pulse power and fixing the pulse width to $100\,ns$ and b) varying pulse width and fixing the pulse power to $6.1\,mW$.

If pulses with energies that can heat up the GST far beyond its melting point are used to *Write*, then the material conditioning may be destroyed and ablation can also take place.

For this reason, pulse widths shorter than $100\,ns$ were employed, and the transitions were induced only by controlling the pulse power. Contrary to what is broadly accepted, under this configuration the rise/fall times of the *Write* pulses were not relevant. This contradicts the times reported in literature that indicate that the pulse edges should be below $10\,ns$ [12], otherwise the cooling is not fast enough and the recrystallisation dynamics may overtake amorphisation. However, for the experiments reported in this thesis, different pulse generators were used: some offering $500\,ps$ rise/fall times, others with $5\,ns$, and even arbitrarily created pulses with $50\,ns$ fall times. The result was the same; all pulses tested were still able to amorphise GST, indicating that the only important parameters were the pulse power and width (i.e. the pulse energy). This is a finding that requires further research.

5.3.2 *Erase* (crystallisation)

While a single pulse was used to *Write* (amorphise), to achieve the $T_n \rightarrow T_0$ transition (i.e. to switch back to the pure crystalline state), a train of consecutive $100\,ns$ pulses with gradually decreasing power was used to *Erase*. This procedure, found empirically, consists of k pulses with powers $P_{n,m}^{erase} = P_n^{write} - m\Delta P$, where n stands for the starting transmission level and $m = 0, 1, 2...k-1$. Such pulses are sent consecutively in time intervals limited only by the cooling rate of GST. ΔP was set to be approximately $0.40\,mW$. Each pulse in the *Erase* procedure recrystallises in small steps, but all together drive the transmission towards T_0. The number k will be given by the condition $P_{n,k-1}^{erase} \approx P_{min}$ when T_0 is reached. Pulses beyond this condition should not modify the transmission as the material is transformed to the fully crystalline state. Pulse powers and widths can be chosen accordingly, as long as the energy (pulse width multiplied by power) remain in the same range.

Following this *Erase* procedure enables the memory element to operate with high repro-

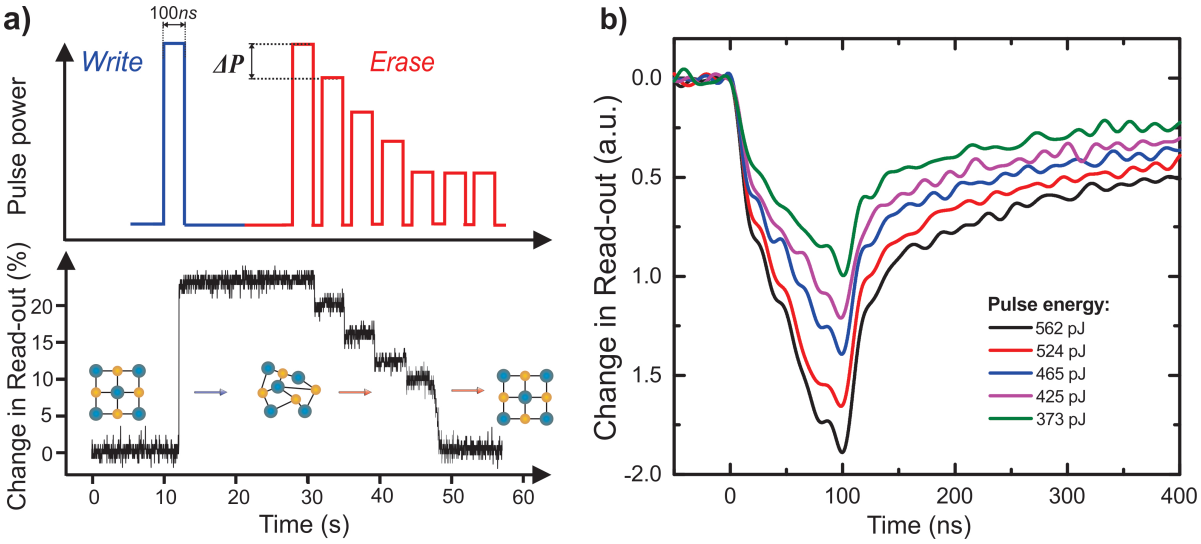

Figure 5.8: Demonstration of a full switching cycle. a) Sketch of the *Write/Erase* process (upper panel) and the change in read-out they induce in long time scales (lower panel). $\Delta P \approx 0.40\,mW$ is the power step between two consecutive *Erase* pulses. The initial state was established by using a *Write* pulse of $562\,pJ$ and $100\,ns$ (thus, with a power of $5.62\,mW$). The *Erase* pulse had a width of $100\,ns$ and powers: $5.62\,mW$, $5.24\,mW$, $4.65\,mW$, $4.25\,mW$, and $3.73\,mW$ for the three last ones. b) Changes in read-out in short-time scales. The thermo-optical effect is observed during the partial recrystallisations initiated by the $100\,ns$ *Erase* pulses. The initial state was established by using a *Write* pulse of $562\,pJ$ and $100\,ns$ (thus, with a power of $5.62\,mW$).

ducibility. Data on a full switching cycle are presented in Fig. 5.8a. The optical pulses that were used are represented in the upper panel. In contrast, the read-out, in the lower panel, was measured at all times during this cycle with a low-noise photodetector. First, the $5\,\mu m$ long GST device was amorphised with a single $100\,ns$ pulse with $500\,ps$-fall and of $562\,pJ$ energy (equivalent to a power of $5.62\,mW$ at the GST), leading to a change in read-out transmission of 28%. Afterwards, the *Erase* was carried out by seven pulses with $562\,pJ$, $524\,pJ$, $465\,pJ$, $425\,pJ$ and three of $373\,pJ$, respectively. Each of these pulses initiated a partial recrystallisation of the GST. The respective switching dynamics for each of these pulses, recorded by a $125\,MHz$ photodetector, is shown in Fig. 5.8b. In this figure, it is observed that during the time when the switching pulse interacts with the GST $(0 - 100\,ns)$, an exponential decay of read-out transmission takes place. Subsequently, the transmission increases asymptotically $(100 - 400\,ns)$ as a result of the GST cooling

(thermo-optical effect). However, given that the pulse induces partial recrystallisation, the absorption by the GST increases and the transmission reaches a lower level than that before the pulse. The result is the transmission steps observed in both Fig. 5.8a and b. The thermo-optical effect shown in Fig. 5.8b is a fast-response measurement taken with a 125 *MHz* detector (see Sec. 4.1.2). This fast transient behaviour is not perceptible in the long-time measurements in Fig. 5.8a, given that they were taken with a 200 *kHz* photodetector.

On the *Erase* switching dynamics

As shown above, and contrary to the *Write* process, full recrystallisation (*Erase*) with a single light pulse is challenging. One of the reasons for this is significant decrease in absorption upon amorphisation. When erasing, the memory operation requires the stepwise scheme detailed above, which is not yet optimal due to speed concerns. The reason why several pulses are required to recrystallise is not completely understood, yet in practice, this method, found empirically, has proven to work well. There are two competing effects that can help to understand this phenomenon:

- Crystallisation takes place before the end of each *Erase* pulse; therefore, the remaining optical energy supply heats up the GST further to the melting temperature and causes immediate reamorphisation. Because of the temperature variation across the memory cell [99], however, this cannot be prevented completely since not all parts of the GST crystallise simultaneously. This effect is proposed to be a consequence of the change in absorption experienced by the pump pulse, as observed experimentally in Fig. 5.3—where the shape of the pulses change within the pulse width, thus showing that there are drastic variations in the material attenuation as it heats up. Nevertheless, this explanation does not provide an answer as to why shorter pulses were not more effective, which should have been the case following this reasoning.
- Given the refractive-index modulation towards a less absorptive state, the optical

mode within the waveguide is distorted when part of the memory cell is amorphised. Therefore, energy is absorbed in a different and less efficient manner than when it is fully crystalline. By sending a first pulse, the GST will be heated to a temperature between the glass-transition temperature and the melting point (provided the correct pulse energy is used), and thus a small area is crystallised. Subsequently, the GST gets slightly more absorptive, yet not completely crystalline. This implies that the next pulse would then require less energy to heat up the material to the same temperature reached by its predecessor, and thus to crystallise more of the cell. The process continues in the same way until the whole cell is crystallised by a train of pulses with decreasing power/energy. If the power is not reduced, then further amorphisation takes place instead, as the high absorption may lead to a melting temperature again.

The latter effect was modelled using FEM on COMSOL Multiphysics® to find qualitative information that can provide insights into the real switching mechanism behind the *Erase* process. The results of this study are presented in Fig. 5.9. In particular, Fig. 5.9a shows the attenuation coefficient calculated for the cross-section of the rib-waveguide with partial amorphous sections on top. This, in turn, offers qualitative information on the amount of light that will be absorbed after a *Write* pulse melt-quenches and amorphises areas embedded in the crystalline GST. These areas, as shown previously in Fig. 5.2, expand from the centre toward the edges as the heat increases with the pulse power. The heat transfer by a subsequent pump pulse is affected by the presence of an amorphous area in the centre of the GST cell. Such variations are plotted in Fig. 5.9b where the normalised heat transfer is calculated inside the GST at half of its thickness, thus crossing the crystalline and the amorphous regions. From this figure, a dip in the heat transfer due to the low extinction coefficient of the amorphous area in the centre can be observed. Therefore, if further pulses are sent when GST is in any of these intermediate states, higher temperatures will be reached at the boundaries between the amorphous

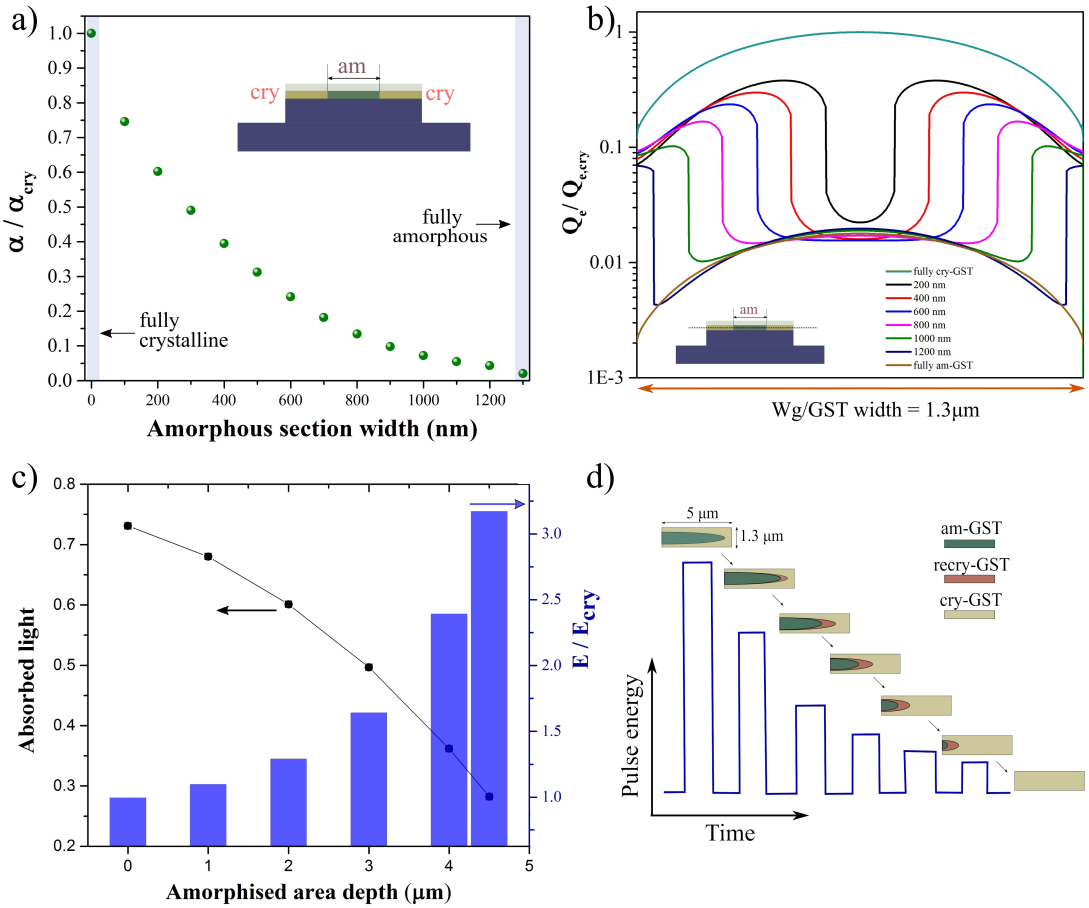

Figure 5.9: *Erase* scheme computational modelling. a) Normalised attenuation coefficient as function of the amorphous section width, embedded into crystalline GST, as shown in the inset. The α_{cry} corresponds to the attenuation when GST is fully crystalline, which can be measured experimentally. b) Normalised electromagnetic heat transfer (Q_e)—with respect to the maximum heat transfer when GST is fully crystalline $Q_{e,cry}$—traced on the horizontal line parallel to the substrate and crossing the GST at half-height (at $5\,nm$, as shown in the inset), including the embedded amorphous section. c) Light absorption calculated for $5\,\mu m$ long GST considering: 1) an initial amorphisation (*Write*) depth of $4.5\,\mu m$ with $0.9\,\mu m$ of width; 2) the experimental attenuation calculated for fully amorphous and fully crystalline GST; and 3) the partial-amorphous attenuation values reached in intermediate recrystallisation steps, calculated using a), until the amorphous area is completely recrystallised (i.e. the amorphised area depth is equal to zero). The bars indicate the pulse energies required to transfer the same energy E to the material via absorption, as a function of the energy required to heat-up over the crystallisation temperature (and below the melting temperature) when the material is in a fully-crystalline state, which can be experimentally measured. d) Sketch of the full *Erase* as understood from the simulations, requiring thus an energy-decreasing train of pulses. The GST sections sketches are plotted as seen from the top.

and the crystalline areas of GST where the heat transfer is greatest. Furthermore, if parabolic-shaped amorphous areas are considered on the light propagation axis—based on the simulations in Fig. 5.2—then one recrystallisation step can be understood as the small crystallisation that takes place at the edges of the amorphous area, which gets significantly larger as the parabolic shape gets narrower (heat transfer is higher for narrower amorphous embedded areas), and eventually is maximum when the pulse faces only crystalline GST. Multiple recrystallisation steps will then be required, given that it is not possible to heat up the centre of the amorphous material directly. Instead, several pulses, each one crystallising a bit of amorphous materials on the edges at the time, are required until the whole amorphous area—created with the single *Write* pulse—is back to fully crystalline.

While the explanation presented above provides an answer to why several pulses are used in the *Erase* process to recrystallise, it does not explain why a train of energy-decaying pulses are necessary. To find a reasonable answer to this, the results in Fig. 5.9a are once again analysed. As GST recrystallises, the attenuation increases, given that there will be a higher portion of crystalline GST than of amorphous GST (i.e. the amorphous volume decreases). Therefore, the attenuation that the first pump pulse in the *Erase* undergoes is much lower than that of any of the following pulses; thus, more energy is required for this pulse than for the subsequent ones, if the material is to be heated up over the crystallisation temperature. Hence, pulse-energy requirements decrease as the attenuation increases. If considering, for instance, a memory cell of $5\,\mu m$ and a *Write* pulse that amorphises GST to a depth of $4.5\,\mu m$ (i.e. if $Q_e = 0.4Q_e^{cry}$ is enough to switch in Fig. 5.2), then every subsequent pulse in the *Erase* will reduce the size of the amorphous area. By studying the evolution of the attenuation of the entire GST cell, the total amount of light that is absorbed after propagating through the cell can be calculated. This is done by following these steps:

1. Calculate the total area that is amorphised by an initial *Write* pulse using the isosurfaces for the heat transfer shown in Fig. 5.2d. Following with the example above, the area is given by the depth of $4.5\,\mu m$ and the initial width of $0.9\,\mu m$ that decreases in a parabolic-like way.

2. Divide the amorphous area in differential sections in the propagation direction, taken here as $0.5\,\mu m$ in depth.

3. Use α in Fig. 5.9a to calculate the attenuation of each differential section as a function of the amorphous section width embedded in crystalline GST.

4. Compute the total absorption (from the total attenuation) as the sum of the contributions by every differential section.

5. Repeat 1 to 4 for the decreasing amorphous area after each recrystallisation pulse. In this case, it is assumed that the amorphous GST is made smaller in 0.5 to $1\,\mu m$ steps after each pulse. This choice does not affect accuracy but rather the number of points on the same curve—or the number of recrystallisation pulses in the experiment, which can be measured.

The results for the absorbed light in this particular memory cell are shown in Fig. 5.9c, together with the modulation in pulse energy to obtain the same absorption in every intermediate state. These results demonstrate that an exponentially decreasing series of pulse energies are required to achieve the same absorption for the material, i.e. to heat it up to the same temperature, as recrystallisation takes place, just as done experimentally in Fig 5.8.

Finally, in Fig. 5.9d, the whole recrystallisation process is summarised and sketched. Pulses of decreasing energy are required to transfer the same amount of electromagnetic heat, so as to reach the right temperature needed to crystallise the GST at the edges

of the amorphous volume. This method represents the less time-consuming process as the energy modulation implies the minimum number of pulses. Alternatively, a larger number of pulses of a constant, but lower energy can be used to recrystallise GST in even smaller steps. This alternative may represent a more energetically efficient option, but would increase the total duration of the recrystallisation, thus making the memory operation times longer. Also, given that the attenuation is calculated for differential sections, which could have been taken in a different order with the same result, then the actual place where recrystallisation takes place—including different recrystallisation areas to that in the vicinity of the edges as considered in the hypothesis above—would lead to a similar train of pulses with decreasing energy.

Further investigation is required to determine the real nature of the *Erase* process and to find alternative ways to carry out the GST recrystallisation. However, to circumvent this issue the *Erase* scheme based on stepwise partial recrystallisation presented above is employed throughout this thesis as a proof of concept. This scheme, performed by a train of consecutive energy-decreasing pulses, represents thus far the only solution for repeatable back-and-forth switching under this architecture, regardless of the speed limitations and energy efficiency.

5.3.3 *Read*

The read-out of the information stored in the GST is done with either CW lasers or low-power optical pulses, at any wavelength inside the specific bandwidth of the circuit. The only important aspect here is that the energy of the *Read* light is not so powerful as to induce any sort of switching, but enough to offer good SNR. In this work, *Read* was done in a pump-probe scheme where, in real time, it propagated together with the pump *Write/Erase* pulse inside the waveguide. This meant that two light sources were required and wavelength-filtering was used to separate both signals and avoid interferences or

cross-talk. This was done with the aim of obtaining the real time dynamics of the GST. However, a single light source can be used to switch and subsequently read if no real-time dynamics information, but rather long-term transmission data, is required.

5.3.4 Binary operation

Following the *Write* and *Erase* protocols described above and using the pump-probe setup described in Ch. 4, back-and-forth switching is achieved in a controlled and repetitive manner between the crystalline and partially amorphised GST. In Fig. 5.10, the change in read-out transmission upon repeated switching between low (Level 0), and high (Level 1) transmission states of the GST is shown for one $5\,\mu m$ memory cell under two different pulse energies. These results demonstrate unequivocal binary data storage in this photonic memory with good reversibility and transmission contrast, which can also be tailored by controlling the *Write* pulse energy. The oscillations observed in the lower level are due to the optical amplification of noise, which in turn heats up the GST cell and slightly modifies the transmission without switching. The noise originates from the laser and amplified by the EDFA (which also adds noise from spontaneous emission) when setting the current to prepare *Write* pulses. When using high power pulses, it is important to add a second wavelength filter after the amplifier, as described in Sec. 4, to reduce the noise at wavelengths different to that of the pulse. In the same figure, the multiple steps when returning from Level 1 to Level 0 due to the *Erase* stepwise protocol are also visible.

Moreover, as illustrated in Fig. 5.11, the switching process is highly reproducible over one hundred cycles with a measured confidence interval (shaded area) of $\pm 7.1\%$ measured as the interval between two standard deviations and the central transmission value for the upper level. This number of cycles, however, was chosen deliberately given the manual operation of the experimental setup. It does not represent the number of cycles before

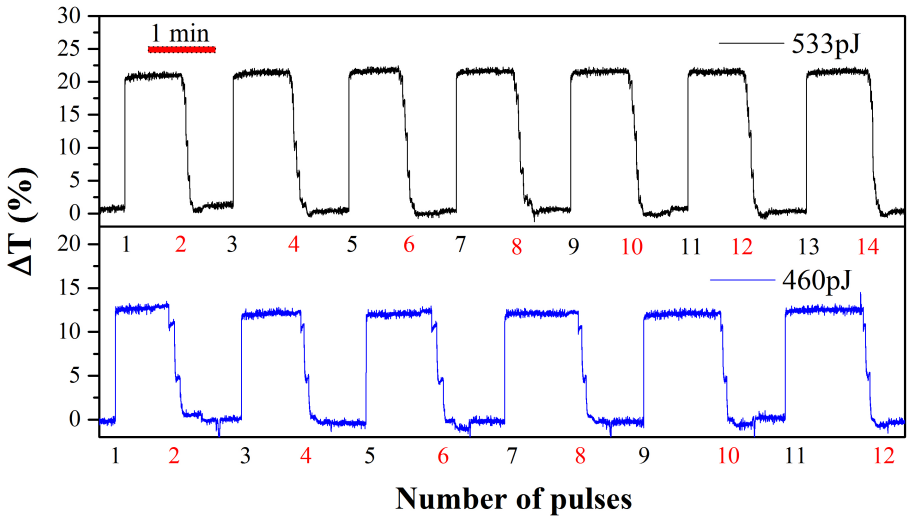

Figure 5.10: Non-volatile, binary memory operation on phase-change photonic memories using two different *Write* powers. ΔT stands for the change in transmission between the fully crystalline and the partially amorphous state. Pulse energies correspond to powers of $5.33\,mW$ and $4.6\,mW$ and $100\,ns$ in length. The read-out was done using CW at $\lambda_{probe} = 1570\,nm$. The *Write/Erase* pump pulses were set to $\lambda_{pump} = 1560\,nm$.

failure; measurement that would require an automated version of the same experiment. The low-transmission state (Level 0) was initially prepared from the fully crystallised phase in such a way that reversibility of the operation is ensured. On the other hand, the absolute transmission at Level 1 is determined by the switching energy, which defines the final level of amorphisation, and the GST dimension along the waveguide, which defines the modulation depth. To ensure high transmission contrast between the amorphous and crystalline states, $5\,\mu m$ length cells were used; with this device, a change in read-out of transmission of 21 % is achieved using a single $100\,ns$ *Write* pulse of $533\,pJ$ energy. Since the GST cell absorbs nearly 80.7% of the pulse in the crystalline state (derived from the measured optical attenuation of $-7.14\,$dB calculated in Sec. 5.1.1 and in [27]), this corresponds to a switching energy of $430\,pJ$. Further demonstrations of binary operation were realised by employing devices with smaller GST lengths and lower *Write* pulse energy, as described in Sec. 5.4.3. In particular, modulation depths up to 58.2% and binary operation with pulses as short as $10\,ns$ with switching energies of $13.4\,pJ$ were

achieved. While the data in Fig. 5.10 demonstrate the non-volatility of the phase-change photonic memory for several minutes (indicated by the time bar), it has been shown in a similar configuration that the phase-state is preserved over much longer times, up to a period of at least three months [67]. Indeed, extrapolating from the well-studied data-retention properties of GST, all-optical phase-change memories can be expected to remain non-volatile at room-temperature on a timescale of years [12, 14].

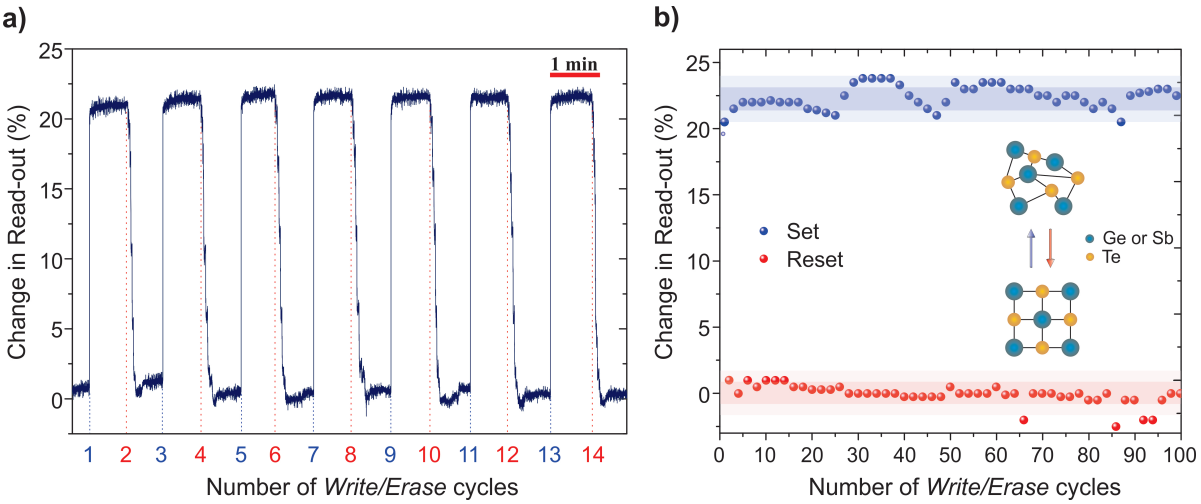

Figure 5.11: Reversible and reproducible single-shot switching. a) Demonstration of binary memory operation between the crystalline (lower Level 0) and amorphous (upper Level 1) state of a $5\,\mu m$ GST device with a total change in read-out transmission of 21%. The Write step (blue) is initiated by a single $100\,ns$ pulse, while for the *Erase* step (red) a fixed sequence of six consecutive $100\,ns$ pulses with decreasing power are employed, as described in Sec. 5.3.2. Time scale is $1\,min$. b) Further repetition of the same switching cycles, as in a). The number of cycles was chosen deliberately as proof of concept and does not represent the number of cycles before failure. The dark and light shaded areas represent one and two standard deviations, respectively.

5.4 Multi-level phase-change photonic memory

Multi-level memory operation is found by establishing and freely accessing intermediate states between fully crystalline (after annealing) and the partially amorphised state achieved after the most energetic available *Write* pulse. This in turn, represents one path, besides reducing the form-factor, of how phase-change-based photonic memories can

improve the data-storage density as multiple bits can be stored in a single memory element. Intermediate levels, when writing, are obtained readily by controlling the amount of GST that is amorphised, taking advantage of the fact that the pulse penetration depends on its energy. Therefore, by controlling the power, different levels of transmission can be obtained by writing different partial amorphous states, as already shown in Fig. 5.7. Moreover, when erasing, although the dynamics are more complicated and the real nature of the small crystallisation steps, explained in Sec. 5.8, is not completely certain, the *Erase* process has proved to work well and it can be stopped at certain pulse energy/power values to retrieve any intermediate level, as explained below. This way, intermediate levels are accessible for any intra-band level combination—from and to any arbitrary level.

5.4.1 n-level assessment method

In multi-level operation, to *Write* from a Level n to a Level $n' > n$, one pulse with power $P_{n'}^{write}$ is sent to the memory cell. This pulse will reliably take the cell to the Level n', regardless of the Level n of origin, as long as the transmission of the Level n' is larger that the transmission of the Level n (i.e. if further amorphisation takes place).

Partial *Erase* (i.e. accessing intermediate states) from any Level n to a Level $n'' < n$ is possible by repeating the same *Erase* process, explained in Sec. 5.3.2, until the condition on the pulse power $P_{n,m}^{erase} = P_{n''}^{write}$ is fulfilled. The energy of the final pulse determines which lower transmission level is achieved. This can be the fully crystalline or any intermediate state which is also retrieved when writing with a pulse $P_{n''}^{write}$. Hence, the same level is reachable by means of either *Write* or *Erase*, depending only on whether the starting point is a higher or lower transmission level.

The reproducibility of these levels depends on the conditioning process described in

Sec. 5.5. If the conditioning is done several times using the same series of pulses for amorphisation and crystallisation, then the intermediate levels are reachable with high reliability. Moreover, the number of possible levels in a memory cell is limited by the separation (difference in transmission) between the highest and lowest states and the required confidence interval of an intermediate level. The transmission contrast between levels can be increased by using either a larger memory cell or finding the highest, optimal pulse energy for switching. The confidence interval, on the other hand, is mainly limited by the minor variations in the switching and by the signal-to-noise ratio (SNR) of the read-out measurement. Therefore, the number of memory levels can be increased by just using a higher read-out power ensuring a better SNR (without exceeding switching power P_{min}). The highest available transmission can also be manipulated by using higher power pulses just before the ablation threshold; this threshold, however, is hard to determine given that it has been different for each device fabricated for this thesis.

5.4.2 Experimental implementation

Using the simple but effective *Write/Erase* and *Read* techniques, multi-level access is experimentally demonstrated in Fig. 5.12a-c for four clearly distinct levels. The presented data were recorded in a $5\,\mu m$ long GST element, with each transition between levels being initiated by a single $100\,ns$ light pulse, manually and individually triggered. The four levels were reached with pulses of level-specific switching energies (i.e. the energy absorbed by the GST only) in the range 465 to $601\,pJ$ (see figure caption for specific details). Despite this cell being of similar size to that in Sec. 5.3.4, it obeys a different conditioning process, which is device specific and, for this case, optimised for intra-level transitions (See Sec. 5.5). For this reason, the transmission levels and pulse energies differ. In Fig. 5.12a, levels were reached in a serial manner and subsequently the *Erase* operation was carried out from Level 3. Furthermore, the same levels were also shown to be accessible in any combination from a lower to a higher level, as shown in Fig. 5.12b.

The *Erase* operation (i.e. to return to Level 0) was not only possible from the highest transmission state, but from any intermediate level as well, as shown in Fig. 5.12c. These results demonstrate that both *Write* and *Erase* operations, to and from any level, are possible with high accuracy, allowing a reliable multi-bit memory operation. This exciting and seemingly straightforward aspect of this photonic memory is particularly attractive because such arbitrary transitions are very difficult to achieve in electronic memories employing phase-change materials, where iterative write-and-erase algorithms involving multiple (typically 3 to 5) write/read(/re-write) cycles are needed to achieve a pre-defined level, adversely affecting the overall write speed and power consumption [105].

The number of possible levels in a memory cell, as explained in the previous section, is limited by the SNR of the read-out measurement. That being so, it was possible to increase the number of memory levels by using a higher read-out power ensuring a better SNR. This is demonstrated in Fig. 5.12d, where 8-levels of state discrimination (i.e. 3 bits per cell) within a single photonic memory cell are shown. Each level corresponds to a partial crystalline state, presenting a specific change in transmission by applying pulses with varying energies, as presented in Fig. 5.12e. Once again, a conditioning process was carried out, which implied a renormalisation in transmission that led to different figures for the change in read-out. The individual levels were reached with pulses P_n of level-specific energies in the range 372 to 601 pJ. In the same figure, it is observed that the difference between the transmissions of any two consecutive levels was much higher than the level uncertainty marked by the colour coded background. In Fig. 5.12d, it is also demonstrated that each level was reachable from both directions (i.e. with an amorphisation as well as a crystallisation step). This implies that any level is accessible from all others, with very accurate control of the transmission levels and remarkable repeatability, just by applying the appropriate *Write* pulse or *Erase* sequence. The total number of such pulses, all of 100 ns without a fixed pulse separation (each pulse was

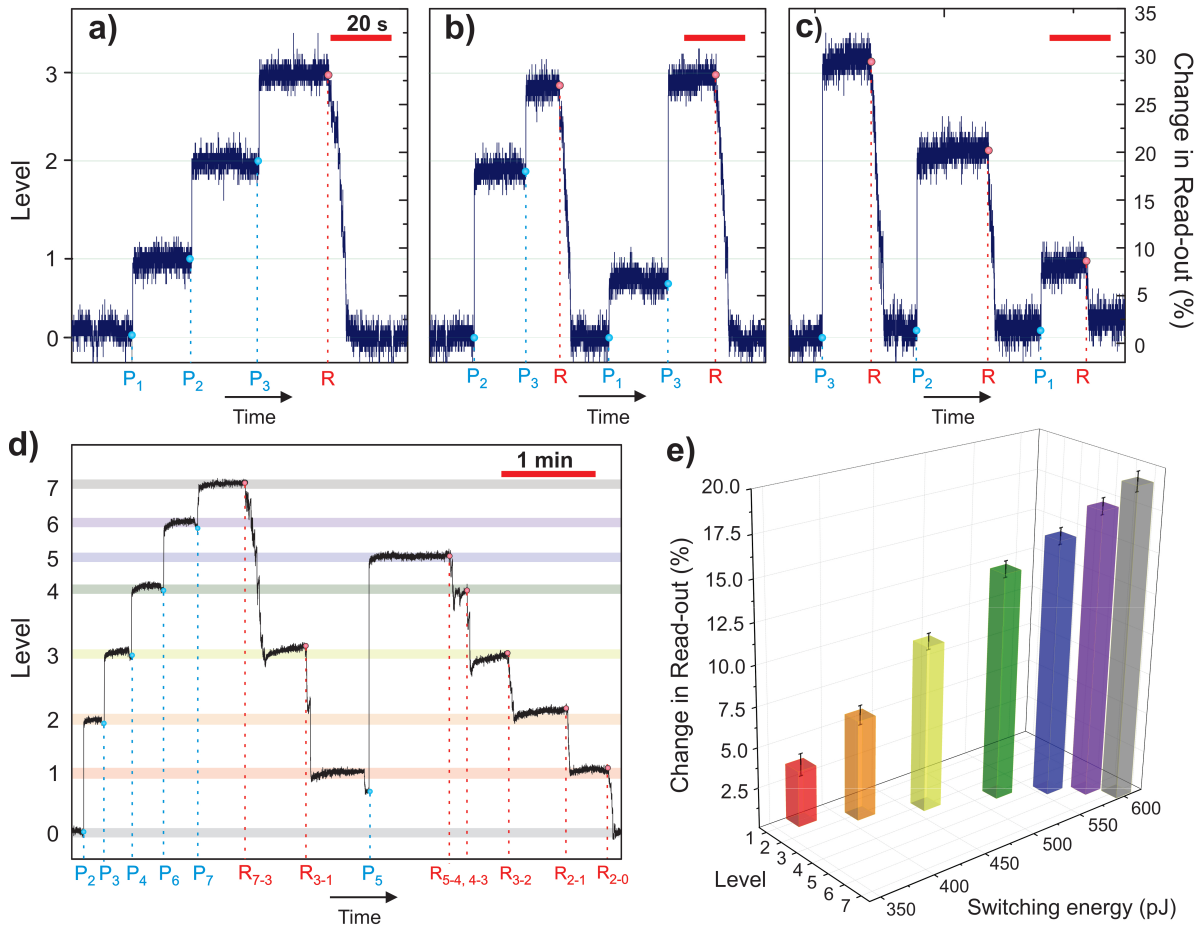

Figure 5.12: Multi-level operation of a phase-change photonic memory. a) Four clearly distinguishable levels were reached with $100\,ns$ *Write* pulses P_n of level-specific energy (i.e. Pulse power × pulse width) $E_{P_1} = (465 \pm 13)\,pJ$, $E_{P_2} = (524 \pm 14)\,pJ$ and $E_{P_3} = (585 \pm 14)\,pJ$ in a $5\,\mu m$ GST device. Levels are shown to be accessible in a) consecutive or b) arbitrary ascending order by the respective *Write* pulses P_n. c) Each level is also independently reached and erased. Scale bar in a)-c) is $20s$. d) Reducing the SNR by increasing the read-out power by a factor of 10 enables one to operate the same device as in a)-c) with 8-levels. The shaded areas correspond to the confidence interval of each level (i.e. the interval between two standard deviations and the central value for transmission) calculated from at least ten transitions. In addition, it is shown that each level m can be reached from a higher level n by applying a partial *Erase*, denoted here by R_{n-m}, which is described in the Sec. 5.3.2. Therefore, each level can directly be accessed from any other level. The energies for the Pulses P_n are those leading to Level n in subfigure e), following the same colour scheme ($E_{P_1} = (372 \pm 12)\,pJ$, $E_{P_2} = (415 \pm 13)\,pJ$, $E_{P_3} = (465 \pm 13)\,pJ$, $E_{P_4} = (524 \pm 14)\,pJ$, $E_{P_5} = (561 \pm 14)\,pJ$, $E_{P_6} = (585 \pm 14)\,pJ$ and $E_{P_7} = (601 \pm 15)\,pJ$). e) Relation between used pulse energy, addressed level and corresponding change in read-out transmission for the *Write* operations used in d). Error bars show the uncertainty in the level attainability.

sent manually), for any arbitrary transition in this 3-bit demonstration is shown in the following table:

Table 5.1: Number of *Write* and *Erase* light pulses required to switch between arbitrary levels in the 3-bit memory cell shown in Fig. 5.12d. The levels on the vertical axis represent the level number before either *Write* (if getting to a higher level) or *Erase* (if getting to a lower level). The levels on the horizontal axis represent the level to which the *Write* or *Erase* process is switching to. Any *Write*, i.e. $n \rightarrow n+1$ transition, is a single-shot process.

		To level							
		0	**1**	**2**	**3**	**4**	**5**	**6**	**7**
From level	**0**	-	1	1	1	1	1	1	1
	1	4	-	1	1	1	1	1	1
	2	7	4	-	1	1	1	1	1
	3	10	7	4	-	1	1	1	1
	4	13	10	7	4	-	1	1	1
	5	15	12	9	6	3	-	1	1
	6	17	14	11	8	5	3	-	1
	7	19	16	13	10	7	5	3	-

After the thermal excitation, the GST was found to require at least twice the time of the pump pulse in order to cool down, as described in the optical switching dynamics in Sec. 5.2. Therefore, from the figures in Table 5.1, *Write* time was $200\,ns$ for any transition, given that a single $100\,ns$ light pulse is enough. However, *Erase* times were $800\,ns$ or $600\,ns$ for transitions $n \rightarrow n-1$ (either 4 or 3 pulses were enough) and $3.8\,\mu s$ in the maximum transition $7 \rightarrow 0$ (19 pulses). These times were decreased by using pulses of $20\,ns$ and $50\,ns$ with successful multi-level performance at the cost of lower number of levels (3 and 5, respectively) and lower contrast transitions. Although there is plenty of room for improvement, all these capabilities already provide a leap forward in terms of functionality and will be crucial for the realisation of practicable photonic memories.

5.4.3 Modulation depth

The modulation depth is defined as the static change in optical transmission for a particular memory cell upon switching. The modulation depth is stated with respect to the read-out transmission of the base (Level 0) crystalline state. The switching energy, on the other hand, is defined as the amount of absorbed optical power (calculated from the known GST absorption and the total energy of the pump-pulse before the interaction) required for this phase-transition. In phase-change photonic memories, the contrast of the transmission levels before and after switching depends on the dimensions of the PCM element. Short PCM sections provide low optical attenuation and therefore high transmission. In this configuration, the contrast in transmission between the amorphous and the crystalline state is notably small, which limits the number of achievable memory levels. On the other hand, shorter PCM devices require lower energies to switch the material. In the following, two types of devices based on GST with a length of $1\,\mu m$ and $5\,\mu m$, respectively, are compared in terms of the required switching energy and read-out contrast. The results are summarised in Table 5.2. With $5\,\mu m$ long GST devices, high contrast up to 58.2% is obtained using long pulses of $200\,ns$ duration. In this case, the switching energy amounts to $596\,pJ$. For $1\,\mu m$ long devices, the maximum contrast reaches 16% when using $200\,ns$ long pulses, at a lower switching energy of $194\,pJ$. A higher transmission contrast can therefore be obtained at the expense of higher switching energy and larger footprint.

The values presented in Table 5.2 correspond to multilevel memories that were controlled using the *Write/Erase* process described in Sec. 5.3.1 and 5.3.2, with the pump-probe experimental scheme presented beforehand in Ch. 4. In particular, other devices including memory cells with $0.5\,\mu m$, $1\,\mu m$, $5\,\mu m$ and $10\,\mu m$ long, $1.3\,\mu m$ wide, and $10\,nm$ thick GST, were fabricated and tested. It was found, following the same conclusion as in

Table 5.2: Multilevel modulation depth

	$1\,\mu m$ **GST**		$5\,\mu m$ **GST**	
Attenuation	-0.97 dB		-7.14 dB	
Pulse Length(ns)	**Max. Contrast (%)**	**Min. switching energy (pJ)**	**Max. contrast (%)**	**Min. switching energy (pJ)**
10	0.67 ± 0.50	13.4 ± 0.6	1.8 ± 2.0	42.0 ± 0.3
25	2.34 ± 0.52	30.1 ± 1.3	9.9 ± 2.5	105.2 ± 0.7
50	3.60 ± 0.50	48.5 ± 2.6	16.8 ± 2.4	186.7 ± 0.7
100	8.60 ± 0.48	97.2 ± 5.1	31.8 ± 2.2	298.0 ± 2.0
200	16.2 ± 0.46	194 ± 10	58.2 ± 2.0	596.0 ± 4.0

Table 5.2, that transmission-level distinguishability upon switching (i.e. level contrast), is directly proportional to the cell dimensions. Short cells, shorter than $800\,nm$ along the waveguide axis, present low insertion loss due to an attenuation coefficient that scales down with the size. Therefore, for these short memory cells, higher SNR transmission signals are measured, which is favourable for detecting small phase-changes in GST. However, the contrast between the transmission in the amorphous and the crystalline states also scales down with size [27]. Hence, only when most of the GST is amorphised is the change in transmission significant enough to be differentiated from the fully crystalline state, which in turn limits the number of reachable intermediate levels. This effect was visible in the smallest devices, with $0.5\,\mu m$ long memory cells, for which pulses that provide switching energies greater than $120\,pJ$ could induce switching to a distinguishable state, but the contrast was not enough to establish intermediate levels in between. Alternatively, detectors with better SNR could be employed to distinguish several levels within small variations in transmission. On the other hand, when using very long GST cells, such as $10\,\mu m$, the probe signal is almost completely absorbed. Accordingly, the SNR for the readout pulse is poor and the transmission measurements become challenging. The solution in this case is to use higher energy *Write* pulses to amorphise large GST areas until transmission variations overcome the noise and become distinguishable. In conclusion, the longer the GST, the better the contrast between levels, but the lower the probe transmission signal.

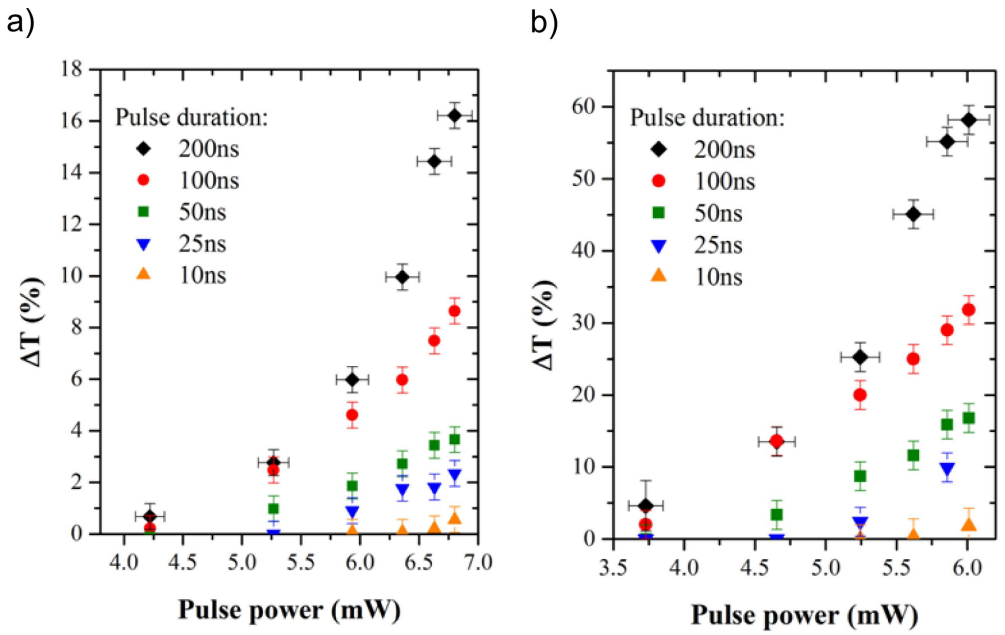

Figure 5.13: Change in transmission (ΔT) as a function on pulse power and pulse width. a) The measured change in transmission. Data are shown for devices with GST cells with lengths of $1\,\mu m$ in a) and $5\,\mu m$ in b).

Given that the goal is to obtain low-energy yet fast memory operation, GST lengths in between $1\,\mu m$ and $5\,\mu m$ were found to be optimum. This length range offers the ideal trade-off between level contrast and measurable signals. Moreover, these dimensions allowed for fast operation, as shown in Fig. 5.13, where *Write* pulses, as short as $10\,ns$, were successfully employed with switching energies as low as $13.4\,pJ$. The results plotted in Fig. 5.13b for $100\,ns$ pulses correspond to the same situation illustrated in Fig. 5.12 for the 8-level memory operation. The measurements in this figure were carried out on the same two memory devices, thus demonstrating that after the conditioning process each memory can be operated with a different set of pulses conserving the level structure and able to return to the same crystalline Level 0. After every *Write* step towards a fixed transmission point in the plot, there followed an *Erase* process towards Level 0 before achieving the next level. With this approach, every level can be independently addressed with high reproducibility. Contrasts of up to 60% were demonstrated for $5\,\mu m$ long GST

devices in Fig. 5.13b as the pulse energy reached nearly $1200\,pJ$.

5.5 Conditioning process

The accurate reproducibility of the level memory operation is ensured by an initial conditioning step. If a complete *Write/Erase* cycle, as described in Sec. 5.3.1 and 5.3.2, turns out to reach a minimum transmission level T_0' lower or higher than the starting point T_0, then the cycle needs to be repeated several times. Within the first few cycles, the read-out transmission, which initially varies slightly from cycle to cycle, stabilises to a fixed value (within a confidence margin), thus conditioning the material to a particular and unique series of pulses that are sent during both processes. The conditioning process can be changed at any time. In Fig. 5.13, for instance, two memory cells were successfully conditioned several times to operate for each different pulse width and power.

The conditioning process is key to guarantee the correct operation of the memory. Even after annealing, the GST cell may not be completely crystalline and only after conditioning is a true minimum of transmission achieved, as obtained in the measurements in Fig. 5.14a. This minimum sets the basis for the other levels. When realising the conditioning of the material, defects may appear as the result of poor fabrication or exposure to the environment. A common problem is oxidation, which may take place when the GST is heated up by the pulse and exposed to the O_2 in air, at the same time. Over time, as more material oxidises, the phase switching is prevented, levels are not reproducible, and the lower transmission level increases as the crystalline materials becomes less absorptive, as plotted in Fig. 5.14b. Eventually, oxidation will take place over the whole GST junction—or the active area—and the transmission will be completely static. Moreover, if high-energy pulses are employed, ablation may also take place. In this case, shown in Fig. 5.14c, high and irreversible transmission jumps occur, which

should not be confused with large amorphisation. In the case of long transmission jumps due to ablation, it is still possible to establish a conditioning that allows for memory operation with what is left from the material, although the original lower transmission level (or Level 0) cannot be recovered.

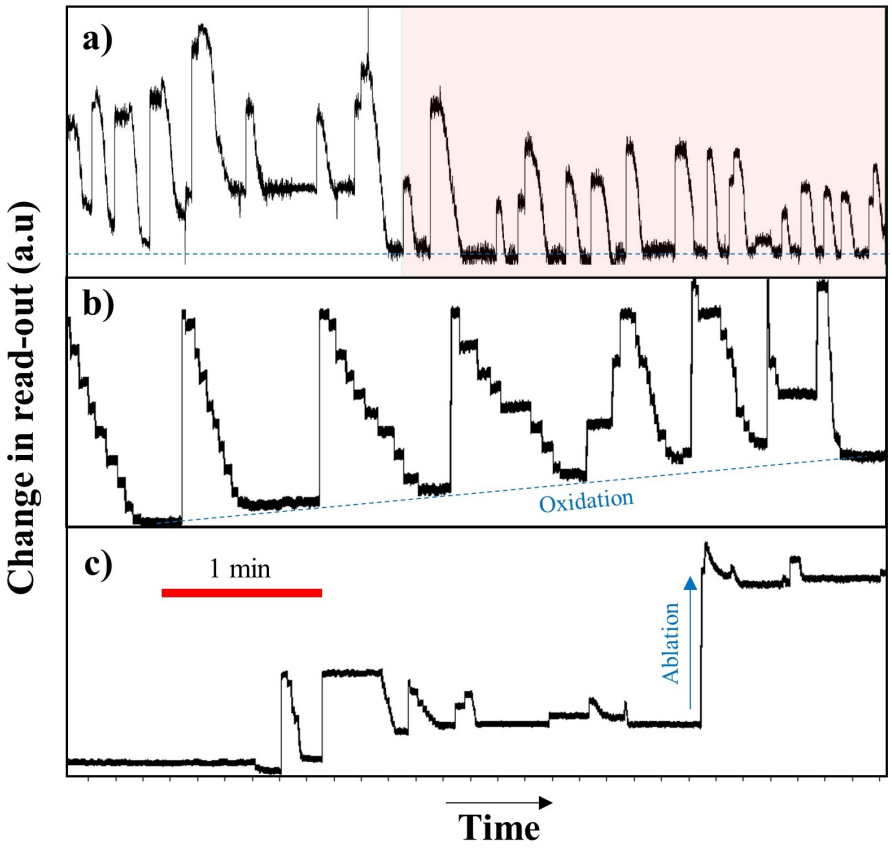

Figure 5.14: Conditioning process in a phase-change photonic memory with: a) correct operation, where a stable minimum of transmission (Level 0) is reached and higher transmission levels are repeatedly achieved (highlighted in the shaded area); b) GST oxidation problems, which does not allow for a stable Level 0; and c) when high pulse power induces ablation and, thus, a big irreversible transmission change.

Furthermore, the conditioning process is the main reason why the memory operation is started from the crystalline state instead of the amorphous state. As-deposited amorphous GST is in a unique random state after deposition that cannot be reproduced once the material is partially or completely crystallised. Therefore, it is not reliable to start in such a state as it is unlikely to reach the same level after a couple of cycles. Moreover, if the

Erase process is started from as-deposited GST, then the train-like nature of this process (which will require high energies due to the low attenuation) means that eventually there will be a T_0 where the material will not crystallise further. However, even if the process is repeated several times in order to condition the material to specific transmission levels, many different T_0' are reached. When trying this experimentally, the crystallisation was leading to random levels of transmission that could not be controlled, and thus a memory application could not be built. This was experimentally found in the first efforts to build phase-change photonic memories before realising that rather than a top transmission level, what it was really needed was a reliable minimum, i.e. fully crystallised GST as the operational starting point. Starting from the crystalline state also guarantees lower operation energies due to the large absorption in this state.

5.6 Speed, energy, and drift considerations

Another crucial aspect of data storage is the energy consumption per bit. Since, in the phase-change photonic memory, both writing and erasing rely on phase transitions of the PCM, the switching energy is given by the amount of energy that is required to heat the GST above the melting (amorphisation) or glass-transition (crystallisation) temperature, respectively. Therefore, the energy consumption is directly related to the volume of the memory element and read-out contrast. This relationship between switching energy and read-out contrast is shown in Fig. 5.12e. In binary operation, a read-out contrast of 21% with $430\,pJ$ switching energy was obtained (See Fig. 5.11). On the other hand, switching energies as low as $13.4\,pJ$ were measured for a reduced contrast of 0.7%, which still enabled a clear distinction of the two levels (See Table 5.2). This energy consumption can be improved by up to one order of magnitude by operating the memory with sub-nanosecond instead of tens of nanosecond pulses. The thermo-optical analysis presented in Ref.[67] estimates that the portion of absorbed energy that gets lost due to thermal

diffusion increases significantly with increasing pulse width. Therefore, shorter and more intense pulses would be beneficial in terms of energy requirement by quickly heating up the PCM to the required transition temperature while reducing thermal diffusion losses.

In this very first prototype of a phase-change all-photonic memory, the energy consumption and speed achieved in these experiments compares well with pre-existing electrical counterparts. For example, current commercial PCM-based electrical memories (at the $45\,nm$ node) typically require SET pulses of $50-100\,ns$ duration and RESET pulses of 10 ns (considerably longer than the $10\,ns$ write and $/500\,ps$ read, if using pulses instead of CW[67], for the operation of this photonic memory), along with $5-10\,pJ$ write energy (c.f. $\approx 13\,pJ$ here). Research-level electrical devices improve on such performance figures (e.g. $3.4\,pJ$ write energy and $20\,ns$ write pulses in Ref. [46]). The performance of phase-change photonic memories can be more energy consuming if opto-electronic conversion is further required in hybrid chip architectures. Moreover, the transmission contrast between states (up to 60 % in photonic memories) is low compared to the three orders of magnitude in resistance change in electrical memories. The photonic memory can, however, be further improved by operating them with shorter pulses and by moving to devices with a smaller footprint, as well as through the development of new materials with faster and lower temperature switching. Higher signal-to-noise ratio to improve the read-out contrast could also be obtained with the use of optical cavities, which would also reduce switching energies, as discussed theoretically in [26].

In addition, level drift has been a significant issue when employing phase-change materials in memory applications. This effect is well known in electronic PCM-based memories, in which the atomic configuration of the melt-quenched amorphous phase as a whole collectively relaxes towards a more favourable equilibrium state, thus having a temporal evolution of the resistance [106]. In optical memories, however, there is not yet any strong

evidence of drift given that such collective relaxation does not imply a significant change in refractive index. Preliminary results from the experiments done within this project suggest that there is a variation of 1 % in transmission over $10^5\,s$; however, systematic experiments are required to confirm this, given that there are other factors, such as fibre array - Bragg grating misalignment over time (due to pico-motors relaxation) that contributes to this change. Other experiments, using ring-resonators with near-field coupling, similar to the experiments presented herein, have found the same transmission level after 3 months ($\approx 10^7\,s$) [67], thus proving the non-volatility nature of the phase-change photonic memories. Despite the lack of experimental evidence around optical drift, the CD and DVDs, which are based on optical measurements, provide a good insight into how durable and reliable GST is in terms of optical operation.

5.7 Summary

This chapter has presented the fundamentals and experimental implementation of near-field light coupling to low-dimensional phase-change memory elements integrated onto silicon nitride waveguides. FEM computational simulations were realised for a qualitative description of the propagating mode coupling to amorphous and crystalline GST, the electromagnetic heat transfer, and the amorphisation and re-crystallisation processes. Moreover, the experimental implementation of such devices using a pump-probe setup has led to the first prototype of an integrated, all-photonic, truly-non-volatile memory that provides multi-level storage in a single cell. The ability to switch readily and directly between the multiple memory levels was demonstrated with accurate control of the readout signal and excellent repeatability. Furthermore, the capability for fast ($\approx 10\,ns$), low energy ($\approx 13\,pJ$), and single-shot readout of the memory state, along with repeated *Write/Erase* cyclability—while maintaining high readout contrast—has also been demonstrated.

Chapter 6

Phase-Change Optoelectronics: bistable nanodisplays

This chapter describes the implementation of $Ag_3In_4Sb_{76}Te_{17}$ (AIST) and $Ge_2Sb_2Te_5$ (GST), growth- and nucleation-dominated phase-change alloys, respectively, in multilayer optical cavities for colour modulation in uniform surfaces and nanoscale pixels. In particular, depth-modulation capability (i.e. grey-scale) is demonstrated for the first time for phase-change-based displays. The limits of this technique are also studied in terms of resolution and switching energy, together with a comparison between the performance of AIST and GST as candidates for bistable nanodisplay materials.

6.1 Modelling and design

Thin-film optics theory is required for understanding the operation of the optical cavities and the way colour modulation is performed. To do so, the total reflectance of a multilayer stack can be calculated from the interferences that take place locally in each of the layers

[50]. This particular algorithm is based on a transfer-matrix method, which is presented in the following section, together with its computational implementation to design the samples and optimise their characteristics. In particular, this section will study the simulations carried out for samples containing both GST and AIST. However, for the sake of simplicity, and given the similarity in their optical properties, some computational results will be plotted for one material but not for the other.

6.1.1 Transfer Matrix

A total of q layers, with complex refractive index and arbitrary thickness, are considered to be stacked in the z-direction while being infinitely extended in the other two orthogonal coordinates. From the continuity condition of the tangential electric (E) and magnetic (H) fields at each film boundary and the directionality of the incident radiation, the transmittance, reflectance, and absorptance can be computed by means of the transfer-matrix formulation. The electromagnetic fields propagating through the bottom interface towards the substrate (given by the amplitudes E_{subs}, H_{subs}) and reflected towards air (given by E_{air}, H_{air}) are obtained from the product of the matrices carrying the contribution of the local interference in each intermediate thin-film layer. They are given by the equation (for more details see [50]):

$$\begin{bmatrix} E_{air}/E_{subs} \\ H_{air}/E_{subs} \end{bmatrix} = \begin{bmatrix} B \\ C \end{bmatrix} = \left\{ \prod_{r=1}^{q} \begin{bmatrix} \cos\delta_r & i\sin\delta_r/\eta_0 \\ i\eta_0\sin\delta_r & \cos\delta_r \end{bmatrix} \right\} \begin{bmatrix} 1 \\ \eta_m \end{bmatrix}, \tag{6.1}$$

where $\delta_r = \frac{2\pi d_r}{\lambda}\left(n_r^2 - k_r^2 - n_0^2\sin^2\vartheta_0 - 2in_rk_r\right)$ is the phase difference introduced to the light after propagating through film r ($r = 1, 2, ..., q$, 1 being the topmost layer) of thickness d_r with complex refractive index $\overline{n}_r = n_r + ik_r$. The beam strikes the first layer at an angle ϑ_0. η_r is the tilted optical admittance, either $\eta_r = \gamma n_r\cos\vartheta_r$ for Transverse Electric (TE) or $\eta_r = \gamma n_r/\cos\vartheta_r$ for Transverse Magnetic (TM) polarised incident light, with γ being the optical admittance in vacuum, defined in terms of the electrical

permittivity ε_0 and the magnetic permeability μ_0 as $\gamma = (\varepsilon_0/\mu_0)^{1/2} = 2.6544 \times 10^{-3}\,\Omega^{-1}$. The sub-index m refers only to the substrate medium, q stands for the total number of layers, and the sub-index 0 for the incident medium. From the transfer matrix and by introducing appropriately the wavelength, incoming angle, refractive index, and thickness of each layer, the total reflectance (R), transmittance (T) and absorptance (A)—constrained by energy conservation: $R + T + A = 1$—can be computed from [50]:

$$R = \left|\frac{\eta_0 B - C}{\eta_0 B + C}\right|^2, \quad T = \frac{4\eta_0 Re(\eta_m)}{|\eta_0 B + C|^2}, \quad A = \frac{4\eta_0 Re(BC^* - \eta_m)}{|\eta_0 B + C|^2}. \tag{6.2}$$

R, T, and A are in general wavelength-dependent functions; therefore Eq. 6.2 should be computed for every wavelength within the spectral range of interest.

6.1.2 CIE XYZ tristimulus: from spectra to colour

In 1931, the International Commission on Illumination (or CIE from its original name in French) created the CIE 1931 colour spaces, the first attempt to quantitatively link wavelengths in the electromagnetic spectrum to colours perceived by the human eye. The mathematical relationships that define these colour spaces allow to convert the real physical response of our eyes—when exposed to inks, displays, etc.—into a universal numerical colour tool. This, in turn, allows the inverse engineering problem: to design inks or devices to obtain a particular colour response in the human eye [209, 210].

The CIE XYZ tristimulus, in particular, is a colour space that encompasses all sensations that an average person can experience. It serves as a standard reference against which many other colour spaces are defined. Y is defined as the luminance. Z is an approximated value to the blue stimulation, or the S (small) cone response, in a healthy human retina. X is a linear combination of cone-response curves chosen to be non-negative [210]. This, considering that the average human eye has three types of cone cells responsive to light,

with spectral sensitivity peaks in short (S): $420 - 440\,nm$, middle (M): $530 - 540\,nm$, and long (L): $560 - 580\,nm$ wavelengths.

In the case of reflective samples for display applications, the illumination provided by a given light source is characterised by its energy distribution $D(\lambda)$. In this chapter, in particular, the CIE normalised illuminant $D65$ will be considered. This particular energy distribution closely matches the daylight spectrum, thus allowing to simulate how samples will look when viewed by the naked eye in normal, natural conditions. Assuming that the sample has a reflectivity $R(\lambda)$, which can be computed for multilayer stacks from the algorithm presented in Sec. 6.1, it is possible to calculate the CIE XYZ tristimulus values for reflectance, according to:

$$X = \frac{1}{k}\int_{Vis} D(\lambda)R(\lambda)\overline{x}(\lambda)d\lambda, \quad Y = \frac{1}{k}\int_{Vis} D(\lambda)R(\lambda)\overline{y}(\lambda)d\lambda, \quad Z = \frac{1}{k}\int_{Vis} D(\lambda)R(\lambda)\overline{z}(\lambda)d\lambda, \tag{6.3}$$

where *Vis* stands for the visible spectrum in a typical human eye (i.e. wavelengths in the $390 - 700\,nm$ range), in which the integrals are evaluated. The weighting functions $\overline{x}, \overline{y}, \overline{z}$ are the standard CIE spectral tristimulus values [209] and k is a normalisation factor defined in such a way that an object with a uniform reflectivity $R(\lambda) = 1$ gives a luminance component $Y = 1$, thus taking the form:

$$k = \int_{Vis} D(\lambda)\overline{y}(\lambda)d\lambda. \tag{6.4}$$

Since the human eye has three types of colour sensors that respond to different ranges of wavelengths [211], a full plot of all visible colours would require a 3D figure. However, a colour can be divided into brightness and chromaticity. While two colours can present the same chromaticity, their brightness can differ; an example being white and grey. Therefore, if only the chromaticity is considered, a 2D figure or "colour gamut" can be

built in representation of the colour perceived by the human eye without brightness information [212]. This chromaticity is defined by the parameters x and y, two of the three normalised values which are functions of the XYZ tristimulus:

$$x = \frac{X}{X+Y+Z}, \quad y = \frac{Y}{X+Y+Z}, \quad z = \frac{Z}{X+Y+Z} = 1 - x - y. \tag{6.5}$$

In the numerical calculations to find x and y, and to plot them on the colour gamut map, all the integrals are replaced with discrete sums. In particular, to perform this calculations, the function $r2xyz$ written for Matlab was used [213]. Also, the wavelengths that will be considered in this chapter lie in the range $350 - 800\,nm$. This is done to obtain more details of the near infra-red and ultraviolet spectrum beyond the average human eye bandwidth.

6.1.3 Colour modulation

Highly absorbing materials have been historically avoided in optical coatings, given that light propagation through such media undergoes strong attenuation, and often high reflectance. However, it was recently demonstrated that those materials with low dimensionality—a few nanometers, thin enough to avoid significant absorption—can induce strong interferences, enabling colour-related effects [55]. Notwithstanding the considerably large refractive index and extinction coefficient of both AIST and GST (See Sec. 2.1), ultra-thin films of around $10\,nm$ samples are, following the same principle, capable of achieving functionalities such as anti- or high-reflection, and dichroism. In particular, colours can be obtained in both reflection and transmission modes by considering multilayer stacks that involve multiple reflections using transparent layers and at least one ultra-thin phase-change materials—each layer having a thickness smaller than the wavelength, as will be shown below.

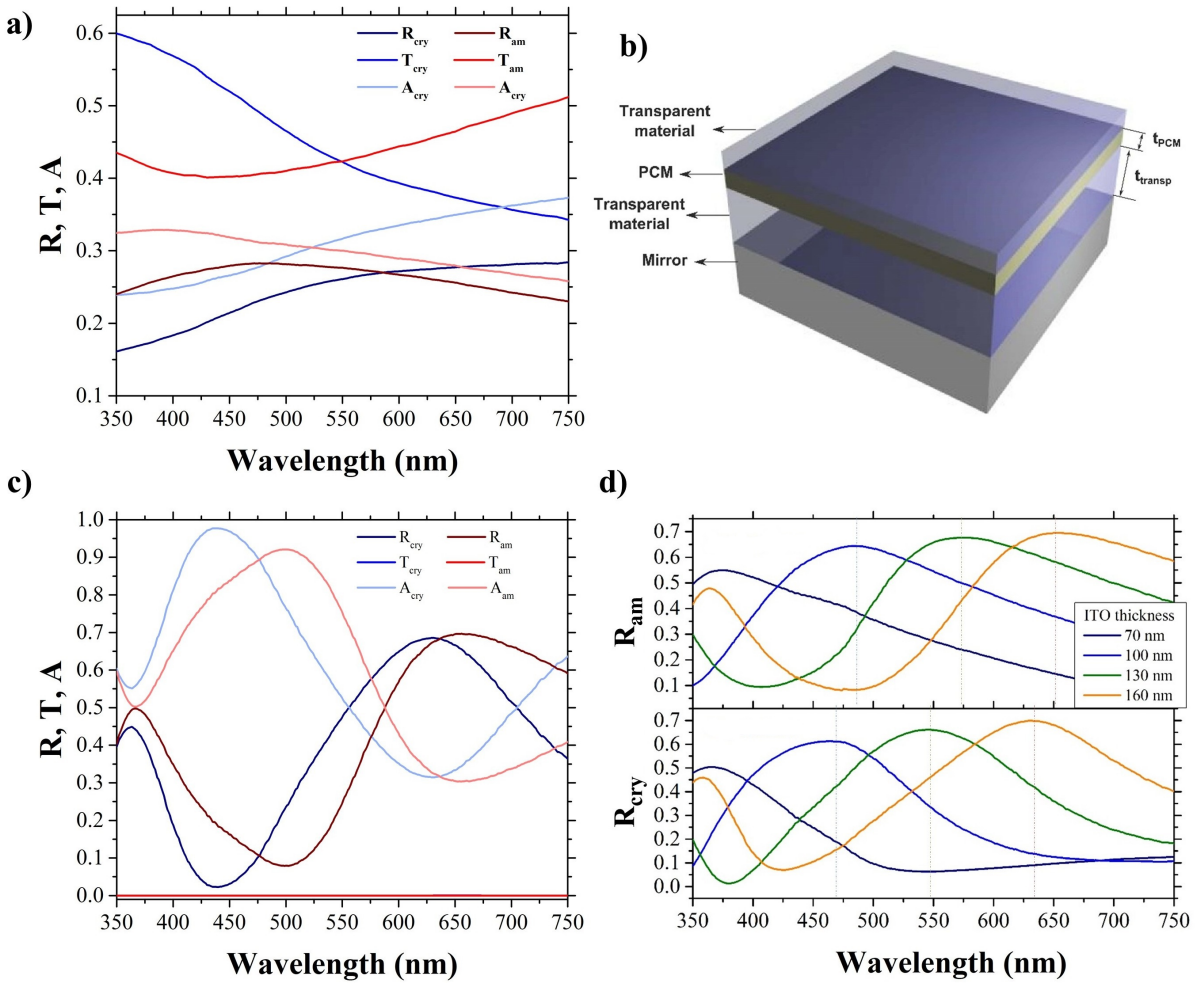

Figure 6.1: Phase-change-based optical-cavity computational modelling. a) Simulation of air/10 nm ITO/7 nm AIST/160 nm ITO/air under normal incidence. b) Sketch of the multilayer stack considered in this thesis featuring a bottom mirror. c) Same sample and conditions as a) but including a Pt mirror at the bottom. d) Spectra for samples with varying bottom ITO thickness: 10 nm ITO/7 nm AIST/t_{ITO} ITO/Pt mirror for $t_{ITO} = 70, 100, 130$ and 160 nm in both the amorphous and the crystalline state.

To calculate the reflectance, transmittance, and absorptance of any multilayer stack containing GST and AIST phase-change materials, the transfer-matrix formalism presented in Sec. 6.1.1 was used. The generality of this method gives an account of all the possible interference effects that occur inside the layers, including the Fabry-Perot-type, which dominate inside the optical cavities formed between two absorptive layers [33]. To do so, a customised code was implemented on MATLAB, such that an arbitrary number of layers with arbitrary complex refractive indices could be studied. In addition, it allowed

control of the physical parameters for the light source, such as incident angle, polarisation, intensity, and wavelength(s). This code was tested and calibrated by comparing to experimental data, as shown in Sec. 6.3. Fig. 6.1a shows a typical output of this modelling tool for a multilayer stack of indium-tin oxide (ITO)/AIST/ITO, with air as the incident and substrate medium. In this case, different values are obtained for R, T, and A, depending on the phase state of the AIST. However, if a particular colour needs to be enhanced in reflection mode, it is important to use a mirror at the bottom. In this case, the optical cavity is created between the real AIST layer and a virtual one: its own mirror reflection. This cavity, sketched in Fig. 6.1b, enhances Fabry-Perot effects and thus allows for constructive interference at wavelengths that can be chosen by tailoring the thickness of the layers, as calculated in Fig. 6.1c. Under this layer configuration, $T = 0$ for all the wavelengths due to the addition of the mirror; hence the energy is either absorbed by the phase-change material or reflected back to air. In the computation for samples with and without a mirror, normal incidence was considered; therefore, the type of polarisation had no relevance.

In a more realistic model, and taking into account that electrical switching is necessary, the final configuration chosen for the stack consisted of—from bottom to top—a mirror made out of Pt or Al, a transparent conductive (ITO) layer, a phase-change material thin film, and a thin transparent capping layer (ITO). The reflected colour (i.e. the wavelength at the reflectance spectrum maximum) is chosen by varying the thickness of the bottom transparent layer, ITO in this case, as shown in the results of Fig. 6.1d. Moreover, the same figure shows colour modulation on switching the AIST from the amorphous to the crystalline state. The contrast between the reflectance at the amorphous and the crystalline phase state is defined by the PCM thickness, as explained in Sec. 6.1.4.

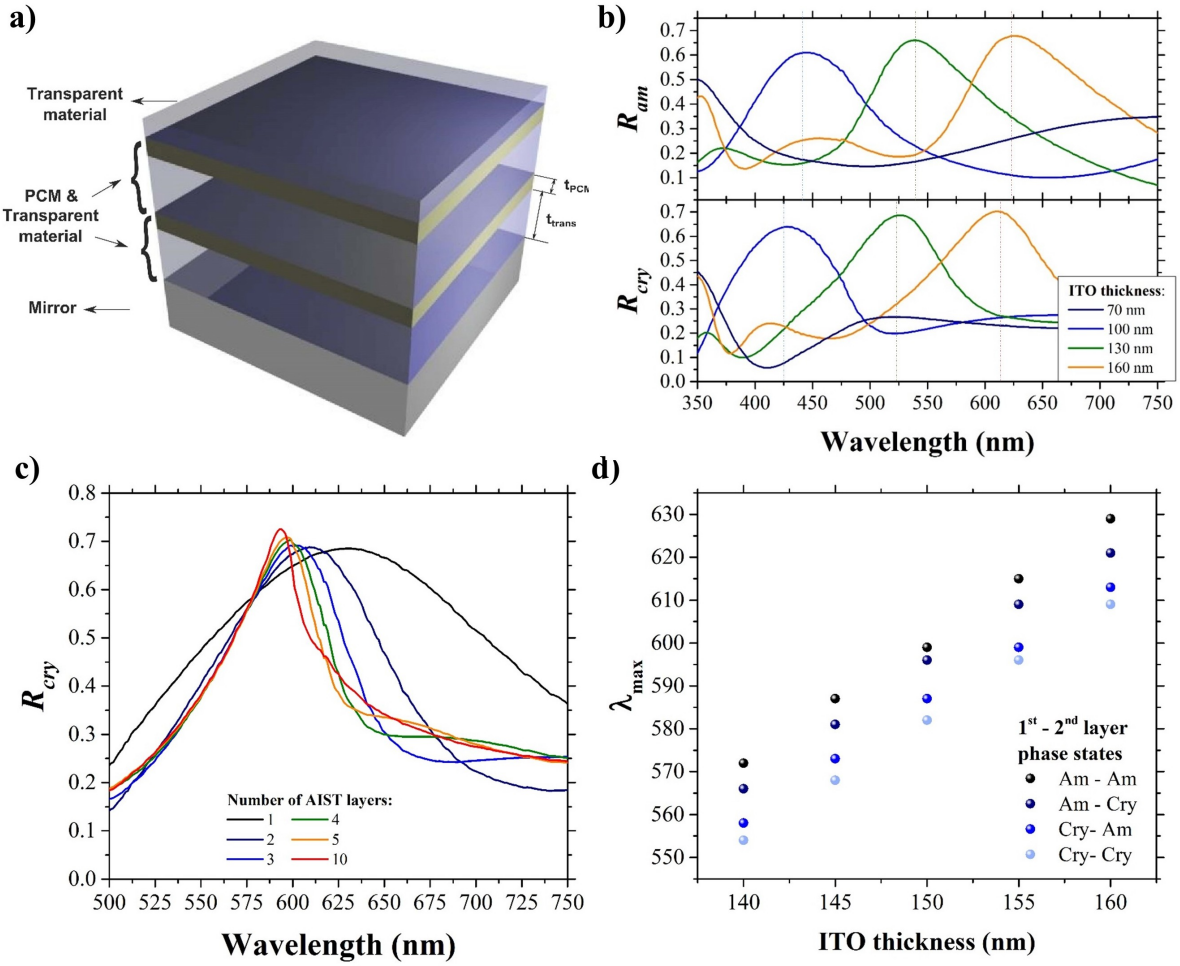

Figure 6.2: Modelling of optical cavities with more than one phase-change material layer. a) Sketch of the multilayer stack considered in these simulations. b) Spectra for samples with $10\,nm$ ITO/$7\,nm$ AIST/t_{ITO} ITO/$7\,nm$ AIST/t_{ITO} ITO/Pt mirror, $t_{ITO} = 70, 100, 130$ and $160\,nm$ when both layers are in the amorphous and the crystalline state. c) Reflectance-peak evolution as $1, 2, 3, 4, 5$ and 10 AIST/ITO pair of layers are added on top, plotted only for the crystalline phase. d) Wavelength at the spectrum maximum variation for samples: $10\,nm$ ITO/$7\,nm$ AIST/t_{ITO} ITO/$7\,nm$ AIST/t_{ITO} ITO/Pt mirror, with $t_{ITO} = 140, 145, 150, 155$ and $160\,nm$ as result of the four possible combinations of phase-states of both AIST layers.

Successive identical layers including more than one phase-change material can be added on top to improve the quality of the reflected colour, i.e. to get narrower reflectance spectrum peaks, by improving the confinement of light within the cavity and turning the sample into a one-dimensional photonic crystal cavity [214]. Considering the sample shown in Fig. 6.2a, with two AIST/ITO pair of layers of identical thickness, different reflectance spectra were obtained when varying the thickness of both ITO layers simultaneously

and considering the same phase-states for both PCM layers (amorphous-amorphous or crystalline-crystalline), as plotted in Fig. 6.2b. There is a clear improvement over its single AIST layer counterpart in Fig. 6.1c, where broader peaks and thus less defined colours were obtained. This process can, in principle, be repeated for n-layers of AIST in order to improve the reflected colour even further, as shown in Fig. 6.2c for 1, 2, 3, 4, 5 and 10 layers of crystalline AIST. It is, however, important to add that, as PCM layers are added, the absorptance becomes larger (due to their extinction coefficient), as well as possible losses due to accumulated defects in fabrication. Finally, another advantage of using multiple layers is that multiple reflected colours can be obtained from the same sample by switching the PCM layers individually. In the case of two AIST (or GST) layers, for instance, four combinations are possible: amorphous-amorphous, amorphous-crystalline, crystalline-amorphous, and crystalline-crystalline. However, the difference in terms of wavelength at the maximum reflectance peak are small, as shown in Fig. 6.2d, which means that the four colours would look similar to the naked eye. Further development and parameter optimisation is required in order to obtain better colour modulation in this latter layer arrangement.

Furthermore, using the computational values for the reflectance spectra of samples with one and two AIST layers, all the achievable colours using the XYZ tristimulus values were calculated. To do so, the reflectance data were converted into XYZ values using the MATLAB function *r2xyz* [213]. This software is capable of realising the calculations discussed in Sec. 6.1.2 and adds tools, such as plotting directly on a colour gamut map. Using this tool, the colour maps shown in Fig. 6.3 were calculated for different thicknesses of the phase-change material and the ITO, only when the AIST layers are crystalline. The real colours that the human eye would perceive are the same displayed on this colour map, from where it is clear that better colour selection is achieved with two layers of AIST instead of one, but only when the AIST thickness is $\leq 6\,nm$.

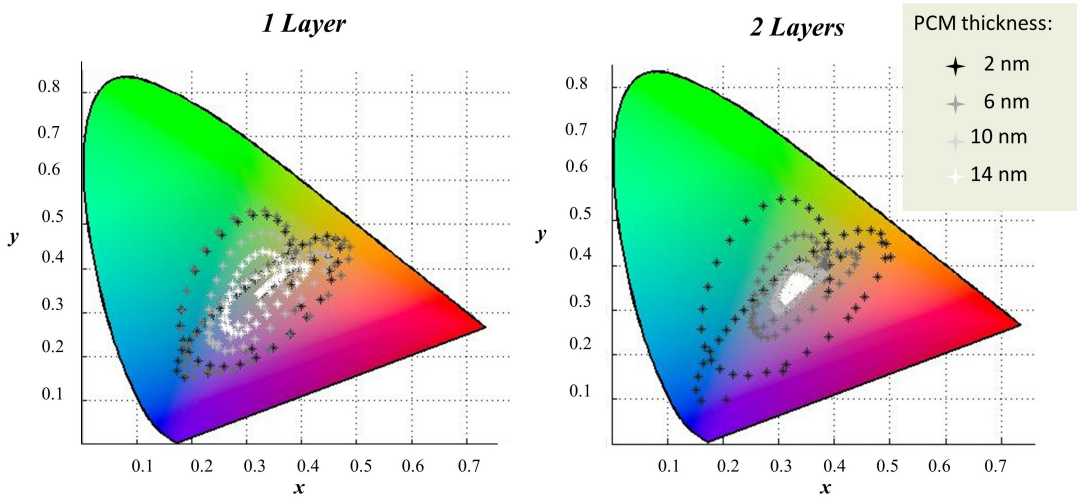

Figure 6.3: Full colour gamut calculated for samples containing crystalline AIST with different thicknesses and one or two PCM layers.

6.1.4 Colour contrast

Upon phase-change switching, the reflectance peak undergoes a blue-shift, as observed above in Fig. 6.1 and 6.2. Despite the shift, there is no significant contrast between the main wavelength (i.e. wavelength at the peak maximum) in one state, and the reflection at the same wavelength in the other, given the considerable width of the spectra—especially when using only one layer of either GST or AIST. However, the same configuration of layers allows for high contrast at other wavelengths, for example, at wavelengths that have negligible reflectance for either the amorphous or the crystalline state but is reflected when switched to the opposite state. Obtaining this information is important to improve the design of future high-contrast colour phase-change material-based displays and for applications in security marks where wavelength-sensitive measurements are carried out [123]. The contrast is defined as:

$$\Delta R_{\%} = \frac{R_{crystalline} - R_{amorphous}}{R_{amorphous}} \cdot 100. \tag{6.6}$$

Simulations were carried out to calculate $\Delta R_{\%}$ from reflectance data obtained using the transfer-matrix implementation in MATLAB, described in the previous section. In

particular, the code was used to calculate the values for the contrast under normal incidence while taking different values for the ITO spacer and PCM thicknesses. Given the similarity in terms of complex refractive index, as discussed in Sec. 6.4, similar contrast variations were observed for optical cavities featuring both AIST and GST. Their behaviour is qualitatively comparable making them equally good for any possible technological implementation. For this reason, only samples with GST are shown in Fig. 6.4. In this figure, the contrast scales vary rapidly as the GST gets smaller, reaching points where the contrast leads to $50,000$ times more transmission at $\lambda = 650\,nm$ in the crystalline than in the amorphous state, for a $250\,nm$ thick ITO spacer. As an example, using the data for one of the devices simulated in Fig. 6.1, the stack $10\,nm$ ITO/$7\,nm$ GST/$160\,nm$ ITO/Pt, there is a maximum reflectance peak at around $\lambda = 640\,nm$ in the crystalline and $\lambda = 675\,nm$ in the amorphous state. However, the maximum contrast, $\sim 200\%$, between those states is given at around $\lambda = 500\,nm$ (from Fig. 6.4 top-right).

6.1.5 Angular dependency

The colour reflected by a stack of thin layers is subjected to the angle of the incident light with respect to the surface normal. In the specific case of phase-change materials, alternating with transparent ITO films, it has been shown in previous sections that the reflected colour can be selected by engineering the thickness of the layers and can also be tuned by switching between the amorphous and the crystalline phase states. However, the light polarisation needs to be taken into account when considering light with oblique incidence. This effect originates from the dependence of the tilted optical admittance η_r on the polarisation: $\eta = \gamma n \cos\vartheta$ for TE or $\eta = \gamma n / \cos\vartheta$ for TM; this adopts the same value under normal incidence, in which case $\eta_0 = \gamma n_0$. Here, TE stands for the transverse electric—electric field parallel to the surface—- and TM for transverse magnetic fields—magnetic field parallel to the surface.

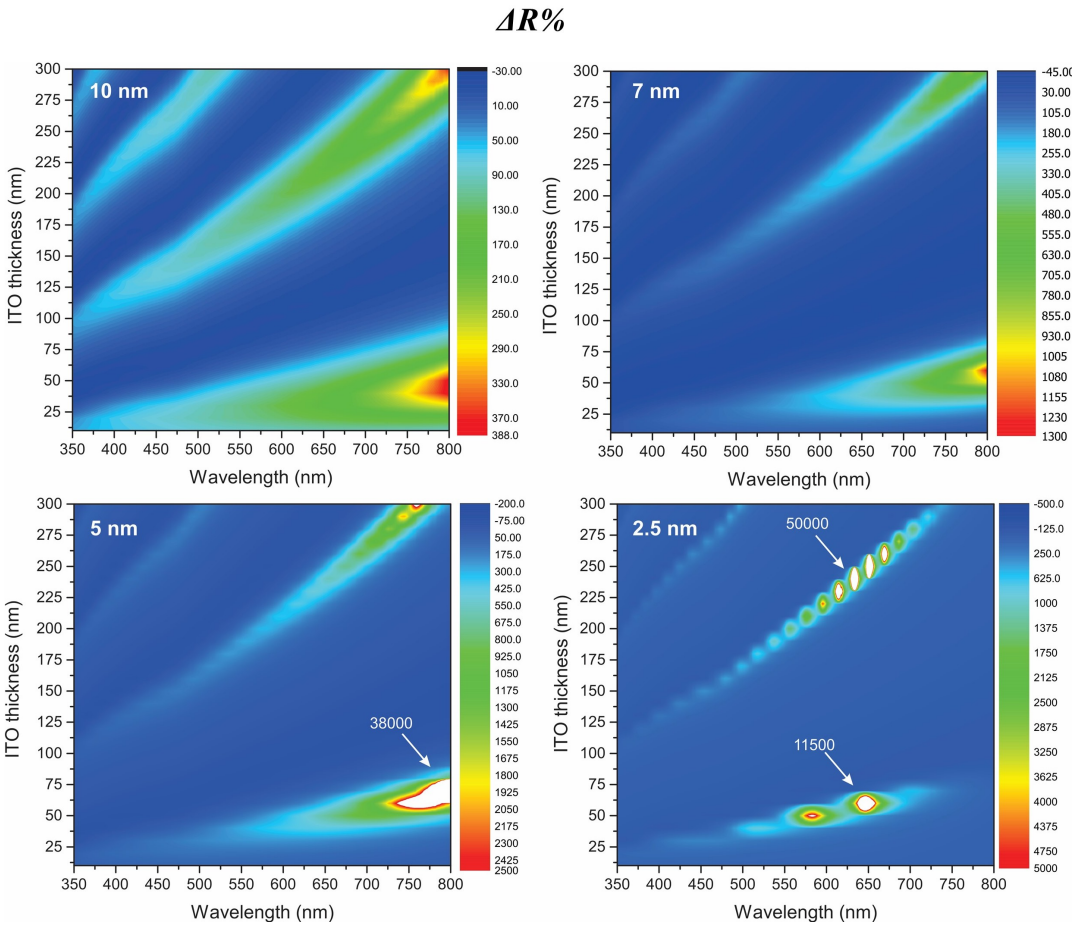

Figure 6.4: Contrast (colour bars) in reflectance between amorphous and crystalline states of 10, 7, 5 and 2.5 nm thick GST in a multilayer cavity. Negative values refer to higher reflectance in amorphous state from Eq. 6.6. The maximum contrast value in the scale bar was set to figures that allow good data visualisation of the map. However, it leaves the points in white out of range due to their high values, which are annotated separately.

To study the influence of oblique incidence on the samples shown in Fig. 6.1, computational modelling was carried out using a modified version of the MATLAB implementation of the transfer matrix (Eq. 6.1). In this case, the incident angle was swept from 0° to 90°, using 0.5° steps. Simulations were run accounting for both polarisations and both phase states of AIST in the configuration: 10 nm ITO/7 nm AIST/150 nm ITO/Pt mirror. The results are shown in Fig. 6.5. For TE light, it can be seen how the colour at $\vartheta_r = 0°$ presents initially a modest broad peak. As the incident angle increases, the spectra undergo a blue-shift and the reflectance peak gets even broader. Eventually, the

calculated spectra will "reflect" all the light when the angle is parallel to the surface, i.e. $\vartheta_r = 90°$ which is a measure of the accuracy of the code. On the other hand, for TM polarisation, the reflectance spectrum at normal incidence is the same as for TE but for some angles presents little or no light reflected as a result of reaching the Brewster angle [215], which cancels out all the incident light with this polarisation. Under random polarisation incidence, such as that from the sun, the reflectance is a superposition of both spectra.

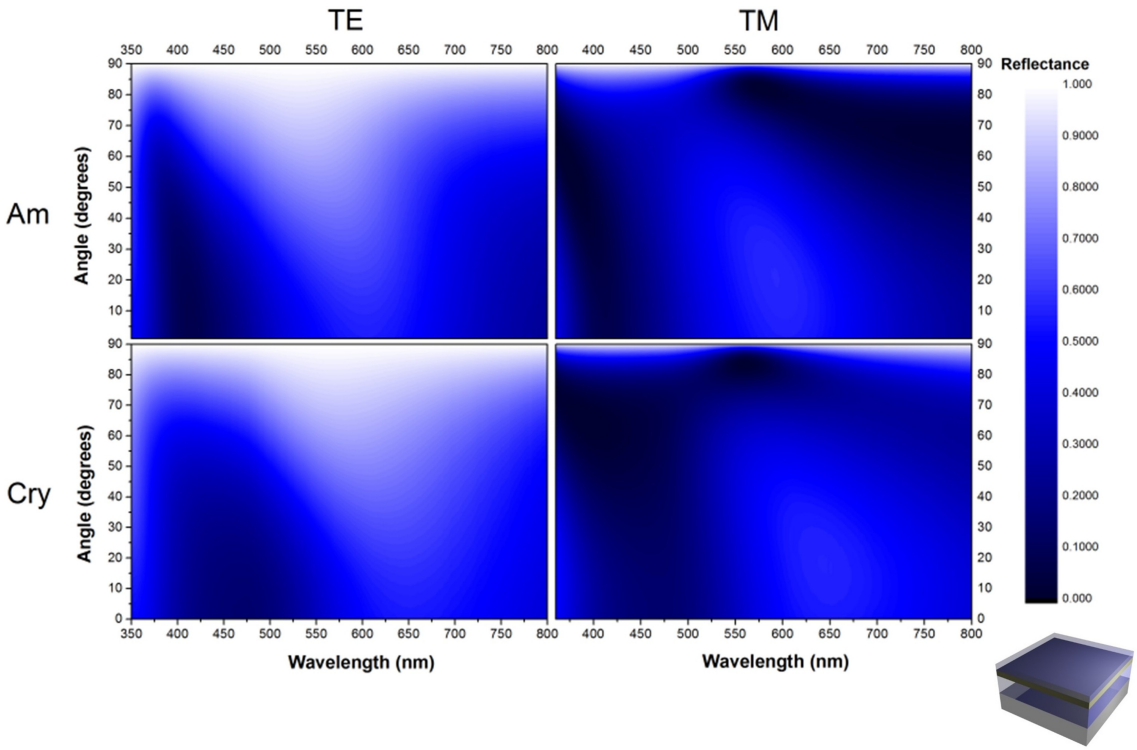

Figure 6.5: Calculations for the angular dependency of the reflected colour as a function of AIST phase state and polarisation, for the particular stack: 10 nm ITO / 7 nm AIST / 150 nm ITO/mirror (with a transmission centred in red colour). The angle is measured from the surface normal.

The selection of the colours (i.e. reflectance peaks in the spectrum) can be improved by increasing the number of layers in the stack, as mentioned in Sec. 6.1.3. This means that the width of the reflectance peak is reduced, offering a purer colour, as shown in Fig. 6.6 for two AIST layers, although a similar response to oblique incidence is observed. Using the stack 10 nm ITO/7 nm AIST/150 nm ITO/7 nm AIST/150 nm ITO/Pt mirror, the

colour under normal incidence is red, but when $\vartheta = 60°$, it is greenish. These colour variations could be useful in security systems, for instance, where tests are done under specific polarisations and angles on optical marks or security tags attached to notes, cards, etc.

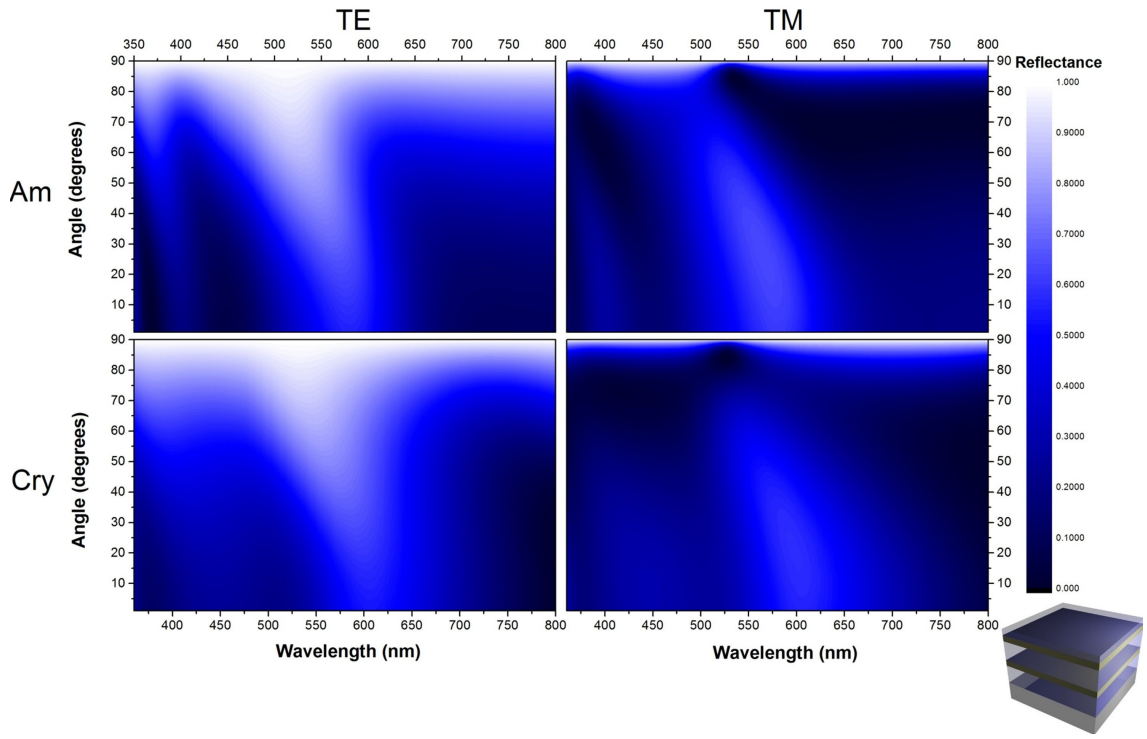

Figure 6.6: Colour angular dependence as a function of AIST phase state and polarisation for the particular stack: 10 nm ITO / 7 nm AIST / 150 nm ITO / 7 nm GST / 150 nm ITO /mirror (with a maximum in red colour). Amorphous (Am) and crystalline (Cry) refers to both AIST layers in that specified state.

Similar spectral variations were observed for optical cavities featuring GST instead of AIST. For the sake of simplicity, they are not shown here, but their behaviour is qualitatively comparable given the similarity of the complex refractive indices of both materials.

6.2 Experimental methods

The simplicity of the samples in this approach is reflected in relatively easy fabrication, optical/electrical calibration, and measurement. Although the multilayer stack can, in principle, be deposited on top of any kind of substrate, including flexible materials, the results presented in this thesis refer only to samples using solid substrates, as described below.

6.2.1 Sample fabrication

Thermally grown SiO_2 wafers (IDB Technology, UK) were used as substrates for the devices. A standard cleaning process in acetone with ultrasonic agitation, isopropanol, distilled water, and dried nitrogen was used beforehand. All thin films were sputtered at room temperature using a Nordiko® system in 100 $sccm$ (standard cubic centimetres per minute) argon atmospheres. Base pressures were $\approx 3 \times 10^{-7}\,torr$ and a working pressure of 0.5 $mtorr$. The mirror was fabricated by depositing 100 nm of platinum on top of the silica wafer. Indium-tin oxide (Testbourne, UK) was sputtered from a 3″ target at 120 W DC at a rate of 11 nm/min. Solid targets of 2″ in diameter containing 99.99% pure $Ag_3In_4Sb_{76}Te_{17}$ and $Ge_2Sb_2Te_5$ (Super Conductor Materials, USA) were used to sputter at 30 W DC at rates of 3.4 nm/min and 3.6 nm/min, respectively.

The electrical measurements required physical contact between the bottom Pt mirror or ITO layer (acting as electrode) and the electrical probe. For this reason, the areas where deposition of ITO and phase-change materials was to be avoided were covered using kapton tape.

6.2.2 Measurement Setup

The spectroscopic measurements were carried out in a Lambda 1050 spectrometer (Perkin Elmer, USA) in reflection mode. The measurements were calibrated against commercial aluminium standards within the wavelength range $350 - 750\,nm$. The optical images written on top of the samples were obtained using standard $100\times$ microscope objectives. Conductive atomic force microscopy (Asylum Research MFP-3D), using ORCA accessories with conductive diamond tips (Bruker, DDESP-FM-10), was used to realise, in contact mode, measurements of nuclei size. Cr/Pt tips (BudgetSensors, Multi75E-Gto) were employed to measure the switching voltage vs. force data in Fig. 6.16. Both kind of tips were successfully tested on binary and grey-scale image writing.

6.3 Experimental results

The devices studied in this chapter were optical cavities consisting of two transparent conducting layers of Indium-Tin Oxide (ITO) sandwiching a thin film of phase-change material, either AIST or GST, on top of a mirror, as sketched in Fig. 6.7. ITO was selected among other optically transparent materials due to its conductivity [206], which in turn is useful for electrical switching. The top ITO layer has no effect on the colour being reflected and is used only to protect the phase-change layer from oxidation; its thickness was fixed to be $10\,nm$. On the other hand, the bottom ITO layer plays a crucial role as it is the medium inside the optical cavity formed between two ultra-thin absorptive layers (before and after the mirror reflection). Therefore, the reflected colour (i.e. the resonance condition of the cavity) depends mainly on the thickness of this layer.

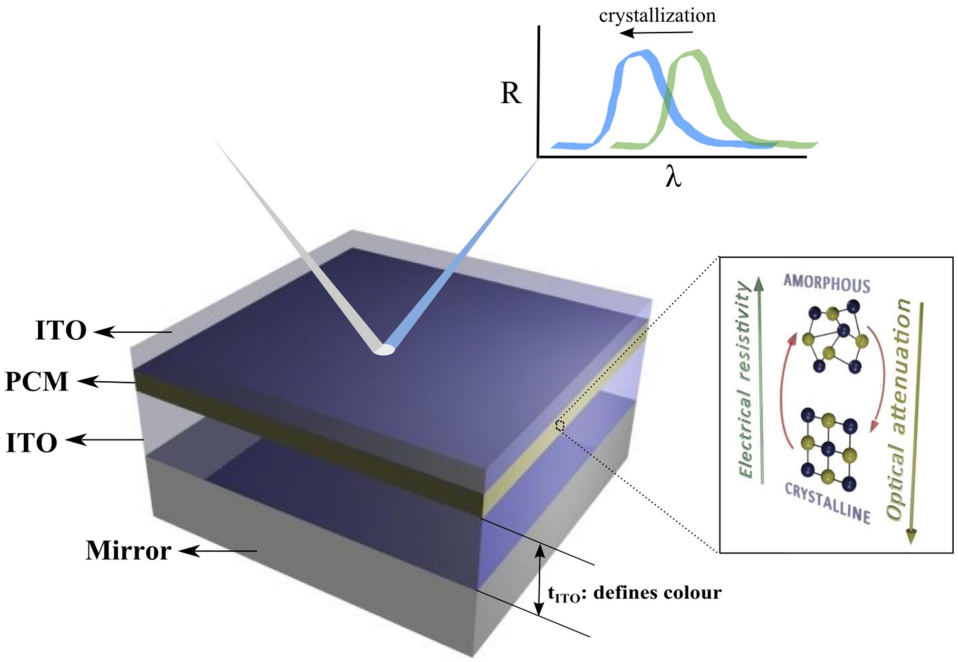

Figure 6.7: Schematic diagram of the multilayer stack and principle of operation.

6.3.1 Colour switching

Using the multilayer stack presented in Fig. 6.7, engineering the AIST and ITO layer thickness with the thin-film optics theory presented in Sec. 6.1.1, and sputtering the samples with the methods presented in Sec. 6.2.1, resulted in the colour samples shown in Fig. 6.8a. As theoretically predicted, the reflectance spectra of such samples depend on the ITO thickness and the PCM crystallographic state. Good agreement was obtained between the calculated and the measured spectra, as plotted in Fig. 6.8b, which also shows a wavelength blue-shift of up to $50\,nm$ that takes place upon material switching. Here, the crystallisation of as-deposited AIST was obtained after annealing for $5\,min$ at $250°C$ on a hotplate.

Despite the positive advantages of having more than one phase-change layer, as discussed in Sec. 6.1.3, only samples with one layer of AIST or GST were successfully fabricated as part of this project. Unfortunately, the old Nordiko sputtering system used for the

comparisonv4.jpg

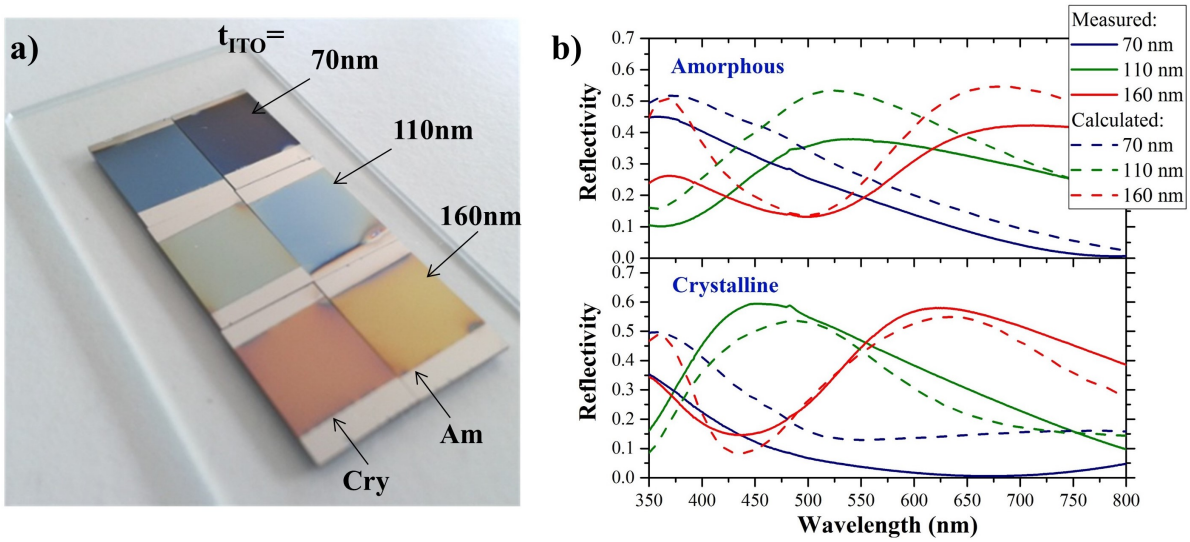

Figure 6.8: Experimental colour modulation using AIST thin films. a) An image demonstrating colour modulation obtained upon phase switching under natural sunlight on films stacks of 10 nm ITO/ 7 nm AIST / t_{ITO} ITO/mirror where t_{ITO} = 70 nm, 110 nm and 160 nm are shown. b) Calculated and measured reflectance spectra for the samples shown in a), where crystalline corresponds to the phase state reached after annealing.

fabrication of these samples did not provide the film surface uniformity required to deposit many layers on top of each other. This meant that very rough surfaces were obtained when sputtering more than three layers, and thus scattering effects became more relevant. Although the results of this chapter led to a patent [73] to hold the intellectual property of these findings, other groups of scientists have independently found similar multi-colour approaches and confirmed the computational-only results presented herein [74].

6.3.2 AIST-based nanodisplay

Samples in an as-deposited amorphous state were switched locally by applying a voltage bias between a conductive AFM cantilever and the ITO film under the PCM, as sketched in Fig. 6.9a. This allowed a demonstration of the application of phase-change materials in nano-displays by locally changing colour and thus enabling sub-nanometric images. Using the high electrical conductivity of ITO, nanopixels can be modified one at a time by Joule heating of the PCM, which switches it to crystalline state. This can be done

locally, either by switching points independently, or by modulating the applied voltage while scanning the surface. Using the scanning mode at 0.5 Hz, 512 pixels per line, and setting $0\,V$ to black and $7\,V$ to white, $70 \times 70\,\mu m^2$ binary images were written onto the PCM layer, as shown in Fig. 6.9b. These images present an outstanding resolution with features as small as $500\,nm$. Given that, in this demonstration, AFM was used to show nanopixel writing, the impedances are not perfectly matched. This means that, under the current experiment conditions, it was not possible to get the nanosecond pulses required to erase (i.e. to reamorphise). However, it has been reported in [33] that on-chip cross-bar devices with similar multilayer stacks are able to operate as an active re-writeable colour pixel by electrically switching the PCM. Thus, with erasability and re-writing already demonstrated, the focus here is on further capabilities, properties and limits of the PCM nano-displays.

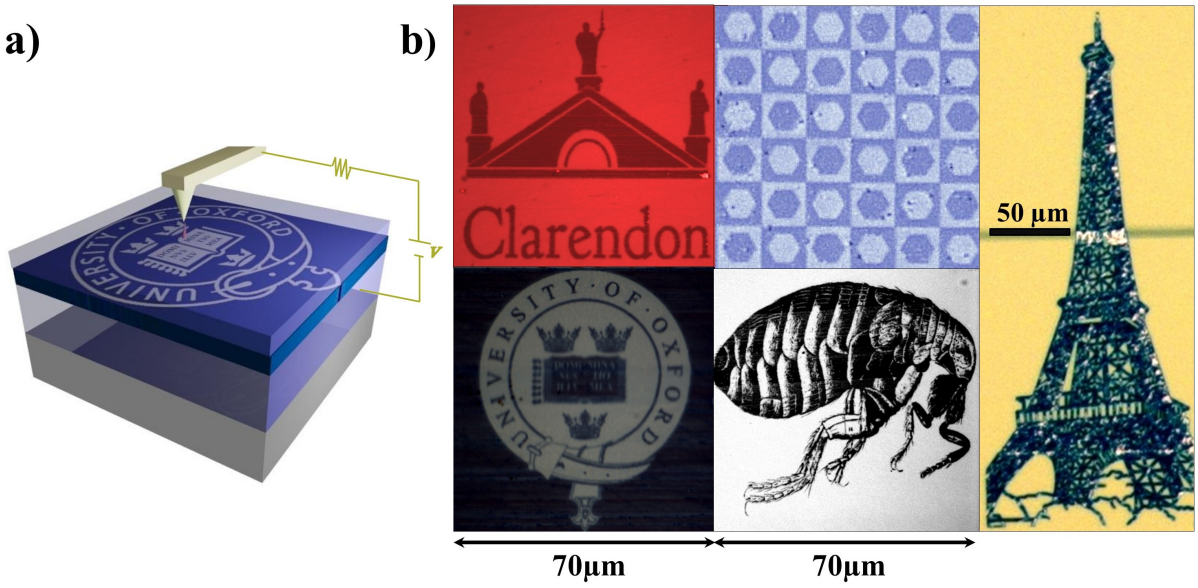

Figure 6.9: Nano-display applications of AIST. a) Sketch of the experimental setup. A Conductive AFM is used to locally switch AIST by applying voltage between the two ITO layers. b) Optical microscope images of electrically written objects on continuous ITO/AIST/ITO/Pt stacks with different colours and sizes.

In Fig. 6.10, $5 \times 5 \mu\, m^2$ and $7 \times 7\, \mu m^2$ images are transferred to AIST using electrical switching with $7\, V$ and $10\, V$ for white, respectively, and no voltage to keep the background colour. The voltage had anomalous variations while modulating the signal due to the experimental challenge of scanning such a small area, as seen in the "Writing" image, which corresponds to the image that the AFM wrote (i.e. the applied electrical modulation). Given the resolution limit of optical microscopes, these instruments were not able to produce an accurate visualization of the image. Instead, the same AFM was used to inspect the image that has been transferred by creating an image from the changes in resistance of the surface. In this case, a constant voltage equal to $0.5\, V$ was applied, which was lower than the crystallisation threshold, but enough to differentiate the resistivity of the two states of the PCM. This approach allows retrieval of the image, as shown in the "Scanning" image in Fig. 6.10, where white areas represent more conductive, crystalline areas. Despite the modulation deficiencies and the randomness of the crystalline nuclei generation, both written images reproduce the original ones at this scale with features down to approximately $250 - 300\, nm$. Such low resolution might be impractical for displays where pixels of few microns are used. However, it would allow for better and re-writeable holograms where such resolutions enable high-fidelity reconstruction of the 3D image. Moreover, the low dimensionality could represent a new parameter for security tags where optically hidden features are exploited.

6.3.3 Colour-depth modulation

The amount of crystallised PCM in a certain scanned area is linked to the final colour perception of the image. If the separation between two pixels is smaller than the size of the nuclei after applying a voltage pulse, then a fully crystallised area is obtained in between, and therefore the colour will correspond completely to that of the crystalline state. On the other hand, if the separation is larger, then some amorphous material will

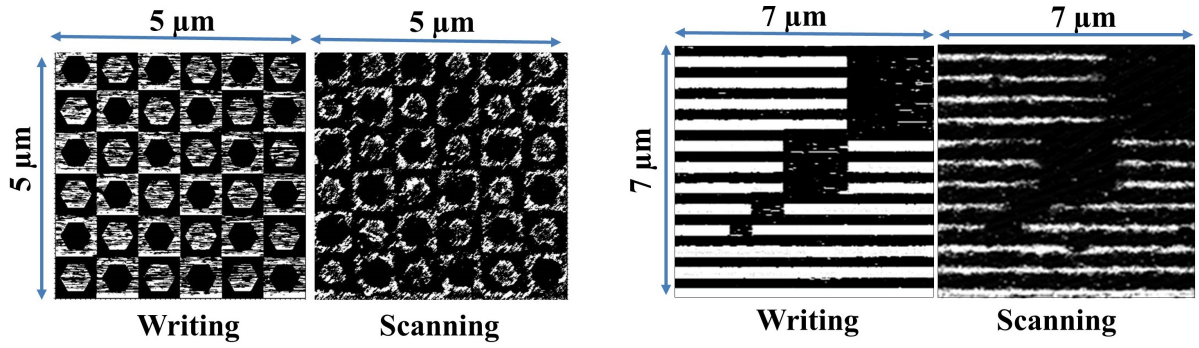

Figure 6.10: Scanning mode resolution limit. (left) Voltage modulation using CAFM $5 \times 5\,\mu m^2$ and $7 \times 7\,\mu m^2$ binary images when writing with $7\,V$ and $10\,V$, respectively. (right) constructed image read electrically by scanning with a $0.5\,V$ bias.

remain in between and therefore the colour will adopt an intermediate state between that of the amorphous and crystalline state. Those intermediate states give account of the colour-depth between one state and the other, in analogy to black and white and the grey-scale colours in between. In this particular experiment, the size of the nuclei was determined by the voltage, whilst the separation was determined by the scanning speed. To corroborate this, voltages of 0, 2, 4, 6, 8 and $10\,V$ were applied while scanning at a fixed frequency of $1\,Hz$ onto a $70\mu m \times 70\,\mu m$ square sample with $10\,nm$ ITO/ $7\,nm$ AIST/ $70\,nm$ ITO layers. The results are shown in Fig. 6.11a, where the colour clearly gets deeper (i.e. closer to that corresponding to a completely crystalline state) as the voltage increases. Moreover, even $2\,V$ was enough to induce colour switching, although with a lower contrast given that the crystallisation threshold was measured to be $1.40 \pm 0.05\,V$, as will be detailed below. Subsequently, the 0 to 255 grey-level scale was mapped to a continuous voltage range 0 to $7\,V$ for the electrical pulses applied during CAFM scanning. By doing so, it was possible to write the $70 \times 70\,\mu m^2$ grey-scale image shown in Fig. 6.11b onto the same sample with perceptible colour-depth modulation, as depicted in the optical microscope image in Fig. 6.11c. Lower voltages corresponding to those darker areas in the original image led to a lower contrast in the written image as the colour switching is not significantly high and the material remains mostly in the amorphous state. However, for voltages larger than $4\,V$, the colour is clearly and

continuously modulated to intermediate states between the amorphous and the crystalline phases, allowing for a grey-scale image.

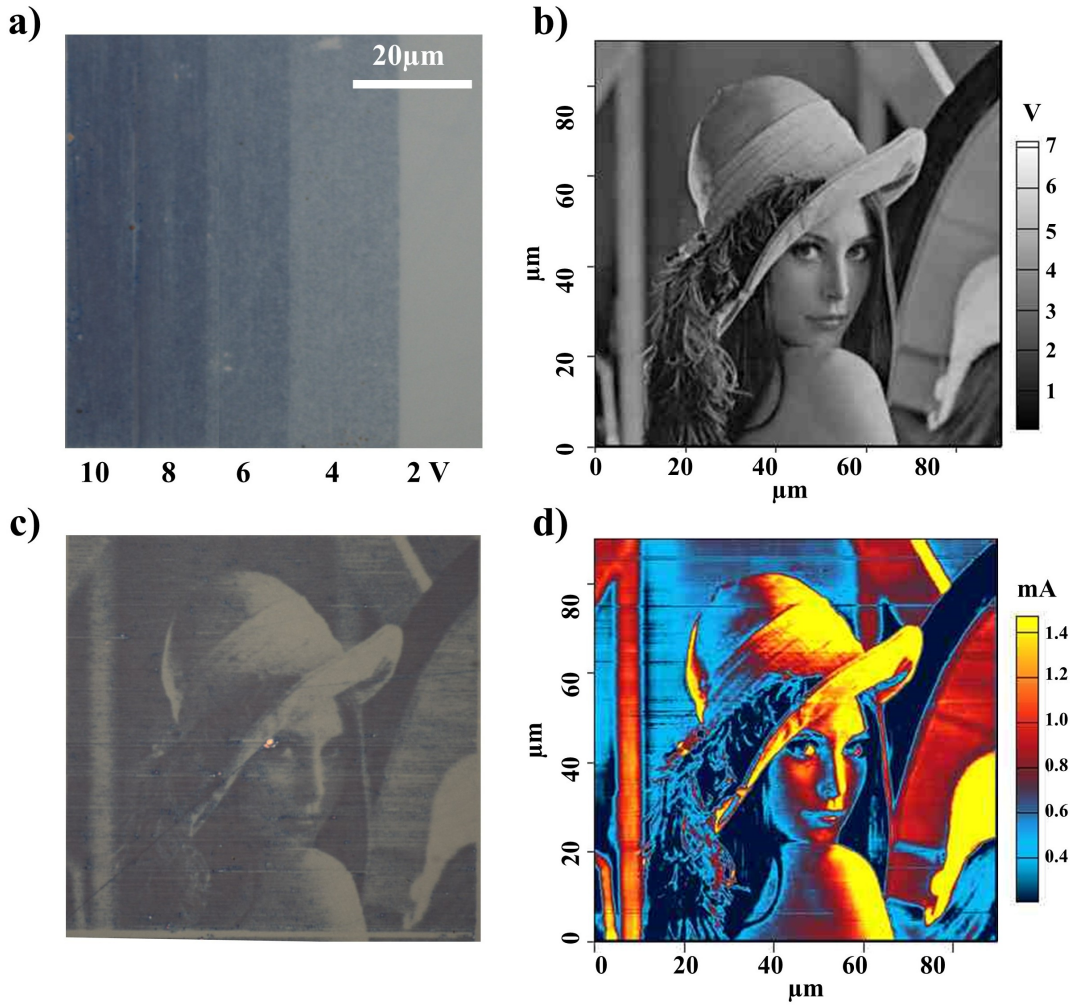

Figure 6.11: Grey-scale image rendering. a) Scanning voltage varying between 0 and $10\,V$ induces different levels of crystallisation and therefore, different colours in reflection mode. b) Image with the equivalent map between grey-scale and voltage for the electrical pulses applied during the scanning. c) Optical microscope image of the picture in b) written on $90 \times 90\,\mu m^2$ of AIST. d) Conductivity measurement while the image c) is written in scanning mode. a) and c) were written using CAFM on $10\,nm$ ITO/$7\,nm$ AIST/$70\,nm$ ITO/Pt samples.

For a better visualisation of the crystallisation that takes place during the scanning, the corresponding "electrical image" (caused by the change in electrical resistance) was mapped by measuring the current through the ITO/AIST/ITO stack while scanning in a

CAFM. The results are shown Fig. 6.11d, where the different degrees of crystallisation are visible as variations in conductance when switching takes place. Such conductivity depth offers better contrast than the reflectivity changes upon switching; thus, the "electrical image" is more detailed than its optical counterpart, allowing for a better differentiation of intermediate states that are not distinguishable with the naked eye.

6.4 $Ge_2Sb_2Te_5$ vs. $Ag_3In_4Sb_{76}Te_{17}$

The performance of $Ge_2Sb_2Te_5$ and $Ag_3In_4Sb_{76}Te_{17}$, nucleation- and growth-dominated phase-change materials respectively, is comparable due to the similarity of their complex refractive indices, as shown in Fig. 6.12 [6, 216]. In this section, a comprehensive comparison using experimental data is presented between the two materials in terms of colour gamut, resolution, and energy consumption.

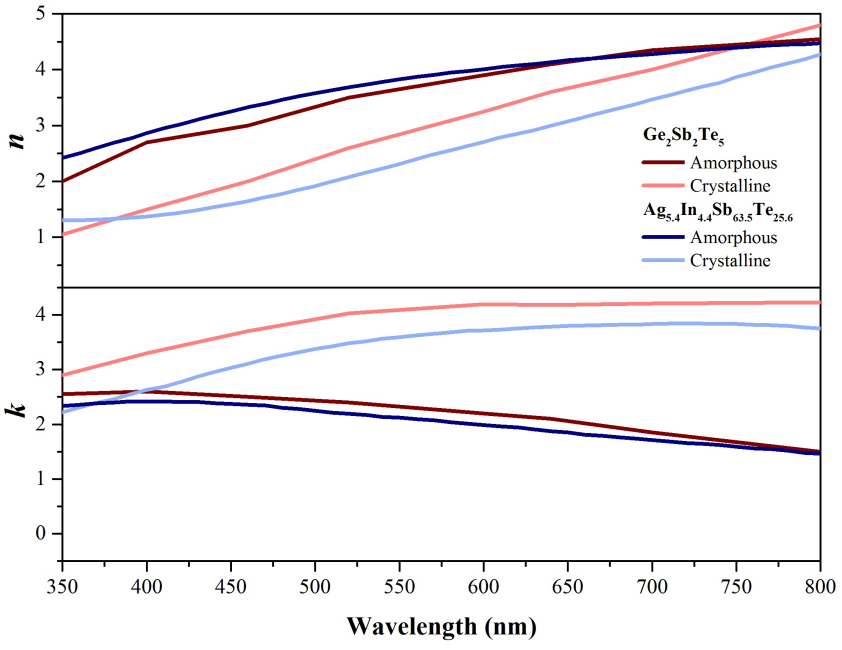

Figure 6.12: Real (n) and imaginary (k) components of the complex refractive index of GST and AIST.

6.4.1 Colour switching

The colour generation and modulation between samples containing either GST or AIST were studied from the reflectance spectra obtained using the transfer matrix in Eq. 6.1. Moreover, using these computational values for the reflectance spectra, all the achievable colours using the XYZ tristimulus [217] values were calculated as a function of PCM and ITO thicknesses for both the amorphous and the crystalline phases. In Fig. 6.13, the XY colour gamut is shown on a chromaticity diagram that represents the ultimate colour perceived by the human eye. Here, the ITO thickness was varied from 0 to 300 nm (one mark per 5 nm) which covers a vast range of colours in both phase states of the PCMs. From these results, very similar colour gamuts were obtained for the amorphous phase of both AIST and GST, as expected from their comparable refractive indices (see Fig. 6.12). This can also be inferred by comparing the experimental spectra for AIST in Fig. 6.8b with previously reported experiments for GST in [33]. However, when both materials are switched to the crystalline state, AIST presents a similar but broader colour gamut than GST only if the PCM layer is 6 nm or thicker. For thicknesses of 2 nm, the slight difference in the refractive index between the two materials plays a significant role in influencing the interference conditions; as it is seen for this case only, GST allows for a better colour switching. This could be a considerable advantage for GST, as thinner films also lead to greater colour contrast upon switching.

Furthermore, the wavelength at peak maximum of the spectra was calculated as a function of three parameters: phase state, ITO and PCM thickness, as presented in Fig. 6.14 for AIST and GST. Reflectance peaks centred at any colour in the visible spectrum are achievable for both materials by changing only the ITO spacer dimensions. Moreover, the same device (i.e. same ITO spacer thickness) leads to similar colour when using either phase-change alloy, notwithstanding the different nature of their crystallisation

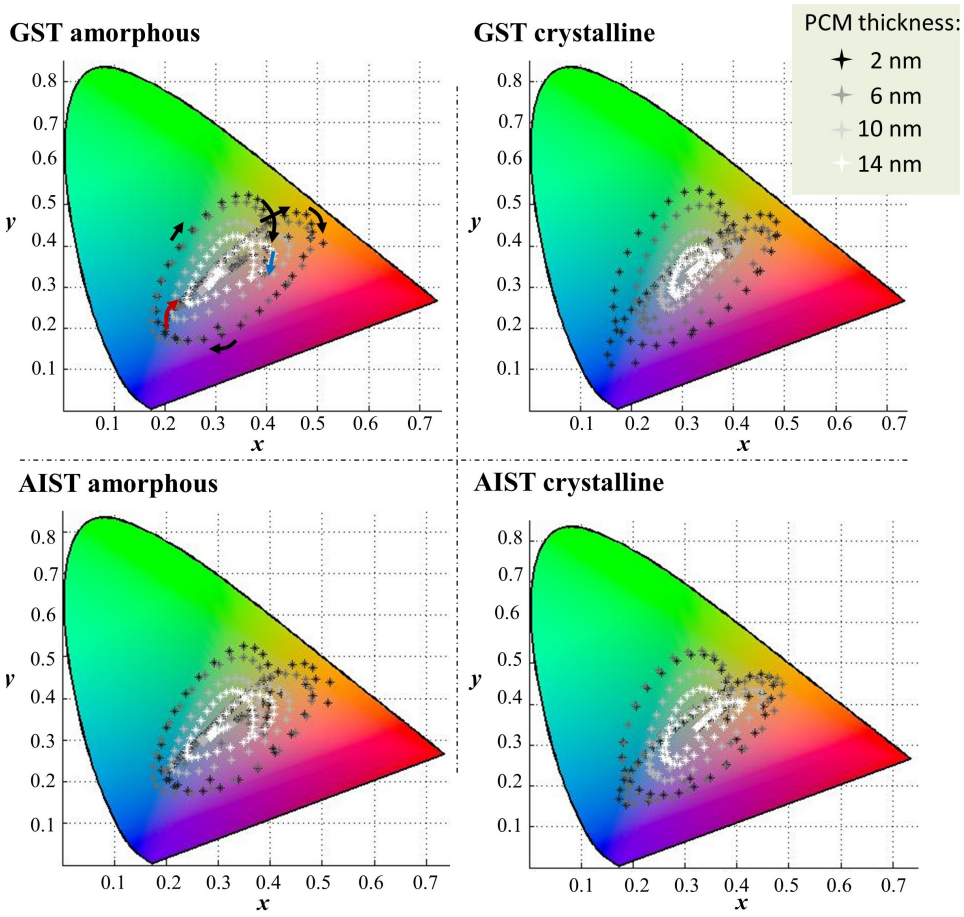

Figure 6.13: Colour gamut comparison between AIST and GST. Calculated XY colour gamut on the chromaticity diagram for ITO/PCM/ITO/Pt samples. The bottom ITO spacer is swept from $0\,nm$ to $300\,nm$ in steps of $5\,nm$ (one step = one mark on the graph) to study the resulting colour when the PCM, either AIST or GST, has four different thicknesses. On the top left panel, the arrows start with the red one ($0\,nm$ ITO) and finish with the blue one ($300\,nm$ ITO), showing the direction for increasing ITO thickness (for all figures and thicknesses).

processes. The effect of the thickness of the PCMs results only in a slight red-shift in the spectrum as it gets thicker, in both cases. However, the blue-shift resulting from the high-to-low real refractive-index and low-to-high extinction-coefficient change, when switching from amorphous to crystalline state, is definitely more pronounced and the reason why the colour switching is possible. Considering the shift between spectra in amorphous and crystalline states (for ITO thicknesses in the range $100 - 160\,nm$), AIST presents, on an average, a modest peak shift of $6\,nm$ larger than for GST.

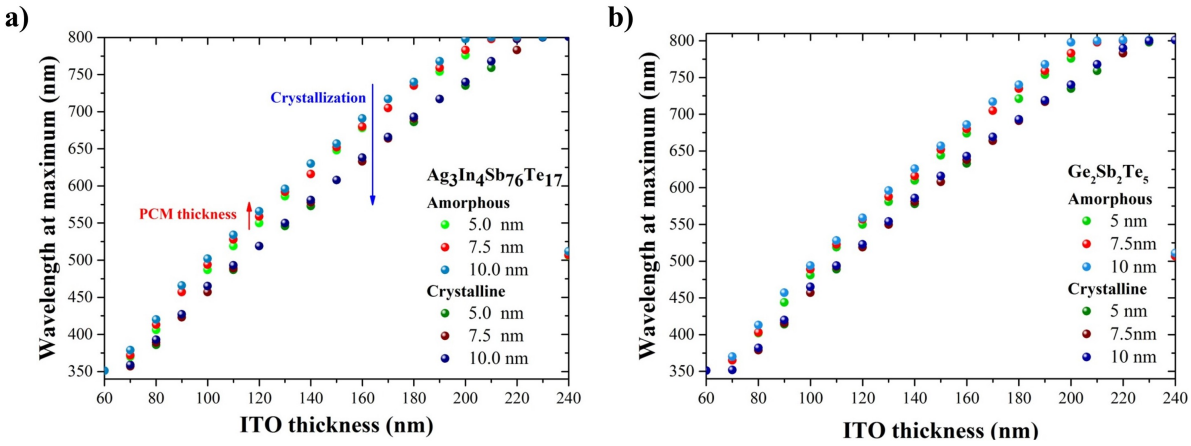

Figure 6.14: Wavelength at maximum reflectance as function of ITO and PCM thickness for: a) AIST and b) GST.

6.4.2 Resolution and Energy consumption

The maximum resolution allowed by each material and the energy required to switch were measured using conductive AFM to locally switch one pixel at a time and compare the resulting nuclei sizes and IV curves. Although uniform layer samples were used in these experiments, patterned samples featuring ITO/PCM/ITO stack nanopillars on top of the mirror were employed without considerable differences. Triangular-shaped pulses from $0\,V$ to $10\,V$ and down to $0\,V$—as in an IV curve measurement—were applied to randomised pixels in order to crystallise the PCM. Subsequently, the surface was scanned while applying a constant voltage of $0.5\,V$ in order to visualise changes in conductivity, and therefore the nuclei generated in the previous step. Electrically imaged nuclei are depicted in Fig. 6.15a for AIST and Fig. 6.15c for GST. A large voltage of $10\,V$ was used for the sake of visualisation, given that lower voltages induced weak switching, forming small nuclei which are challenging to image in an AFM. Together with changes in conductivity, surface height variations were observed ranging from 2 to $4\,nm$, as expected due to the volume contraction of PCMs under crystallisation [218]. A direct comparison leads to the inference that AIST, because of its growth-dominated crystallisation, presents larger and denser nuclei. On the other hand, GST presents smaller and more

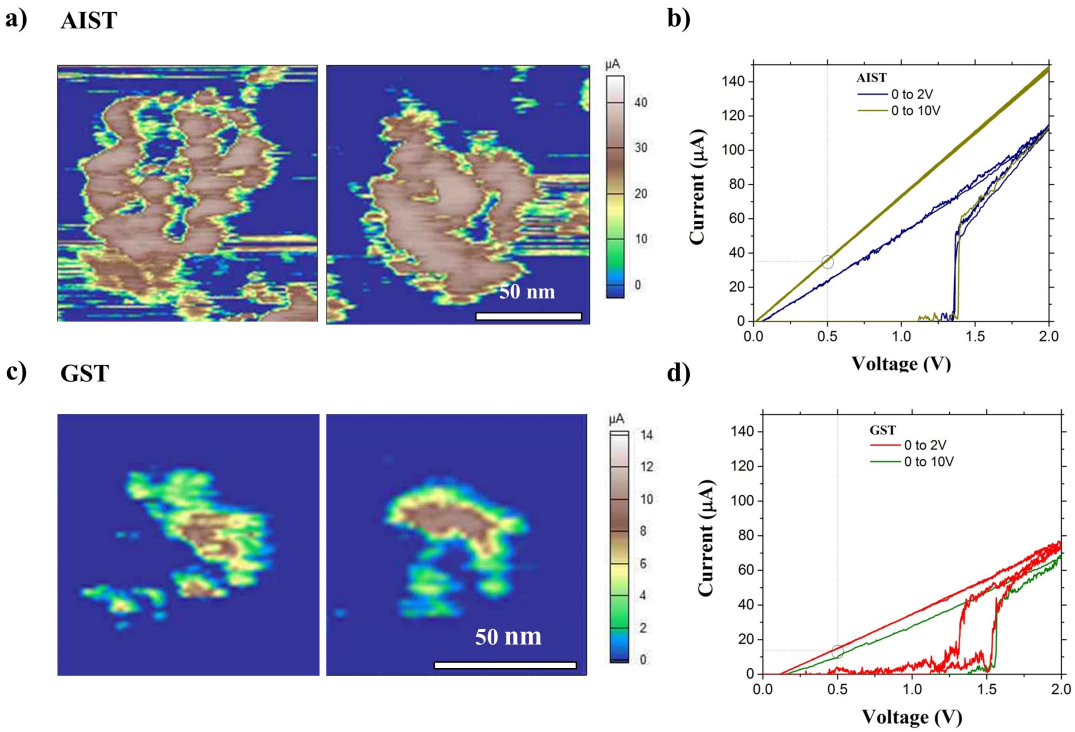

Figure 6.15: Resolution and electrical switching comparison between GST and AIST. a) Two AIST nuclei (nanopixels) generated with a $0-10-0\,V$ triangular electrical pulses using CAFM and reconstructed by electrically scanning the area with a $0.5\,V$ bias. b) Characteristic IV curves during AIST switching. The 0 to $10\,V$ ramp data (shortened for the sake of visualization) correspond to that in a). The highlighted region corresponds to the IV characteristics at $0.5\,V$. The corresponding current is in good agreement with the value measured for the crystalline areas in a). 0 to $2\,V$ ramps are also plotted to demonstrate the minimum bias voltage required to properly switch the material, although the sizes of the nuclei are much smaller, and therefore difficult to visualise. c) and d) analogous to a) and b) but for GST.

dispersed nuclei characteristic of nucleation-dominated materials. The corresponding IV curves from the previous experiments are plotted in Fig. 6.15b and 6.15d. There is good agreement between the current measured at $0.5\,V$ when switching with a $0-10-0\,V$ triangular pulse (IV curve measure) and the current measurements when scanning the nuclei with $0.5\,V$ in the scales of Fig. 6.15a and 6.15a. IV curves from 0 to $2\,V$ are also plotted to measure the crystallisation threshold, which for AIST was $1.40 \pm 0.15\,V$ and $1.50 \pm 0.15\,V$ for GST (values averaged over several pixels). It is important to take into account the resistance between the tip and the ITO top layer, as well as possible effects on the measured IV characteristics, especially the threshold voltage. Impurities and

other possible interface phenomena meant that switching voltages ranging from $\approx 1\,V$ to $\approx 5\,V$ were obtained whilst writing, thus increasing the uncertainty of the measurement. Because of this, even though results for GST suggest a larger crystallisation threshold, it is not considerably higher than for AIST; from a practical point of view, both devices behave essentially identically.

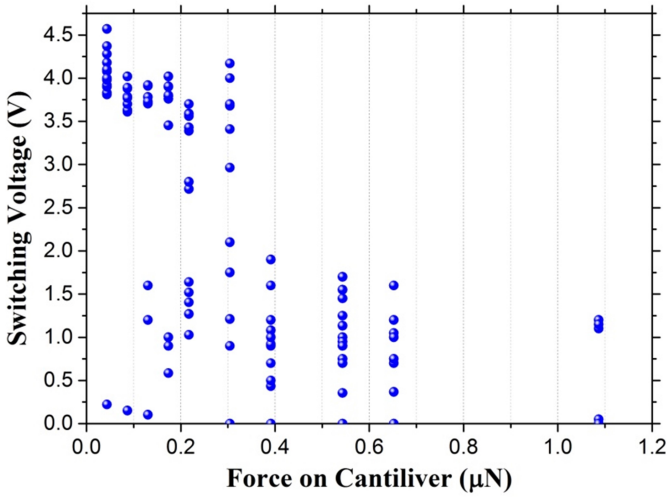

Figure 6.16: Switching voltage vs. force on cantilever when performing 0 to $5\,V$ IV measurements. Dots at $0\,V$ mean that there was a short circuit at that specific point.

To understand the nature of the huge variation of the switching voltage described above, similar measurements with 0 to $5\,V$ triangular pulses were carried out in contact mode with varying AFM tip forces. The results in Fig. 6.16 clearly demonstrate that the higher the force, the lower the switching voltage, as the tip makes better contact with the top ITO layer (top electrode) and overcomes any surface dirt. To obtain reliable and repeatable switching voltages, forces over a threshold of $400\,nN$ are required.

6.5 Summary

This chapter has offered theoretical fundamentals for the calculation of reflectance, transmittance, and absorptance of a stack of thin films and the mathematical transformation

to convert spectra into real, eye-perceived colours. These formulations were programmed in MATLAB in order to model and predict the reflected colour of any multilayer stack containing phase-change materials. Multiple scenarios based on these codes have been studied towards optimising the different parameters and finding new interesting features that could lead to new applications of these devices.

On the experimental side, this chapter demonstrated that AIST, a growth-dominated phase-change material, can be used as an active material for bistable colour switching in multilayer optical cavities. The contrast between the reflected colours achieved with amorphous and crystalline AIST was used in this chapter to write images on the PCM layer. This was done by locally switching with electrical pulses featuring voltages as low as $2\,V$ and following predetermined 2D patterns. Resolutions down to $300\,nm$ in scanning mode and less than $50\,nm$ in pixel-by-pixel mode were also demonstrated. Furthermore, the very first demonstration of non-binary colour rendering has been presented on a single device (pixel) by exploiting the dependency of the degree of crystallisation on the applied voltage. Using this, continuous "grey-scale" images were obtained, which in turn adds a new degree of functionality to the newly emerging field of PCM displays [17,24]. A comparison between $Ge_2Sb_2Te_5$ and $Ag_3In_4Sb_{76}Te_{17}$ was presented; both materials offer very similar properties and performance. Finally, resolution limits below $50\,nm$ were found in both materials using the pixel-by-pixel approach, with differences in the nucleation formation due to the different crystallisation dynamics of both materials.

Chapter 7

Conclusion and Outlook

The work described in this thesis has studied physical phenomena enabled by the uniqueness of phase-change materials switching between two structural states, which, in turn, offer two very distinct optical properties. Upon switching, the refractive index of such materials change to values that, together with the phase state, remain stable over time. Such a modulation means that the optical phase of electromagnetic waves, as well as the attenuation, could be tuned in a nonvolatile manner if propagated through, or coupled to, phase-change material nanoscale sections or films. This fact was studied and experimentally exploited herein by using two different architectures: multi-stack optical cavities—featuring at least one PCM thin-film layer—for nanodisplay applications, and integrated photonic circuits with near-field coupling to PCMs for light modulation and memory applications. The results obtained in this work demonstrate the versatility of phase-change materials for tunable photonic and optoelectronic applications, and offer new tools for future developments in a new-born, yet fast-growing field.

7.1 Phase-change materials for photonics

The very first protocol for all-photonic control of phase-change materials on integrated silicon-based photonic circuits was described. The approach consisted of low-dimensional phase-change material (here GST) elements integrated with silicon nitride waveguides. In such devices, the switching between states and the transmission measurements were carried out by near-field coupling to light travelling along the waveguide. Therefore, there is no restriction in size by the diffraction limit. In this way, a purely photonic application of phase-change materials with a totally new switching mechanism was demonstrated.

To circumvent the elusive full and repeatable switching cycle—the major obstacle in photonic and plasmonic applications of phase-change materials—reliable *Write* and *Erase* schemes, enabled by a material pre-conditioning process, were experimentally demonstrated based on nanosecond pulses and stepwise partial recrystallisation. These results led to the first prototype of an integrated, all-photonic, truly-nonvolatile memory that provides multi-level (here 8 level) storage in a single cell. Furthermore, the ability to switch readily and directly between the multiple memory levels was shown with accurate control of the readout signal and excellent repeatability. This exciting and seemingly straightforward aspect of this photonic memory is particularly attractive because such arbitrary transitions are very difficult to achieve in electronic memories employing phase-change materials, where iterative write-and-erase algorithms involving multiple (typically 3 to 5) write/read(/re-write) cycles are needed to achieve a pre-defined level, adversely affecting the overall write speed and power consumption [105].

The capability for fast ($\approx 10\,ns$), low power ($\approx 13\,pJ$), single-shot readout of the memory state, along with repeated ($\times 100$) write/erase cycling while maintaining high readout contrast was demonstrated. This first experimental implementation is not only promising,

but demonstrates significantly more potential than existing integrated optical memories, in which both non-volatility and multi-level storage have been elusive. Such capabilities provide a leap forward in terms of functionality and will be crucial for the realisation of practicable and commercial photonic memories. Moreover, this phase-change photonic framework is fully scalable: large arrays of all-optical memory elements can be envisioned using wavelength division multiplexing techniques. In doing so, several memories can be conveniently addressed through photonic circuitry, which is an essential attribute for the realisation of practical on-chip optical interconnects. Hybrid circuits exploiting phase-change materials can also now be enabled using this type of memory, leading directly to new forms of non-conventional (non-von Neumann) computation and processing, as described below in Sec. 7.3. Additionally, optically accessible memories could potentially solve the von-Neumann bottleneck of current computer architectures by eliminating electro-optical conversion, thus avoiding latencies, heat, bandwidth, and speed limitations in the communication between the processing and the memory units.

On-chip photonic architectures cannot yet offer circuit densities similar to those in silicon electronics. In fact, the photonic memories presented herein cannot yet achieve sufficient memory densities close to the best non-volatile solid-state disks. The main limitation in form factor to improve density is the use of waveguides, which, even in the visible spectrum, require geometries in the scale of hundreds of nanometers. Moreover, there needs to be a gap of the order of microns between two consecutive waveguides to avoid evanescent coupling. However, the promise of all-photonic phase-change memories relies on those new functionalities, such as reliable multilevel operation and wavelength multiplexing, which are challenging in electronics. Together with the advantages of photonic processing, such as low heat losses, faster operation and low cross-talk, all-photonic memories exhibit unique properties that can be harnessed in new technologies and in boosting the performance of current ones.

7.2 Phase-change materials for optoelectronics

The use of growth-dominated phase-change materials (AIST) as the active material to obtain off-line colour modulation was also studied and demonstrated. Switching electrically to obtain different optical responses (changes in reflectivity) shows that optoelectronic devices and methods can be used to control and exploit, simultaneously, the electrical and optical properties of phase-change materials. Switching voltages as low as $1.4\,V$, resolutions down to $300\,nm$ in scanning mode, and less than $50\,nm$ in pixel-by-pixel mode were demonstrated using multilayer optical cavities based on AIST. Furthermore, the very first demonstration of non-binary colour rendering has been presented on a single device (pixel) by exploiting the dependency of the degree of crystallisation on applied voltage. Using this, continuous "grey-scale" images were obtained, which in turn adds a new degree of functionality to the newly emerging field of phase-change nanodisplays [33]. A comparison between $Ge_2Sb_2Te_5$ and $Ag_3In_4Sb_{76}Te_{17}$ was presented, which demonstrates that both materials offer very similar properties and performance. Finally, resolution limits below $50\,nm$ were achievable in both materials, in the pixel-by-pixel approach, with differences in nucleation formation due to the different crystallisation dynamics of both materials. These results, together with previous reported capabilities, such as reversible switching on cross-bar devices and the feasibility of nano-displays on flexible substrates, offer new tools for a new emerging generation of bistable, ultra high-resolution, and flexible display technologies in parallel with other potential applications in nanophotonics and optoelectronics, as discussed below.

7.3 Outlook

Although the results presented in this work hold promise for many potential applications, the field of phase-change materials for photonics and optoelectronics requires further

investigation in several aspects before technological implementations can be real. In the particular case of phase-change photonic memory described in this work, even when they already represent a breakthrough in photonics and materials science [30], these types of memories are still at the embryonic stage, with plenty of room for improvement in design, functionality, and performance. Particular focus should be paid to the development of phase-change materials with better optical performance, i.e. higher values in the imaginary refractive index for more absorptive alloys (to enable the use of less energy to switch and smaller dimensions for colour modulation) while having fast phase switching. Advances in material design, together with the already fast growing silicon photonics field, would enable fascinating integration that could lead to new science and technology. Beyond data storage, the non-volatile tunability of on-chip propagating modes (i.e. information) could also enable applications in optical switching, routing, demultiplexing, sensors, etc. Moreover, the optoelectronic control of PCMs could enable the next generation of bistable displays, smart glasses, and colour-based security schemes. A combination of both approaches could also lead to the implementation of PCMs in optoelectronic circuits which could enable the integration of an all-photonic approach with conventional electronic circuits, and thus the current CMOS technology. Some of the main aspects to consider for the future of phase-change materials for photonics and optoelectronics with some potential applications are listed below.

Device improvement

The performance of phase-change photonicc memories can be further improved by operating with shorter pulses, exploiting other optical properties such as polarisation, moving to devices with smaller footprints, and employing new materials with faster and lower temperature switching. Higher signal-to-noise ratios to improve the read-out contrast could also be obtained with the use of optical cavities, which would also reduce switching energies, as discussed theoretically in [26]. To reduce the device footprint, alternative

architectures, such as plasmonic antennas could be explored. Alternatively, scaling down is plausible by using photonic circuitry operating at shorter wavelengths (therefore, narrower waveguides) or by using phase-change materials with higher differences in refractive index in the *C* and *L*-band. In this way, small devices will lead to reasonable good contrasts. While multi-bit access is achieved with micro-ring resonators with relatively large footprints [67], alternative technologies, such as ultra-compact on-chip optical multiplexers/demultiplexers can be employed for size reduction. In addition, optical cavities with smaller mode volume, such as photonic crystal devices, would localise the interaction volume of the optical mode with the memory element further and thus lead to a smaller system size for wavelength-selective memory access.

Further investigation is required to determine with precision the nature of the near-field switching, and thus the *Write* and *Erase* processes, would also enable the phase-change photonic memories. Understanding the switching dynamics will allow for optimisation of the geometric and the physical parameters, which can in turn improve energy efficiency and processing speed.

As for the colour modulation, reliable back-and-forth switching of large areas remains a challenge. Cross-bar electrodes can be used to switch repetitively between the two states in $\approx 300\,nm$ pixels. In addition, arrays of such pixels, in a matrix configuration, could be a solution for large-area switching, adding electronic complexity to the device. In this technology, slow switching is not inconvenient, is the eye response the ultimate determining factor. Therefore, having new materials that switch on longer time scales, such as microseconds, but require lower switching energies, would facilitate the colour tunability of large areas if considering not pixel arrays but uniform films, in which theoretically large amounts of energy are required.

Large-scale photonic integration and applications

The direct integration of nanoscale phase-change material memories into nanophotonic circuits would open new avenues for chip-scale photonics and related fields. By using broadband waveguides, memory cells could be operated over a very large frequency bandwidth and tailored towards specific optical needs, extending beyond memory applications to include, for example, photonic computing, integrated photonic modulators, and tunable photonics and optoelectronics. Furthermore, the hybrid integration of phase-change materials with traditional silicon technology could bridge gaps in optical-material science and integrate several cutting-edge research topics. In particular, this would put an end to the long-standing challenge of passive silicon circuits with active functionality. All-optical switches are good examples of possible active functionalities which, in addition, could be benefited by off-line operation. Using phase-change materials to modify the coupling conditions of directional couplers, photonic crystal cavities, or ring-resonators could enable 2×1 and 2×2 optical swtiches and light couplers.

The implications of large-scale integration of phase-change photonic memories could be tremendous for optical computing. Not only are they optical memories that remain active without power input, the multi-level operation means that they represent a route to increase storage capacity. Furthermore, with multi-level access in one memory cell (analogous to some proposals in the electrical domain [105]) it could be possible to perform computation and data storage simultaneously, at the same physical location. Thus, this platform provides a promising route for implementing unconventional computing strategies, including photonic neuro-synaptic and (non von-Neumann) arithmetic processing. Additionally, optically accessible memories could potentially solve the von-Neumann bottleneck of conventional computer architectures. By eliminating electro-optical conversions, photonic memories could reduce latencies, heat, bandwidth, and speed limitations in the data traffic between the processing and the memory units.

All this, however, requires further research to determine the optimum integration architectures to be able to address independent memory cells within a large on-chip photonic circuit. Light routing plays an important role; the pump pulses to *Write* or *Erase* should be able to reach a specific memory within the architecture without interfering with other elements or the signal itself. In this direction, only one solution has been successfully demonstrated using wavelength division multiplexing based on ring-resonators [67]. Nonetheless, there is a long way before a large number of memories can be integrated within one architecture with real functionality.

Mixed-mode devices

A combination of electronics and optics could lead to multiple options when employing PCMs. To switch between states, either short optical or electrical pulses can be used to heat up or melt-quench the alloy. To retrieve the phase state, the high contrast in the optical reflectivity, the optical attenuation, and the electrical resistivity allow for the clear differentiation of the amorphous and the crystalline phases, and even partial crystallisation levels in between. There are many options. Purely optical or electrical devices can be built, as well as hybrid optoelectronic devices where the switching is done optically and the readout electrically, or vice-versa. All these options could imply interesting nano- and macroscopic applications ranging from light/current modulators to unconventional computation architectures that simultaneously harness the memristive and accumulation/multilevel properties of PCMs. In particular, the advanced technology in silicon electronics permits a better on-chip control of PCMs. If this feature is integrated into a photonic circuit, then electrical pulses could be used to switch while optical modes could read out and process the information. This, in turn, would facilitate tremendously the positioning, local switching, control, and integration of a high number of memory cells within one-chip architecture.

Colour-modulation applications

PCMs are good candidates for the next generation of display technology thanks to the achievable ultra-high resolution, flexibility, and bistability [33]. These future displays could be used in reflective-type devices which can be operated under direct sunlight, given the good contrast between colours in either crystallographic states of PCMs. Moreover, by exploiting the non-volatile nature of the pixels, the power consumption of a display can be reduced, given that no refreshing is required, contrary to conventional displays. Only pixels that require to switch will use power, leaving the rest unchanged and unbiased. This feature could save battery life in devices such as mobile phones, in which the screen consumes a significant amount of the battery power, even when idling. Lastly, flexible displays can be achieved with PCM-based devices, given their low dimensionality.

As a newborn application, nano-pixel technologies using phase-change materials represent a highly promising research field for PCMs in applications such as holography and nano-optical security tags. Future work could be done in exploring other volatile (VO_2) and non-volatile (AgInSbTe, GeTe, etc) alloys in the quest for best colour range and lower switching energies. Moreover, the development of a real display with $N \times M$ switchable pixels represents a challenge that could be addressed using arrays of electrical cross-bars which could lead to better displays.

Besides displays, a possible application is to use the maximum contrast, the low resolution, or the polarisation dependency as security marks. One way to hide information could be achieved by using the high resolution of the pixels in optical cavities, including PCMs, to codify information (bar-codes and QR-codes, for instance) in low-dimensional features that can be read with specialised equipment. The colour contrast between states of a particular sample also can be used to codify the same information in the light-source wavelength. If the colours are hard to differentiate with the naked eye, a

monochromatic light source tuned at the maximum contrast wavelength can be used to properly discriminate between areas in the amorphous and the crystalline state. Moreover, the angular colour and polarisation dependence can be used to fabricate security marks as commonly used with holograms; the advantage, however, would be the option of writing and erasing patterns. These multiple options could lead to the implementation of multi-level security schemes where security checks plus several write/erase processes can be carried out by exploiting the non-volatility of phase-change materials and the back-and-forth switching between the two states.

Publications, patents, and conferences

The direct contributions of this thesis are summarised in the following list of publications, conferences, and patents.

Publications in peer-reviewed journals:

- **C. Ríos**, P. Hosseini, R.A. Taylor, and H. Bhaskaran. Color Depth Modulation and Resolution in Phase-Change Material Nanodisplays. *Advanced Materials*, 28(23), pp.4720-4726. 2016.
- **C. Ríos**, M. Stegmaier, P. Hosseini, D. Wang, T. Scherer, C.D. Wright, H. Bhaskaran, and W.H.P Pernice. Integrated all-photonic non-volatile multi-level memory. *Nature Photonics*, 9(11), pp.725-732, 2015.
- M. Stegmaier, **C. Ríos**, H. Bhaskaran, and W.H.P. Pernice. Thermo-optical Effect in Phase-Change Nanophotonics. *ACS Photonics*, 3(5), pp.828-835, 2016.
- M. Stegmaier, **C. Ríos**, H. Bhaskaran, C.D. Wright, and W.H.P. Pernice. Non-volatile All-Optical 1×2 Switch for Chipscale Photonic Networks. *Advanced Optical Materials*, *In press*, 2016.

Publication in preparation:

- **C. Ríos**, M. Stegmaier, W.H.P. Pernice, and H. Bhaskaran. Near-field switching dynamics of phase-change materials on photonic circuits.

Publications in peer-reviewed conferences:

- **C. Ríos**, M. Stegmaier, C.D. Wright, W.H.P Pernice, and H. Bhaskaran. Phase-change nanophotonic memories. *Submitted* to 2016 IEEE Electron Devices Meeting, 2016.
- **C. Ríos**, M. Stegmaier, W.H.P Pernice, and H. Bhaskaran. Multi-level storage in non-volatile phase-change nanophotonic memories. In 29^{th} IEEE Photonics Conference (IPC). *Accepted for publication*, 2016.

- M. Stegmaier, J. Feldmann, **C. Ríos**, C.D. Wright, H. Bhaskaran, and W.H.P Pernice. Integrated phase-change photonics for all-optical processing. In the European Phase Change and Ovonic Symposium, E/PCOS, 2016.

- P. Hosseini*, **C. Ríos***, C.D. Wright, and H. Bhaskaran, H. Phase change materials in light modulating applications beyond data storage. In the European Phase Change and Ovonic Symposium, E/PCOS 2015.

- M. Stegmaier, **C. Ríos**, P. Hosseini, C.D. Wright, H. Bhaskaran, and W.H.P. Pernice, 2015, October. All-photonic nonvolatile memory cells using phase-change materials. In 28^{th} IEEE Photonics Conference (IPC) (pp. 484-485). 2015.

- M. Stegmaier, **C. Ríos**, C.D. Wright, H. Bhaskaran, and W.H.P Pernice. Thermo-optic effect of GeSbTe in on-chip photonic circuitries at telecommunication wavelengths. In the European Phase Change and Ovonic Symposium, E/PCOS 2015.

* These authors contributed equally

Oral presentations in conferences:

- **C. Ríos**, M. Stegmaier, H. Bhaskaran, and W.H.P Pernice. Multi-level storage in non-volatile phase-change nanophotonic memories. In 29^{th} IEEE Photonics Conference (IPC). Hawaii, USA. 2016.

- **C. Ríos**, M. Stegmaier, P. Hosseini, C.D. Wright, H. Bhaskaran, and W.H.P Pernice. Integrated All-photonic Data Storage Enabled by Phase-change Materials. In 5th International Conference Smart and Multifunctional Materials, Structures and Systems, CIMTEC 2016, Abstract K-2-L10. Perugia, Italy, 2016.

- **C. Ríos**, M. Stegmaier, P. Hosseini, C.D. Wright, H. Bhaskaran, and W.H.P Pernice. Phase-Change Chalcogenide Photonics. In Glass Reflections Conference, Cambridge, UK, 2015.

- **C. Ríos**, M. Stegmaier, P. Hosseini, C.D. Wright, H. Bhaskaran, and W.H.P Pernice. Nanophotonics meets phase-change materials. In SPIE- FOCUS Latin America 2014. Medellín, Colombia. 2014.

Poster presentations in conferences:

- **C. Ríos**, P. Hosseini, C.D. Wright, H. Bhaskaran, and W.H.P Pernice. Growth and nucleation dominated phase-change materials for nano-optoelectronics and display technology. The 11th International Nanotechnology Conference on Communication and Cooperation, INC 11. Fukuoka, Japan. 2015.

Invited talks:

- **C. Ríos**. Photonic circuits: processing and storing data using light. Linacre College Seminars. Oxford, UK. 2015.

- **C. Ríos**. Nanofotónica Integrada: óptica en un chip (Integrated nanophotonics: light on a chip). Reunión de Fibras Ópticas y Procesado de Señal. Valencia, Spain, 2014.

Patents:

- Zengguang Chen, **Carlos A. Ríos Ocampo**, Wolfram H.P. Pernice, and Harish Bhasakaran. Optical device (Low-loss non-volatile optical switch using directional couplers). Filed in April 2016. Pending.
- **Carlos A. Ríos Ocampo**, Matthias Stegmaier, Gerardo Rodríguez-Hernández, Wolfram H.P. Pernice, and Harish Bhasakaran. Photonic Device (Tunable photonic circuits based on GST). PCT application number: PCT/GB2016/052871. Filed in Oct. 2014
- Peiman Hosseini, **Carlos A. Ríos Ocampo**, and Harish Bhaskaran. Optical Device (to exploit colour variations of optical nanocavities employing phase-change materials). United Kingdom patent publication No. WO/2015/097469. PCT international application number: PCT/GB2016/053826. Filed in Dec. 2014.

Bibliography

[1] S. R. Ovshinsky. Reversible electrical switching phenomena in disordered structures. *Phys. Rev. Lett.*, 21:1450–1453, 1968.

[2] J. Feinleib, J. de Neufville, S. C. Moss, and S. R. Ovshinsky. Rapid reversible light-induced crystallization of amorphous semiconductors. *Appl. Phys. Lett.*, 18:254, 1971.

[3] M. Chen, K. Rubin, and R. W. Barton. Compound materials for reversible, phase-change optical data storage. *Appl. Phys. Lett.*, 49(9):502, 1986.

[4] N. Yamada, E.i Ohno, N. Akahira, K. Nishiuchi, K. Nagata, and M. Takao. High Speed Overwritable Phase Change Optical Disk Material. *Proc. Int. Symp. on Optical Memory*, 26:61–66, 1987.

[5] D.J. Gravesteijn. Materials developments for write-once and erasable phase-change optical recording. *Appl. Opt.*, 27(4):6–8, 1988.

[6] S. Y. Kim, S. J. Kim, H. Seo, and M. R. Kim. Variation of the complex refractive indices with Sb-addition in Ge-Sb-Te alloy and their wavelength dependence. *Proc. SPIE*, 3401:112–118, 1998.

[7] I. Friedrich, V. Weidenhof, W. Njoroge, P. Franz, and M. Wuttig. Structural transformations of $Ge_2Sb_2Te_5$ films studied by electrical resistance measurements. *J. Appl. Phys.*, 87:254, 2000.

[8] D Loke, T H Lee, W J Wang, L P Shi, R Zhao, Y C Yeo, T C Chong, and S R Elliott. Breaking the speed limits of phase-change memory. *Science*, 336(6088):1566–1569, 2012.

[9] N. Yamada and T. Matsunaga. Structure of laser-crystallized $Ge_2Sb_{2+x}Te_5$ sputtered thin films for use in optical memory. *J. Appl. Phys.*, 88:7020–7028, 2000.

[10] S. Raoux, G. W. Burr, M. J. Breitwisch, C. T. Rettner, Y. C. Chen, R. M. Shelby, M. Salinga, D. Krebs, S. H. Chen, H. L. Lung, and C. H. Lam. Phase-change random access memory: A scalable technology. *IBM J. Res. Dev.*, 52:465–479, 2008.

[11] E. R. Meinders, A. V. Mijritskii, L. van Pieterson, and M. Wuttig. *Optical Data Storage: Phase Change Media and Recording*. Springer, Berlin, 2006.

[12] M. Wuttig and N. Yamada. Phase-change materials for rewriteable data storage. *Nature Mater.*, 6:824–832, 2007.

[13] D. Lencer, M. Salinga, and M. Wuttig. *Phase-Change Materials for Data Storage Applications*. Springer, 2014.

[14] S.-H. Lee, Y. Jung, and R. Agarwal. Highly-scalable nonvolatile and ultra-low power phase-change nanowire memory. *Nat. Nanotechnol.*, 2:626–630, 2007.

[15] T. Tuma, A. Pantazi, M. Le Gallo, A. Sebastian, and E. Eleftheriou. Stochastic phase-change neurons. *Nat. Nanotech.*, 11:693–699, 2016.

[16] P. Hosseini, A. Sebastian, N. Papandreou, C.D. Wright, and H. Bhaskaran. Accumulation-based computing using phase-change memories with fet access devices. *IEEE Electron Device Lett.*, 2015.

[17] F. Bedeschi, R. Fackenthal, C. Resta, E.M. Donze, M. Jagasivamani, E.C. Buda, F. Pellizzer, D.W. Chow, A. Cabrini, G.M.A. Calvi, et al. A bipolar-selected phase change memory featuring multi-level cell storage. *IEEE J. Solid-State Circuits*, 44(1):217–227, 2009.

[18] W.W. Koelmans, A. Sebastian, V.P. Jonnalagadda, D. Krebs, L. Dellmann, and E. Eleftheriou. Projected phase-change memory devices. *Nat. Commun.*, 6, 2015.

[19] R.E. Simpson, P. Fons, a V. Kolobov, T. Fukaya, M. Krbal, T. Yagi, and J. Tominaga. Interfacial phase-change memory. *Nat. Nanotech.*, 6(8):501–505, 2011.

[20] T. Matsunaga, J. Akola, S.i Kohara, T. Honma, K. Kobayashi, E. Ikenaga, R. O Jones, N. Yamada, M. Takata, and R. Kojima. Recrystallization dynamics in $AgInSbTe$ phase-change materials. *Nat. Mater.*, 10:129–134, 2011.

[21] G. W. Burr, M. J. Brightsky, A. Sebastian, H. Y. Cheng, J. Y. Wu, S. Kim, N. E. Sosa, N. Papandreou, H. L. Lung, H. Pozidis, E. Eleftheriou, and C. H. Lam. Recent progress in phase-change memory technology. *IEEE Journal on Emerging and Selected Topics in Circuits and Systems*, 6(2):146–162, June 2016.

[22] D. Kuzum, R.G.D. Jeyasingh, B. Lee, and H.S.P. Wong. Nanoelectronic programmable synapses based on phase change materials for brain-inspired computing. *Nano Lett.*, 12:2179–2186, 2012.

[23] C.D. Wright. Phase-change devices: Crystal-clear neuronal computing. *Nat. Nanotech.*, 11:655–656, 2016.

[24] M. Suri, O. Bichler, D. Querlioz, B. Traoré, O. Cueto, L. Perniola, V. Sousa, D. Vuillaume, C. Gamrat, and B. DeSalvo. Physical aspects of low power synapses based on phase change memory devices. *J. Appl. Phys.*, 112:054904, 2012.

[25] G W Burr, R M Shelby, C Nolfo, J W Jang, R S Shenoy, P Narayanan, K Virwani, E U Giacometti, B Kurdi, and H Hwang. Experimental demonstration and tolerancing of a large-scale neural network (165,000 synapses), using phase-change memory as the synaptic weight element. *International Electron Devices Meeting Proceeding*, 2014.

[26] W. H. P. Pernice and H. Bhaskaran. Photonic non-volatile memories using phase change materials. *Appl. Phys. Lett.*, 101:171101, 2012.

[27] C. Ríos, P. Hosseini, C.D. Wright, H. Bhaskaran, and W.H.P. Pernice. On-Chip Photonic Memory Elements Employing Phase-Change Materials. *Adv. Mater.*, 26(9):1372–7, 2013.

[28] M. Rudé, J. Pello, R. E. Simpson, J. Osmond, G. Roelkens, J. J. G. M. van der Tol, and V. Pruneri. Optical switching at 1.55 μm in silicon racetrack resonators using phase change materials. *Appl. Phys. Lett.*, 103(14):141119, 2013.

[29] Q. Wang, E.T.F. Rogers, B. Gholipour, C.-M. Wang, G. Yuan, J. Teng, and N.I. Zheludev. Optically reconfigurable metasurfaces and photonic devices based on phase change materials. *Nat. Photon.*, 10(1):60–65, 2016.

[30] E. Kuramochi and M. Notomi. Optical memory: Phase-change memory. *Nat. Photon.*, 9(11):712–714, 2015.

[31] P. Li, X. Yang, T.W.W. Maß, J. Hanss, M. Lewin, A.-K.U. Michel, M. Wuttig, and T. Taubner. Reversible optical switching of highly confined phonon-polaritons with an ultrathin phase-change material. *Nat. Mater.*, 15:870–875, 2016.

[32] S. Cueff, D. Li, Y. Zhou, F.J. Wong, J.A. Kurvits, S. Ramanathan, and R. Zia. Dynamic control of light emission faster than the lifetime limit using VO_2 phase-change. *Nat. Commun.*, 6, 2015.

[33] P. Hosseini, C. D. Wright, and H. Bhaskaran. An optoelectronic framework enabled by low-dimensional phase-change films. *Nature*, 511(7508):206–211, 2014.

[34] E. Kuramochi, K. Nozaki, A. Shinya, K.i Takeda, T. Sato, S.i Matsuo, H. Taniyama, H. Sumikura, and M. Notomi. Large-scale integration of wavelength-addressable all-optical memories on a photonic crystal chip. *Nat. Photon.*, 8(6):474–481, 2014.

[35] M.T. Hill, H.J.S. Dorren, and T.D. Vries. A fast low-power optical memory based on coupled micro-ring lasers. *Nature*, 432:11–14, 2004.

[36] S. Zimmermann. A Semiconductor-Based Photonic Memory Cell. *Science*, 283(5406):1292–1295, 1999.

[37] T. Tanabe, M. Notomi, E. Kuramochi, A. Shinya, and H. Taniyama. Trapping and delaying photons for one nanosecond in an ultrasmall high-Q photonic-crystal nanocavity. *Nat. Photon.*, 1(1):49–52, 2007.

[38] L. Liu, R. Kumar, and K. Huybrechts. An ultra-small, low-power, all-optical flip-flop memory on a silicon chip. *Nat. Photon.*, 4:182–187, 2010.

[39] H. John Caulfield and Shlomi Dolev. Why future supercomputing requires optics. *Nat. Photon.*, 4:261–263, 2010.

[40] G. T. Reed. *Silicon Photonics: The State of the Art*. Springer, Berlin, 2008.

[41] M.H.R. Lankhorst, B.W.S Ketelaars, and R. Wolters. Low-cost and nanoscale non-volatile memory concept for future silicon chips. *Nat. Mater.*, 4(4):347–52, 2005.

[42] C. D. Wright, P. Hosseini, and J. A. Vazquez-Diosdado. Beyond von-Neumann computing with nanoscale phase-change memory devices. *Adv. Funct. Mater.*, 23:2248–2254, 2013.

[43] D. Lencer, M. Salinga, and M. Wuttig. Design rules for phase-change materials in data storage applications. *Adv. Mater.*, 23:2030–2058, 2011.

[44] G. T. Reed, G. Mashanovich, F. Y. Gardes, and D. J. Thomson. Silicon optical modulators. *Nature Photon.*, 4:518–526, 2010.

[45] R. Jeyasingh, S.W. Fong, J. Lee, Z. Li, K-W. Chang, D. Mantegazza, M. Asheghi, K.E. Goodson, and H-S.P. Wong. Ultrafast characterization of phase-change material crystallization properties in the melt-quenched amorphous phase. *Nano Lett.*, 14(6):3419–26, 2014.

[46] S. Raoux, F. Xiong, M. Wuttig, and E. Pop. Phase change materials and phase change memory. *MRS Bulletin*, 39(08):703–710, 2014.

[47] G.W. Burr, M.J. Breitwisch, M. Franceschini, D. Garetto, K. Gopalakrishnan, B. Jackson, B. Kurdi, C. Lam, L.A. Lastras, A. Padilla, et al. Phase change memory technology. *J. Vac. Sci. Technol., B*, 28(2):223–262, 2010.

[48] M. Stanisavljevic, H. Pozidis, A. Athmanathan, N. Papandreou, T. Mittelholzer, and E. Eleftheriou. Demonstration of reliable triple-level-cell (tlc) phase-change memory. In *2016 IEEE 8th International Memory Workshop (IMW)*, pages 1–4. IEEE, 2016.

[49] Y. Ikuma, Y. Shoji, M. Kuwahara, X. Wang, K. Kintaka, H. Kawashima, D. Tanaka, and H. Tsuda. Small-sized optical gate switch using $Ge_2Sb_2Te_5$ phase-change material integrated with silicon waveguide. *Electronics Letters*, 46(5):368, 2010.

[50] H.A. Macleod. *Thin-film optical filters*. CRC Press, 2010.

[51] P Yeh. *Optical waves in layered media*. Wiley series in pure and applied optics. Wiley, New York, 1988.

[52] M.S. Unlu and S. Strite. Resonant cavity enhanced photonic devices. *J. Appl. Phys.*, 78(2):607, 1995.

[53] P. Yeh, A. Yariv, and Y. Cho. Optical surface waves in periodic layered media. *Appl. Phys. Lett.*, 32(2):104–105, 1978.

[54] M. Kats and F. Capasso. Ultra-thin optical interference coatings on rough and flexible substrates. *Appl. Phys. Lett.*, 105(13):131108, 2014.

[55] M. Kats, R. Blanchard, P. Genevet, and F. Capasso. Nanometre optical coatings based on strong interference effects in highly absorbing media. *Nat. Mater.*, 12(1):20–4, 2013.

[56] C Granqvist. Electrochromism and smart window design. *Solid State Ion.*, 53-56:479–489, 1992.

[57] P. Monk, R. Mortimer, and D. Rosseinsky. *Electrochromism and electrochromic devices*. Cambridge University Press, 2007.

[58] R.H. Yan, R. J. Simes, and L. A. Coldren. Electroabsorptive Fabry-Perot modulators with asymmetric mirrors. *IEEE Photonics Technology Letters*, 1(9):273–275, 1989.

[59] A. Seeboth, D. Loetzsch, and R. Ruhmann. Piezochromic Polymer Materials Displaying Pressure Changes in Bar-Ranges. *American Journal of Materials Science*, 1(2):139–142, 2012.

[60] S.J. Tan, L. Zhang, D. Zhu, X.M. Goh, Y.M. Wang, K. Kumar, C.-W. Qiu, and J.K.W. Yang. Plasmonic color palettes for photorealistic printing with aluminum nanostructures. *Nano Lett.*, 14(7):4023–9, jul 2014.

[61] T.S. Enda, Y.-J.C. Ho, T.H. Irakawa, and H.O. Kamoto. Development of Full-Color Display Combined with Ultraviolet-Electroluminescence / Photoluminescence Multilayered Thin Films. *Jpn. J. Appl. Phys.*, 39(8):4716–4720, 2000.

[62] A.C. Arsenault, T.J. Clark, G. von Freymann, L. Cademartiri, R. Sapienza, J. Bertolotti, E. Vekris, S. Wong, V. Kitaev, I. Manners, R.Z. Wang, S. John, D. Wiersma, and G. Ozin. From colour fingerprinting to the control of photoluminescence in elastic photonic crystals. *Nat. Mater.*, 5(3):179–184, 2006.

[63] M.A. Kats, D. Sharma, J. Lin, P. Genevet, R. Blanchard, Z. Yang, M.M. Qazilbash, D. N. Basov, S. Ramanathan, and F. Capasso. Ultra-thin perfect absorber employing a tunable phase change material. *Appl. Phys. Lett.*, 101(22):221101, 2012.

[64] A.C. Arsenault, D.P. Puzzo, I. Manners, and G. Ozin. Photonic-crystal full-colour displays. *Nat. Photon.*, 1(8):468–472, 2007.

[65] K.M. Charipar, N.A. Charipar, and A. Piqué. Bistable, multi-color electrowetting displays. In *2015 IEEE Photonics Conference (IPC)*, pages 55–56. IEEE, 2015.

[66] H. Fudouzi and Y. Xia. Colloidal crystals with tunable colors and their use as photonic papers. *Langmuir*, 19(23):9653–9660, 2003.

[67] C. Ríos, M. Stegmaier, P. Hosseini, D. Wang, T. Scherer, C.D. Wright, H. Bhaskaran, and W.H.P. Pernice. Integrated all-photonic non-volatile multi-level memory. *Nat. Photon.*, 9:725–732, 2015.

[68] J. Siegel, A. Schropp, J. Solis, C. N. Afonso, and M. Wuttig. Rewritable phase-change optical recording in $Ge_2Sb_2Te_5$ films induced by picosecond laser pulses. *Appl. Phys. Lett.*, 84(13):2250, 2004.

[69] D. Lencer, M. Salinga, B. Grabowski, T. Hickel, J. Neugebauer, and M. Wuttig. A map for phase-change materials. *Nat. Mater.*, 7(12):972–977, dec 2008.

[70] F.F. Schlich, P. Zalden, A.0M. Lindenberg, and R. Spolenak. Color Switching with Enhanced Optical Contrast in Ultrathin Phase-Change Materials and Semiconductors Induced by Femtosecond Laser Pulses. *ACS Photonics*, 2:178–182, 2015.

[71] B.-S. Lee, J. R. Abelson, Bishop S. G., D. H. Kang, Cheong B.-K., and K.-B Kim. Investigation of the optical and electronic properties of $Ge_2Sb_2Te_5$ phase change material in its amorphous, cubic, and hexagonal phases. *J. Appl. Phys.*, 97:093509, 2005.

[72] Carlos A. Ríos Ocampo, Matthias Stegmaier, Gerardo Rodríguez-Hernández, Wolfram H.P. Pernice, and Harish. Bhasakaran. *Photonic Device (Tunable photonic circuits based on GST).* Number PCT/GB2016/052871. Application number PCT/GB2016/052871. Filed in Oct. 2014.

[73] Peiman Hosseini, Carlos A. Ríos Ocampo, and Harish. Bhasakaran. *Optical Device (to exploit colour variations of optical nanocavities employing phase-change materials).* Number PCT/GB2016/052871. United Kingdom patent publication No. WO/2015/097469. PCT international application number: PCT/GB2016/053826. Filed in Dec. 2014.

[74] S. Yoo, T. Gwon, T. Eom, S. Kim, and C.S. Hwang. Multi-color changeable optical coating by adopting multiple layer of the ultrathin phase change material film. *ACS Photonics*, 3(7):1265–1270, 2016.

[75] A. Sharma, V.V. Tyagi, C.R. Chen, and D. Buddhi. Review on thermal energy storage with phase change materials and applications. *Renewable and Sustainable Energy Reviews*, 13(2):318–345, 2009.

[76] S. Raoux and M. Wuttig. *Phase Change Materials: Science and applications.* Springer, Berlin, 2009.

[77] L. F. Cabeza and H. Mehling. Review on thermal energy storage with phase change: materials, heat transfer analysis and applications. *Applied Thermal Engineering*, 23:251–283, 2003.

[78] D.C. Hyun, N.S. Levinson, U. Jeong, and Y. Xia. Emerging applications of phase-change materials (PCMs): teaching an old dog new tricks. *Angewandte Chemie (International ed. in English)*, 53(15):3780–95, 2014.

[79] G.-F. Zhou. Material aspects in phase change optical recording. *Mater. Sci. and Eng. A*, 73:304–306, 2001.

[80] L. van Pieterson, M. H. R. Lankhorst, M. van Schijndel, E. T. Kuiper, and J. H. J. Roosen. Phase-change recording materials with a growth-dominated crystallization mechanism: A materials overview. *J. Appl. Phys.*, 97(8):083520, 2005.

[81] B-S. Lee, R. Shelby, S. Raoux, C. T. Retter, G. Burr, S. Bogle, K. Darmawikarta, S. G. Bishop, and J. R. Abelson. Nanoscale nuclei in phase change materials: Origin of different crystallization mechanisms of $Ge_2Sb_2Te_5$ and $AgInSbTe$. *J. Appl. Physics*, 115(6):063506, 2014.

[82] J. H. Coombs, a. P. J. M. Jongenelis, W. van Es-Spiekman, and B.J. Jacobs. Laser-induced crystallization phenomena in GeTe-based alloys. I. Characterization of nucleation and growth. *J. Appl. Phys.*, 78(8):4906, 1995.

[83] B.-S. Lee, R.M. Shelby, S. Raoux, C.T. Retter, G.W. Burr, S.N. Bogle, K. Darmawikarta, S.G. Bishop, and J.R. Abelson. Nanoscale nuclei in phase change materials: Origin of different crystallization mechanisms of $Ge_2Sb_2Te_5$ and AgInSbTe. *J. Appl. Phys.*, 115(6):063506, 2014.

[84] B-S. Lee, R.M. Shelby, S. Raoux, C.T. Retter, G.W. Burr, S.N. Bogle, K. Darmawikarta, S.G. Bishop, and J.R. Abelson. Nanoscale nuclei in phase change materials: Origin of different crystallization mechanisms of $Ge_2Sb_2Te_5$ and *aginsbte*. *J. Appl. Phys.*, 115(6):063506, 2014.

[85] N. Yamada. Origin, secret, and application of the ideal phase-change material GeSbTe. *Physica Status Solidi (B)*, 249(10):1837–1842, 2012.

[86] W. K. Njoroge, H. W. Woltgens, and M. Wuttig. Density changes upon crystallization of $Ge_2Sb_{2.04}Te_{4.74}$ films. *J. Vac. Sci. Technol. A*, 20:230–233, 2002.

[87] W. K. Njoroge. *Phase Change Optical Recording Preparation and X-ray Characterization of GeSbTe and AgInSbTe films*. PhD thesis, Rheinisch-Westfaelischen Technischen Hochschule Aachen, 2001.

[88] T. Tsafack, E. Piccinini, B.-S. Lee, E. Pop, and M. Rudan. Electronic, optical and thermal properties of the hexagonal and rocksalt-like $Ge_2Sb_2Te_5$ chalcogenide from first-principle calculations. *J. Appl. Phys.*, 110:063716, 2011.

[89] A. Chabli, C Vergnaud, F Bertin, V Gehanno, B Valon, B Hyot, B Bechevet, M Burdin, and D Muyard. Temperature dependence of structural and optical properties of GeSbTe alloy thin films. *Journal of Magnetism and Magnetic Materials*, 249(3):509–512, 2002.

[90] A. V. Kolobov, P. Fons, A. I. Frenkel, A. L. Ankudinov, J. Tominaga, and T. Uruga. Understanding the phase-change mechanism of rewritable optical media. *Nat. Mater.*, 3(10):703–8, 2004.

[91] S. Kohara, K. Kato, S. Kimura, H. Tanaka, T. Usuki, K. Suzuya, H. Tanaka, Y. Moritomo, T. Matsunaga, N. Yamada, Y. Tanaka, H. Suematsu, and M. Takata. Structural basis for the fast phase change of $Ge_2Sb_2Te_5$: Ring statistics analogy between the crystal and amorphous states films studied by electrical resistance measurements. *Appl. Phys. Lett.*, 89:201910, 2006.

[92] J. A. Kalb, M. Wuttig, and F. Spaepen. Calorimetric measurements of structural relaxation and glass transition temperatures in sputtered films of amorphous te alloys used for phase change recording. *J. Mater. Res.*, 22:748–754, 2007.

[93] P. W. Anderson. Absence of diffusion in certain random lattices. *Phys. Rev.*, 109:1492–1505, 1958.

[94] N. Yamada, R. Kojima, M. Uno, T. Akiyama, H. Kitaura, K. Narumi, and K. Nishiuchi. Phase-change material for use in rewritable dual-layer optical disk. *Proc. SPIE*, 55:4342, 2002.

[95] J. Robertson and B. Huang. Bonding and optical contrast in phase change memory materials. *Physica Status Solidi (B) Basic Research*, 249:1867–1873, 2012.

[96] A. V. Kolobov, P. Fons, A. I. Frenkel, A. L. Ankudinov, J. Tominaga, and T. Uruga. Understanding the phase-change mechanism of rewritable optical media. *Nature Mater.*, 3:703–708, 2004.

[97] W. Welnic, A. Pamungkas, R. Detemple, C. Steimer, S. BlÃ¼gel, and M. Wuttig. Unravelling the interplay of local structure and physical properties in phase-change materials. *Nature Mater.*, 5:56 – 62, 2006.

[98] K. Shportko, S. Kremers, M. Woda, D. Lencer, J. Robertson, and M. Wuttig. Resonant bonding in crystalline phase-change materials. *Nat. Mater.*, 7(8):653–8, 2008.

[99] M. Stegmaier, C. Ríos, H. Bhaskaran, and W.H.P. Pernice. Thermo-optical effect in phase-change nanophotonics. *ACS Photonics*, 3(5):828–835, 2016.

[100] S.C. Agarwal. Role of potential fluctuations in phase-change GST memory devices. *Physica Status Solidi (B) Basic Research*, 249:1956–1961, 2012.

[101] A. Pirovano, A.L. Lacaita, A. Benvenuti, F. Pellizzer, S. Hudgens, and R. Bez. Scaling analysis of phase-change memory technology. *IEEE International Electron Devices Meeting 2003*, 2003.

[102] S. Hudgens. Progress in understanding the Ovshinsky Effect: Threshold switching in chalcogenide amorphous semiconductors. *Physica Status Solidi (B) Basic Research*, 249:1951–1955, 2012.

[103] W. Czubatyj and S.J. Hudgens. Invited paper: Thin-film Ovonic threshold switch: Its operation and application in modern integrated circuits. *Electronic Materials Letters*, 8:157–167, 2012.

[104] F. Xiong, A.D. Liao, D. Estrada, and E. Pop. Low-Power switching of Phase-Change Materials with carbon nanotube electrodes. *Science*, 332:2–5, 2011.

[105] A Pantazi, A Sebastian, N Papandreou, M J Breitwisch, C Lam, H Pozidis, and E Eleftheriou. Multilevel phase-change memory modeling and experimental characterization. *EPCOS 2009 conference proceedings*, pages 34–41, 2009.

[106] A. Sebastian, D. Krebs, M. Le Gallo, H. Pozidis, and E. Eleftheriou. A collective relaxation model for resistance drift in phase change memory cells. In *2015 IEEE International Reliability Physics Symposium*, pages MY–5. IEEE, 2015.

[107] L. Chua. Memristor-The missing circuit element. *IEEE Transactions on Circuit Theory*, 18, 1971.

[108] D.B. Strukov, G.S. Snider, D.R. Stewart, and R.S. Williams. The missing memristor found. *Nature*, 453(7191):80–3, 2008.

[109] S.H. Jo, T. Chang, I. Ebong, B.B. Bhadviya, P. Mazumder, and W. Lu. Nanoscale memristor device as synapse in neuromorphic systems. *Nano Lett.*, 10(4):1297–301, 2010.

[110] J. Borghetti, G.S. Snider, P.J. Kuekes, J.J. Yang, D.R. Stewart, and R.S. Williams. 'Memristive' switches enable 'stateful' logic operations via material implication. *Nature*, 464(7290):873–6, 2010.

[111] D. Choquet and A. Triller. The dynamic synapse. *Neuron*, 80:691–703, 2013.

[112] M. Suri, O. Bichler, D. Querlioz, O. Cueto, L. Perniola, V. Sousa, D. Vuillaume, C. Gamrat, and B. DeSalvo. Phase change memory as synapse for ultra-dense neuromorphic systems: Application to complex visual pattern extraction. *2011 International Electron Devices Meeting*, pages 4.4.1–4.4.4, 2011.

[113] S. Woźniak, T. Tuma, A. Pantazi, and E. Eleftheriou. Learning spatio-temporal patterns in the presence of input noise using phase-change memristors. In *2016 IEEE International Symposium on Circuits and Systems (ISCAS)*, pages 365–368. IEEE, 2016.

[114] G.W. Burr, R.S. Shenoy, K. Virwani, P. Narayanan, A. Padilla, B. Kurdi, and H. Hwang. Access devices for 3d crosspoint memory. *J. Vac. Sci. Technol., B*, 32(4):040802, 2014.

[115] C. a. Volkert and M. Wuttig. Modeling of laser pulsed heating and quenching in optical data storage media. *J. Appl. Phys.*, 86(4):1808, 1999.

[116] Lutz Waldecker, Timothy A Miller, Miquel Rudé, Roman Bertoni, Johann Osmond, Valerio Pruneri, Robert E Simpson, Ralph Ernstorfer, and Simon Wall. Time-domain separation of optical properties from structural transitions in resonantly bonded materials. *Nat. Mater.*, 14(July):1–6, 2015.

[117] C. D. Wright, Y. Liu, K.I. Kohary, M. M. Aziz, and R. J. Hicken. Arithmetic and biologically-inspired computing using phase-change materials. *Adv. Mat.*, 23:3408–3413, 2011.

[118] H. Tsuda, T. Moriyama, P. Jain, D. Tanaka, M. Kuwahara, and X. Wang. Compact optical switch using phase-change material for transparent photonic network. *EPCOS 2013 conference proceedings*, pages 2–5, 2013.

[119] T. Moriyama, D. Tanaka, P. Jain, H. Kawashima, M. Kuwahara, X. Wang, and H. Tsuda. Ultra-compact, self-holding asymmetric mach-zehnder interferometer switch using $Ge_2Sb_2Te_5$ phase-change material. *IEICE Electron. Expr.*, 11(15):20140538–20140538, 2014.

[120] R. M. Briggs, I. M. Pryce, and H. A Atwater. Compact silicon photonic waveguide modulator based on the vanadium dioxide metal-insulator phase transition. *Opt. Express*, 18(11):8837–8845, 2010.

[121] J. D Ryckman, K. A Hallman, R. E. Marvel, R. F. Haglund, and S. M. Weiss. Ultra-compact silicon photonic devices reconfigured by an optically induced semiconductor-to-metal transition. *Opt. Express*, 21(9):438–446, 2013.

[122] C. Rios, H. Peiman, C. D. Wright, H. Bhaskaran, and W. H. P. Pernice. Tunable nanophotonic circuits based on phase-change materials. In *E/PCOS 2013 Proceedings*, 2013.

[123] P. Hosseini and H. Bhaskaran. Colour performance and stack optimisation in phase change material based nano-displays. *Proc. SPIE*, 9520:95200M–95200M–7, 2015.

[124] G. Bakan, S. Ayas, T. Saidzoda, K. Celebi, and A. Dana. Ultrathin phase-change coatings on metals for electrothermally tunable colors. *Appl. Phys. Lett.*, 109(7):071109, 2016.

[125] C. Ríos, P. Hosseini, R.A. Taylor, and H. Bhaskaran. Color depth modulation and resolution in phase-change material nanodisplays. *Adv. Mater.*, 28(23):4720–4726, 2016.

[126] K-T Lee, S. Seo, and L. J. Guo. High-Color-Purity Subtractive Color Filters with a Wide Viewing Angle Based on Plasmonic Perfect Absorbers. *Adv. Opt. Mater.*, 2014.

[127] A. Faraon, D. Englund, D. Bulla, B. Luther-Davies, B. J. Eggleton, N. Stoltz, P. Petroff, and J. Vuckovicc. Local tuning of photonic crystal cavities using chalcogenide glasses. *Appl. Phys. Lett.*, 92(4):043123, 2008.

[128] B. J. Eggleton, B. Luther-Davies, and K. Richardson. Chalcogenide photonics. *Nat. Photon.*, 5(3):141–148, 2011.

[129] L. Zou, M. Cryan, and M. Klemm. Phase change material based tunable reflectarray for free-space optical inter/intra chip interconnects. *Opt. Express*, 22(20):24142–24148, 2014.

[130] W. Dong, Y. Qiu, J.K.W. Yang, R.E. Simpson, and T. Cao. Wideband absorbers in the visible with ultrathin plasmonic-phase change material nanogratings. *J. of Phys. Chem. C*, 120(23):12713–12722, 2016.

[131] S. G.-C. Carrillo, G.R. Nash, H. Hayat, M.J. Cryan, M. Klemm, H. Bhaskaran, and C.D. Wright. Design of practicable phase-change metadevices for near-infrared absorber and modulator applications. *Opt. Express*, 24(12):13563–13573, 2016.

[132] T. Cao, G. Zheng, S. Wang, and C. Wei. Ultrafast beam steering using gradient $Au - Ge_2Sb_2Te_5 - Au$ plasmonic resonators. *Opt. Express*, 23(14):18029–18039, 2015.

[133] T. Cao, C. Wei, and L. Mao. Numerical study of achiral phase-change metamaterials for ultrafast tuning of giant circular conversion dichroism. *Sci. Rep.*, 5, 2015.

[134] N. Syafawati, B. Humam, Y. Sato, M. Takahashi, S. Kanazawa, N. Tsumori, P. Regreny, M. Gendry, and T. Saiki. Redshifted and blueshifted photoluminescence emission of InAs / InP quantum dots upon amorphization of phase change material. *Opt. Express*, 22(12):14830–14839, 2014.

[135] X. Yin, M. Schäferling, A.-K.U. Michel, A. Tittl, M. Wuttig, T. Taubner, and H. Giessen. Active chiral plasmonics. *Nano Lett.*, 15(7):4255–4260, 2015.

[136] A. Tittl, A.-K.U. Michel, M. Schäferling, X. Yin, B. Gholipour, L. Cui, M. Wuttig, T. Taubner, F. Neubrech, and H. Giessen. A switchable mid-infrared plasmonic perfect absorber with multispectral thermal imaging capability. *Adv. Mater.*, 27(31):4597–4603, 2015.

[137] P. Bharadwaj, B. Deutsch, and L. Novotny. Optical Antennas. *Advances in Optics and Photonics*, 1(3):438, 2009.

[138] A. K. Michel, D. N. Chigrin, T.W.W. Mass, K. Scho, M. Salinga, M. Wuttig, and T. Taubner. Using Low-Loss Phase-Change Materials for Mid-Infrared Antenna Resonance Tuning. *Nano Lett.*, 13(8):3470–3475, 2013.

[139] R. Alaee, M. Albooyeh, S. Tretyakov, and C. Rockstuhl. Phase-change material-based nanoantennas with tunable radiation patterns. *Opt. Lett.*, 41(17):4099–4102, Sep 2016.

[140] M.J. Polking, P.K. Jain, Y. Bekenstein, U. Banin, O. Millo, R. Ramesh, and A.P. Alivisatos. Controlling localized surface plasmon resonances in $GeTe$ nanoparticles using an amorphous-to-crystalline phase transition. *Phys. Rev. Lett.*, 111:037401, Jul 2013.

[141] A-K. Michel, P. Zalden, D.N. Chigrin, M. Wuttig, A.M. Lindenberg, and T. Taubner. Reversible optical switching of infrared antenna resonances with ultrathin phase-change layers using femtosecond laser pulses. *ACS Photonics*, page 140821162721001, 2014.

[142] B. Gholipour, J. Zhang, K.F. MacDonald, D.W. Hewak, and N.I. Zheludev. An all-optical, non-volatile, bidirectional, phase-change meta-switch. *Adv. Mater.*, 25(22):3050–3054, 2013.

[143] G. Kaplan, K. Aydin, and J. Scheuer. Dynamically controlled plasmonic nano-antenna phased array utilizing vanadium dioxide. *Opt. Mater. Express*, 5(11):2513–2524, 2015.

[144] O.L. Muskens, L. Bergamini, Y. Wang, J.M. Gaskell, N. Zabala, C.H. De Groot, D.W. Sheel, and J. Aizpurua. Antenna-assisted picosecond control of nanoscale phase-transition in vanadium dioxide. *Light: Science & Applications*, pages 1–25, 2016.

[145] Y. Abate, R.E. Marvel, J.I. Ziegler, S. Gamage, M.H. Javani, M.I. Stockman, and R.F. Haglund. Control of plasmonic nanoantennas by reversible metal-insulator transition. *Sci. Rep.*, 5, 2015.

[146] Z.L. Sámson, S.-C. Yen, K.F. MacDonald, K. Knight, S. Li, D.W. Hewak, D.-P. Tsai, and N.I Zheludev. Chalcogenide glasses in active plasmonics. *physica status solidi (RRL)-Rapid Research Letters*, 4(10):274–276, 2010.

[147] M. Rudé, R.E. Simpson, R. Quidant, V. Pruneri, and J. Renger. Active control of surface plasmon waveguides with a phase change material. *ACS Photonics*, 2(6):669–674, 2015.

[148] I. Staude and C. Rockstuhl. Surface phonon-polaritons: To scatter or not to scatter. *Nat. Mater.*, 15(8):821–822, 2016.

[149] A. Karvounis, B. Gholipour, K.F. MacDonald, and N.I. Zheludev. All-dielectric phase-change reconfigurable metasurface. *Appl. Phys. Lett.*, 109(5):051103, 2016.

[150] Y. Chen, X. Li, Y. Sonnefraud, A.I. Fernández-Domínguez, X. Luo, M. Hong, and S.A. Maier. Engineering the phase front of light with phase-change material based planar lenses. *Sci. Rep.*, 5, 2015.

[151] A. Shinya, S.i Matsuo, Yosia, T. Tanabe, E. Kuramochi, T.i Sato, T. Kakitsuka, and M. Notomi. All-optical on-chip bit memory based on ultra high Q InGaAsP photonic crystal. *Opt. Express*, 16(23):19382–7, 2008.

[152] C.A. Barrios and M.l Lipson. Silicon photonic read-only memory. *J. Lightwave Technol.*, 24(7):2898, 2006.

[153] S. Pitris, C. Vagionas, G. Kanellos, R. Kisasic, T. Tekin, R. Broeke, and N. Pleros. Optical static *RAM* cell using a monolithically integrated *InP* flip-flop and wavelength-encoded signals. In *Optical Fiber Communication Conference*, pages Tu2K–7. Optical Society of America, 2016.

[154] J.-F. Song, X.-S. Luo, A.E-J. Lim, C. Li, Q. Fang, T.-Y. Liow, L.-X. Jia, X.-G. Tu, Y. Huang, H.-F. Zhou, et al. Integrated photonics with programmable non-volatile memory. *Sci. Rep.*, 6, 2016.

[155] Y. Zhou, S.-T. Han, X. Chen, F. Wang, Y.-B. Tang, and V. L. Roy. An upconverted photonic nonvolatile memory. *Nat. Commun.*, 5:4720, 2014.

[156] M.A. Karim and A. A. Awwal. *Optical Computing: An Introduction*. John Wiley & Sons, Inc., New York, NY, USA, 1st edition, 1992.

[157] M. Di Ventra and Y. V. Pershin. The parallel approach. *Nature Physics*, 9(4):200–202, 2013.

[158] D. Woods and T. J. Naughton. Optical computing: Photonic neural networks. *Nature Physics*, 8(4):257–259, 2012.

[159] D.R. Solli and B. Jalali. Analog optical computing. *Nat. Photon.*, 9(11):704–706, 2015.

[160] C. Sun, M.T. Wade, Y. Lee, J.S. Orcutt, L. Alloatti, M.S. Georgas, A.S. Waterman, J.M. Shainline, R.R. Avizienis, S. Lin, et al. Single-chip microprocessor that communicates directly using light. *Nature*, 528(7583):534–538, 2015.

[161] Y. Shen, S. Skirlo, M. Soljacic, D.R. Englund, and N. Harris. On-chip optical neuromorphic computing. In *CLEO*, pages SM3E–2. Optical Society of America, 2016.

[162] S. Debnath, N.M. Linke, C. Figgatt, K.A. Landsman, K. Wright, and C. Monroe. Demonstration of a small programmable quantum computer with atomic qubits. *Nature*, 536(7614):63–66, 2016.

[163] Nicolas A., L. Veissier, L. Giner, E. Giacobino, D. Maxein, and J. Laurat. A quantum memory for orbital angular momentum photonic qubits. *Nat. Photon.*, 8(3):234–238, 2014.

[164] D. Paredes-Barato and C. S. Adams. All-optical quantum information processing using rydberg gates. *Phys. Rev. Lett.*, 112:040501, 2014.

[165] V.R Almeida, C.A Barrios, R.R Panepucci, and M. Lipson. All-optical control of light on a silicon chip. *Nature*, 431:1081–1084, 2004.

[166] P. Dong, G. Duan, Y.-K. Chen, and D.T. Neilson. *Merits and Potential Impact of Silicon Photonics*, pages 397–420. Springer Berlin Heidelberg, Berlin, Heidelberg, 2016.

[167] M. Li, W.H.P. Pernice, C. Xiong, T. Baehr-Jones, M. Hochberg, and H.X. Tang. Harnessing optical forces in integrated photonic circuits. *Nature*, 456(7221):480–484, 2008.

[168] F. Priolo, T. Gregorkiewicz, M. Galli, and T.F. Krauss. Silicon nanostructures for photonics and photovoltaics. *Nat. Nanotech.*, 9(1):19–32, 2014.

[169] R.S. Savelev, S.V. Makarov, A.E. Krasnok, and P.A. Belov. From optical magnetic resonance to dielectric nanophotonics (a review). *Opt. Spectrosc*, 119(4):551–568, 2015.

[170] A. E-J. Lim, J. Song, Q. Fang, C. Li, X. Tu, N. Duan, K.K. Chen, R. P-C.r Tern, and T-Y. Liow. Review of silicon photonics foundry efforts. *IEEE J. Sel. Topics Quantum Electron.*, 20(4):405–416, 2014.

[171] W. Bogaerts, D. Taillaert, B. Luyssaert, P. Dumon, J. Van Campenhout, P. Bienstman, D. Van Thourhout, R. Baets, V. Wiaux, and S. Beckx. Basic structures for photonic integrated circuits in silicon-on-insulator. *Opt. Express*, 12:1583–1591, 2004.

[172] B. Jalali and S. Fathpour. Silicon photonics. *J. Lightwave Technol.*, 24:4600–4615, 2006.

[173] S. V. Deshpande, E. Gulari, S. W. Brown, and S. C. Rand. Optical properties of silicon nitride films deposited by hot filament chemical vapor deposition. *J. Appl. Phys.*, 77:6534, 1995.

[174] W. Stutius and W. Streifer. Silicon nitride films on silicon for optical waveguides. *Appl. Opt.*, 16:3218, 1977.

[175] T. Baak. Silicon oxynitride; a material for grin optics. *Appl. Opt.*, 21:1069, 1982.

[176] A. Arbabi and L. L. Goddard. Measurements of the refractive indices and thermo-optic coefficients of Si_3N_4 and SiO_x using microring resonances. *Opt. Lett.*, 38(19):3878–3881, 2013.

[177] K. Y. Fong, W. H. P. Pernice, M. Li, and H. Tang. High Q optomechanical resonators in silicon nitride nanophotonic circuits. *Appl. Phys. Lett*, 97:073112, 2010.

[178] A. Gondarenko, J. A. Levy, and M. Lipson. High confinement micron-scale silicon nitride high Q ring resonator. *Opt. Express*, 17:11366, 2009.

[179] S. Zheng, H. Chen, and A. Poon. Microring-resonator cross-connect filters in silicon nitride: Rib waveguide dimensions dependence. *IEEE J. Sel. Top. Quant. Electron.*, 12:1380–1387, 2005.

[180] F. Morichetti, A. Melloni, M. Martinelli, R. G. Heideman, A. Leinse, D. H. Geuzebroek, and A. Borreman. Box-shaped dielectric waveguides: A new concept in integrated optics. *J. Lightwave Technol.*, 25:2579–2589, 2007.

[181] R. Paschotta. *Field Guide to Lasers*. SPIE Press, Bellingham, WA, 2008.

[182] K. Okamoto. *Fundamentals of Optical Waveguides*. Academic Print, Elsevier., 2006.

[183] A. Yariv and P. Yeh. *Photonics: optical electronics in modern communications. Oxford series in electrical and computer engineering*. Oxford University Press, NY., 2007.

[184] R. A. Soref, J. Schmidtchen, and K. Petermann. Large single-mode rib waveguides in Ge-Si and Si-on-SiO_2. *IEEE J. Quantum Electron.*, 27:1971–1974, 1991.

[185] J. T. Boyd and S. Sriram. Optical coupling from fibers to channel waveguides formed on silicon. *Appl. Opt.*, 17:895–898, 1978.

[186] W. K. Burns and G. B. Hocker. End fire coupling between optical fibers and diffused channel waveguides. *Appl. Opt.*, 16:2048, 1977.

[187] H. Tang and W.H.P. Pernice. Integrated optomechanical circuits and nonlinear dynamics. In *Cavity Optomechanics*, pages 169–194. Springer, 2014.

[188] D. Sarid. High efficiency input-output prism waveguide coupler: an analysis. *Appl. Opt.*, 18:2921–2926, 1979.

[189] M. L. Dakss, L. Kuhn, P. F. Heidrich, and B. A. Scott. Grating coupler for efficient excitation of optical guided waves in thin film. *Appl. Phys. Lett.*., 16:523, 1970.

[190] D. Taillaert, W. Bogaerts, P. Bienstman, T. Krauss, P. Van Daele, I. Moerman, S. Verstuyft, K. De Mesel, and R. Baets. An out-of-plane grating coupler for efficient butt-coupling between compact planar waveguides and single-mode fibers. *IEEE J. Quant. Electron.*, 38:949–955, 2002.

[191] D. Taillaert, W. Bogaerts, P. Bienstman, T. Krauss, P. Van Daele, I. Moerman, S. Verstuyft, K. De Mesel, and R. Baets. Channel optical waveguide directional couplers. *Appl. Phys. Lett.*, 46:1654468, 1973.

[192] J.-M. Liu. *Photonic devices*. Cambridge Univ. Press., 2005.

[193] G. Lifante. *Integrated photonics: fundamentals*. Wiley Online Library, 2003.

[194] A. Ganjoo, H. Jain, C. Yu, R. Song, J.V. Ryan, J. Irudayaraj, Y.J. Ding, and C.G. Pantano. Planar chalcogenide glass waveguides for ir evanescent wave sensors. *J. Non-Cryst. Solids*, 352(6):584–588, 2006.

[195] V. Ruddy, B.D. MacCraith, and J.A. Murphy. Evanescent wave absorption spectroscopy using multimode fibers. *J. Appl. Phys.*, 67(10):6070–6074, 1990.

[196] A. Messica, A. Greenstein, and A. Katzir. Theory of fiber-optic, evanescent-wave spectroscopy and sensors. *Appl. Opt.*, 35(13):2274–2284, 1996.

[197] H. Haus and J. Melcher. *Electromagnetic fields and energy*. Prentice Hall, 1989.

[198] J. D. Jackson. *Classical electrodynamics*. Wiley, 1999.

[199] T.L. Bergman, F. Incropera, D. DeWitt, and A. Lavine. *Fundamentals of heat and mass transfer*. John Wiley & Sons, 2011.

[200] Z. Chen. *Finite element methods and their applications*. Springer, Berlin, 2005.

[201] C.A. Rios Ocampo. Tunable nanophotonic circuits based on phase-change materials. Master's thesis, Karlsruhe Institute of Technology, Germany, 2013.

[202] N. Gruhler. Graphene-based optoelectronic devices embedded in nanophotonic circuits. Master's thesis, Karlsruhe Institute of Technology, 2013.

[203] E.F. Schubert. Materials refractive-index and extinction-coefficient. `http://www.rpi.edu/~schubert/Educational-resources/Materials-Refractive-index-and-extinction-coefficient.pdf`, 2017.

[204] M.l Antelius, K.B. Gylfason, and H. Sohlström. An apodized *SOI* waveguide-to-fiber surface grating coupler for single lithography silicon photonics. *Opt. Express*, 19(4):3592–3598, 2011.

[205] Y. Ding, H. Ou, and C. Peucheret. Ultrahigh-efficiency apodized grating coupler using fully etched photonic crystals. *Opt. Lett.*, 38(15):2732–2734, 2013.

[206] H. Kim, C. M. Gilmore, A. Piqué, J. S. Horwitz, H. Mattoussi, H. Murata, Z. H. Kafafi, and D. B. Chrisey. Electrical, optical, and structural properties of indium tin oxide thin films for organic light-emitting devices. *J. Appl. Phys.*, 86:6451–6461, 1999.

[207] Z. Zhu and T. G. Brown. Stress-induced birefringence in microstructured optical fiber. *Opt. Lett.*, 28:2306–2308, 2003.

[208] E.L. Wooten, K.M. Kissa, A. Yi-Yan, E.J. Murphy, D.A. Lafaw, P.F. Hallemeier, D. Maack, D.V. Attanasio, D.J. Fritz, G.J. McBrien, et al. A review of lithium niobate modulators for fiber-optic communications systems. *IEEE J. Sel. Topics Quantum Electron.*, 6(1):69–82, 2000.

[209] C CIE. Commission internationale de l'eclairage proceedings, 1931, 1932.

[210] T. Smith and J. Guild. The cie colorimetric standards and their use. *Transactions of the Optical Society*, 33(3):73, 1931.

[211] G. Wyszecki and W.S. Stiles. *Color science*, volume 8. Wiley New York, 1982.

[212] J. Morovic and M.R. Luo. The fundamentals of gamut mapping: A survey. *J. Imaging Sci. Technol.*, 45(3):283–290, 2001.

[213] Stephen Westland, Caterina Ripamonti, and Vien Cheung. *Computational colour science using MATLAB*. John Wiley & Sons, 2012.

[214] K. Vahala. *Optical microcavities*, volume 5. World Scientific, 2004.

[215] E. Hecht. *Optics, 4th Edition*. Addison-Wesley Longman Inc., 2002.

[216] Z. Guang-Jun, G. Dong-Hong, and G. Fu-Xi. Optical properties and structure of Sb-rich AgInSbTe phase change thin films. *Chinese Phys.*, 14(01):0218–05, 2005.

[217] H. Levkowitz. *Color theory and modeling for computer graphics, visualization, and multimedia applications*, volume 402. Springer Science & Business Media, 1997.

[218] K. Do, D. Lee, D.-H. Ko, H. Sohn, and M.-H. Cho. TEM Study on Volume Changes and Void Formation in $Ge_2Sb_2Te_5$ Films, with Repeated Phase Changes. *Electrochem. Solid-State Lett.*, 13(8):H284, 2010.